A Thesis Submitted for the Degree of PhD at the University of Warwick

Material and Design Optimisation of Low Temperature Direct Ammonia Fuel Cells

Georgina Jeerh

A thesis submitted for the degree of Doctor of Philosophy in Engineering

University of Warwick, School of Engineering

September 2022

Table of Contents

List of Tables and Illustrated Materials 5
Acknowledgements 15
Declaration 17
List of Publications 19
Abstract 21
Abbreviations 22
CHAPTER 1 Introduction 25
1.1. Energy Demand 25
1.2. Fuel Cells 28
1.2.1. Terminology 28
1.2.2. Hydrogen as a Fuel 32
1.2.3. Alternatives to Hydrogen 33
1.3. Direct Ammonia Fuel Cells 36
1.3.1. Reaction Mechanism 39
1.3.2. Challenges 40
1.4. Aim of Project 41
CHAPTER 2 Literature Review 43
2.1. Introduction 43
2.1.1. Direct Ammonia Fuel Cells 43
2.1.2. Membrane Choice 46
2.1.3. Electrocatalyst Choice 48
2.2. Aim of Review 50
2.3. Perovskite Oxide Catalysts 50
2.3.1. Background 50
2.3.2. Key Factors Influencing Oxygen Reduction Activity 53
2.3.3. Potential Towards Ammonia Oxidation Activity 64
2.4. Perspective of Perovskites as Cathodes 65
2.5. Conclusions 70
CHAPTER 3 Experimental Details 73
3.1. Sample Preparation 73

3.1.1. Pechini Method 73
3.1.2. Ink Composition 73
3.2. Physicochemical Characterisation 74
3.2.1. X-ray Diffraction 74
3.2.2. Scanning Electron Microscopy and Energy Dispersive X-ray Spectroscopy 77
3.2.3. Raman Spectroscopy 79
3.2.4. X-ray Photoelectron Spectroscopy 82
3.2.5. N_2 Chemisorption Isotherms 84
3.3. Electrochemical Characterisation 86
3.3.1. Rotating Disk Electrode 86
3.3.2. Electrochemical Impedance Spectroscopy 89
3.4. Fuel Cell Experiments 94
CHAPTER 4 Ammonia Oxidation Reaction 97
4.1 Background 97
4.2 Experimental 99
4.2.1 Materials 99
4.2.2. Synthesis of Perovskite Oxide Powders 99
4.2.3. Physicochemical Characterisation 100
4.2.4. Electrochemical Characterisation 101
4.3. Results and Discussion 102
4.3.1. Sample Characterisation 102
4.3.2. Evaluation of Ammonia Oxidation Reaction 107
4.3.3. Ammonia Electrolysis 116
4.4. Perspective of Perovskites as Anodes 125
4.5. Conclusion 126
CHAPTER 5 Fuel Cell Design and Assembly 129
5.1. Background 129
5.2. Material Consideration 131
5.2.1. End Plates 132
5.2.2. Current Collectors 133
5.2.3. Flow Field Plates 134
5.2.4. Gaskets 135
5.3. Numerical Methodology 137

5.3.1. Numerical Procedure 137
5.3.2. Governing Equations 138
5.3.3. Material Selection 140
5.3.4. Computational Domain 140
5.3.5. Physical Assumptions 142
5.3.6. Experimental Validation 144
5.4. Result and Discussion 145
5.4.1. Effects of Manifold Tapering 145
5.4.2. Extent of Manifold Tapering 150
5.4.3. Testing in 3D models 153
5.4.4. Laboratory Scale 156
5.5. Fuel Cell Build 160
5.6. Conclusion 163
CHAPTER 6 Perovskite Oxides for Oxygen Reduction Reaction 167
6.1. Background 167
6.2. Experimental 169
6.2.1. Materials 169
6.2.2. Synthesis of Perovskite Oxide Powders 169
6.2.3. Physicochemical Characterisation 170
6.2.4. Electrochemical Characterisation 171
6.3. Results and Discussion 172
6.3.1. Sample Characterisation 172
6.3.2. Evaluation of Oxygen Reduction Reaction 186
6.4. Conclusions 201
CHAPTER 7 Optimisation of Cathode Electrode in a Direct Ammonia Fuel Cell 203
7.1. Background 203
7.2. Experimental 205
7.2.1. Materials 205
7.2.2. Electrode Preparation 205
7.2.3. Physicochemical Characterisation 207
7.2.4. Single Cell Evaluation Test 207
7.3. Results and Discussion 207
7.3.1. Effect of Carbon Content 211

7.3.2. Effect of PTFE Content 217

7.3.3. Effect of Ionomer Content 222

7.3.4. Varying Operating Conditions 226

7.3.5. Comparison with PGM-based CCL 230

7.4. Conclusion 236

CHAPTER 8 Conclusions and Future Work 239

8.1. Conclusions 239

8.2. Future Work 242

Bibliography 247

List of Tables and Illustrated Materials

Table 1.1. Comparison of properties between hydrogen and ammonia [1, 25, 45-48]……………………………………………………………………34

Table 1.2. Different DAFCs categorised according to electrolyte, conduction ion and operating temperatures…………………………………………….37

Table 2.1. Open circuit voltage (OCV) and peak power density (PPD) of different DAFCs [1]..……………………………………………………44

Table 4.1. Structural features including crystallite sizes of A- and B-site modified LNC [69]……………………………………………………..104

Table 4.2. Structure and lattice parameters of LNCF-90 [69]...…………………………………………………………………...105

Table 4.3. Oxygen vacancy content of different perovskites as determined by iodometric titration [69]………………………………………………..105

Table 4.4. Elemental weight (%) of modified A- and B-site taken from map sum spectra [69]……..………………………………………………... 106

Table 4.5. Performance of AOR on different electrocatalysts [69]………114

Table 5.1. Properties of fuel cell components……………………………140

Table 5.2. Dimensions of the flow fields…………………………………142

Table 5.3. Physical properties used in the simulations……………………143

Table 6.1. Structural features of synthesised perovskite oxides [67]…….174

Table 6.2. Structure and lattice parameters of LCFCO determined by Reitveld refinement [67]……………………………………………………....175

Table 6.3. Elemental analysis of synthesised perovskite oxides [67]…….177

Table 6.4. The BE and relative proportion (%) of Co^{2+}/Co^{3+} from Co $2p_{3/2}$ XPS data [67]……………………………………….........................178

Table 6.5. The BE and relative proportion (%) of Cr^{3+}/Cr^{6+} from Cr $2p_{3/2}$ XPS data [67]…………………………………………………………..…179

Table 6.6. The BE and relative concentration of oxygen species from the deconvoluted O 1s XPS peak [67]…………………………………..……182

Table 6.7. Particle sizes and SSA of the synthesised perovskite oxides

[67]……………………………………………………………..……185

Table. 7.1. DAFC performances based on varying carbon, PTFE and ionomer content in CCLs [69]……………………………………………………...211

Table 7.2. Surface area of materials used in catalyst layers [69]…………216

Fig. 1.1. Global energy consumption (TWh) and global CO_2 emissions (billion tonnes) from 1990-2021, plot created from Ref [2,4]……………...25

Fig. 1.2. (a) Pie chart illustrating the global breakdown of energy during 2021, plot created from Ref [2]. (b) Proportion of global electricity supplied by non-renewable and renewable resources during 2021, plot created from Ref [5]. (c) Global renewable energy contribution towards electricity production from 2000-2021, plot created from Ref [5]………………………………………26

Fig. 1.3. (c) Renewable energy contribution towards UK electricity production from 2000-2021, plot created from Ref [5]……………………27

Fig. 1.4. Polarisation curve showing the electrochemical efficiency of a fuel cell with the dominating sources of overpotential highlighted over the operating range...30

Fig. 1.5. Schematic representation of a direct ammonia fuel cell…………..40

Fig. 2.1. Schematic illustration of low temperature DAFC [1]…..……….....44

Fig. 2.2. Schematic representation of deal cubic ABO_3 structure highlighting the BO_6 octahedron [69]..…………………………………………………..51

Fig. 2.3. (a) Shape of the e_g electron pointing directly towards the surface O atom which plays an important role during O_2^{2-}/OH^- exchange. O, B and H atoms are in red, blue and green respectively [31]. (b) Potentials at 25 μAcm^{-2}_{ox} as a function of e_g orbital in perovskite-based oxides [31]. (c) Proposed ORR mechanism on perovskite oxide catalyst. (d) Schematic of the electron orbital filling in Cr^{3+}, Co^{3+} and Fe^{3+}……………………………………...55

Fig. 2.4. (a) ORR mechanism in perovskites based on bidentate adsorption in alkaline media. (b) Schematic representation of the effect of thermal treatment in oxygen on $Ba_{0.5}Sr_{0.5}Co_{0.8}Fe_{0.2}O_{3-\delta}$ (BSCF558) to generate oxygen vacancy sites [152]. (c) Schematic demonstrating how A-site deficiency create oxygen vacancy sites in perovskite crystal structure…......57

Fig. 2.5. Schematic illustration of (a) perovskite/carbon composites in ORR. (b) Possible origin of the synergistic effect between the perovskite and carbon arising from the ligand effect………………………………………………61

Fig. 2.6. Proposed OH^- mechanism through the hydrogen-bonded water network solvated by hydrophilic side chains (top) and illustration of an efficient ionic network on introduction of ionomer in the CL (bottom) [70]…..…………………………………………………………..68

Fig. 3.1. Illustration of Bragg's law……………………………………...75

Fig. 3.2. Schematic illustration of the principles for EDS………..……...79

Fig. 3.3. Schematic illustration of the three types of scattering processes that can occur when incoming light interacts with a molecule…………………..80

Fig. 3.4. Jablonski diagram showing possibilities of Rayleigh, Stokes and anti-Stokes Raman scattering………………………………………………81

Fig. 3.5. Schematic illustration of the principles for XPS……………..……83

Fig. 3.6. Schematic of the adsorption of gas molecules onto the surface of a sample showing monolayer adsorption assumed by the Langmuir theory and multilayer adsorption modelled by BET theory……………………………85

Fig. 3.7. Flow pattern of solution near the disk electrode surface (where *r* is the coordinate direction parallel to the disk surface and *Φ* is the coordinate direction of the electrode rotation). (b) Flow rate distribution near the electrode surface along the direction parallel to the electrode surface……...87

Fig. 3.8. Set up of RDE apparatus with zoom of glassy carbon electrode…..89

Fig. 3.9. Schematic interpretation of sinusoidal current response……….....91

Fig. 3.10. Impedance *Z* plotted as a planar vector…………………………..92

Fig. 3.11. (a) Illustration of Nyquist plot. (b) Example of a circuit: R_s is solution resistance (ohmic resistance), R_a and R_c are the anodic and cathodic polarisation resistances respectively and CPE is the constant phase element………………………………………………………………………..93

Fig. 3.12. Set up of fuel cell system……………………………………...95

Fig. 4.1. (a) XRD analysis of synthesised $LaNi_{0.6}Cu_{0.4-x}Fe_xO_{3-\delta}$ (x = 0, 0.05, 0.1) in air [69]. (b) XRD analysis of synthesised $LaNi_{0.6}Cu_{0.4-x}Fe_xO_{3-\delta}$ (x = 0,

0.05, 0.1); XRD patterns in the 2θ range 30 to 35° (right) [68]. (c) XRD analysis of synthesised $La_yNi_{0.6}Cu_{0.35}Fe_{0.05}O_{3-\delta}$ (y = 0, 0.05, 0.1); XRD patterns in the 2θ range 30 to 35° (right) [68]. (d) Refined XRD pattern of LNCF-90 [69]………………..…………………………………………103

Fig. 4.2. SEM image, elemental mapping and elemental point analysis of La, Ni, Cu, Fe and O in (a) LNCF-05 and (b) LNCF-90 with gold used as coating material [69]…...107

Fig. 4.3. (a) CV performances of catalysts in 0.5 M KOH + 55 mM NH_4Cl [68]. (b) CV performance of LNCF-05 in 0.5 M KOH with and without 55 Mm NH_4Cl [69]. (c) LSV performances of catalysts 0.5 M KOH + 55 mM NH_4Cl [69]. (d) LSV performance of LNCF-05 in 0.5 M KOH with and without 55 mM NH_4Cl [69]. (e) Tafel plots of Pt/C, LNC, LNCF-05 and LNCF-10. (f) Chronoamperometry analysis of catalysts in 0.5 M KOH + 55 mM NH_4Cl [69]..……………………………………………………….109

Fig. 4.4. (a) CV performances of catalysts in 0.5 M KOH + 55 mM NH_4Cl [69]. (b) CV performance of LNCF-90 in 0.5 M KOH with and without 55 Mm NH_4Cl [69]. (c) LSV performances of catalysts in 0.5 M KOH + 55 mM NH_4Cl [69]. (d) LSV performance of LNCF-90 in 0.5 M KOH with and without 55 mM NH_4Cl [69]. (e) Tafel plots of LNCF-05, LNCF-95 and LNCF-90 [69]. (f) Chronoamperometry analysis of catalysts in 0.5 M KOH + 55 mM NH_4Cl [69]..…………………………………………………….113

Fig. 4.5. (a) CV and (b) LSV of LNCF-90 in simulated and real wastewater with and without 0.5 M KOH [69]...………….…………………………119

Fig. 4.6. (a) Electrolysis profile of LNCF-90 in simulated wastewater with the addition of 0.5 M KOH, insert of electrolysis cell [69]. (b) Ammonia concentration and removal efficiency of LNCF-90 in simulated wastewater in 0.5 M KOH [69]. (c) Ammonia concentration and removal efficiency of LNCF-90 in real wastewater in 0.5 M KOH [69]. (d) Removal efficiency profiles of LNCF-90 in simulated and real wastewater with the addition of 0.5 M KOH [69]. (e) XRD analysis of LNCF-90 electrode before and after electrolysis test [69]. (f) EDS point analysis of LNCF-90 electrode before and after electrolysis test [69]……………………….……………………...120

Fig. 4.7. SEM and EDS analysis of LNCF-90 electrode after test in real wastewater scaled to 25 µm bar [69]……….…………………………...123

Fig. 4.8. SEM imaging of LNCF-90 electrode after electrolysis test in real wastewater along with SEM and EDS imaging of LNCF-90 electrode after electrolysis test in real wastewater [69]……………….…………………..124

Fig. 5.1. Illustration of (a) parallel (b) serpentine and (c) interdigitated flow field patterns……………………………………………………………130

Fig. 5.2. Schematic illustrating individual components of a typical DAFC assembly…………………………………………………………….132

Fig. 5.3. Illustration demonstrating how cone can be considered as a series of cylindrical pipes with varying radii and an arrow to illustrate direction of flow. …………………………...……………………………………….139

Fig. 5.4. Schematic view of PFFP-2D illustrating parameters described in the study……………………………………………………………………141

Fig. 5.5. Photograph of the experimental set up (left) and zoom of the PFF-2D acrylic cell (right)…………………………………………………..144

Fig. 5.6. Pressure contours for different FFPs fed with air at the cathodic site: (a) conventional PFFP, (b) PFFP-1D and (c) PFFP-2D. Velocity fields for different FFPs fed with air at the cathodic site: (d) conventional PFFP, (e) PFFP-1D and (f) PFFP-2D. The arrow represents the direction of flow…147

Fig. 5.7. Pressure contours for different FFPs fed with water at the anodic site: (a) conventional PFFP, (b) PFFP-1D and (c) PFFP-2D. Velocity fields for different FFPs fed with water at the anodic site: (d) conventional PFFP, (e) PFFP-1D and (f) PFFP-2D. The arrow represents the direction of flow…………………………………………………………………….149

Fig. 5.8. Pressure contours (a) and velocity profile (b) for PFFP-2D with tapering scale factor of 1.5:1. Pressure contours (c) and velocity profile (d) for PFFP-2D with tapering scale factor of 2:1. Pressure contours (e) and velocity profile (f) for PFFP-2D with tapering scale factor of 3:1. The arrow represents the direction of flow…………………………………………...151

Fig. 5.9. Flow patterns of fluorescein disodium salt solution through the 3D printed (a) PFFP, (b) PFFP-1 and (c) PFFP-2D models. The arrow represents the direction of flow…..……………………………………………..154

Fig. 5.10. Velocity profile along each channel (left) with arrows showing the direction of flow, and velocity values mapped along each channel (right) for (a) PFFP, (b) PFFP-1D and (c) PFFP-2D design with an active area of 1cm^2……………………………………………………………………158

Fig. 5.11. Individual components of DAFC…………………………………157

Fig. 5.12. Illustration of assembled DAFC with zoom of FFP employing PFFP-2D design…………………………………………………………..161

Fig. 5.13. Pressure paper results obtained from applying different torques to the assembled DAFC…………………………………………………...162

Fig. 6.1. (a) Schematic illustration of the preparation process of LCO-based perovskite oxide powders by a Pechini method [68]. (b) XRD patterns of the prepared LCO, LCCO, LFCO and LCFCO perovskite oxide powders; XRD patterns in the 2θ range 22.8 to 23.6° (right) [68]. (c) Rietveld refinement pattern of synthesised LCFCO [68]. (d) Raman spectra of LCO, LCCO, LFCO and LCFCO [68]. …..……………………………………………...173

Fig. 6.2. SEM images of (a) LCO (b) LCCO (c) LFCO and (d) LCFCO. (e) Corresponding EDS elemental mapping of La, Cr, Fe and Co in LCFCO [68]…...……..…………………………………………………………..…176

Fig. 6.3. XPS analysis of LCO demonstrating (a) La and (b) Co spectra [68]..……………………………………………………………………178

Fig. 6.4. XPS analysis of LCCO demonstrating (a) La, (b) Cr and (c) Co spectra [68]..…………………………………………………………179

Fig. 6.5. XPS analysis of LFCO demonstrating (a) La, (b) Fe and (c) Co spectra [68]..…………………………………………………………180

Fig. 6.6. XPS analysis of LCFCO demonstrating (a) La (b) Cr (c) Fe and (d) Co spectra [68]...…………………………………………………………181

Fig. 6.7. Deconvoluted O 1s spectra for the LCO, LCCO, LFCO and LCFCO perovskite powders [68]…..……………………………………………182

Fig. 6.8. (a) XRD patterns of the prepared LCFCO-600, LCFCO-700,

LCFCO-800, LCFCO-900 and LCFCO perovskite powders [68]…..……………………………………………………………....184

Fig. 6.9. SEM images of (a) LCFCO, (b) LCFCO-900, (c) LCFCO-800 and (d) LCFCO-700 [68]..…………………………………….………..…..185

Fig. 6.10. (a) Illustration of RDE technique used for testing ORR activity of different perovskite oxide materials [68]. Polarisation curves obtained for the (b) LCO, (c) LCCO, (d) LFCO and (e) LCFCO perovskite oxides in O_2-saturated 0.1 M KOH solution: RDE rotation rates of 100, 400, 900 and 1600 rpm [68]. (f) Comparison of polarisation curves of the perovskite oxides in O_2-saturated 0.1 M KOH solution at RDE rotation rates of 1600 rpm [68]..………………………………………………………………….187

Fig. 6.11. (a) Example determination of E_{onset} for the LCO electrocatalyst in O_2-saturated 0.1 M KOH solution [68]. (b) Onset potential values for the tested electrocatalysts in O_2-saturated 0.1 M KOH solution and room temperature; RDE rotation rate of 1600 rpm [68]. (c) Example determination of $E_{1/2}$ for the LCO electrocatalyst in O_2-saturated 0.1 M KOH solution [68]. (d) Zoomed comparison of E_{onset} between the Pt/C and LCFCO in O_2-saturated 0.1 M KOH solution [68]. (e) Polarisation curves of Pt/C and LCFCO electrocatalysts with $E_{1/2}$ difference noted in O_2-saturated 0.1 M KOH solution: RDE rotation rate of 1600 rpm [68]. (f) Corresponding Tafel plots for perovskite oxides in O_2-saturated 0.1 M KOH solution [68]..…...190

Fig. 6.12. (a) Bar graphs showing the tested LCO, LCCO, LFCO and LCFCO electrocatalyst current density responses at selected potentials [68]. (b) Koutecky-Levich (K-L) plots for the LCO, LCCO, LFCO and LCFCO perovskites at a potential of -0.55 V vs. Ag/AgCl (0.41 V vs. RHE) [68]. (c) Calculated electron transfer number n for ORR using K-L slopes [68]. (d) Area ratio O2/(O1+O3+O4) in the tested electrocatalysts as deduced from XPS analysis [68]..……………………………………………………..193

Fig. 6.13. (a) Chronopotentiometry analysis of the LCO, LCCO, LFCO and LCFCO perovskites held at a fixed potential of -0.4 V vs. Ag/AgCl in O_2-saturated 0.1 M KOH solution: RDE rotation rate of 1600 rpm [68]. (b) Chronopotentiometry analysis of the Pt/C and LCFCO electrocatalysts held

at a fixed potential of -0.4 V vs. Ag/AgCl in O_2-saturated 0.1 M KOH solution [68]..……………………………………………………………………194

Fig. 6.14. (a) Polarisation curves of the LCFCO-700 perovskite in O_2-saturated 0.1 M KOH solution; RDE rotation rates of 100, 400, 900 and 1600 rpm [68]. (b) Polarisation curves obtained for the LCFCO-700 and LCFCO perovskites in O_2-saturated 0.1 M KOH solution: RDE rotation rate of 1600 rpm [68]. (c) Polarisation curves of Pt/C and LCFCO-700 electrocatalysts in O_2-saturated 0.1 M KOH solution; RDE rotation rate of 1600 rpm [68]. (d) Polarisation curves obtained for the LCFCO-700 in O_2-saturated 0.1 M KOH solution with and without 0.1 M NH_3: RDE rotation rate of 1600 rpm [68]..……………………………………………………………………198

Fig. 6.15. (a) Chronopotentiometry analysis of LCFCO and LCFCO-700 perovskites held at a fixed potential of -0.4 V vs. Ag/AgCl in O_2-saturated 0.1 M KOH solution: RDE rotation rate of 1600 rpm [68]. (b) Chronopotentiometry analysis of the Pt/C and LCFCO-700 electrocatalysts held at a fixed potential of -0.4 V vs. Ag/AgCl in O_2-saturated 0.1 M KOH solution [68]………………………………..…………………………..200

Fig. 7.1. General experimental procedure with weight percentages given with respect to perovskite weight [70]……………..………………………...206

Fig. 7.2. Prepared MEA for DAFC………………………………………208

Fig. 7.3. Illustration demonstrating the contributing effects of different components within CCLs for DAFCs [70]..…………………………..…..209

Fig. 7.4. (a) Polarisation and power density curve and (b) EIS data of CCLs with varying carbon content [70]. (c) Polarisation and power density curve and (d) EIS data of CCLs with varying PTFE content [70]. (e) Polarisation and power density curve [70]. (f) EIS data of CCLs with varying ionomer content [70]. Anode: 2.2 mg_{PGM} cm^{-2} PtIr(40 wt. %)/C(60 wt. %). Cathode: LCFCO. Test conditions: (1) Anode: 2 mL min^{-1} of 7 M NH_4OH with 1 M KOH; Anode back pressure: 3 bar_g (2) Cathode: 180 mL min^{-1} CO_2-free air through humidifier of T = 95 ^oC; Cathode back pressure: 2 bar_g. Cell temperature: 80 ^oC……………………………………………………...210

Fig. 7.5. XRD analysis of carbon cloth (blue), LCFCO perovskite powder (green) and CCL-C50 (pink) [70]..……………………………………..215

Fig. 7.6. Water droplet formation on gas diffusion layer surface with PTFE loadings reflective of (a) 0, (b) 10, (c) 35 and (d) 50 wt. % with respect to perovskite [70]..…………………………………………………….220

Fig. 7.7. SEM images of (a) CCL-P0, (b) CCL-C50, (c) CCL-P35 and (d) CCL-P50 [70]..……………………………………………………….222

Fig. 7.8. Drawing demonstrating an efficient ionic network on introduction of ionomer (right) in the CCL…………………………………………..223

Fig. 7.9. SEM images of (a) CCL-I0, (b) CCL-C50, (c) CCL-I35 and (d) CCL-I50 [70]..………………………………………………………225

Fig. 7.10. Polarisation and power density curve of CCLs with varying (a) carbon, (b) PTFE and (c) ionomer content [70]. Anode: 2.2 mg_{PGM} cm^{-2} PtIr(40 wt. %)/C(60 wt. %). Cathode: LCFCO. Test conditions: (1) Anode: 2 mL min^{-1} of 7 M NH_4OH with 1 M KOH; Anode back pressure: 3 bar_g (2) Cathode: 180 mL min^{-1} CO_2-free air through humidifier of T = 95 °C; Cathode back pressure: 2 bar_g. Cell temperature: 100 °C. (d) Polarisation and power density curve of CCL-C50. Anode: 2.2 $mg_{PGM}cm^{-2}$ PtIr(50 wt. %)/C(50 wt. %). Cathode: 3.4 $mg_{oxide}cm^{-2}$ LCFCO-700(50 wt. %)/C(50 wt. %) [68]. Test conditions: (1) Anode: 2 $mLmin^{-1}$ of 7 M NH_4OH with 1 M KOH; Anode back pressure: 3 bar_g (2) Cathode: 180 $mLmin^{-1}$ CO_2-free air through humidifier of T = 95 °C; Cathode back pressure: 2 bar_g. Cell temperature: 20, 40, 60, 80 and 100 °C…………………………………………………..227

Fig. 7.11. Polarisation and power density curves of DAFC employing CCL-C50 fed with 7 M NH NH_4OH and different hydroxide concentrations at an operating temperature of 80 °C [70]..…………………………………..229

Fig. 7.12. Polarisation and power density curve of DAFC. (a) Anode: 2.2 $mg_{PGM}cm^{-2}$ PtIr(50 wt. %)/C(50 wt. %). Cathode: 0.4 $mg_{PGM}cm^{-2}$ Pt/C. Test conditions: (1) Anode: 2 $mLmin^{-1}$ of 7 M NH_4OH with 1 M KOH; Anode back pressure: 3 bar_g (2) Cathode: 180 $mLmin^{-1}$ CO_2-free air through humidifier of T = 95 °C; Cathode back pressure: 2 bar_g. Cell temperature: 80 and 100 °C [68]. (b) Comparison between DAFC employing Pt/C (pink) and

LCFCO-700 (orange) cathode at 80 ^{o}C [67]. (c) Comparison between DAFC employing Pt/C (pink) and LCFCO-700 (orange) cathode at 100 ^{o}C [67]. (d) Stability test of DAFC employing LCFCO-700 and Pt/C-based catalysts at operating temperature of 100 ^{o}C [68]……..………………………………231

Fig. 7.13. (a) Photo of the CCL-C50 layer deposited onto the AEM after testing. (b) XRD of carbon cloth, LCFCO perovskite oxide, CCL-C50 before and after fuel cell durability test [70]. Anode: 2.2 mg$_{PGM}$ cm^{-2} PtIr(40 wt. %)/C(60 wt. %). Cathode: 1.23 mg$_{oxide}$ cm^{-2} LCFCO or 0.45 mg$_{PGM}$ cm^{-2} Pt/C. Test conditions: (1) Anode: 2 mL min^{-1} of 7 M with 1 M KOH; Anode back pressure: 3 bar$_{g}$ (2) Cathode: 180 mL min^{-1} CO$_{2}$-free air through humidifier of T = 95 ^{o}C; Cathode back pressure: 2 bar$_{g}$. Cell temperature: 80 ^{o}C [69]. Point analysis of CCL-C50 Elemental point analysis (c) before and (d) after durability test [70]………………………………………………..…….234

Fig. 7.14. (a) SEM of CCL-C50 after testing. Elemental mapping of (b) La, (c) Cr, (d) Fe, (e) Co and (f) O elements via EDS after testing [70]..………235

Fig. 7.15. Photo of corrosion displayed on current collector post testing….236

Acknowledgements

Firstly, I would like to thank my supervisor Professor Shanwen Tao for offering me a position in his research group and giving me the opportunity to explore clean energy. During this time, I have gained a deeper interest in fuel cell technology, driving my passion to continue in this direction. It is thanks to Shanwen that I have been able to publish articles and add my contribution to the field. My gratitude also goes to Professor Andre van Veen for always believing in me and never failing to provide me with guidance, laughter, and a hot chocolate. It was through our countless interactions that I gained the confidence to truly explore outside of my comfort zone. I will always admire his light-heartedness, his indispensable joke-telling ability whilst waiting for our simulations to compute, and his bold outfit choices.

I would like to dedicate appreciation to all members of my group for their advice and friendship throughout the years. A special thank you to Peimiao for always offering a helping hand, all the late nights running experiments together, and for leaving snacks on my desk. My gratitude extends to John Pillier for his help, humour and countless conversations about comfort food, and to Professor Peter Gammon, who has given his continued assistance over my course. Thank you to the department and academics who have helped me along the way, as well as ESPRC for the funding that has allowed me to pursue my journey as a scientist.

Many thanks also go to my dearest family and friends for their encouragement during my PhD. A special shout out to Vai for her continued support, invaluable friendship, and ability to point out when my sentences were too long. I would also like to acknowledge Sammy for helping me remain positive in the months leading up to my thesis submission through his unmatched company, questionable puns, and latenight adventures to get apple pies. Thank you for being ‘the engineer’ that I could always rely on. A massive thank you to my boyfriend, Matheus, for always believing in me and providing me with endless love and laughter. I am truly grateful to have had him by my side during this time. Finally, a huge appreciation goes towards my parents for always supporting me both financially and emotionally, and for having faith in me, even though they still do not quite understand the depth of my research! Thank you, mum and dad.

Declaration

This thesis is submitted to the University of Warwick in support of my application for the degree of Doctor of Philosophy. It has been composed by myself and no portion of this work has been submitted in support of an application for another degree at any other university or institute. This work has been my own except where indicated otherwise.

The thesis includes material that has been published or submitted to journals prior to submission.

The works in chapter **1. INTRODUCTION** form part of a publication: **G. Jeerh**, M. Zhang, S. Tao, Recent progress in ammonia fuel cells and their potential applications, Journal of Materials Chemistry A, 9 (2021) 727-752.

The works in chapter **2. LITERATURE REVIEW** form parts of the publications: **G. Jeerh**, M. Zhang, S. Tao, Recent progress in ammonia fuel cells and their potential applications, Journal of Materials Chemistry A, 9 (2021) 727-752; **G. Jeerh**, P. Zou, M. Zhang, S. Tao, Perovskite oxide $LaCr_{0.25}Fe_{0.25}Co_{0.5}O_{3-\delta}$ as an efficient non-noble cathode for direct ammonia fuel cells, Applied Catalysis B: Environmental, 319 (2022) 121919 and **G. Jeerh**, P. Zou, M. Zhang, S. Chen, J. Humphreys, S. Tao, Electrooxidation of ammonia on A-site deficient perovskite oxide $La_{0.9}Ni_{0.6}Cu_{0.35}Fe_{0.05}O_{3-\delta}$ for wastewater treatment, Separation and Purification Technology, 297 (2022) 121451. The content also forms part of a paper by the author which is currently under review: **G. Jeerh**, P. Zou, M. Zhang, S. Tao, Optimisation of a perovskite oxide-based cathode catalyst layer on performance of direct ammonia fuel cells, Submitted to ACS Applied Materials & Interfaces, (2022).

The works in chapter **4. AMMONIA OXIDATION REACTION** form part of a publication: **G. Jeerh**, P. Zou, M. Zhang, S. Chen, J. Humphreys, S. Tao, Electrooxidation of ammonia on A-site deficient perovskite oxide $La_{0.9}Ni_{0.6}Cu_{0.35}Fe_{0.05}O_{3-\delta}$ for wastewater treatment, Separation and Purification Technology, 297 (2022) 121451.

The works in chapter **6. PEROVSKITE OXIDES FOR OXYGEN REDUCTION** form part of a publication: **G. Jeerh**, P. Zou, M. Zhang, S. Tao, Perovskite oxide $LaCr_{0.25}Fe_{0.25}Co_{0.5}O_{3-\delta}$ as an efficient non-noble cathode for direct ammonia fuel cells, Applied Catalysis B: Environmental, 319 (2022) 121919.

The works in chapter **7. OPTIMISATION OF CATHODE ELECTRODE IN A DIRECT AMMONIA FUEL CELL** form parts of the publications: **G. Jeerh**, P. Zou, M. Zhang, S. Tao, Perovskite oxide $LaCr_{0.25}Fe_{0.25}Co_{0.5}O_{3-\delta}$ as an efficient non-noble cathode for direct ammonia fuel cells, Applied Catalysis B: Environmental, 319 (2022) 121919. The content also forms part of a paper by the author which is currently under review**:** **G. Jeerh**, P. Zou, M. Zhang, S. Tao, Optimisation of a perovskite oxide-based cathode catalyst layer on performance of direct ammonia fuel cells, Submitted to ACS Applied Materials & Interfaces, (2022).

List of Publications

[1] **G. Jeerh**, P. Zou, M. Zhang, S. Tao, Optimisation of a perovskite oxide-based cathode catalyst layer on performance of direct ammonia fuel cells, Submitted to ACS Applied Materials & Interfaces, (2022).

[2] **G. Jeerh**, P. Zou, M. Zhang, S. Tao, Perovskite oxide $LaCr_{0.25}Fe_{0.25}Co_{0.5}O_{3-\delta}$ as an efficient non-noble cathode for direct ammonia fuel cells, Applied Catalysis B: Environmental, 319 (2022) 121919.

[3] M. Zhang, J. Zhang, **G. Jeerh**, P. Zou, B. Sun, M. Walker, K. Xie, S. Tao, A symmetric direct ammonia fuel cell using ternary NiCuFe alloy embedded in carbon network as electrodes, Journal of Materials Chemistry A, (2022).

[4] M. Zhang, P. Zou, **G. Jeerh**, B. Sun, M. Walker, S. Tao, Oxygen Vacancy-Rich $La_{0.5}Sr_{1.5}Ni_{0.9}Cu_{0.1}O_{4-\delta}$ as a High-Performance Bifunctional Catalyst for Symmetric Ammonia Electrolyzer, Advanced Functional Materials, 2022, 2204881.

[5] **G. Jeerh**, P. Zou, M. Zhang, S. Chen, J. Humphreys, S. Tao, Electrooxidation of ammonia on A-site deficient perovskite oxide $La_{0.9}Ni_{0.6}Cu_{0.35}Fe_{0.05}O_{3-\delta}$ for wastewater treatment, Separation and Purification Technology, 297 (2022) 121451.

[6] M. Zhang, H. Li, X. Duan, P. Zou, **G. Jeerh**, B. Sun, S. Chen, J. Humphreys, M. Walker, K. Xie, S. Tao, An Efficient Symmetric Electrolyzer Based On Bifunctional Perovskite Catalyst for Ammonia Electrolysis, Advanced Science, DOI: 10.1002/advs.202101299 (2021) 2101299.

[7] S. Chen, P. Sun, J. Humphreys, P. Zou, M. Zhang, **G. Jeerh**, B. Sun, S. Tao, N,N-Dimethylacetamide-Diluted Nitrate Electrolyte for Aqueous Zn//$LiMn_2O_4$ Hybrid Ion Batteries, ACS Applied Materials & Interfaces, 13 (2021) 46634-46643.

[8] S. Chen, P. Sun, J. Humphreys, P. Zou, M. Zhang, **G. Jeerh**, S. Tao, Acetate-based ‘oversaturated gel electrolyte’ enabling highly stable aqueous Zn-MnO_2 battery, Energy Storage Materials, 42 (2021) 240-251.

[9] M. Zhang, **G. Jeerh**, P. Zou, R. Lan, M. Wang, H. Wang, S. Tao, Recent development of perovskite-based electrocatalysts and their applications in low to intermediate temperature electrochemical devices, Materials Today, (2021).

[10] **G. Jeerh**, M. Zhang, S. Tao, Recent progress in ammonia fuel cells and their potential applications, Journal of Materials Chemistry A, 9 (2021) 727-752.

[11] M. Zhang, P. Zou, **G. Jeerh**, S. Chen, J. Shields, H. Wang, S. Tao, Electricity Generation from Ammonia in Landfill Leachate by an Alkaline Membrane Fuel Cell Based on Precious-Metal-Free Electrodes, ACS Sustainable Chemistry & Engineering, 8 (2020) 12817-12824.

[12] P. Zou, S. Chen, R. Lan, J. Humphreys, **G. Jeerh**, S. Tao, Investigation of perovskite oxide $SrFe_{0.8}Cu_{0.1}Nb_{0.1}O_{3-\delta}$ as cathode for a room temperature direct ammonia fuel cell, International Journal of Hydrogen Energy, 44 (2019) 26554-26564.

Abstract

To optimise electrode-electrolyte interactions, which are at the heart of fuel cells, the design of the device as well as the materials implemented are of extreme importance. Such interactions are, for example, dependent on the ability of the catalyst to carry out the given reaction, the composition of the catalyst layers and the ability of fresh fuel/oxidant to reach the active sites. These factors influence the low, middle and high current density regimes of polarisation curves respectively and are therefore vital for efficient fuel cell performance.

Herein, a low temperature direct ammonia fuel cell is investigated in terms of its design and material choice. The individual components of the fuel cell are carefully selected to consider strength, cost and compatibility. A fuel cell is built in-house to improve fuel/oxidant flow to and from the active sites of the cell to improve mass transport. Upon doing so, the materials used at the cathode site are explored. Typical electrocatalysts at these sites depend on platinum group metals which unequivocally increase the cost of the device and limit scale up potential. In this work, non-platinum group metals, namely perovskite oxides, are manipulated towards the catalysis of oxygen reduction that occurs at the cathode. The tailored perovskite oxide electrocatalyst is implemented into the fuel cell and the composition of the cathode catalyst layer is explored to optimise interactions at the electrode-electrolyte interface. The resulting direct ammonia fuel cell is tested under a range of operating conditions and shows comparable performance to a fuel cell utilising a platinum group metal-based cathode. The performance reveals that through strategic design, an efficient and low-cost fuel cell can be assembled. Furthermore, a perovskite oxide is also tested towards ammonia oxidation which occurs at the anode. Although not explicitly implemented into the cell, the perovskite shows promising catalytic activity towards the given reaction. This work therefore provides a route for future innovation in the field.

Abbreviations

AEM	Alkaline Exchange Membrane
AMFC	Alkaline Membrane Fuel Cell
AOR	Ammonia Oxidation Reaction
BE	Binding Energy
BET	Bruanauer-Emmett-Teller
BSCF	$Ba_{0.5}Sr_{0.5}Co_{0.8}Fe_{0.2}O_{3-\delta}$
CB	Carbon Black
CL	Catalyst Layer
CCL	Cathode Catalyst Layer
CCL-C10	Cathode Catalyst Layer - 10 wt. % Carbon with respect to Perovskite
CCL-C30	Cathode Catalyst Layer - 30 wt. % Carbon with respect to Perovskite
CCL-C50	Cathode Catalyst Layer - 50 wt. % Carbon with respect to Perovskite
CCL-C80	Cathode Catalyst Layer - 80 wt. % Carbon with respect to Perovskite
CCL-I0	Cathode Catalyst Layer - 0 wt. % Ionomer with respect to Perovskite
CCL-I35	Cathode Catalyst Layer - 35 wt. % Ionomer with respect to Perovskite
CCL-I50	Cathode Catalyst Layer - 50 wt. % Ionomer with respect to Perovskite
CCL-P0	Cathode Catalyst Layer - 0 wt. % PTFE with respect to Perovskite
CCL-P35	Cathode Catalyst Layer - 35 wt. % PTFE with respect to Perovskite
CCL-P50	Cathode Catalyst Layer - 50 wt. % PTFE with respect to Perovskite
CCM	Catalyst Coated Membrane
CPE	Constant Phase Element
CV	Cyclic Voltammetry
DAFC	Direct Ammonia Fuel Cell
DFT	Density Functional Theory
DoE	Design of Experiment
EDS	Energy Dispersive X-ray
EIS	Electrochemical Impedance Spectra
EPDM	Ethylene Propylene Diene Terpolymer
FFP	Flow Field Plate
FRA	Frequency Response Analyser
GC	Glassy Carbon
GDE	Gas Diffusion Electrode
GDL	Gas Diffusion Layer

HS	High Spin
IS	Intermediate Spin
K-L	Koutecky Levich
LCO	$LaCoO_{3-\delta}$
LCCO	$LaCr_{0.5}Co_{0.5}O_{3-\delta}$
LCFCO	$LaCr_{0.25}Fe_{0.25}Co_{0.5}O_{3-\delta}$
LCFCO-700	$LaCr_{0.25}Fe_{0.25}Co_{0.5}O_{3-\delta}$ fired at 700 ^{o}C
LCFCO-800	$LaCr_{0.25}Fe_{0.25}Co_{0.5}O_{3-\delta}$ fired at 800 ^{o}C
LCFCO-900	$LaCr_{0.25}Fe_{0.25}Co_{0.5}O_{3-\delta}$ fired at 900 ^{o}C
LFCO	$LaFe_{0.5}Co_{0.5}O_{3-\delta}$
LNC	$LaNi_{0.6}Cu_{0.4}O_{3-\delta}$
LNCF-05	$LaNi_{0.6}Cu_{0.35}Fe_{0.05}O_{3-\delta}$
LNCF-10	$LaNi_{0.6}Cu_{0.3}Fe_{0.1}O_{3-\delta}$
LNCF-95	$La_{0.95}Ni_{0.6}Cu_{0.35}Fe_{0.05}O_{3-\delta}$
LNCF-90	$La_{0.9}Ni_{0.6}Cu_{0.35}Fe_{0.05}O_{3-\delta}$
LS	Low Spin
LSV	Linear Sweep Voltammetry
MEA	Membrane Electrode Assembly
OCV	Open Circuit Voltage
ORR	Oxygen Reduction Reaction
PAP-BP	Biphenyl Backbone Poly(aryl piperidinium)
PAP-TP	Triphenyl Backbone Poly(aryl piperidinium)
PEMFC	Proton Exchange Membrane Fuel Cell
PFFP	Parallel Flow Field Plate
PFFP-1D	Parallel Flow Field Plate with Manifold Tapering in 1D
PFFP-2D	Parallel Flow Field Plate With Manifold Tapering in 2D
PGM	Platinum Group Metal
PPD	Peak Power Density
PTFE	Polytetrafluoroethylene
RDE	Rotating Disk Electrode
RHE	Reversible Hydrogen Electrode
SEM	Scanning Electron Microscopy
SHE	Standard Hydrogen Electrode
SOFC	Solid Oxide Fuel Cell
SSA	Specific Surface Area
TEM	Transmission Electron Spectroscopy
TPB	Triple-Phase Boundary
XPS	X-ray Photoelectron Spectroscopy
XRD	X-ray Diffraction

CHAPTER 1 Introduction

The works in this chapter form part of a publication by the author in Journal of Materials Chemistry A [1].

1.1. Energy Demand

Energy plays an integral role in our economic and social development. It is a powerful resource directly related to the progression and standards of living. A continuous growth in global population over the years has been paralleled by a continuous growth in energy consumption, demonstrated by the trend over the past three decades (Fig. 1.1). Notably, there was tremendous impact on energy demand during the COVID-19 pandemic in 2020, evidenced by a 4.5 % decline in global energy consumption. However, an overall positive correlation remains, as global energy consumption was rebounded by 5 % in 2021 [2]. Such demand undoubtedly coincides with an increase in global greenhouse gas emissions, such as CO_2, which are notoriously linked to global warming [3, 4].

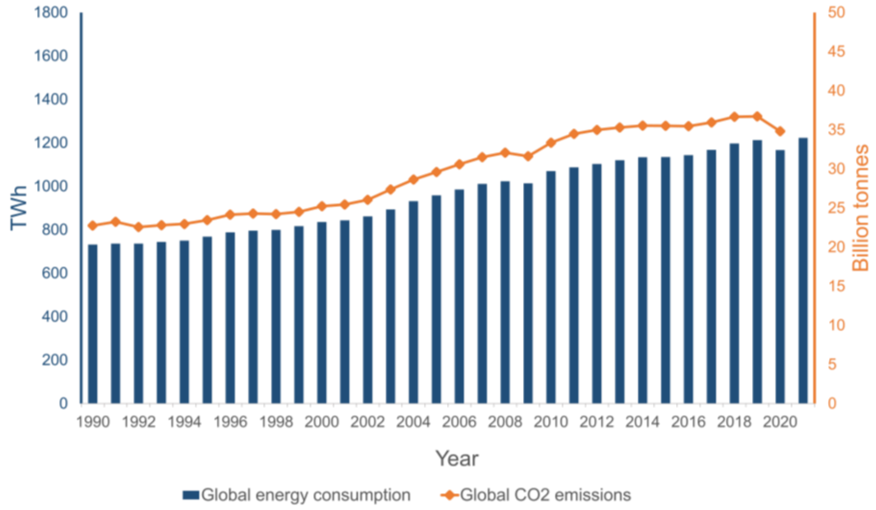

Fig. 1.1. Global energy consumption (TWh) and global CO_2 emissions (billion tonnes) from 1990-2021, plot created from Ref [2, 4].

Current production of such energy is primarily delivered through fossil fuel exploitation, making up 80 % of the mainstream supply in 2021. A pie chart showing the breakdown of energy during this year is shown in Fig. 1.2a, whereby a significant proportion is being supplied by oil (29 %), coal (27 %) and gas (24 %) [2]. Reliance on such means of energy can explain the trends in atmospheric pollutants and thus emphasises the need for clean energy production. This has subsequently become an important point of discussion in today's society and has led to enormous efforts into the investment of clean and renewable energy.

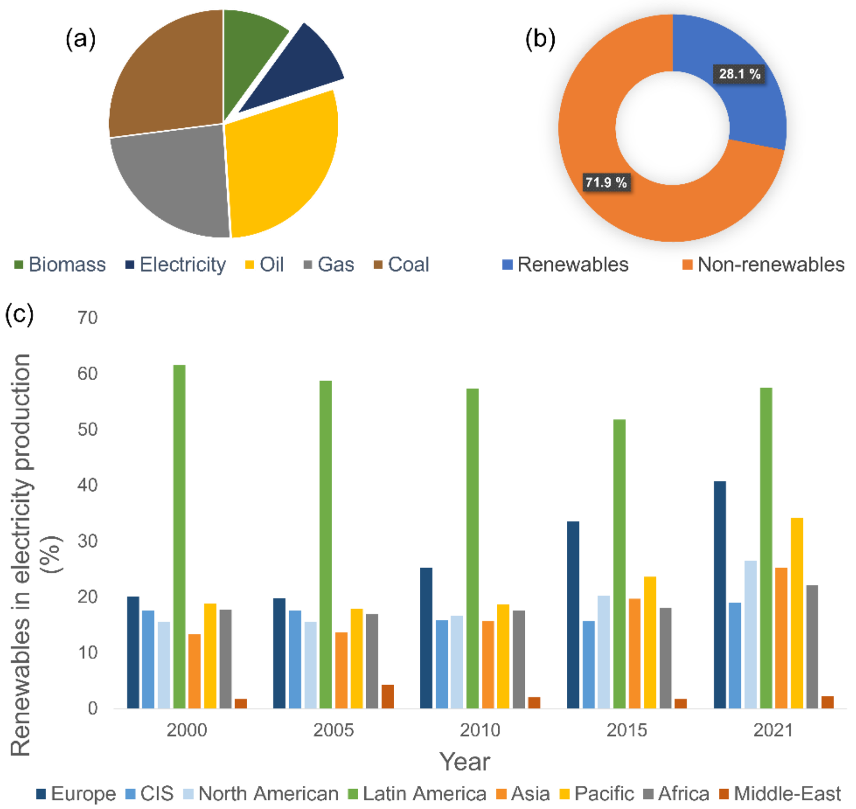

Fig. 1.2. (a) Pie chart illustrating the global breakdown of energy during 2021, plot created from Ref [2]. (b) Proportion of global electricity supplied by non-renewable and renewable resources during 2021, plot created from Ref [5]. (c) Global renewable energy contribution towards electricity production from 2000-2021, plot created from Ref [5].

As of 2021, 28.1 % of the global energy production that comes from electricity is supplied through renewable energy (Fig. 1.2b). Global recognition towards the need and development of such clean energy is evidenced by the increasing segment of renewable energy over the past few decades (Fig. 1.2c). It should be noted that the portion of renewable energy that contributes towards electricity production varies from country to country and is heavily regional dependent, for example, in the UK this fraction has increased from 3.4 to 40.7 % from 2000 to 2021, as can be seen in Fig. 1.3 [5].

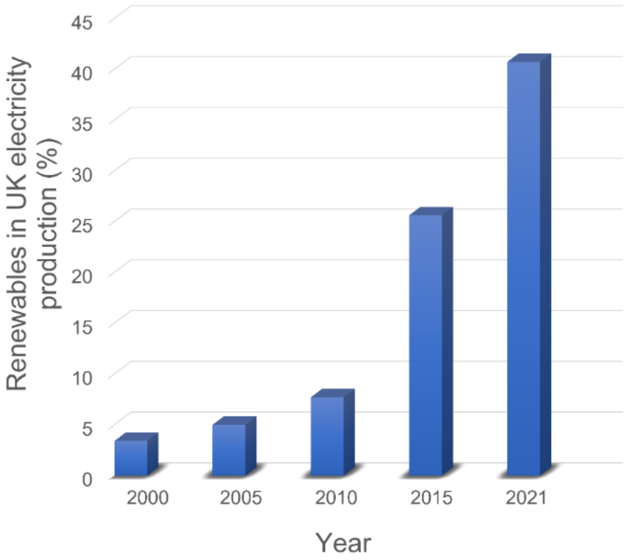

Fig. 1.3. (c) Renewable energy contribution towards UK electricity production from 2000-2021, plot created from Ref [5].

Several renewable energy sources have been proposed with the potential to replace conventional routes of energy generation [6]. Renewable sources like wind and solar power for example, are considered a clean technology [7]. However, these sources are often regarded as unreliable as they are intermittent in nature, relying heavily on external geological factors such as altitude, wind speed and UV exposure [8]. This imposes regional limitations and restricts the extent to which renewable energy sources can contribute towards energy production. Subsequently, there is a driving incentive to find reliable and regular sources of clean energy that can be used in conjunction with existing technology to create a stable and reliable network of renewable energy production.

1.2. Fuel Cells

Fuel cells are electrochemical devices that convert chemical energy stored within a fuel into electrical energy. This technology type is particularly attractive as a clean energy device due to various reasons [9]:

i. Efficiency. In theory, fuel cells deliver a greater electricity generation efficiency than conventional methods.
ii. Simplicity. The essentials of a fuel cell involve very few moving parts which can lead to highly reliable and durable systems.
iii. Low emissions. Many fuels utilised within fuel cells release benign by-products such as water. Consequently, the device is essentially considered ‘zero emission’. This is particularly attractive for global strategies to reduce carbon emissions.
iv. Silence. Fuel cells are extremely quiet, even with additional fuel processing equipment. This is especially important for portable and local power generation.
v. Scale of applicability. Fuel cells offer a wide scope of applications from utility power stations to portable laptops [10]. They are also encouraging devices for delivering energy to less developed regions where there is limited or no access to the public grid or a large price associated with connecting electricity.

1.2.1. Terminology

To judge the output of fuel cells and determine how well the device is performing, it is important to understand how to interpret their performance. The most common way of characterising the performance of different fuel cells is through current-potential relationship curves, also known as polarisation curves. The magnitude of deviation from the expected potential, otherwise known as the overpotential (η), experienced within these polarisation curves is specific to the cell construction and varies across operational conditions such as electrode shape, size and design, electrolyte composition and concentration, operating temperature, etc [11].

Since electrode reactions take place at the electrode-electrolyte interface, the electrode process includes some or all the following elementary electrochemical steps [11]:

1. Mass transport: transport of reactants from bulk electrolyte to the electrode surface.
2. Surface conversions preceding the electron transfer: including rearrangements of reactant molecules, adsorption on the electrode surface, chemical reactions, etc.
3. Electron transfer at the electrode surface of the electrode-electrolyte interface.
4. Surface conversions following the electron transfer: including chemical reactions, desorption from the electrode surface, insertion into the crystal lattice, etc.
5. Mass transport: the transport of products away from the electrode surface to the bulk electrolyte.

In practice, each step above occurs at a finite rate and can individually contribute to the overpotential. The three main types of overpotential are: (i) activation overpotential (η_a), (ii) ohmic overpotential (η_o) and (iii) concentration overpotential (η_c), and their dominating contributions towards fuel cell polarisation curves is shown in Fig. 1.4. This can also be expressed by the following equation [11-14]:

$$\eta = \eta_a + \eta_o + \eta_c \tag{1.1}$$

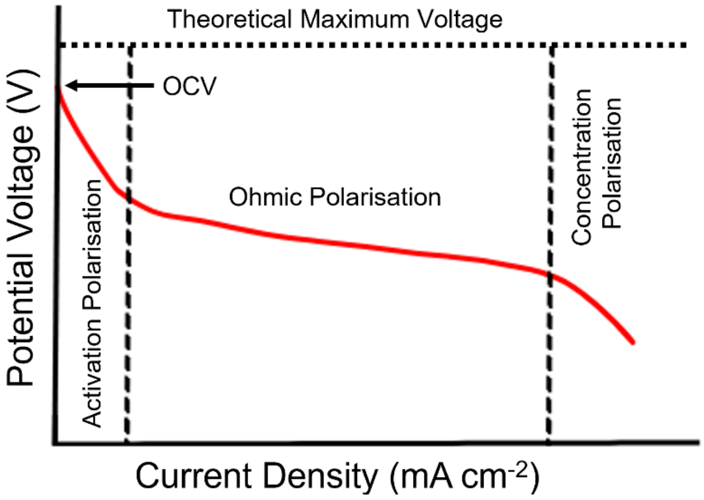

Fig. 1.4. Polarisation curve showing the electrochemical efficiency of a fuel cell with the dominating sources of overpotential highlighted over the operating range.

Activation overpotential (η_a) is a function that describes the charge transfer kinetics of an electrochemical reaction and dominates losses at low current density. More specifically, it is the potential difference above equilibrium value required to produce a current and is determined by the activation energy required to transfer an electron at the electrode interface [11-16]. This overpotential is closely related to the steps 2-4 above. It can be caused, for example, by electron accumulation and inefficient electron transport at the electrode surface, which in turn produces an energy barrier for the incoming electrons. It may also be related to the surface conversion steps preceding or following the electron transfer step, such as catalytic decomposition or crystallisation [11]. For the above reasons, η_a can also be referred to as electron transfer overpotential since it is specifically related to electron transfer at the interface as well as the catalyst/electrode properties [11, 15].

Every conductive material has an intrinsic resistance (R) to charge, subjecting all electrochemical cells to loss in cell potential known as ohmic overpotential (η_o). Ohmic overpotential follows Ohm's law. When current is applied to the cell, the ohmic potential drop iR varies linearly with this applied current [11-13, 15, 16]. This type of polarisation is responsible for losses in the middle regime of polarisation curves and can be categorised into electron resistances

(R_{elec}) and ionic resistances (R_{ionic}). This can be mathematically expressed as the following [13, 16]:

$$\eta_o = iR = i(R_{elec} + R_{ionic}) \tag{1.2}$$

R_{elec} considers the combined electrical resistances from the cell components such as the electrolyte, catalyst layer, gas diffusion layer (GDL), flow field plates (FFPs), current collector and interface contacts [13, 15]. Subsequently, the entirety of the fuel cell build plays a role in ohmic overpotential and thus cell performance. R_{ionic} on the other hand, considers ionic resistances experienced within the device.

Since a fuel cell must be continuously supplied with fresh fuel and oxidant to produce electricity and products must be simultaneously removed for maximum fuel cell efficiency, the reactant and product concentration profiles within the catalyst layer and electrode interface heavily influences fuel cell performance [13]. Concentration overpotential (η_c) is caused by the concentration gradient profile that develops between the bulk electrolyte and electrode surface due to slowness in the mass transport mechanisms described in steps 1 and 5 as the cell reaction proceeds [11]. Due to limitations in mass transport, the reactant molecules cannot reach and/or the product molecules cannot depart from the reaction sites which leads to depletion of the reactants or accumulation of the products at the electrode surface [11, 12]. This type of overpotential dominates losses at high current density [12]. Such mass transport in fuel cell electrodes and flow structures occur on a microscale and are often dominated by diffusion. These concentration losses can be minimised by optimising mass transport within the fuel cell electrodes, as well as the flow structures embedded into FFPs, to provide sufficient pathways for reactants and/or products to diffuse to/from the electrode surface [13].

The above terminology helps describe the behaviour and nature of the polarisation curves obtained by fuel cell devices. With a basic understanding of such devices, the following sections introduce the different types of fuel cells and presents the aims of this study.

1.2.2. Hydrogen as a Fuel

The discovery of fuel cells was made by William Grove who published a description of the first cell in 1839 [17]. Since then, enormous amounts of effort have been devoted towards the development of these devices.

The use of hydrogen within fuel cells, such as in proton exchange membrane fuel cells (PEMFCs) for example, remains most popular. The development of fuel has accompanied the path of increasing hydrogen amount, from coal to petroleum to natural gas. Reaching a state of pure hydrogen is therefore a systematic direction for fuel evolution [18]. Hydrogen fuel cells are considered a clean technology since they have a low polluting nature and produce water, an environmentally benign product [19, 20]. This makes it attractive for electric vehicles with no expected emissions on the consumer end [6, 21]. Moreover, the chemical energy within hydrogen may be stored for prolonged periods of time, making it ideal to combine with intermitted renewable energy during phases of low energy production. [22]

Despite being a promising candidate for clean energy generation, hydrogen as a fuel has limitations. Perhaps the biggest challenges of using hydrogen are its current storage and transportation networks, with no existing infrastructure for the vast distribution of hydrogen and such systems requiring large amounts of money.

At present, hydrogen is most commonly stored using two methods; (a) compression and (b) liquefaction, both of which have difficulties associated with on-board storage [18]. Amongst the two, compression may be the easiest way to store hydrogen. Nevertheless, relatively high pressures are required to satisfy a viable driving distance and although there have been advances in the electrochemical compression of hydrogen which has led to pressures of up to 100 MPa, it is not convenient from a practical and energetic point of view [23, 24]. The biggest problem associated with liquefying hydrogen on the other hand, is the continuous boil-off of liquid. Gasification of liquid hydrogen within a cryogenic vessel (21.2 K) is unavoidable, even if a perfect insulation procedure is employed. This type of storage demands insulated cryogenic tanks and refrigeration units which add additional weight and cost. In both cases of storage, unexpected release of hydrogen into the atmosphere is a great safety threat since it is an odourless gas, which makes it difficult to control and dangerous, especially for consumer use. Furthermore, hydrogen has a large flammability range in air, stretching between 4-74 %, in contrast to gasoline and natural gas for example, which have a flammability range of 1.4-7.6 and 5.3-15 % respectively [25-27]. Thus, hydrogen being the current preferred fuel choice for fuel cells ironically hinders the large-scale implementation of today's fuel cells.

Moreover, commercial expansion of PEMFCs is largely limited by the high expense associated with platinum group metal (PGM) electrocatalysts [28-35]. For perspective, electrocatalysts account for greater than 30 % of the total PEMFC cost [36-38]. Sectors such as the automotive industry, for example, are especially demanding and require sufficient cost reductions to be made for fuel cells to be cost competitive with current technologies in the sector [39].

1.2.3. Alternatives to Hydrogen

To tackle the difficulties related to hydrogen and truly value the concept of hydrogen economy, there has been growing incentive for the use of hydrogen carries. Methanol, for example, has often been proposed as an indirect hydrogen storage media to generate electricity. The first direct methanol fuel cell was proposed by Justi and Winsel in 1955 and the potential of methanol has since been explored for several decades due to its low cost and reactivity [40, 41].

Despite developments, the prospects of methanol fuel cells remain rather limited due to its properties. Methanol is completely miscible in water making it extremely difficult to separate and severely problematic if the liquid is released into drinking supplies. Given that the lethal dose is around 30 to 240 mL or 1 g per kg, extreme caution must be carried out when handling methanol [42]. Moreover, methanol, along with other organic-based fuels such as ethanol, contain carbon and will ultimately release CO_2 upon utilisation. Use of such fuels within fuel cells therefore requires the presence of a steam reformer to extract hydrogen from the carbon source and a carbon capture and storage unit, which in turn would contribute weight, additional space and cost.

This has driven progression towards the use of nitrogen-based fuels like ammonia and hydrazine as carbon-free indirect hydrogen storage media [25, 43]. Ammonia contains 17.7 wt% hydrogen and unlike ethanol and methanol, contains no carbon and therefore will not release CO_2 upon decomposition. [25, 44] For comparison, a range of hydrogen and ammonia fuel characteristics are illustrated in Table 1.1.

Table 1.1. Comparison of properties between hydrogen and ammonia [1, 25, 45-48].

Fuel	**Temp (K)**	**Pressure (MPa)**	**Weight (H_2 %)**	**Energy Density (MJL^{-1})**	**Flammable Range (%)**	**Cost**
Gaseous Hydrogen	298	35	100	2.76	4-74	High
		70		5.60		
Liquid Hydrogen	38	0.1	100	8.60	4-74	High
Liquid Ammonia	298	1	17.6	12.9	16-25	Low

As can be seen from the table above, ammonia offers several appealing properties. Unlike hydrogen, ammonia has a much more confined flammability range of 16-24 % and has a much less stringent pressure demand at 298 K. Most striking perhaps, is the greater energy density stored within liquid ammonia, compared to gaseous and liquid hydrogen. The cost factor also presents an attractive selling point of ammonia as a potential fuel for fuel cells.

1.2.3.1. Ammonia Production

The manufacture of ammonia is already well established, with a global production of around 180 million tons being reported in 2015 [21, 49]. This large scale production is mainly owed to the extensive use of ammonia within the fertiliser industry and as a precursor for chemical syntheses and industrial refrigerants [50]. Due to its vast synthesis and worldwide use, a network for supplying ammonia is already well known. This indicates that ammonia can easily be globally transported as a fuel which is especially important for countries that have little or no access to grid transmission or fossil fuels [51].

Currently, production is predominantly carried out through the Haber–Bosch process which is quite energy extensive [52]. However, due to the recent interest in ammonia as an energy storage medium, concepts of green ammonia are quickly emerging as cleaner and more energy efficient methods of ammonia generation. Since use of ammonia in a fuel cell is essential CO_2-free on the user end, renewably sourcing ammonia would lead to a much more sustainable life cycle analysis of the fuel [25, 51, 53-56]. This demonstrates the excellent potential of ammonia as an environmentally friendly vector and its possible role as a sustainable fuel for the future.

1.2.3.2. Safety and Handling

To consider ammonia as a fuel for wide range use and availability to the public, safety and handling of the chemical must be addressed. Ammonia can be easily dissolved in water to give a solution with 35 wt. % that can simply be stored in a glass bottle with no specialised equipment required [25]. Yet it should be noted that ammonia is corrosive by nature, with the potential to cause dehydration, severe skin burns and eye damage as well as respiratory difficulties on inhalation at vapour concentrations of 1700 ppm [6, 57]. However, suitable safety measures can be put in place when handling ammonia [6]. For example, the smell of ammonia is easily detected by nose at concentrations as low as 1 ppm due to its sharp and irritating odour [6].

1.3. Direct Ammonia Fuel Cells

Given the above, ammonia fuel cells are a particularly interesting branch of fuel cells due to the fuel's high energy density, large-scale global production, extensive existing infrastructure, and low cost per unit energy [53, 58-62]. Although ammonia fuel cells are not as widely explored as hydrogen counterparts, they do have explicit advantages over other fuel cell types. For example, durability increases since corrosion of these devices is less of an issue in alkaline environments. Consequently, thinner and more easily manufactured hardware can be used. This is advantageous from a commercialisation perspective. Furthermore, operating under alkaline conditions allows for a wider choice of catalysts to be used such as metals, alloys, oxides and hydroxides, all of which are chemically stable under alkaline environments. This will be discussed in greater detail in later chapters.

Ammonia fuel cells can be considered as either direct or indirect, depending on where the decomposition of ammonia occurs. This study focuses on direct ammonia fuel cells (DAFCs) since these systems reap the benefits of using ammonia directly within the fuel cell and truly utilise the chemical energy stored within ammonia itself. Unlike indirect fuel cells, where ammonia is decomposed for on-site hydrogen generation, DAFCs bypass the cracking step and consequently reduces the need for onboard hydrogen storage. This leads to savings in operating costs and improvements in the overall efficiency [8, 25, 59, 63-65].

Due to the vast advancements in DAFCs, their use in potential applications have been explored. These have included: (i) hybrid technology such as integrated ammonia fuel cell-gas turbines, ammonia-hydrogen fuel cell blends and fuel cell-battery hybrid systems, (ii) transportation such as in cleaner railway applications and fuel cell vehicles and (iii) wastewater treatment due to the high content of ammonia in industrial wastewater such as landfill leachate. Efforts towards the development of direct ammonia fuel cells and their potential applications within such future technology makes these devices worthwhile exploring.

Notably, DAFCs can be categorised according to different criteria such as electrolyte, temperature, reactant-based and ion transfer-based classifications. Common categories of DAFCs and their basic properties are highlighted in Table 1.2.

Table 1.2. Different DAFCs categorised according to electrolyte, conduction ion and operating temperatures.

Type	**Electrolyte**	**Conducting Ion**	**T (°C)**	**Key Advantages**	**Key Disadvantages**
Oxygen anion conducting solid oxide fuel cells	Metal oxide solid ceramics (e.g. Y_2O_3-stabilised ZrO_2 zirconia)	O^{2-}	500-1000	• Elevated temperatures allow for combination of cracking and electricity generation process. • Fuel flexibility.	• Possibility of NO_x formation. • Long start up and cool down times. • Materials that can endure elevated temperatures over long durations.

					• Thermal mismatch of components may lead to mechanical failure.
Proton conducting solid oxide fuel cells	Metal oxide solid ceramics (e.g. $BaZr_{1-x}Y_xO_3$)	H^+	500-700	• No possibility of NO_x formation. • Lower operating temperatures compared to SOFC-O.	• Long start up and cool down times. • Materials that can endure elevated temperatures over long durations. • Thermal mismatch of components may lead to mechanical failure.
Alkaline fuel cells	Molten hydroxide electrolyte (e.g. NaOH/KOH)	OH^-	50-450	• Relatively low operating temperature.	• Reaction with CO_2 in air leads to formation of carbonate ions, which poison cell.
Alkaline membrane fuel cells (AMFCs)	Alkaline exchange membrane (AEM)	OH^-	50-120	• Not poisoned by carbonate formation. • Low operation temperature. • Enhanced thermodynamic efficiency.	• Difficult to obtain good catalytic activity at low operating temperature. • Currently reliant on PGM catalysts.
Microbial ammonia fuel cells	-	-	-	• Utilise microorganisms to convert energy from biodegradable material. • Useful in waste-	• Presence of biofouling due to biofilm formation on cathode. • Deterioration of catalyst. • Cleaning controls needed.

				water treatment.	

As can be seen from Table 1.2, the scope of DAFCs is vast, all of which cannot be covered within the content of this study. Due to their advanced current progression, enhanced thermodynamic efficiencies and quick start up times, this work focuses on low temperature (< 120 ^{o}C) DAFCs, namely AMFCs. High temperature fuel cells such as solid oxide fuel cells (SOFCs) along with alkaline fuel cells and microbial ammonia fuel cells are therefore not considered in the scope of this study. Therefore, DAFCs mentioned in this work simply refer to those based on AMFCs.

1.3.1. Reaction Mechanism

To exploit the basic nature of ammonia, the fuel cell is often operated under alkaline conditions. In these fuel cells, oxygen is introduced at the cathode and reacts with water to generate OH$^-$ ions. These ions are transported across an AEM to the anodic side where they react with ammonia to produce nitrogen and water. The electrons flow through an external circuit creating a flow of electricity [66]. The overall reactions that take place are as follows [64]:

$$Anode: 2NH_3 + 6OH^- \rightarrow\ N_2 + 6H_2O + 6e^- \tag{1.3}$$

$$Cathode: \frac{3}{2}O_2 + 3H_2O + 6e^- \rightarrow 6OH^- \tag{1.4}$$

$$Overall: 2NH_3 + \frac{3}{2}O_2 \rightarrow\ N_2 + 3H_2O \tag{1.5}$$

This type of fuel cell can effectively be regarded as an alkaline analogue of PEMFCs. A schematic representation of these devices is shown in Fig. 1.5. This technology type can be considered a promising candidate for use in wastewater treatment and in small-medium range power devices such as electric vehicles, trains and ships.

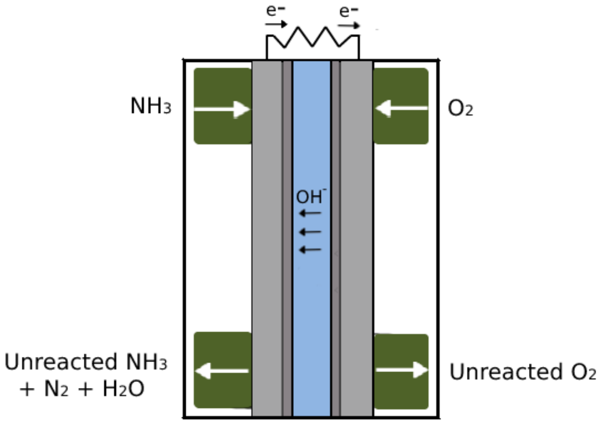

Fig. 1.5. Schematic representation of a direct ammonia fuel cell.

1.3.2. Challenges

Although fuel cell technology stands on the brink of large-scale commercialisation, the transition from laboratory to commercial scale has proven to be difficult. This is largely due to the search of appropriate materials and manufacturing methods that are required for this technology type to become competitors of existing power generation systems. Currently, a PEMFC stack costs around \$75/kW at high volume production where the catalyst layers account for over 40 % of overall costs due to the employment of PGMs. For fuel cell electric vehicles to be cost competitive, the goal is \$30/kW for light duty purposes and \$60/kW for heavy duty [67]. In the direction of catalyst development, there has been significant reduction in Pt loading, however, the increasing cost of Pt still hinders this progress further. Two strategies are often proposed: (i) the design of Pt-based catalysts with enhanced intrinsic activity or (ii) complete replacement of Pt and other PGM-based catalysts [39]. The latter is especially applicable in DAFCs which allow for a wide scope of materials to be used.

Despite DAFCs offering such flexibility, the search for low-costing materials with high catalytic activity remains a key topic of interest, with many methods currently being investigated to overcome such hurdles. A suitable material must not only be cheap, but also be durable and able to bind to reactant molecules with sufficient strength to break bonds under low temperature. This continues to be a challenging area of research.

1.4. Aim of Project

Much focus on DAFCs to date has regarded material optimisation. However, to truly exploit the advantages of employing non-PGM materials as catalysts at the electrodes, the whole fuel cell design must be considered. The activity of a given material for example, may be overshadowed by other limitations such as interactions at the electrode-electrolyte interface and the design of the device itself. The aims of this study focus on optimising parameters that can affect the activation, ohmic and concentration overpotential of DAFCs, in turn improving overall performance of the cell. The aims of this study and are essentially threefold:

1. To optimise fluidic flow distribution in the flow field plates to enhance mass transport across the cell active area. Construction of DAFC hardware components with compatibility and cost will be considered. This is imperative since entirety of the cell may contribute to ohmic overpotential. Design of the FFPs will also be explored and optimised for efficient mass transport of gas and liquid to/from the active sites of the catalyst surface at the electrode-electrolyte interface. This is vital to reduce concentration overpotential.

2. Design and optimisation of a perovskite oxide to assist in the catalysis of the oxygen reduction reaction (ORR) at the cathodic site of a DAFC. Strategic design of catalysts is important to emphasise the ability of a material to catalyse the given reaction and to reduce activation overpotential. The notion behind this aim is to alleviate reliance on conventional Pt/C-based electrodes. Characterisation of the half-cell reaction will be essential in evaluating the potential of these materials and developing structure-property relationships. The design and optimisation of a perovskite oxide to assist in the catalysis of

ammonia oxidation reaction (AOR) will also be investigated although not explicitly introduced into a DAFC.

3. Implementation of the perovskite oxide catalyst into the assembled DAFC. Proper optimisation of an effective cathode catalyst layer (CCL) is crucial to truly exploit the capability of the catalyst in a DAFC and to enhance polarisation performance by optimising interactions at the electrode-electrolyte interface. This will in turn aim to reduce overpotential of the cell. The result of varying CCLs on cell performance will therefore be studied. For comparative purposes, a DAFC employing a Pt-based CCL will also be explored to observe performance differences between the non-PGM and PGM-based cells.

This work aims to show that strategic design and optimisation of a DAFC employing a non-PGM-based electrode may be a promising route for fuel cell progression.

CHAPTER 2 Literature Review

The works in this chapter form parts of the publications by the author in Journal of Materials Chemistry A [1]; Applied Catalysis B: Environmental [68] and Separation and Purification Technology [69]. The content also forms part of a paper by the author which is currently under review in ACS Applied Materials & Interfaces [70].

2.1. Introduction

This section focuses on current literature regarding development and progression of AMFCs, hereby referred to as DAFCs. The review will consider studies that show key performance to date and provide insight into the challenges as well as the perspective of these devices. The review will play close attention to the types of materials that can be used for oxygen reduction at the cathode and routes to optimising these electrodes for the future of these systems.

2.1.1. Direct Ammonia Fuel Cells

The first DAFC based on an AEM was reported by Tao's group in 2010 [64]. In these systems, oxygen is introduced at the cathodic component where a reaction with water occurs to generate OH^- ions. The OH^- ions are then transported across the AEM to the anodic side, where they react with ammonia to produce nitrogen and water [64]. This is expressed by Eqs. (1.3-1.5)

A schematic overview of the reactions that occur at the anode and cathode are provided in Fig. 2.1.

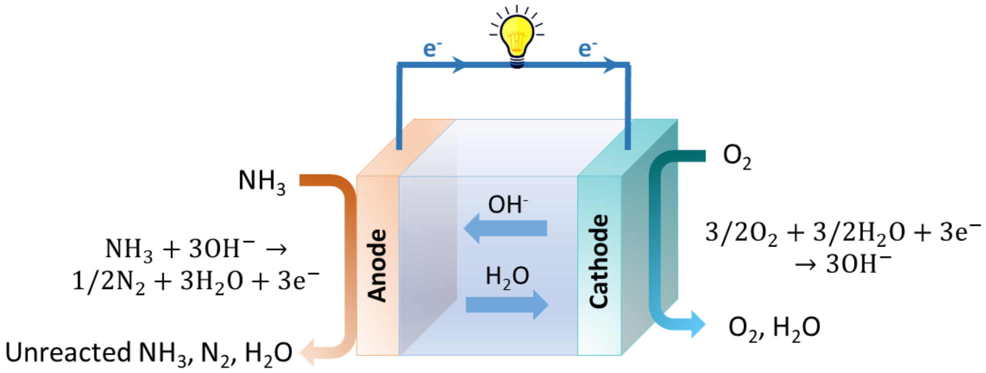

Fig. 2.1. Schematic illustration of low temperature DAFC [1].

This is considered a clean technology since the only products of the cell are water and nitrogen. Unlike SOFCs, where the ammonia is initially decomposed into its constituent elements, DAFCs use ammonia directly as a fuel. This mitigates the need for high temperatures and the reaction proceeds regardless of the decomposition step [71, 72]. Effectively, DAFCs are considered an attractive competitor of PEMFCs, where the latter of the two operates under acidic conditions and subsequently must employ expensive Pt-based electrocatalysts to endure such harsh pH environments. DAFCs however, are compatible with a greater selection of materials and has consequently led to much progression being conducted within such systems [63]. Table 2.1 lists some DAFC compositions which have demonstrated good performance in recent literature.

Table 2.1. Open circuit voltage (OCV) and peak power density (PPD) of different DAFCs [1].

Anode	**Cathode**	**Membrane**	**Fuel**	**Oxidant**	**T (°C)**	**OCV (V)**	**PPD (mW cm^{-2})**	**Ref**
PtIr	Acta 4020	PAP-TP (10 µm)	3 M NH_4OH + 1 M KOH	O_2	80	0.63	121	[58]
			3 M NH_4OH + 3 M KOH				135	
			3 M				117	

			NH_4OH + 5 M KOH					
Pt-based	non-Pt-based	Commercial AEM	NH_4OH + aq. Base	O_2	100	0.70	450	[73]
NiCu	Pt	Laminar Flow	1 M NH_4OH + 1 M KOH	H_2SO_4	25	1.15	5.06	[74]
			1 M NH_4OH + 2 M KOH			1.30	9.21	
			1 M NH_3H_2O + 3 M KOH			1.31	10.94	
Cr-Ni	MnO_2	Resin-PVA	35 % NH_4OH	O_2	25	~0.82	~9	[64]
		CPPO-PVA	Gaseous NH_3			~0.65	~11	
Pt/Ru	Pt	Mg-Al-CO_3^{2-} layered double hydroxide (500 μm)	5 M NH_4OH + 1 M KOH	Air	20	~0.40	~1.25	[75]
					50	0.45	~3.20	
					80	~0.55	~4.5	
NiCu	$SrCo_{0.8}Cu_{0.1}Nb_{0.1}O_{3-\delta}$	Commercial AEM	35 % NH_4OH + 1 M KOH	Air	25	0.45	0.25	[34]
NiCu	$SrFe_{0.8}Cu_{0.1}Nb_{0.1}O_{3-\delta}$	Commercial AEM	0.02 M NH_3H_2O	Air	25	0.35	0.03	[33]
PtIr	Fe-N-C	PAP-TP (18 μm)	GaseousNH_3 + 400 mlmin^{-1} N_2	O_2	95	0.56	75	[76]
Pt_1Ir_{10}	Ag	Tokuyama membrane	16 M NH_4OH		120	0.68	180	
			12 M NH_4OH + 2.5 M KOH		100	0.72	280	
PtIr	$MnCo_2O_4$	PAP-TP-85	7 M NH_4OH + 1.25 M KOH	O_2	110	~0.70	235	[77]
	$FeCo_2O_4$						~100	
	Co_3O_4						~150	
NiCuFe	NiCuFe	Commercial AEM	7 M NH_4OH + 3 M KOH	Air	80	0.62	8.90	[78]

It should be acknowledged that studies demonstrating enhanced DAFC performances employ pure O_2 as the oxidant at relatively high flow rates (500 mLmin^{-1}) [58, 73, 76, 77]. This, however, introduces further limitations when considering this technology for scale up purposes, especially for applications such as transport where consumer safety is of utmost importance.

Furthermore, from the table above, it should be noted that OH^- ions are typically introduced to the anodic component. This is often to increase the rate of the reaction stated in Eq. (1.3) and to limit the ammonia oxidation reaction (AOR) becoming restricted by mass transfer resistance of OH^- ions across the membrane. Hence many researchers not only investigate the effects of ammonia in DAFCs, but also that of OH^- ion concentration and transportation. For effective transportation of OH^- ions from the cathode to anode, an adequate AEM must be chosen. This is discussed in the section below.

2.1.2. Membrane Choice

The choice of AEM for DAFCs are based on good chemical stability, high ionic conductivity and robust mechanical properties [79]. Since these systems are also concerned with the transportation of OH^- ions produced at the cathode and consumed at the anode, the chosen membrane must also demonstrate resistance to water swelling. Water uptake is therefore another important parameter regarding membrane employment [79-82].

DAFCs typically operate at a temperature which is determined by the durability of the AEM [83]. Commercially available AEMs such as Tokuyama A201 are offered for use within such fuel cells and have specific operating conditions that they can withstand, for example, these membranes are typically tested up to 80 ^{o}C. Beyond these limits, the membranes lose their functionality and are deemed unstable for use [84].

Recently, the power density and longevity of membranes to be used within DAFCs have been improved due to the development of AEMs with high conductivity and better chemical and mechanical stability [85]. Great efforts have been devoted towards synthesising AEMs with alkaline stability at 80 °C or higher [80, 81, 83, 86]. These membranes are typically designed based on two distinctive features: a polymer backbone and an ion conductive moiety [87]. Wang et al. reported the synthesis of a poly(aryl piperidinium) (PAP) membrane and showed a steady increase in OH^- conductivity across the membrane as temperature was increased [86]. The conductivity more than doubled, from 78 to 193 mS cm^{-1}, as the temperature was elevated from 20 to 95 °C. Increased OH^- ion conductivity across the membrane can in turn lead to faster reaction kinetics at the anodic side since OH^- ions are delivered at a faster rate. Likewise, Lee et al. demonstrated a similar trend when using a PAP membrane [80]. It was found that OH^- conductivity increased from 54 to 112 mS cm^{-1} as temperature was elevated from 25 to 80 °C. It should also be noted that at elevated temperatures, a greater water uptake was also observed. Nevertheless, use of such polymer-based membranes is an encouraging direction for DAFCs to overcome the temperature dependent limitations associated with conventional AEMs.

It should be noted, however, that all alkaline membranes are susceptible to reacting with CO_2 in air, leading to the formation of CO_3^{2-} ions [6]. The presence of CO_3^{2-} ions is challenging since these ions have a relatively low specific conductivity, four times lower than that of OH^- ions. This reduces the overall conductivity of the membrane, increases resistance and consequently leads to reduced performance. Along with lowered conductivity, the presence of CO_3^{2-} ions dilutes the number of available OH^- ions available to react with ammonia and lowers local pH values [88]. The carbonation reaction of OH^- ions is shown below:

$$CO_2 + 2OH^- \rightarrow CO_3^{2-} + H_2O \tag{2.1}$$

Good chemical stability of a hydroxide-conducting membrane is crucial to accomplish practical longevity of DAFCs. More than often, pure O_2 or CO_2 free air is used as the oxidant at the cathode to avoid the formation of CO_3^{2-}

ions [66, 88]. From this point of view, it is desired to develop CO_2-tolerant OH^- ion conductors to be used as electrolytes for DAFCs.

Along with the inherent properties of the materials used, it is important to note that external properties such as the thickness of the membrane can also affect cell performance. The internal resistance of a fuel cell will reduce by utilising a thinner membrane by reducing the pathway that the OH^- ions must cross, so the reactant can be delivered to the anode at a faster rate. Whilst pursuing thinner membranes, good mechanical properties and mechanical robustness must not be compromised [88]. Reducing the membrane thickness too greatly could lead to fuel permeation across the membrane, resulting in fuel crossover and potential flooding of the cathode side [59]. This has been observed in cases which have led to a reduced OCV and overall fuel cell performance [89]. A trade-off must therefore be implemented to ensure that the electrolyte is thin but with reasonable mechanical strength. Since thickness of the electrolyte has a direct effect on the fuel cell performance

Nonetheless, the recent progression in AEMs has undoubtedly opened pathways for excellent DAFC performance to be attained and the flexibility in such designs offers a variety of thicknesses to be selected depending on individual user discretion.

2.1.3. Electrocatalyst Choice

The electrocatalysts employed at the anode and cathode sites of DAFCs must be able to assist the ammonia oxidation and oxygen reduction reactions respectively. It is widely known that PGMs such as Pt and Pd have proven to be excellent electrocatalysts in electrochemical storage and conversion systems [90]. This is evidenced by most studies displaying excellent performance in Table 2.1 still relying on PGM-based catalysts at the anode and/or cathode of DAFCs. Commercial expansion of fuel cells (including PEMFCs) however, are largely limited by the sluggish nature of the ORR even on such PGM-based surfaces, along with the scarcity and high expense associated with these electrocatalysts [28-39]. On this basis, exploration of effective electrocatalysts to assist ORR at the lowest possible cost is essential for future use of these devices [29, 35].

ORR is often regarded as an important process within renewable energy applications such as DAFCs (including SOFCs) and metal-air batteries which are electrochemical cells that employ a pure metal negative anode and an external positive cathode of ambient air [29, 35, 91-98]. ORR occurs at the cathodic site and plays an important role in the overall performance of fuel cells due to the sluggish kinetics associated with the reaction. The exact mechanism and rate determining steps in alkaline media are determined by the electrocatalyst and involves either a $4e^-$ or $2e^-$ pathway as shown in Eq. (2.2) and Eq. (2.3) respectively [28, 99]. The mechanistic factors governing ORR in alkaline media, however, are not widely understood and have proven to be rather complex [28, 31, 32, 100].

$$O_2 + 2H_2O + 4e^- \rightarrow 4OH^- \quad E^0 = 0.401 \text{ V vs. SHE} \tag{2.2}$$

$$O_2 + H_2O + 2e^- \rightarrow HO_2^- + OH^- \quad E^0 = -0.076 \text{ V vs. SHE} \tag{2.3}$$

The alkaline environment of DAFCs allow for faster ORR kinetics, the use of less corrosive conditions and use of cheaper non-PGM electrocatalysts. This in turn enables a wider range of stable materials to be explored. Such non-PMG electrocatalysts often include carbon-transition metal hybrids, doped nanocarbons and perovskites [28-34]. Yet, the majority of research to date still heavily relies on PGMs. The use of such non-PGM electrocatalysts for ORR and their applicability as cathodes in DAFCs is subsequently imperative for future progression and potential commercialisation of DAFCs.

2.2. Aim of Review

Due to the importance of ORR in energy storage technology, along with the high cost of current electrocatalysts which largely involve PGM or PGM-based materials, the need for efficient and cost-friendly catalysts is essential.

The aim of this section of the review is to better appreciate and understand how non-PGM materials, such as perovskite oxides, can be used as electrocatalysts within DAFCs. Doing so may provide a route to cheap, clean and reliable energy devices for the future. Furthermore, careful preparation of a suitable cathode catalyst layer is required to optimise interactions at the electrode-electrolyte interface of working DAFCs. This not only requires a suitable material to catalyse the given reaction, but also a good pathway for electrons, ions and reactant/products to and from active sites. This review is subsequently subdivided into two main sections. Section 2.3 explores literature regarding the nature and design of perovskite oxides, where key factors determining their ORR activity will be considered. In this section, a brief insight into how perovskite oxides may be used as ammonia oxidation catalysts is also introduced. Section 2.4 more closely discusses strategies to implement such catalysts as cathodes for DAFCs and the design of cathode catalyst layers. The contents of this review therefore aims to shed light on the design and potential of non-PGM-based electrodes for real energy conversion technologies.

2.3. Perovskite Oxide Catalysts

2.3.1. Background

Over the past few decades, perovskite oxides have emerged as an important family of functional materials that offer the use of cheap and earth-abundant constituent elements and have shown ability to catalyse an array of electrochemical reactions [35, 101-107]. They were first discovered in 1893, where Gustav Rose found calcium titanium oxide ($CaTiO_3$), which was later named by mineralogist Lev Perovski [108]. Since then, the term perovskite has been used to describe organic and inorganic materials based on the crystal structure ABX_3 [109]. In a primitive perovskite structure, the X species that represents the anion is typically O, and so the general formula can more accurately be described as ABO_3. Here, the A-site is occupied by a rare earth or alkaline earth metal (e.g. La, Gd, Pr or alkaline earth metal) usually with dodecahedral coordination, whilst the B-site is generally a transition metal (e.g. Mn, Cr, Fe, Ni, Co) that resides in corner-sharing octahedra, forming a BO_6 octahedron [38, 110]. Typically, the A and B site metals exist in the +3 oxidation state. In a stoichiometric perovskite, the O anion counterbalances these charges. The ideal cubic ABO_3 structure is shown in Fig. 2.2, where the BO_6 octahedron is highlighted.

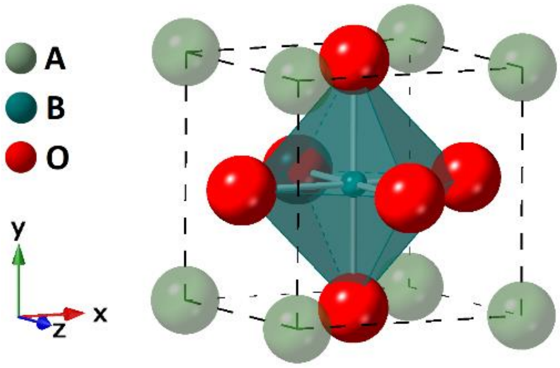

Fig. 2.2. Schematic representation of deal cubic ABO_3 structure highlighting the BO_6 octahedron [69].

These oxides have attracted much attention due to their exceptional properties such as flexibility in their electronic and crystal structure, their ability to host defective sites such as oxygen vacancies and excesses, and their superb transport capacity compared to other non-noble metal oxides [28, 29, 31]. The physio-electrochemical properties of perovskites can therefore be manipulated making these materials easily tailored towards minimising the energy barriers of various electrochemical reactions [35]. Perovskites have subsequently been used as oxygen conductors, proton conductors, mixed ionic-electronic conductors, catalysts for oxygen reduction, oxygen evolution, hydrogen evolution and multi-functional reactions [29, 106, 109, 111, 112]. They have also received considerable interest for various applications such as SOFCs, supercapacitors and heterogenous catalysis [113-122].

Amongst the series of applications for perovskite oxides, they are particularly desirable in the design of highly active and stable ORR electrocatalysts in alkaline media [28, 29, 31, 32, 35, 38, 97, 99, 109, 123-128]. Research into the use of ABO_3-based perovskites as ORR electrocatalysts dates back to as early as 1978, where Yasumiti et al. studied the cathodic reduction potential of $LaNiO_3$ in O_2-saturated alkaline solutions [123]. Since then, they have gained considerable attention due to the variety of perovskites that can be obtained by altering the A and/or B sublattice to form materials with the formula $A_{1-x}A'_xB_{1-y}B'_yO_{3-\delta}$ [29, 31, 129-131]. The BO_6 octahedron can be expanded, contracted or tilted to compensate for any differences between the ionic radii of the doped and parent ions [132]. Such distortions in the perovskite structure can drastically alter the structure and lead to interesting physical and chemical properties. The vast array of possibilities that can be achieved with perovskites makes these materials exciting and promising to explore.

Recently, Xue et al. reported ORR activity of Sr-doped $(La_{1-x}Sr_x)_{0.98}MnO_3$ ($x = 0.2, 0.3, 0.4, 0.5$) in 0.1 M KOH for Al-air batteries [133]. It was found that oxygen adsorption capacity and oxygen reduction activity could be optimised by strategically adjusting the Sr doping content and introducing A-site deficiencies; $(La_{0.7}Sr_{0.3})_{0.98}MnO_3$/C exhibited the highest ORR activity. Strategically doping into the B-site and varying elemental composition has proven to be a promising strategy to design highly active perovskite catalysts for ORR. Safakas et al. studied the effect of gradual substitution of iron by cobalt in $La_ySr_{1-y}Co_xFe_{1-x}O_{3-\delta}$ on ORR activity in 0.1 M KOH; where $La_{0.8}Sr_{0.2}CoO_{3-\delta}$ showed optimum activity [99]. Sunarso et al. compared ORR activity of $LaMO_3$/C and $LaNi_{0.5}M_{0.5}O_3$/C (M = Ni, Co, Fe, Mn and Cr) electrocatalysts in 0.1 M KOH. It was reported that $LaCoO_3$ and $LaNi_{0.5}Mn_{0.5}O_3$/C were the most active amongst the series tested [124]. Sun et al. investigated the structure property relationships between the B-site metal substitution in $LaMn_xCo_{1-x}O_3$ (x = 0, 0.25, 0.3, 0.35, 0.5, 1) and the electrochemical performance. The optimised $LaMn_{0.3}Co_{0.7}O_3$ perovskite demonstrated an enhanced half-wave potential of 0.72 V compared to that of $LaCoO_3$ (0.668 V) in 0.1 M KOH [125]. Wang et al. reported that structural and compositional characterisation revealed that $La_{0.8}Sr_{0.2}Mn_{1-x}Ni_xO_{3-\delta}$ (x = 0.2 and 0.4) contained more oxygen vacancies than undoped $La_{0.8}Sr_{0.2}MnO_3$ as well as a certain amount of Ni^{3+} ($e_g = 1$) on the surface. This allowed for $La_{0.8}Sr_{0.2}Mn_{0.6}Ni_{0.4}O_{3-\delta}$ to exhibit activity similar to that of commercial Pt/C at a reduced cost, making it an efficient cathodic electrocatalyst for Li-air batteries [126]. The reports show how strategic design and implementation of perovskite catalysts can lead to excellent ORR activity. The following section subsequently provides insight into key factors determining oxygen reduction activity for the efficient design of perovskite materials.

2.3.2. Key Factors Influencing Oxygen Reduction Activity

As mentioned above, perovskite oxides possess unique properties in terms of their flexibility in tuning of electronic/crystal structures, ability to host defective sites for oxygen vacancies/excesses and excellent oxygen transport capacity compared to other non-noble metal oxides [28, 29, 31]. They are thus ideal model materials for fundamental electrocatalysis studies and for the manipulation of physical/chemical properties to give desired electrocatalytic activities.

In the following subsections, key factors that may influence the intrinsic ORR activity of perovskites are reviewed. It should be noted that these are not exclusive factors and they may be considered to contribute collectively to the catalytic performance of these materials [29].

2.3.2.1. Electronic structure of the B-site

Although the exact ORR mechanism on perovskite oxides remains ambiguous, there are generally three proposed routes based on the orientation of oxygen adsorption: (i) end-on (ii) side-on and (iii) bidentate absorption. The latter involves participation of oxygen vacancies and the B-site element [127]. Assuming that the O_2 molecule adsorbs in an end-on manner at the surface B site (Fig. 2.3a), the molecular overlap between the e_g orbital of the transition metal with the O-$2p_\sigma$ orbital of the surface bound oxygen molecule (σ^* band formation) is greater than that of the t_{2g} and O-$2p_\pi$ orbital (π^* band formation) respectively [31, 130, 131, 134]. The importance of such σ^* electron transfer in ORR was qualitatively hypothesised by Matsumoto et al., and later quantitatively validated by Suntivich et al. who predicted an e_g-filling of around 1 to be key for developing the highest activity [31, 131, 135]. This suggests that the filling of the e_g orbital, rather than the t_2g orbital, of the B-ion more accurately determines the energy gained by the adsorption/desorption of oxygen. Nature of the e_g orbital therefore more closely reflects the ORR activity [31].

The e_g-filling and therefore nature of the transition metal subsequently provides a possible route to control surface binding energy and in turn, govern the electrocatalytic activity of the perovskite [31, 109, 130]. This has further been supported by studies that have demonstrated catalytic activity of perovskites originating from the degree of σ^* band formation [31, 38, 104, 136].

Given that the optimum activity observed for ORR was found when e_g was around 1, Suntivich et al. established a volcano-type relationship between intrinsic ORR activity and the σ^* orbital (e_g) occupation of B-site ions (Fig. 2.3b) [31]. It can be seen that perovskite oxides with near unity e_g orbital occupancy such as $La_{1-x}Ca_xMnO_3$ ($t_{2g}^3e_g^1$ when x = 0, $t_{2g}^3e_g^{0.5}$ when x = 0.5), $LaCoO_3$ ($t_{2g}^5e_g^1$) and $LaNiO_3$ ($t_{2g}^6e_g^1$), exhibit optimum ORR activity [31, 104]. This can be related to Sabatier's principle of catalysis, whereby the interaction between a catalyst and the surface adsorbed oxygen species is moderate [137]. Unfortunately, it is challenging to directly measure the adsorbate binding energy at the surface experimentally and much work has focused on computational modelling [31, 138]. Focus has therefore been shifted towards identifying activity descriptors, such as e_g-filling, which can be linked to adsorbate binding energy and govern activity [130, 131, 139]. In cases where there was a lack of e_g-filling, such as in $La_{1-x}Ca_xCrO_3$ (where $t_{2g}^3e_g^0$ when x = 0 and $t_{2g}^{2.5}e_g^0$ when x = 0.5) B-O_2 bonding is too strong. Whereas when there is too much e_g-filling, as in $La_{1-x}Ca_xFeO_3$ (where $t_{2g}^3e_g^2$ when x = 0, $t_{2g}^3e_g^{1.75}$ when x = 0.25 and $t_{2g}^3e_g^{1.5}$ when x = 0.5), interaction with O_2 may be too weak. Neither situation is optimum for ORR activity and is evidenced by these materials lying on the far left or far right of the branches in Fig. 2.3b displaying values around four orders of magnitude less than those with $e_g \approx 1$. The correlation between e_g-filling and ORR activity suggests that the e_g-filling acts as a good primary descriptor for the ORR activity of these oxides [31, 130, 131, 139].

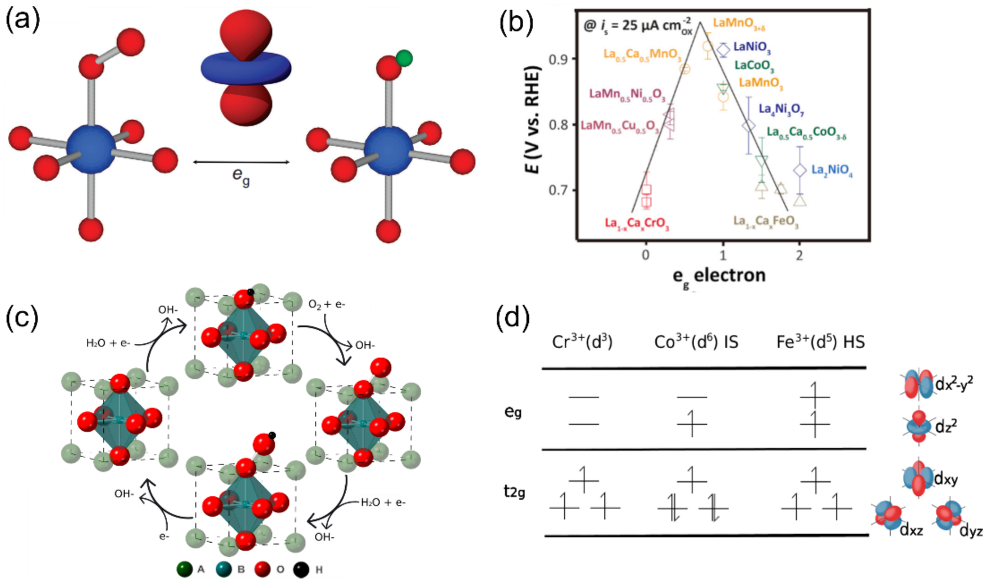

Fig. 2.3. (a) Shape of the e_g electron pointing directly towards the surface O atom which plays an important role during O_2^{2-}/OH^- exchange. O, B and H atoms are in red, blue and green respectively [31]. (b) Potentials at 25 μAcm^{-2}_{ox} as a function of e_g orbital in perovskite-based oxides [31]. (c)

Proposed ORR mechanism on perovskite oxide catalyst. (d) Schematic of the electron orbital filling in Cr^{3+}, Co^{3+} and Fe^{3+}.

Reasoning behind the volcanic trend can be provided by the mechanism of ORR proposed by Suntivich et al., shown in Fig. 2.3. In this scheme, the B-site transition metal with an e_g electron resides in an orbital that is directed towards the surface OH^- ion leading to the formation of a B-OH^- bond (image at top). The presence of single e_g electron in the σ* orbital has the ability to destabilize the B-OH^- bond and promote the O_2^{2-}/OH^- exchange reaction. The B-OH^- bond is subsequently broken and the OH^- ion is displaced in the presence of $O_2 + e^-$ (or $O_{2,ads}^-$) to give a more stable B-O^{2-} configuration (image to right). If the e_g-filling is more than 1 (the right branch in Fig. 2.3b), the O_2^{2-}/OH^- exchange is unable to gain sufficient energy during the displacement process and ORR kinetics are limited by the rate of the O_2^{2-}/OH^- exchange (step 1 in Fig. 2.3c). On the contrary, if the e_g-filling is less than 1 (the left branch in Fig. 2.3b), the B-O^{2-} is not destabilised adequately and the ORR kinetics can instead be assumed to be limited by the rate of surface OH^- regeneration (step 4 in Fig. 2.3c).

Due to the importance of e_g-filling on ORR activity, various methods to manipulate e_g occupancy of the B-site have been investigated. For example, partial substitution at the B-site has widely been used to modify the e_g-filling and bring it closer to near unity, improving ORR activity [35, 125, 140-142]. Based on this, many works have led to the discovery of highly active ORR perovskite catalysts such as $LaNi_{0.25}Co_{0.75}O_{3-\delta}$, $La_{0.8}Sr_{0.2}Mn_{0.6}Ni_{0.4}O_3$, $LaMn_{0.3}Co_{0.7}O_3$, $LaNi_{1-x}Mg_xO_3$, $LaCo_{1-x}Fe_xO_3$ and $LaNi_{1-x}Fe_xO_3$ [125, 126, 143-146]. Furthermore, the effects of structural changes and calcination temperatures have also shown to have an impact on e_g-filling [38].

Even though establishment of e_g-filling as an activity descriptor has been successful, there are still shortcomings. For example, it is difficult to confirm the e_g-filling of active metal sites purely by experimental measurements due to the complex nature of surface spin states and valency [35]. As well as e_g-

filling and metal-oxygen covalency, positioning of the d-band centre, oxidation states and oxygen vacancies have also been reported to affect ORR activity and should not be considered independently [29, 147-149].

2.3.2.2. Oxygen vacancies

Typically, the B-site transition metal has been heavily regarded as the active site for ORR catalysis and the role of oxygen vacancies were frequently overlooked [29]. As mentioned, the exact mechanism of the $4e^-$ oxygen reduction pathway remains ambiguous, however one of the proposed routes based on bidentate absorption involves participation of oxygen vacancies as well as the B-site element (Fig. 2.4a) [127]. Oxygen vacancies have therefore also been recognised as an activity descriptor for ORR and can have a profound effect on the electrochemical activity of perovskite oxides [29, 35, 150, 151].

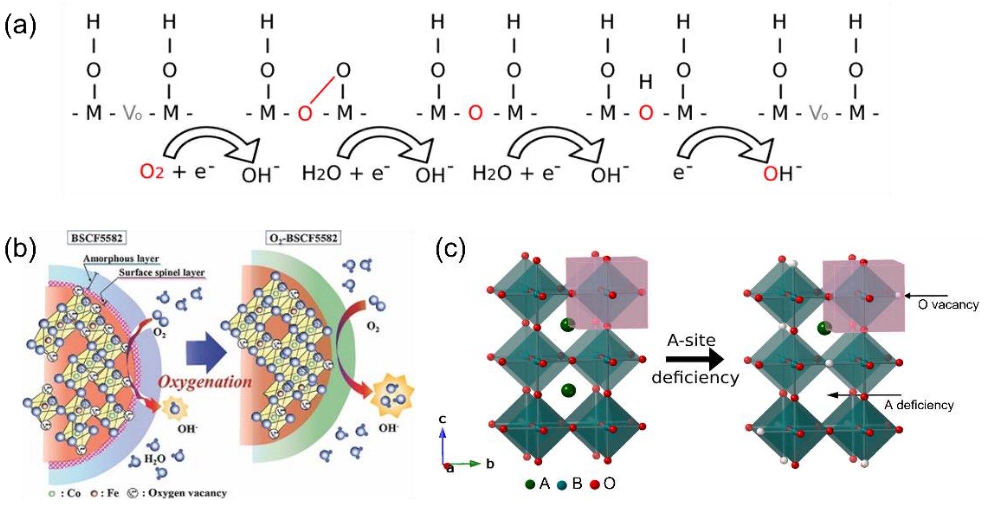

Fig. 2.4. (a) ORR mechanism in perovskites based on bidentate adsorption in alkaline media. (b) Schematic representation of the effect of thermal treatment in oxygen on $Ba_{0.5}Sr_{0.5}Co_{0.8}Fe_{0.2}O_{3-\delta}$ (BSCF558) to generate oxygen vacancy sites [152]. (c) Schematic demonstrating how A-site deficiency create oxygen vacancy sites in perovskite crystal structure.

Density functional theory (DFT) calculations revealed that the O-O bond in molecular oxygen is elongated when interacting with oxygen vacancies and the B-site element. This results in partial dissociation of the absorbed oxygen molecule [153]. Mastrikov et al. also used DFT calculations to demonstrate the role of oxygen vacancies in the chemisorption and dissociation of molecular oxygen on the surface of $LaMnO_3$ during ORR. This mechanism was then extended to other perovskites such as $LaFeO_3$ and $LaCoO_3$ [154, 155]. Moreover, the presence of oxygen vacancies enables lattice oxygen to be mobile on the perovskite surface which lowers the barrier of oxygen migration and allows oxygen species to move more easily into the interior of electrode materials [156].

The participation of oxygen vacancies in ORR has also been experimentally supported [152, 157-159]. For example, Du et al. carried out electrochemical experiments on a series of nonstoichiometric into $CaMnO_{3-\delta}$ ($0 < \delta \leq 0.5$) oxides prepared through a facile low-temperature thermal reduction method. The results showed that an improved mass activity and specific activity was achieved when a moderate amount of oxygen deficiency was introduced into $CaMnO_{3-\delta}$ ($0 < \delta < 0.5$) compared to stoichiometric $CaMnO_3$. Remarkably, when δ was near 0.25, ORR activity was found to be highest and comparable to that of benchmark Pt/C [157]. This shows that an appropriate amount of oxygen vacancy content can directly affect the ORR activity of perovskite oxides. Further to this, Chen et al. used a harsher reductive heat treatment at extremely high temperatures and a vacuum atmosphere to synthesise an oxygen deficient $BaTiO_{2.76}$ perovskite and demonstrated efficient bifunctional oxygen electrocatalysis in alkaline media, shown in Fig. 2.4b [158].

Beside thermal reduction, A-site cation deficiencies or substitution of A-site cations with those of a lower oxidation state is another effective strategy to introduce oxygen vacancies and enhance activity [29, 159-161]. Due to the large degree in compositional and structural flexibility, it is possible to maintain perovskite stability in the presence of A-site deficiencies and to support various oxygen vacancies without structural collapse [162]. When making the A-site deficient, the discrepancy in charge can be compensated by variations in the B-site oxidation state and/or the release of oxygen to maintain charge neutrality, shown in Fig. 2.4c [29, 159-161]. Zhu et al. found that the ORR activity of $LaFeO_3$ was substantially improved by properly tailoring the A-site cation deficiency [159]. The creation of surface oxygen vacancies and the small amount of Fe^{4+} species in the A-site deficient $La_{1-x}FeO_{3-\delta}$ ($x \leq 0.1$) perovskite oxides were responsible for the observed high ORR activity.

An excessive concentration of oxygen vacancies in oxides can occasionally deteriorate ORR activity. This may be owed to reduced conductivity, the presence of impurities or a change in electronic/crystal structure [157, 159, 163]. When introducing oxygen vacancies, the approach and precise amount should subsequently be finely tuned to not adversely impact ORR performance. The perovskite oxide should also be adequately characterised to assess the presence of any impurities or changes in electronic/crystal structure.

2.3.2.3. Crystal Structure

The influence of crystal structure on catalytic performance has been highlighted by many experimental and theoretical investigations [163-166]. Several groups have studied the effect of perovskite crystal structure (including bulk and surface structure) on their electrocatalytic activity. A study by Zhou et al. suggested a correlation between crystal structure and ORR activity for $LaNiO_{3-\delta}$ [103]. The authors prepared $LaNiO_{3-\delta}$ perovskites with different structures by quenching the samples to room temperature from 400, 600 and 800 °C. At room temperature, the perovskite possessed a rhombohedral structure and displayed relatively low ORR activity, as opposed to the cubic structure, obtained at 800 °C, which showed the highest ORR activity in alkaline solution. This was attributed to the slight elongation of the Ni-O bond length that arises in the cubic structure and modulates the binding ability with oxygen to mediate the adsorption and desorption of oxygen accordingly. A similar strategy has been applied to perovskites such as $La_{1-x}Sr_xMnO_3$ and $La_{0.6}Ca_{0.4}CoO_3$ to enhance their ORR capacity [167, 168].

Moreover, the layered and stacking arrangement of crystals has shown to have a profound effect on ORR activity [169, 170]. A representative work by Zhao et al. on the intrinsic properties of $AMnO_3$ (A = Ca, Sr, Br) perovskite oxides included the relationship between the crystal structure, coordination environment and ORR properties [170]. The half-wave potential of the perovskite oxides, which is reflective of their ORR activity, followed the trend: $SrMnO_3$ > $CaMnO_3$ > $BaMnO_3$. This could be related to the corner-sharing and face-sharing octahedron present in the stacking of $SrMnO_3$. The dual coordination of Mn-O corner and Mn-O face environments allowed for regulation of the oxygen intermediate interaction strength at the surface of the perovskite, reducing the *OH desorption energy.

As well as the bulk crystal structure, the surface structure of perovskite oxides can also lead to significant differences in ORR activity. The Cho group has carried out a series of studies based on the $Ba_{0.5}Sr_{0.5}Co_{0.8}Fe_{0.2}O_{3-\delta}$ (BSCF) perovskite [152, 171, 172]. In one of their works, Jung et al. proposed a strategy to tailor the surface structure of BSCF by thermal treatment in oxygen [152]. The thermal treatment process not only promoted crystallinity of the cubic perovskite structure, but also removed a heterogeneous surface layer between an amorphous layer and the bulk cubic structure, boosting ORR activity of BSCF catalyst. Later, the effects of annealing in Ar atmosphere were also investigated. Thermal treatment of BSCF in Ar increased the thickness of the amorphous layer on the surface of the perovskite, from 20 nm to around 200 nm, leading to a decrease in ORR activity. The above demonstrates how the formation and presence of an amorphous layer on the surface of the perovskite oxide suppresses its electrochemical activity.

The above works indicate that the ORR performance of perovskite oxides can be closely related to the bulk and surface crystal structure. Subsequently, efficient design and characterisation is imperative to identify the relationship between structure-chemical properties and verify ORR activity.

2.3.2.4. Electrical Conductivity

To produce high current outputs, electrocatalysis reactions require an efficient flow of electrons. Electrical conductivity of the electrocatalysis is therefore important for highly efficient performance. However, most traditional metal oxides have inherently low electrical conductivity at low temperature, therefore exploiting the true electrocatalytic activity of these catalysts is difficult. In fact, the low intrinsic conductivity of perovskite oxides in particular is a main drawback that makes obtaining the true electrocatalytic activity of these oxides towards ORR difficult [29].

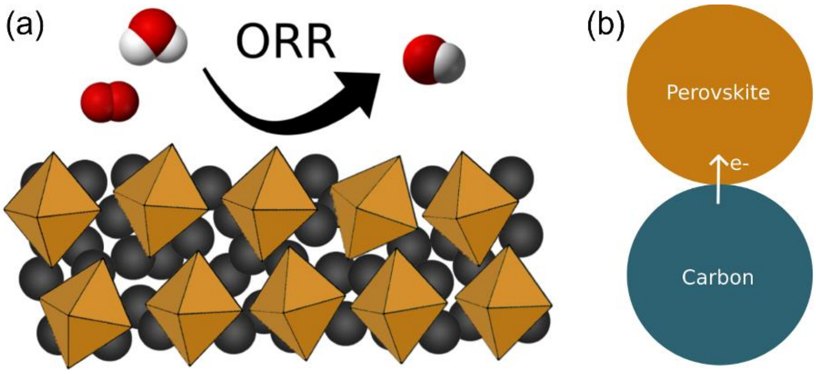

Fig. 2.5. Schematic illustration of (a) perovskite/carbon composites in ORR. (b) Possible origin of the synergistic effect between the perovskite and carbon arising from the ligand effect.

Consequently, the Shao-Horn group established a method to measure and compare the ORR activity of perovskite oxides using a thin film rotating disk electrode (RDE) technique [104, 173]. A homogeneous ink mixture consisting of oxide powder, a polymer binder (e.g., Nafion) and carbon black dispersed in a solvent was prepared for the electrochemical tests. Notably, carbon black was added to form perovskite/carbon composites and remove any electronic conductivity limitations within the electrodes. Various unfunctionalized carbon black such as Vulcan XC-72(R), acetylene black, Ketjen black and Super P/C65 were often utilised. The addition of a highly electron conductive carbon phase proved to be a useful strategy to improve ORR activity and the advantages of doing so were clearly evidenced by RDE experiments [29, 124, 126, 143-145, 157, 158, 169, 174-185].

Furthermore, perovskite oxides in bulk phase tend to be highly sintered since high calcination temperatures are necessary to form pure phase formation. This results in such materials possesses low specific surface areas, and in turn, leads to poor mass activity towards oxygen electrocatalysis. In addition to increasing electrical conductivity, incorporation of carbon also extends the surface utilisation of the perovskite phase. Fig. 2.5a shows a common perovskite/carbon composite, the carbon phase provides an electrically conductive network to connect perovskite particles and maximises utilisation of the perovskite for ORR electrocatalysis.

Addition of carbon black has therefore become a common method to measure and compare ORR activity of transition metal oxides [29]. Literature regarding variations in carbon black type as well as the mass ratio of perovskite:carbon has been explored [29, 124, 126, 143-145, 157, 158, 169, 174-180]. Perovskite/carbon composites described in literature can be roughly categorised into the following categories: (i) perovskite/carbon composites prepared by physical mixing and (ii) perovskite/carbon hybrids by chemical (in situ) synthesis such as chemical vapour deposition, electrospinning and modification of the sol-gel method to incorporate carbon black [29].

The origins of the synergistic effects between the perovskite oxide and carbon phase remains ambiguous. One proposed origin involves the concept of the ligand effect (Fig. 2.5b) [29]. The ligand (electronic) effect traditionally implicates an electronic interaction (charge transfer) between two metals. It is broadly observed in alloys and metal/metal oxide composites for electrocatalysis as well as heterogeneous catalysis and is credited as the major source of enhanced catalytic performance [186-189]. Fabbri et al. used X-ray absorption near edge structure spectroscopy to demonstrate an electronic interaction between the BSCF perovskite and acetylene black and found that the ligand effect was also present in perovskite/carbon composites, playing a key role in the enhanced ORR activity of the composite catalyst [190].

Some studies, however, have suggested that carbon plays a more complex role than just a simple conductive support. It has been suggested, for example, that formation of the perovskite-carbon interface could change the electronic/crystal structure of perovskite oxides by altering the oxidation state of the transition metal. These changes, for example, can be explored through characterisation methods such as x-ray diffraction and neutron powder diffraction which can look at variations in crystal structure. Such changes can subsequently affect the reaction mechanism and the performance towards oxygen electrocatalysis [29, 190, 191]. Moreover, some studies have also suggested that carbon black could also directly join in the oxygen electrocatalysis. Research groups have found that carbon black in perovskite/carbon composites actually participate in the ORR mechanistic pathway by first catalysing O_2 reduction to HO_2^- [29, 182, 183, 185, 192-196].

Despite the precise role of carbon black towards ORR activity in perovskite/carbon composites remains unclear, their overall contribution towards enhancing performance is evident. Yet it is worth noting that the addition of carbon only solves the problem arising from the conduction between oxide particles (external electron pathway), the inherent electronic conductivity of the oxide particles themselves (internal electron pathway), however, remains a challenge [29].

2.3.3. Potential Towards Ammonia Oxidation Activity

Although the aims of this thesis predominantly focus on the use of perovskite oxides to replace dependency on PGMs at the cathodic site to assist ORR, it is important to note that PGMs are also often heavily implemented at the anodic site of DAFCs. This indicates that routes to replacing PGMs at the anode are also worthwhile investigating. Although not widely established for use in AOR, perovskite oxides may have the potential to serve this purpose.

AOR is largely hindered by sluggish ammonia adsorption kinetics on the surface of the electrode and a suitable catalyst is of paramount importance [197, 198]. Conventionally, PGMs such as Pt and Pt-based materials have been employed due to their promising oxidation activity and low overpotential. Such materials, however, are easily poisoned by the strong adsorption of nitrogen bound species (N_{ads}) and have a high cost association, making them unfavourable for large scale application [198-203]. It is therefore crucial to design and engineer new electrocatalysts which meet the criteria of fair cost, reliable synthesis methods, high AOR activity and long-term stability.

Ni-based materials doped with elements such as Co, Zn, Cu and Fe have proven to be encouraging, cost friendly alternatives to PGMs with high activity towards AOR [1, 203-207]. Amongst these materials, those based on Ni and $Ni(OH)_2$ are considered especially promising due to their affordability and high ammonia removal efficiencies of around 40-70 % [204, 205, 207-210]. Much work has since been devoted on the preparation, modification and optimisation of such catalysts. For example, it has been reported that introducing Cu to form NiCu oxyhydroxides has shown to enhance catalytic activity towards AOR through the synergistic effects of Ni and Cu, resulting in an ammonia electrolyser with a removal efficiency of ~ 80 % after 14 hr [204, 205]. More recently, Zhu et al. explored the introduction of a second Fe^{3+} dopant into the NiO_6 framework to further enhance $Ni_{(1-x)}Cu_xOOH$

activity towards AOR [207]. DFT simulations revealed that the lower electronegative Fe^{3+} was able to polarise the electron cloud to a greater extent relative to Ni^{3+}, resulting in a lower Gibbs free energy of adsorption compared to $Ni_{(1-x)}Cu_xOOH$. It was found that the NiCuFe oxyhydroxide electrode demonstrated a promising removal efficiency of 55 % after 24 h in a highly concentrated ammonia electrolyte.

Although not widely explored for this purpose, perovskites may be promising non-PGM-based catalysts for AOR as they are easily tailored towards favouring certain electrochemical reactions, and their use within energy storage and conversion technologies is already extremely attractive [35, 97, 161, 162, 211-219]. Furthermore, the use of perovskites for AOR is especially convincing since Zhu et al. revealed that Ni in NiCu has octahedral geometry, NiO_6, which closely relates to the B-site geometry of perovskites [207]. This implies that perovskite structures can be designed on a similar basis. Recently, Zhang et al. encapsulated NiCu at the B-site of a stoichiometric $LaNi_xCu_{1-x}O_3$ perovskite for use as an AOR catalyst [151]. It was found that annealing in Ar introduced oxygen vacancies into the structure which significantly enhanced activity. Further exploration of oxygen vacancies and manipulation of the B-site however, was not explored. Nevertheless, this illustrates the potential for perovskite oxides to also be used to catalyse AOR and possibly as anode electrodes for DAFCs.

2.4. Perspective of Perovskites as Cathodes

Currently, there are several review papers available on the development of perovskite oxides for applications as SOFC cathodes and heterogeneous catalysts as well as in solar cells [29, 121, 220-223]. There has not, however, been work assessing the advancement of perovskite oxides into CCLs of DAFCs, which work under specific environments such as low temperature and alkaline conditions. Much work has regarded optimisation of electrocatalytic material, yet careful consideration into exactly how these materials are translated into practical DAFCs has not been as widely addressed. Given that these types of fuel cells are relatively new technologies and have shown much potential for progress, the complete development of CCLs in DAFCs should be acknowledged. The following section therefore provides perspective into how current literature can be used as a route to tailor CCLs for DAFCs and provides insight into optimising non-PGM cathodes.

To maximise cell performance, the transport pathways of electrons, ions and reactants should be connected well. This demands for a well-constructed microstructure in the catalyst layer (CL) [224, 225]. The development of high performance and robust CLs can play a key role in reducing cost, increasing power density and prolonging cell life [224]. A successful CL in a working DAFC must not only be able to catalyse the given reaction but must also demonstrate good (i) electron conductivity, (ii) ionic conductivity and (iii) transport pathways for reactant/products to and from the active sites. It is at these well-connected interfaces that the electrochemical reactions take place, therefore design of such is of utmost importance for achieving high utilisation of the catalyst material and improving cell performance in terms of reducing activation, ohmic and concentration overpotentials [226-228].

Normally, the CL is composed of the electrocatalyst, carbon supports, ionomer materials and void regions, in which carbon and ionomer supports are used to provide electronic and ionic conductive networks respectively, and void regions to provide porosity and mass transport channels for reactants and products. Without strategic design of these components, the true capacity of the electrocatalyst may be overshadowed. To really reflect the capability of an electrocatalytic material, a sufficient CCL is subsequently imperative [226-228].

Previously, Zou et al. prepared $SrFe_{0.8}Cu_{0.1}Nb_{0.1}O_3$ and $SrCo_{0.8}Cu_{0.1}Fe_{0.1}O_3$ perovskite catalysts in CCLs of DAFCs [33, 34]. A power density of around 0.30 and 0.25 $mWcm^{-2}$ was achieved respectively in 35 % NH_3H_2O and 1 M

NaOH. Despite implementation of the perovskite oxides as working cathodes in DAFCs, the individual ORR activities of these perovskite oxides were not thoroughly investigated, implying that the specific catalytic activity of these perovskites were not fully explored. Furthermore, the criteria for fulfilling a successful CCL, such as electron and ionomer conductivity, were also not explored, leaving much room for improvement and optimisation.

As mentioned above, the optimisation of CCL in DAFCs is not widely studied, with most literature mainly focusing on the electrocatalytic material strategy. However, optimisation of CLs in PEMFCs may provide useful insight into how to efficiently tailor CCLs for DAFC performance since these devices are effectively analogues of one another. The precise composition of CLs in PEMFCs have shown to have a profound effect on the performance and durability of the cell [224, 226-238]. The design of electrodes for PEMFCs is a delicate balance of transport media, with the conductance of reactant, electrons and protons needing to be optimised and relying on the distribution of the respective conducting network to provide optimum performance [238]. The effects of carbon content within the CCLs of these systems are less studied since they tend to be limited to PGM-based electrodes and often rely on materials such as commercial Pt/C which already have a fixed catalyst:carbon ratio. Nevertheless, the types of carbon black (and their compatibility with perovskite oxides for tailoring towards DAFCs) are discussed in section 2.3.2.4. The components regarding the effects of ionic conductivity and porosity of the CLs in PEMFCs are described in further detail below and are used here to provide perspective into how to effectively tailor CCLs for DAFCs using similar strategies.

Nafion is a well-documented ionomer that is extensively used in PEMFCs to increase proton conductivity within CLs [226]. Thepkaew et al. applied a full factorial design to identify key factors of active layers affecting PEMFC performance and found that Nafion content and carbon type greatly affected ohmic resistance [229, 230]. It has been found that an optimum Nafion morphology in the catalyst ink forms a web-like polymer network which leads to greater stability of the ink, higher proton conductivity and less mass transfer resistance. Such an ionomer, however, is not well suited for DAFCs due its high proton conductivity and its inability to assist in hydroxide transfer. Given that the conductivity of hydroxide ions is inherently low, with the specific conductivity being around half that of proton conductivity in diluted aqueous solution, materials with good OH^- ion conductivity are imperative [239]. As well as high ionic conductivity, the ionomer must also be physically compatible with the membrane employed, possess negligible electronic conductivity and high gas/water permeability [39]. A suitable hydroxide-ion conducting agent must therefore be added to CLs of DAFCs.

Fig. 2.6. Proposed OH^- mechanism through the hydrogen-bonded water network solvated by hydrophilic side chains (top) and illustration of an efficient ionic network on introduction of ionomer in the CL (bottom) [70].

Recently, Wang et al. prepared a series of poly(aryl piperidinium) (PAP) ionomers and found that those based on a biphenyl backbone chain (PAP-BP) displayed excellent hydroxide conductivity and served as suitable ionomers in AMFCs [80]. It can be assumed that in the presence of highly hydrophobic carbon, such as Vulcan XC-72R, the hydrophobic aryl backbone of the ionomer interacts with the surface whilst the hydrophilic piperidinium side chains point away [39, 226]. Although the mechanism of how such polymers interact with hydroxide ions has not been widely established, simulation studies have indicated that flow of ionic current may occur via an OH^- hoping mechanism through the hydrogen-bonded water network solvated by such hydrophilic side chains (Fig. 2.6) [240-246]. Nevertheless, the positive effects of introducing an appropriate amount of ionomer in PEMFCs could be transferred and used as a rational design strategy to improve ionic resistances and hence improve performance of DAFCs, where hydroxide conducting ionomers may be used within the CCLs of these systems.

It has been noted that an increase in porosity of the electrode is known to play a key role in diminishing mass transfer resistance [235]. Polytetrafluoroethylene (PTFE) is subsequently often added to PEMFCs to form a porous CL that efficiently facilitates hydrophobic channelling and transport of reactants and products [224, 226-229, 231-236]. This is crucial to reduce mass transport limitations within the electrode and has a profound effect on performance. Litster and McLean introduced hydrophobic PTFE to the GDL to enhance water management whilst Nafion ionomer was mixed into the CL to improve utilisation of the Pt catalyst [238]. Park et al. found a maximum PEMFC performance was attainable when 20% PTFE loading was used in the CCL [247]. Qi et al., however, found that 35% PTFE within the CCL displayed ideal performance, whilst 45% performed worst [248]. Fiedmann and Nyugen studied various CL compositions and found an optimal ratio of C:Nafion:Teflon being 1:0.875:0.875 was required to provide a hydrophobic pathway without blocking active catalyst sites [237]. The above studies demonstrate that an optimum amount of PTFE within the CCL of PEMFCs enhance overall cell performance.

Despite the clear benefits of adding a hydrophobic phase into the CCLs of PEMFCs, varying hydrophobicity in CCLs of DAFCs have not been as widely investigated. It has been noted, however, that the mere presence of a hydrophobic agent in the catalyst layer can significantly improve DAFC performance and durability. Recently, Wang et al. showed that the rate of water exiting the cathode exhaust when the anode feed was aqueous ammonia was substantially higher than that measured when the anode feed was a hydrogen/water vapor mixture [77]. The results revealed a significant rate of liquid water crossover from anode to cathode in DAFCs, with most water crossing through the cathode CL before exiting the exhaust. To reduce flooding tendency, a gas diffusion electrode (GDE)-based cathode with PTFE was fabricated and an increase in the contact angle of water on the surface was found, thereby providing better resistance to water flooding and facilitation of oxygen transport in the CL. Compared to the catalyst coated membrane (CCM)-based cathode with no PTFE, the GDE-based cathode with PTFE displayed higher performance, validating the need of PTFE. Though, the effects of varying hydrophobicity in CCLs to find optimum DAFC performance was not explored. This is particularly important since it has been noted that excessively high PTFE content can have an adverse impact on performance by blocking gas passageways which may ultimately lead to mass transfer limitations. As a consequence PTFE content is often kept relatively low [229]. A trade-off must subsequently be made, where enough PTFE is added to create void regions for hydrophobic channelling but not excessively such that there is blockage of gas passageways.

The above demonstrates how CCL design in similar fuel cells, such as PEMFCs, which are effectively analogues of DAFCs, can be utilised to provide a viable strategy to create CCLs for DAFCs. The composure of CCLs in such systems should be considered a crucial parameter for the performance of these cells.

2.5. Conclusions

The alkaline environment of DAFCs allows for the use of less corrosive conditions and use of cheaper non-PGM electrocatalysts to be explored, particularly at the cathode site where the oxygen reduction reaction occurs. Such non-PMG electrocatalysts include perovskite oxides. These materials are highly praised for their flexible nature and high degree of tunability, allowing easy manipulation of their electrical and chemical properties to minimise energy barriers and favour certain reactions.

This work reviews key factors influencing perovskite oxide activity towards oxygen reduction, which have included, but are not limited to, electronic structure of the B-site, oxygen vacancy content, crystal structure and electronic conductivity of the materials. Furthermore, direct implementation of such oxides as cathodes for DAFCs requires careful tailoring of the cathode catalyst layers to not only provide good catalytic activity towards the desired ORR reaction, but to also provide adequate hydroxide conductivity, electron conductivity and reactant/product transport throughout the layers. These components must be satisfied to reduce activation, ohmic and concentration overpotentials at the interface and so must also be acknowledged when preparing catalyst layers. Despite the importance of doing so, studies into proper CCL composition in DAFCs have not been widely established. This review subsequently provides insight into how such layers may be prepared and optimised for CCLs in DAFCs using current literature as a guide.

CHAPTER 3 Experimental Details

3.1. Sample Preparation

The electrochemical properties of materials are highly dependent on their synthetic method. Particle size, defects and impurities can vary greatly during the synthesis process and can be key factors in determining electrochemical properties. Sample preparation is therefore important, and a suitable synthesis method should be chosen.

3.1.1. Pechini Method

The changes that occur during the synthesis process of perovskite powders can be complex depending on parameters such as temperature, duration and atmosphere. The samples often contain multiple cations; to avoid formation of multiple phases of the oxides due to differing hydrolysis and condensation rates, a Pechini method is typically used to entrap the cations in a polymer network. Citric acid is used as a chelating agent to surround the cations, then with the aid of a polyalcohol, such as ethylene glycol, the chelates are cross linked to create a gel through esterification. Calcinating the resin causes breakdown of the polymer and at higher temperatures, organic matter is removed, and the cations are oxidised to crystallites of mixed cation oxides. The process is rather complex and has various experimental variables that can influence the final product [249]. The individual procedures for each experiment will be discussed in greater detail in the relevant chapters.

3.1.2. Ink Composition

Once the powders were prepared, they were used to make inks that were deposited onto GDLs to form GDEs.

For reasons given in Chapter 1, the catalysts were physically mixed with carbon black (Vulcan XC-72R), ionomer resin PiperION-B5 (PAP-BP-100, 5 %. w/w, Versogen) and PTFE in appropriate ratios using a pestle and mortar. Following successful mixing of the solids, inks were prepared by suspending the acquired powder into a solution containing appropriate amounts of water and isopropanol to create the required viscosity of the ink. The ink was left to stir before being brushed onto carbon cloth to form the GDE which was dried overnight before use. The individual processing methods will be described in more detail in the relevant chapter.

3.2. Physicochemical Characterisation

3.2.1. X-ray Diffraction

In a crystal solid structure, atoms are arranged in an orderly fashion and form a repetitive pattern that extends in all three spatial dimensions. The structures of crystals are often identified using X-ray diffraction (XRD).

3.2.1.1. Bragg’s Law

The point at which constructive interference occurs follows Bragg’s law: (i) the incident angle θ of an incoming wavelength λ will reflect with the same angle of scattering and (ii) that the path length difference is equal to an integer number of wavelengths. Take Fig. 3.1, if beam A and B are in phase for example, then the path difference d, must be an integer n multiple of wavelength [250]. Here, a single crystal with aligned planes of lattice points separated by some distance d can be modelled by an optical grating.

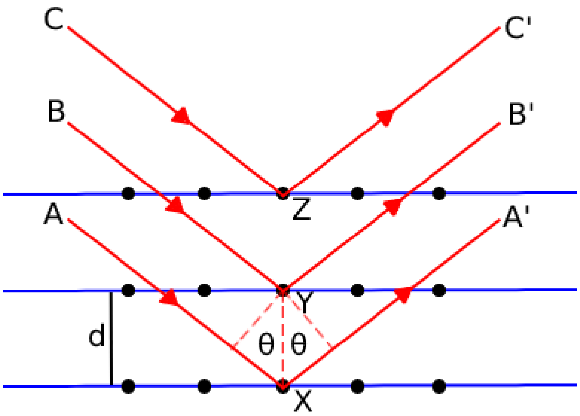

Fig. 3.1. Illustration of Bragg's law.

In the figure depicted above, monochromatic X-rays A, B and C are incident upon the crystal at an angle θ. They reflect off atoms X, Y and Z respectively. The path difference d between the X-rays reflected from atom X and atom Y can also be written as 2XY [250].

Bragg's law can be mathematically expressed as the following:

$$2dsin\theta = n\lambda \tag{3.1}$$

3.2.1.2. d-Spacing Formula

The distance between adjacent atomic planes can be obtained from Bragg's law and used to calculate the unit parameters of a crystal using a d-spacing formula. The diffraction pattern can be indexed to identify the size, shape, and symmetry of the crystallographic unit.

Consider a cubic system where the unit cell parameters are equal (a=b=c) and all angles are equal (α=β=γ=90^o), the following d-spacing formula applies:

$$\frac{1}{d_{hkl}} = \frac{h^2 + k^2 + l^2}{a^2} \tag{3.2}$$

Where h, k and l are Miller indices which indicate the orientation of a set of parallel planes of atoms in a crystal and a, b and c are unit cell parameters. Henceforth by using the appropriate d-spacing formula obtained from Bragg's law, unit parameters can be calculated and reveal information about the crystal system.

In this work, measurements were carried out at room temperature on a PANalytical X'Pert Pro diffractometer (Cu Kα source, 1.5405 Å) and collected in the 2θ range of 20 - 80° with a step of 0.0167° with a counting time of 109.6 s/step. The peaks obtained were computationally indexed using a HighScore software (Malvern Panalytical) which allowed for Miller indices to be assigned and for information regarding the symmetry and phase of the sample to be revealed.

3.2.1.3. Scherrer equation

Data from X-ray diffraction can also be extracted to give useful information regarding crystallite size by using the Scherrer equation:

$$D = \frac{k\lambda}{\beta_{size} cos\theta} \tag{3.3}$$

Where k is the Scherrer constant (k ≈ 0.9), λ is the incident wavelength, θ is the diffraction angle and β_{size} is the experimental full width at half maximum (FWHM). This equation is generally used to obtain a good estimate value of the crystallite sizes.

Crystallite size of the samples were obtained by using Scherrer's equation. Using the OriginPro 2019 software, the Multiple Peak Fit function allowed for analysis of the XRD peaks, giving information regarding the θ and FWHM values.

3.2.1.4. Rietveld refinement

Rietveld refinement offers a route to model a calculated powder pattern described by a set of parameters. Such parameters are influenced by several contributions, for example, the background, crystal lattice, symmetry, crystal structure, microstructure as well as instrumental factors. These parameters can be simultaneously refined by the least-squares method until the calculated pattern matches the experimentally obtained data. Upon finding a good fit, the crystal structure is considered refined [251]. In this work, Rietveld refinement was carried by Professor Shanwen Tao and the lattice parameters a, b and c were optimised using a general structure analysis system (GSAS) and EXPGUI, a graphical user interface for GSAS [252, 253].

3.2.2. Scanning Electron Microscopy and Energy Dispersive X-ray Spectroscopy

Electron microscopes use electron beams to create highly magnified images of a specimen. They are powerful instruments that can give a detailed portrayal of the morphologies or compositions of a specimen. Compared to light microscopes, this type of microscopy has clear advantages in terms of resolution. The resolution of light microscopes are limited by the wavelength λ of visible light. Electrons however, have a much smaller wavelength according to the De Broglie relationship and therefore are capable of achieving clear images in the nanometer range [254].

$$\lambda = \frac{h}{m_e V} \tag{3.4}$$

Where h is Planck's constant 6.63x10^{-34} Js, m_e is the mass of an electron and V is the velocity of the electrons.

There are generally two main electron microscopes that are used in literature, scanning electron microscopy (SEM) and transmission electron microscopy

(TEM). The two types are used for different purposes, with SEM being more concerned with the surface of a solid object and TEM being able to look through a thin slice of specimen. For this work, SEM was used.

SEM is carried out using a beam of electrons that are emitted from an electron gun and accelerated towards a sample. The electrons are passed through several condenser lenses and focused to around 0.4 - 5 nm in diameter before interacting with the atoms of the sample. As a result, electrons and X-rays are ejected from the sample and detectors are used to collect these species and convert this into a signal. The final image is then displayed on a screen similar to that of a television screen [254].

Since SEM utilises vacuum conditions and electrons to produce an image, special preparations must be made to the sample prior to characterisation. In the case of perovskite oxides, conductivity of the sample becomes an issue. Consequently, such samples need to be coated with a thin layer of conductive material. This is often achieved through a technique known as gold sputtering. The sample is placed inside a small vacuum chamber and a sputter coater is used to produce a thin gold coating on the sample leading to enhanced resolution [254].

Energy dispersive X -ray spectroscopy (EDS) is another powerful technique often coupled with SEM that can provide elemental analysis and chemical characterisation of a sample. The technique relies on a high energy beam of electrons bombarding the sample and effectively displacing an electron from the inner shell, generating a vacancy. As a result, an electron from an outer, higher energy shell will fill that electron vacancy, releasing an X-ray with energy equal to that of the difference between these two shells in the process. As the energy differences between electron shells are closely related to atomic structure, the X-ray emitted will be characteristic of a certain atom and allow for elemental compositions to be evaluated [255].

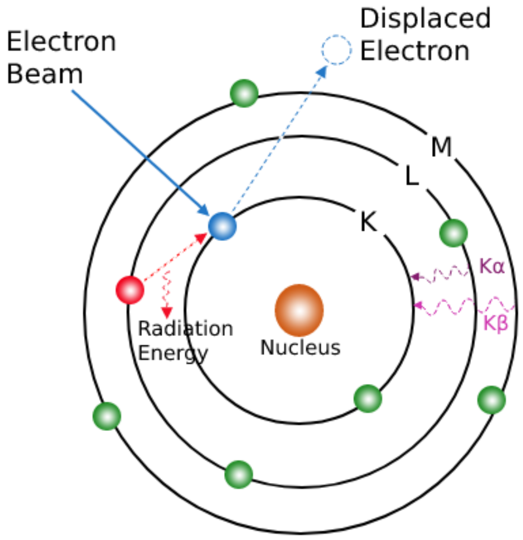

Fig. 3.2. Schematic illustration of the principles for EDS.

In this work, SEM was used to examine the surface morphology of the catalyst using a Zeiss SUPRA 55-VP, equipped with an EDS spectrometer for elemental analysis. Elemental weight (%) at a particular point on the sample can be inferred from the map sum spectra obtained by EDS.

3.2.3. Raman Spectroscopy

The Raman effect is the inelastic scattering of incoming photons by matter, where there is an exchange of energy between the two and a change in the direction of light. It is often exploited to provide both chemical and structural information of a material and to identify such material based on its characteristic Raman fingerprint [256, 257].

Upon absorption of an incident beam of photons, energy is transferred from the photon to the molecule, leaving the latter in a higher, excited energy state. This interaction is thought to lead to the formation of a very short-lived complex between the photon and molecule, commonly referred to as a virtual state. Since this virtual state is not stable, a photon is re-emitted shortly thereafter in the form of scattered light [258].

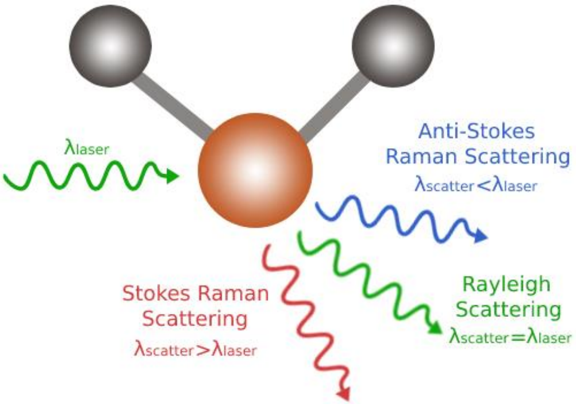

Fig. 3.3. Schematic illustration of the three types of scattering processes that can occur when incoming light interacts with a molecule.

Light possesses a certain probability of being scattered by a material. Of the photons that are scattered, most are scattered elastically, meaning that they have the same energy and henceforth the same frequency and wavelength as the incident photons, despite a change in direction. This type of scattering, where the energy of the scattered photon is conserved, is typically known as Rayleigh scattering and is the dominant process (Fig. 3.3) [258].

Approximately 1 in 10 million photons undergo Raman scattering, where inelastic scattering occurs. In these rarer cases, the molecule may gain energy from the photon during the process. When this occurs, the molecule is excited to a higher vibrational level and the scattered photon subsequently loses energy. In this scenario, the wavelength of the scattered photon increases and is said to have undergone Stokes Raman scattering. In contrast, if the molecule loses energy by relaxing to a lower vibrational level, then the scattered photon gains the resultant energy and its wavelength decreases. This is known as anti-Stokes Raman scattering [258, 259].

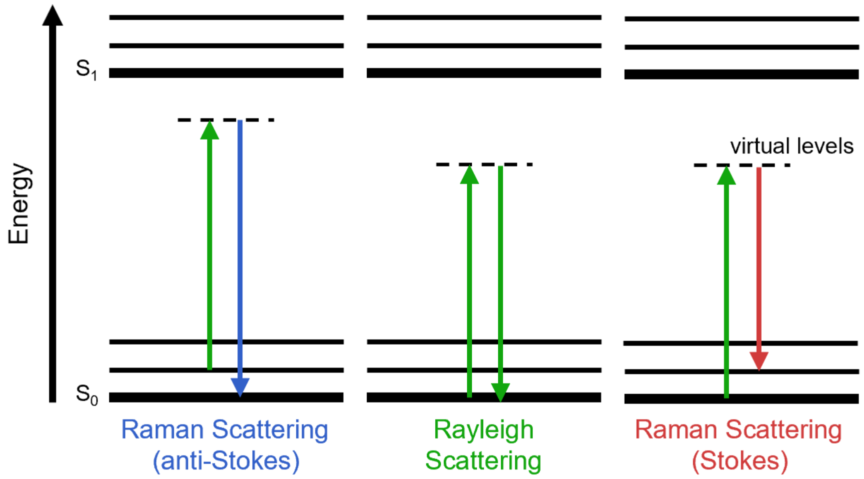

Fig. 3.4. Jablonski diagram showing possibilities of Rayleigh, Stokes and anti-Stokes Raman scattering.

In all three cases described above, the final state has the same electronic energy as the initial state but is in either the same (Rayleigh), higher (Stokes) or lower (anti-Stokes) vibrational energy state. This is visually demonstrated by the Jablonski diagram in Fig. 3.4 [258].

In terms of quantum mechanics, both Stokes and anti-Stokes processes are equally likely processes. However, given that most molecules are initially in a ground vibrational state, Stokes scattering is more statistically probable and is therefore always more intense than anti-Stokes. Due to this, Stokes Raman scattering is measured in Raman spectroscopy [256, 257].

Since the energy and therefore the wavelength of the Raman scattered light depends on the energy of the incident light, the Raman scatter position is converted into a Raman shift for comparative measures between spectra. Raman shift indicates the shift away from excitation wavelength and is expressed as follows [256, 257]:

$$\Delta\tilde{v}(cm^{-1}) = \left(\frac{1}{\lambda_0(nm)} - \frac{1}{\lambda_1(nm)}\right) x \frac{(10^7 nm)}{(cm)} \qquad (3.5)$$

Where $\tilde{\nu}$ is the Raman shift wavenumber, λ_0 is the excitation wavelength and λ_1 is the Raman scatter wavelength.

In this work, a Renishaw InVia Raman Microscope with an excition wavelength of 532 nm was used to explore bonding modes within the perovskite molecule. Due to the complexity of the instrument, manager of the spectrometer, Dr Ben Breeze, carried out the technique.

3.2.4. X-ray Photoelectron Spectroscopy

The surface of a material has high significance as it is the point of contact with the environment and will thus influence factors such as catalytic activity, contact potential, corrosion rates and failure mechanisms. Characterisation of the surface is therefore of utmost importance. The physical and chemical properties of the surface differ from that of the bulk. The topmost atomic layer is particularly interesting since surface atoms are not completely surrounded by atoms, making them more reactive than atoms in the bulk. X-ray photoelectron spectroscopy (XPS) is one of the most employed analytical techniques used for surface characterisation. It is very surface sensitive, with a sample depth of only a few nanometres [260].

The sample is irradiated with a low energy beam of X-rays and the energy spectrum of the emitted photoelectrons is determined by a high-resolution electron spectrometer. The peak positions produced are characteristic of the photoelectron kinetic energy and can be related to a particular electron shell from an atom. This reveals information on the atomic binding energy which can be linked to the oxidation state of atoms at the surface. Developments in the technique have allowed for peak intensities to be interpreted as a quantitative measure of the composition at the sample surface [260].

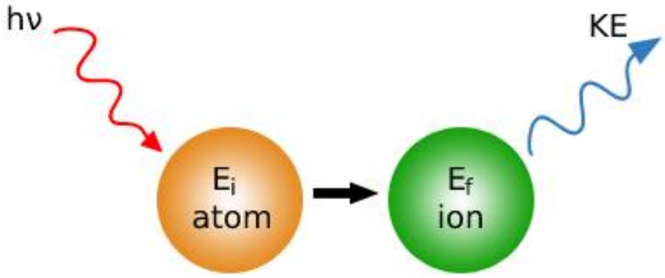

Fig. 3.5. Schematic illustration of the principles for XPS.

Consider the photoemission process. Beforehand, the total energy within the system is that of the incoming X-ray photon energy $h\nu$ plus the energy of the targeted atom in its initial energy state E_i. After emission of the photoelectron, the total energy of the system is the kinetic energy of the emitted photoelectron KE plus that of the atom in its final energy state which is now ionised E_f. Equating the total energy before and after the emission process, it can be deduced that the binding energy of the electron BE is the difference between the final and initial energy states of the atom. The spectrometer work function Φ is also often included in the mathematical expression and is found through calibration [260].

$$h\nu + E_i = KE + E_f \tag{3.6}$$

$$h\nu - KE = E_f - E_i = BE \tag{3.7}$$

$$KE = h\nu - BE - \Phi \tag{3.8}$$

In this work, XPS analysis was used to investigate valency and oxygen vacancies present within the samples. Measurements were conducted using a monochromated Al K_α X-ray source on a Kratos Axis Ultra DLD spectrometer (Kratos Analytical). The data was collected at a take-off angle of 90° to the surface plane and analysed using the Casa XPS package. The spectra were referenced to the C-C peak at 285.5 eV. The synthesised powders were analysed through XPS as prepared with no pre-treatment. Due to the complexity of the instrument, Warwick Photoemission Facility Manager Marc Walker carried out the XPS collection and analysis.

3.2.5. N_2 Chemisorption Isotherms

When studying samples with particles in the nanometer range, very interesting surface properties begin to emerge. Many of these useful properties result from their small size, making it very important to determine surface area. Brunauer-Emmett-Teller (BET) theory is based on the physical adsorption of gas molecules onto a solid surface and is used as a technique to measure the specific surface area of materials [261].

The theory essentially expands on Langmuir theory, which relates the monolayer adsorption of gas molecules, known as absorbates, onto a solid surface to the gas pressure of a medium over the surface at some constant temperature [261].

$$\theta = \frac{\alpha P}{1 + (\alpha P)} \tag{3.9}$$

Where θ is the fractional cover of adsorbates on the surface, P is the gas pressure and α is a constant [261].

Adsorption is the adhesion of adsorbates onto a solid surface. The concentration of adsorbates is dependent on the nature of the exposed surface and on the temperature, gas pressure and strength of interaction between the gas and solid [261].

Langmuir theory is based on the following assumptions: (i) all surface sites (the area on the sample where a molecule can adsorb onto) have the same adsorption energy for the adsorbate (usually argon or nitrogen), (ii) adsorption at one site occurs independently of adsorption at neighbouring sites, (iii) the activity of the adsorbate is directly proportional to its concentrations, (iv) adsorbates form a monolayer on the surface and (v) each active site can only be occupied by one particle [261].

BET theory extends on Langmuir theory in the sense that it takes multilayer adsorption into consideration. BET introduces three additional assumptions: (i) gas molecules will infinitely adsorb onto the solid in layers, (ii) the different adsorption layers do not interact with one another and (iii) the theory can be applied to each layer of the model [261].

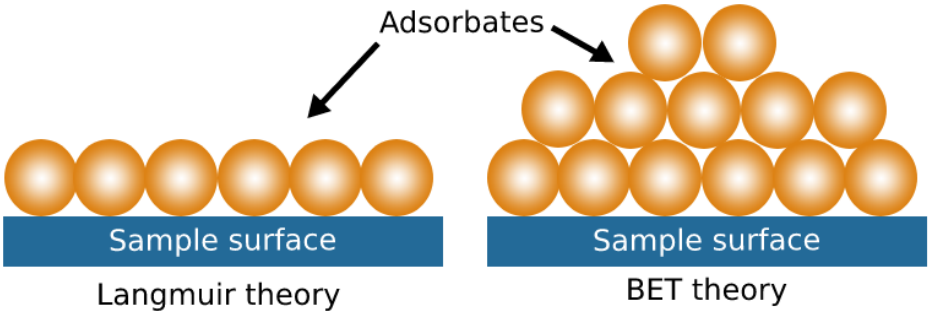

Fig. 3.6. Schematic of the adsorption of gas molecules onto the surface of a sample showing monolayer adsorption assumed by the Langmuir theory and multilayer adsorption modelled by BET theory.

The BET instrument takes advantage of the assumptions made by BET theory. For these tests, samples must be carefully prepared prior to measurements. Firstly, the solid samples are placed in glass cells and degassed to remove the presence of water and other contaminants. This is achieved by degassing in a vacuum at high temperatures. To overcome the typically weak interactions between that of gas and solid phases, and for measurable amounts of adsorption to occur, the surface is cooled using liquid nitrogen.

When analysing N_2 chemisorption isotherms, nitrogen is typically used as the gas due to its availability, high purity, and strong interaction with most solids. A known amount of nitrogen gas is released into the sample cell. After saturation and the formation of adsorption layers, the sample is removed from nitrogen atmosphere and heated to release the absorbed nitrogen from the material. Pressure transducers, which are extremely precise and accurate, are used to monitor the pressure changes. The data collected is displayed in the form of a N_2 isotherm. These plots can then be manipulated and BET can be used as a suitable model to find the specific surface area of the material [261].

In this work, BET instrumentation was used to assess textural properties via N_2 adsorption-desorption isotherms of the perovskite oxides powders recorded at liquid N_2 temperature using a **Micromeritics ASAP 2020** apparatus. Samples were degassed at 300 ^{o}C for 1 h. Due to the sensitivity of the instrument, Assistant Professor Volkan Degirmenci conducted the data collection and analysis.

3.3. Electrochemical Characterisation

3.3.1. Rotating Disk Electrode

To study electrode reaction mechanisms and kinetics, particularly those related to the oxygen reduction reaction, it is imperative to design tools to control and determine reactant transport near the electrode surface and its effect on electron transfer kinetics. RDE is typically used for this purpose and thus a conventional RDE technique was used to research the oxygen reduction reaction activity of perovskite oxides in this study. [262].

These working electrodes are often used in electrochemical applications such as corrosion studies, fuel cell research, catalyst development and in the control of reactant mass transport to the electrode surface. In general, RDE experiments are performed where mass transport to the sample electrode is required [263].

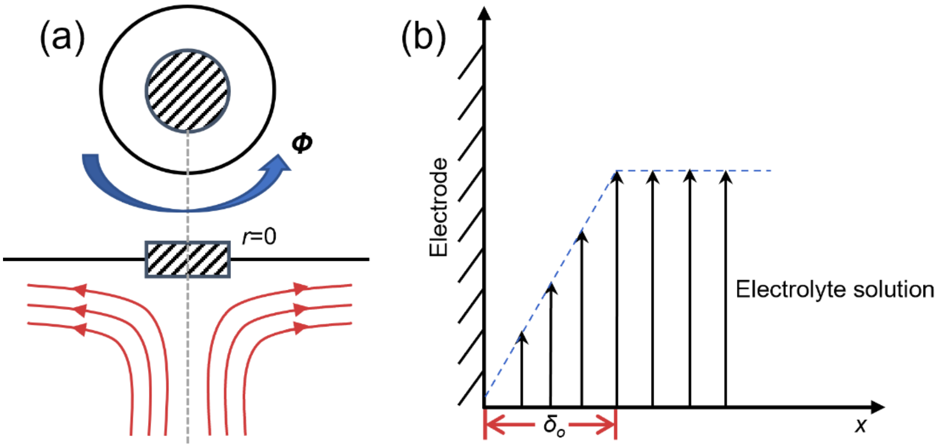

Fig. 3.7. Flow pattern of solution near the disk electrode surface (where *r* is the coordinate direction parallel to the disk surface and *Φ* is the coordinate direction of the electrode rotation). (b) Flow rate distribution near the electrode surface along the direction parallel to the electrode surface.

Mass transport can be defined by three parameters: (i) diffusion, (ii) convention and (iii) ionic migration. For an electrolyte solution in excess, ionic migration can be assumed negligible, indicating that only the former two processes have a significant contribution [262].

In the absence of convection, the steady-state current in still unstirred experiments such as cyclic voltammetry is limited by the diffusion of species [263]. In the presence of forced convection, such as when a RDE is employed, the reactant in electrolyte solution will move with the convection. Fig. 3.7a shows a schematic of the flow of electrolyte solution from the bottom of the electrode edge in an upward direction that is parallel to the electrode surface. A closer look at what is happening at the electrode surface is depicted in Fig. 3.7b. Here, the *x* direction represents the distance from the electrode surface to the bulk electrolyte solution. When far from the electrode surface, the bulk solution remains well-stirred by the convection induced by rotation, whilst solution closer to the electrode surface tends to rotate with the electrode. If viewed from the point of the rotating electrode, then the solution nearer to the surface appears relatively stagnant. This stagnant layer δ_o is where diffusion exists [262, 264]. As the disk continues to rotate, the resultant centrifugal force flings the solution at the hydrodynamic boundary layer, which is a thin layer of fluid in the immediate vicinity of the surface that experiences no-slip, away from the centre of the electrode. More solution from the bulk electrolyte then flows up, perpendicular to the electrode, to replace the boundary layer and the overall result equates to laminar flow of solution towards and across the electrode [263]. Laminar flow can be considered as ‘sheet-like’ flow, as opposed to turbulent flow and Reynolds number (Re) can be used to predict if a fluid demonstrates laminar flow by measuring the ratio of inertial and viscous forces.

The rate of solution flow can be controlled by the electrode’s angular velocity [263]. The faster the electrode spins and the faster the solution flows, the thinner the δ_o thickness is [262]. This laminar flow can quickly achieve conditions in which the steady state current is controlled be the solution flow rather than diffusion [263]. Running linear sweep voltammetry at varying rotational rates allows study into different electrochemical phenomena such as multi-electron transfer, kinetics in a slow electron transfer and electrochemical reaction mechanisms [263].

The RDE equipment (Pine Research) was set up using a RDE glass cell for standard three electrode voltammetry and a glassy carbon RDE tip connected to the centre port. The RDE shaft was connected to a rotation rate control box which carefully controlled the rotation of the electrode, and the rotational speed was adjusted manually by turning the knob. The four side ports were occupied by Platinum mesh and Ag/AgCl (saturated KCl) which were used as the counter and reference electrodes respectively, along with a dual port gas inlet for purging/sparging and a single port gas outlet. The ORR polarisation curves were collected using a Solartron 1470E CellTest System.

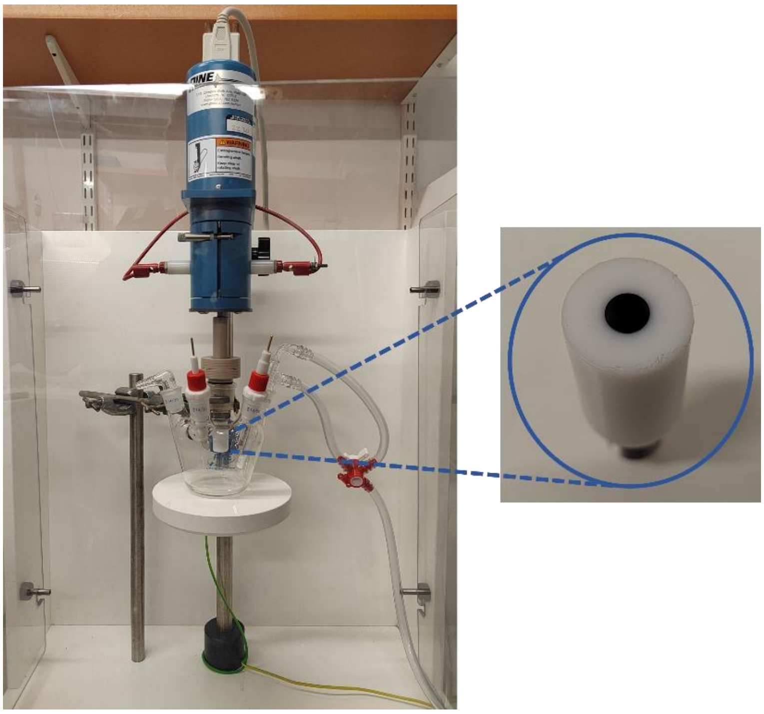

Fig. 3.8. Set up of RDE apparatus with zoom of glassy carbon electrode.

The electrode disk surface is made to be in contact with electrolyte solution (Fig. 3.8). A prepared ink containing the material of interest is deposited and dried onto the glassy carbon centre, whilst hydrophobic Teflon is used to repel the ink solution to retain the deposition within the centre of the electrode and to act as an electronic isolator that covers the remaining part of the disk. An electrical brush is used to make the electrical contact between the electrode shaft and wire whilst the electrode is rotating.

3.3.2. Electrochemical Impedance Spectroscopy

Several microscopic processes take place throughout the cell that can in turn reduce overall conductivity of the system. Such processes include the transport of electrons through electronic conductors, the transfer of electrons at the electrode-electrolyte interfaces (including the oxidation or reduction reactions), and the flow of charge via defects in the system. Current flow therefore depends on the ohmic resistance of the electrodes, electrolyte and on the reaction rates at the electrode-electrolyte interfaces. The flow may be further impeded by defects in the bulk materials. It is usually assumed that the electrode-electrolyte interfaces are perfectly smooth, however, this is not the case. Each interface will interact and polarise in a distinctive way when the system is subjected to an applied potential difference. Impedance spectroscopy is a powerful tool to characterise various electrical properties of materials and their interfaces. This section briefly discusses the theory and applicability of impedance spectroscopy in electrochemical systems [265].

3.3.2.1. Complex Impedance

According to Ohm's law, resistance can be defined as a ratio between voltage and current:

$$R = \frac{V}{I} \tag{3.10}$$

Despite being a well-established relationship, its use is limited to applications in an ideal resistor where resistance is independent of frequency [266]. In the real world, however, circuit elements are more complex in nature and deviate from ideal behaviour. To compensate for this complexity, the concept of impedance is used instead of resistance. Similar to resistance, impedance is a measure of the ability of a circuit to resist the flow of electrical current, but it takes into account factors such as capacitance and inductance which are frequency dependent [265, 266].

Electrochemical impedance spectroscopy (EIS) is usually measured by applying small sinusoidal perturbations, often a voltage potential, at varying frequencies to an electrochemical cell and the resulting current signal is recorded. The current response tends to have the same frequency as the excitation signal, but its phase may be shifted by a certain amount Φ [266]. This is schematically represented in Fig. 3.9. Application of these input and output signals is typically automatically performed by a potentiostat/galvanostat.

Fig. 3.9. Schematic interpretation of sinusoidal current response.

The ability of the capacitor and inductor elements to restrict the flow of electrons between AC circuits is expected. Subsequently, the amount of the resultant current response indicates how the sample interacts with the applied voltage. The phase and amplitude changes reveal how electrons interact with the electrode surface [267].

Since impedance is a complex number, it can be expressed in terms of its real and imaginary components [265]:

$$Z(\omega) = Z' + jZ'' \tag{3.11}$$

Where $Z(\omega)$ is the impedance as a function as frequency and Z' and Z'' are the real and imaginary components respectively. This reveals that resistance makes up the real Z' component of the complex impedance $Re(Z)$, whilst Z'' is the imaginary component of the complex impedance $Im(Z)$, determined by the summation of capacitance and inductance [265, 267]. Furthermore, impedance can be plotted using either cartesian or polar coordinates, as show in Fig. 3.10a. The two cartesian coordinate values are given as [267]:

$$Re(Z) \equiv Z' = |Z|\cos(\theta) \quad Im(Z) \equiv Z'' = |Z|\sin(\theta) \tag{3.12}$$

with the phase angle,

$$\theta = tan^{-1}\left(\frac{Z''}{Z'}\right) \tag{3.13}$$

and modulus,

$$|Z| = \sqrt{(Z')^2 + (Z'')^2} \tag{3.14}$$

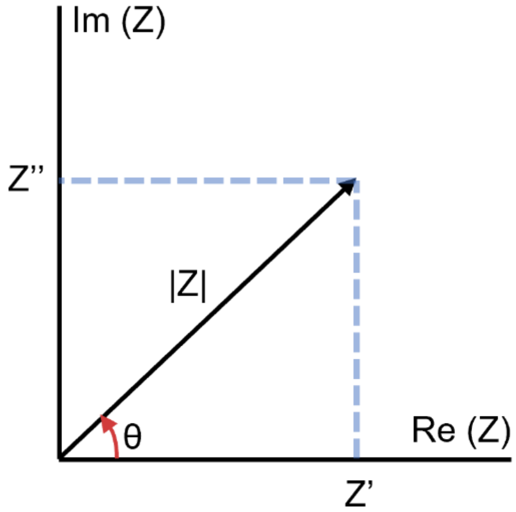

Fig. 3.10. Impedance Z plotted as a planar vector.

3.3.2.2. Data Interpretation and Equivalent Circuits

Referring to Eq. (3.11), impedance $Z(\omega)$ is a function of frequency. Generally, a range of input signal frequencies are applied via a potentiostat which are equally spaced on a descending logarithmic scale from high to low frequencies. This gives rise to the Nyquist plot, shown in Fig. 3.11a. Here, each point on the complex plane plot represents the impedance at a certain frequency. Impedance at high frequency reflects ohmic resistance (R_s) whilst the diameter of the semicircle reflects the polarisation resistance (charge transfer resistance) affected by electrode reaction kinetics [268]. Impedance spectra can also be demonstrated in a Bode plot, however, this study will focus on exploitation of the Nyquist plot.

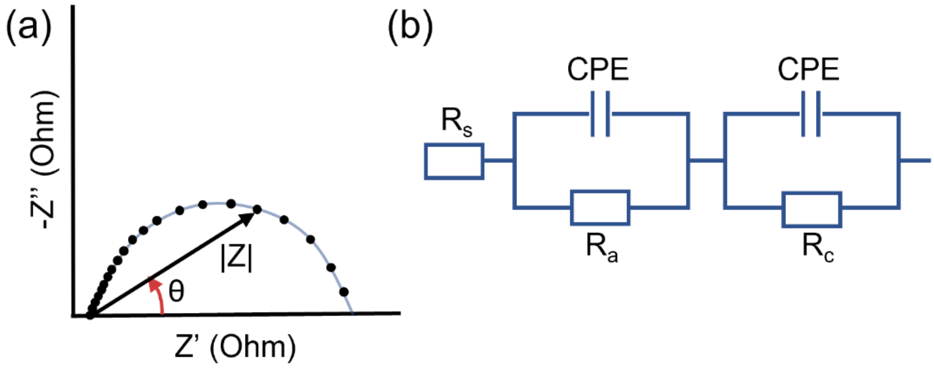

Fig. 3.11. (a) Illustration of Nyquist plot. (b) Example of a circuit: R_s is solution resistance (ohmic resistance), R_a and R_c are the anodic and cathodic polarisation resistances respectively and CPE is the constant phase element.

Due to the complexity of impedance, simplified models are used to better understand the interactions within EIS [267]. An example of a circuit is shown in Fig. 3.11b. The elements of anodic polarisation resistance R_a, cathodic polarisation resistance R_c and solution resistance (ohmic polarisation) R_s can be summed to obtain the internal resistance R_{in}. This reflects the impedance of the individual electrodes and subsequently consists of three components: (i) activation (charge transfer) resistance, ohmic resistance from the solution, electrode materials and membrane and (iii) concentration (diffusion) resistance. A constant phase element CPE typically substitutes capacitance in equivalent circuits due to the inhomogeneous nature of electrochemical systems such as electrode roughness, coating and distribution of reaction rate. A Warburg element may also be added in parallel to R_a or R_c to reflect simple diffusion scenarios (Randles circuit). Equivalent circuits can therefore quickly become very complicated with addition of elements, therefore this study only considers a very simple interpretation [268].

In this study, EIS was conducted on a Solartron 1260A at a frequency range of 1 MHz to 0.01 Hz and the voltage was set to the OCV for each test conducted.

3.4. Fuel Cell Experiments

To test the fuel cell performance, the entire system must be considered. Fig. 3.12 shows the overall experimental set up for fuel cell testing.

The anodic fuel was provided via PTFE tubing shown on the right. PTFE tubing was chosen to provide visual ease when tracking the fluid and to clearly identify sources of leakage. The anodic fuel (7 M NH_3H_2O + 1 M KOH) was contained within a beaker and a HPLC (Shimadzu LC-20AD) pump was used to pump the solution at a flow rate of 2 $mLmin^{-1}$. The tubing was fed through the slits at the back of an oven, allowing the solution to preheat before entering the fuel cell, which was placed into the oven, via a connector at the relevant flow field plate. After passing through the cell, the tubing was fed back out of the oven and connected to a pressure gauge and needle valve, which were used to maintain a backpressure of 2 bar. Finally, the waste solution was dispensed into an empty beaker.

A similar assembly was employed for the oxidant. PTFE tubing was used to connect a cannister of zero air (20 % O_2/80 % N_2) to a flow meter, which held the flow at 180 $mLmin^{-1}$. The tubing was subsequently fed through the slits at the back of an oven and into a stainless-steel humidifier, which was placed into the oven, to humidify the air stream. The humidified air was then introduced into the fuel cell via a connector at the relevant flow field plate. After passing through the cell, the tubing was fed back out of the oven and connected to a pressure gauge and needle valve, which were used to maintain a backpressure of 3 bar. Finally, the tubing was placed into a beaker of water to visually assess bubble formation and confirm that the gas was efficiently passing through the system.

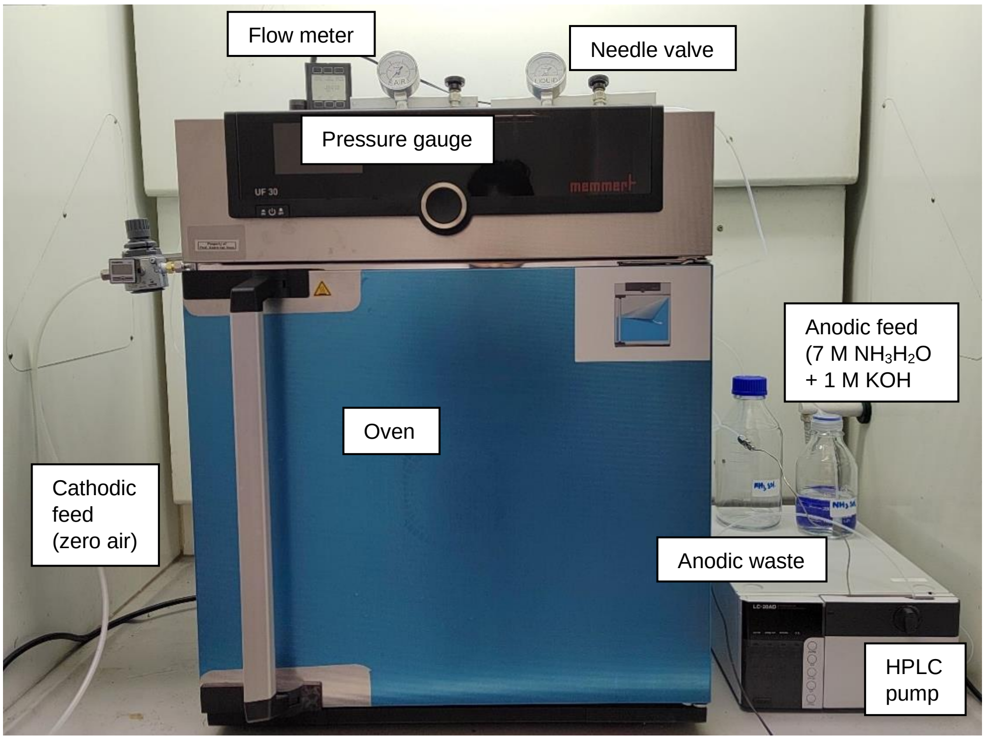

Fig. 3.12. Set up of fuel cell system.

Silver wires were connected to the current collectors of the fuel cell device and connected to Solartron 1287A Electrochemical Station to obtain the corresponding polarisation curves. EIS was conducted on a Solartron 1260A at a frequency range of 1 MHz to 0.01 Hz and fixed potential of 10 mV bias. The exact design of the fuel cell device is discussed in Chapter 5 and forms part of the experimental chapters within this thesis.

CHAPTER 4 Ammonia Oxidation Reaction

The works in this chapter form part of a publication by the author in Separation and Purification Technology [69].

4.1 Background

The content of this thesis primarily focuses on optimisation of the oxygen reduction electrocatalyst and cathode electrode. It should be noted, however, that AOR at the anodic site is also hindered by sluggish ammonia adsorption kinetics on the surface of the electrode and a suitable catalyst is of paramount importance to enhance DAFC performance [197, 198]. Conventionally, PGMs such as Pt and Pt-based materials are often employed due to their promising oxidation activity and low overpotential. This is evidenced by the studies reported in Chapter 2. To date, the most active anode catalysts identified below 120°C are PtIr binary alloy or Pt and Ir mixtures. Even these catalysts, however, display limited catalytic activity, explaining the requirement of cell operation of at least 100°C to reach high peak power densities [77]. Furthermore, such materials are easily poisoned by the strong adsorption of nitrogen bound species (N_{ads}), and have a high-cost association, making them unfavourable for large scale application [198-203]. It is therefore also crucial to design and engineer new electrocatalysts which meet the criteria of fair cost, reliable synthesis methods, good AOR activity and long-term stability. Although testing and implementation of the anode in a working DAFC is out of the scope of this study, this chapter aims to demonstrate how perovskite oxides may also be exploited and tailored towards ammonia oxidation and provides foundation for future work.

Much work has since been devoted on the preparation, modification and optimisation of Ni-based catalysts for AOR and in turn, as working electrodes in ammonia fed electrolysers [203-210]. For example, NiCu oxyhydroxides have shown to enhance catalytic activity towards AOR through the synergistic effects of Ni and Cu, resulting in an ammonia electrolyser with a removal efficiency of ~ 80 % after 14 h [204, 205]. Zhu et al. explored the introduction a second Fe^{3+} dopant into the NiO_6 framework and further enhanced $Ni_{(1-x)}Cu_xOOH$ activity towards AOR. It was found that the NiCuFe oxyhydroxide electrode demonstrated a promising removal efficiency of 55 % after 24 h in a highly concentrated ammonia electrolyte [207]. Recently, Zhang et al. explored Ni-based B-site $LaNi_xCu_{1-x}O_3$ perovskite for use as an AOR catalyst [151]. It was found that annealing in Ar introduced oxygen vacancies into the structure which significantly enhanced activity. Although these works focus on the design of non-PGMs electrodes for use in ammonia electrolysers, similar materials may theoretically be good electrodes for DAFCs, since AOR takes place at the electrodes of both devices.

This chapter aims to strategically design and test a novel perovskite oxide towards AOR activity to lay foundation for future work and demonstrate the perspective of non-PGMs at the anode site of DAFCs. The result of introducing small amounts of Fe into NiCu at the B-site of a $LaNi_{0.6}Cu_{0.4-x}Fe_xO_{3-\delta}$ (x = 0, 0.05, 0.10) perovskite oxide was tested towards AOR in a simple three electrode test. Furthermore, the effects of systemically creating oxygen vacancies by manipulating the A-site and introducing deficiencies to form a series of $La_{1-y}Ni_{0.6}Cu_{0.35}Fe_{0.05}O_{3-\delta}$ (y = 0, 0.05, 0.10) perovskite oxides was also explored. The optimised perovskite oxide was tested as the anode in an ammonia electrolyser cell using simulated and real landfill leachate to reflect the capacity of the catalyst to assist AOR and for wastewater treatment. Ultimately, the findings can be used as a basis to design and optimise perovskite oxides as catalyst layers for working DAFC anodes in future work.

4.2 Experimental

4.2.1 Materials

$La(NO_3)_3{\cdot}6H_2O$ (99.9 wt. %, Alfa Aesar), $Ni(NO_3)_2{\cdot}6H_2O$ (99.9 wt. %, Alfa Aesar), $Cu(NO_3)_2{\cdot}2.5H_2O$ (98.0 wt. %, Alfa Aesar) and $Fe(NO_3)_3{\cdot}9H_2O$ (98+ wt. %, Alfa Aesar) were used as metal precursors with no further purification. Citric acid ((99+ wt. %, Alfa Aesar) was used as the chelating agent. Carbon black (Vulcan XC-72R) and Nafion solution (5 wt. %) (Sigma Aldrich) were added to the ink and carbon cloth (Toray, wet proofing 1-5 %) was used as the electrode substrate. Other chemicals such as Isopropanol and KOH were all analytical reagents purchased from Alfa Aesar.

4.2.2. Synthesis of Perovskite Oxide Powders

Appropriate amounts of $La(NO_3)_3{\cdot}6H_2O$, $Ni(NO_3)_2{\cdot}6H_2O$, $Cu(NO_3)_2{\cdot}2.5H_2O$ and $Fe(NO_3)_3{\cdot}9H_2O$ were dissolved in water. Citric acid was added to the solution in a molar ratio of 1:1.2 of total metal ions:citric acid. The solution was stirred at 120 ^oC for 8 h then heated to 350 ^oC to form a black ash then ground and calcinated in air at 400 ^oC for 1 h with a heating/cooling rate of 5 $^oCmin^{-1}$ to ensure complete combustion. The ash was further reground and calcinated in air at 700 ^oC for 3 h with a heating/cooling rate of 3 $^oCmin^{-1}$ to form a single-phase perovskite. The samples were then placed inside a tube furnace and heated in Ar at 500 ^oC for 1 h with a heating/cooling rate of 5 $^oCmin^{-1}$ to observe the effects of post annealing in Ar. Based on previous work, firing in Ar introduces oxygen defects and vacancies into the structure [151]. The samples were collected and labelled according to (i) the iron occupancy at the B-site: $LaNi_{0.6}Cu_{0.4}O_{3-\delta}$ (LNC), $LaNi_{0.6}Cu_{0.35}Fe_{0.05}O_{3-\delta}$ (LNCF-05), $LaNi_{0.6}Cu_{0.3}Fe_{0.1}O_{3-\delta}$ (LNCF-10) or (ii) the A-site deficiency: $La_{0.95}Ni_{0.6}Cu_{0.35}Fe_{0.05}O_{3-\delta}$ (LNCF-95) and $La_{0.9}Ni_{0.6}Cu_{0.35}Fe_{0.05}O_{3-\delta}$ (LNCF-90).

4.2.3. Physicochemical Characterisation

XRD analysis was used to examine the phase of the samples. Measurements were recorded at room temperature on a PANalytical X'Pert Pro diffractometer (Cu Kα source, 1.5405 Å) and collected in the 2θ range of 10-80° with a step of 0.0167°. Due to complexity, Rietveld refinement was carried by Professor Shanwen Tao using GSAS and EXPGUI [252, 253].

Iodometric titration was used to measure the oxygen vacancy content within the bulk perovskites [151]. In a previous study conducted by Zhang et al, it was found that LNC based samples showed stabilisation of the La^{3+} and Cu^{2+} oxidation state, as expected [151, 269]. It was identified however, that use of XPS was somewhat challenging to determine the valency of nickel due to the overlap of the La $3d_{3/2}$ and Ni $2p_{3/2}$ peaks. Furthermore, the O 1s spectra also presented complicated results, making it difficult to distinguish the oxygen vacancy concentration directly by XPS. Therefore, to study the oxygen vacancy content of the investigated perovskite oxides, iodometric titration was used. Iodometric titration is a useful technique that is often considered when evaluating oxygen defects throughout the whole lattice (surface and bulk) and shows similar trends to XPS analysis when studying oxygen vacancies [270].

Iodometric titration was performed via the reduction of I_2 and the oxidation of I^- to assess the oxygen content. The La A-site was reasonably assumed to be fixed in the +3 oxidation state. Since the B-site was bi- or trivalent, assumptions were made to simplify calculations. It was reasonably assumed that Cu was reduced from Cu^{2+} to Cu^{+} [151]. Any Ni/Fe B-site ions in the B^{3+}/B^{4+} oxidation state were given an average valence of X and ultimately assumed to be reduced to B^{2+} in the presence of iodide. The amount of iodine formed upon the oxidation of iodide was quantified by redox titration with $Na_2S_2O_3$ solution and was used to determine the oxygen non-stoichiometry within the samples [271].

SEM was used to examine the surface morphology of the catalyst using a Zeiss SUPRA 55-VP, equipped with an EDS spectrometer for elemental analysis. Specimens were prepared by depositing small amounts of the samples onto a Cu grid and coating them with Au to prevent charging of the surface.

4.2.4. Electrochemical Characterisation

For electrode preparation, perovskite oxide catalyst powders and carbon black were ground in a 4:1 mass ratio respectively. The powder was then dispersed in isopropanol and water (1:1 v/v) followed by Nafion solution and thoroughly stirred overnight before being brushed onto pre-treated carbon cloth. For comparison, a Pt/C electrode (commercial 20 wt% platinum on carbon black, Alfa Aesar) was prepared in the same way and the loading of Pt on carbon cloth was 0.61 mg cm^{-2}.

To assess AOR activity, electrochemical characterisation of the electrode was determined by cyclic voltammetry (CV), linear sweep voltammetry (LSV) and chronopotentiometry experiments on a Solartron 1470E CellTest System in a three-electrode cell. Pt mesh and Ag/AgCl (saturated KCl) were used as the counter and reference electrodes respectively, whilst the as-prepared catalyst coated carbon cloth was used as the working electrode. The CV plots were recorded between 0-0.8 V vs. Ag/AgCl at a scan rate of 25 mVs^{-1}. LSV experiments were conducted at a scan rate of 2 mVs^{-1}. Chronopotentiometry tests were conducted at room temperature under a constant applied potential of 0.55 V vs. Ag/AgCl.

4.3. Results and Discussion

4.3.1. Sample Characterisation

4.3.1.1. X-ray Diffraction

The $LaNi_{0.6}Cu_{0.4-x}Fe_xO_{3-\delta}$ (LNCF) perovskite oxides were synthesised by a sol-gel method and the respective XRD patterns were studied. During the synthesis method, different amounts of Fe-doped LNCF perovskites ($LaNi_{0.6}Cu_{0.4-x}Fe_xO_{3-\delta}$) were initially prepared at 700°C in air (x = 0, 0.05, 0.10; denoted as LNC-air, LNCF-05-air and LNCF-10-air respectively) and then later annealed in Ar atmosphere. The annealing step was introduced to create defects into the structure which have found to be beneficial towards electrocatalytic activity. In a previous study, it was found that $LaNi_{1-x}Cu_xO_{3-\delta}$ perovskites sintered in air alone did not exhibit significant activity towards ammonia oxidation. However, upon annealing in Ar, the perovskites showed obvious AOR activity due to the presence of lattice defects and oxygen vacancy formation at the surface of the catalyst [151]. Due to this, only the Ar-annealed counterparts, hereby simply referred to as LNC, LNCF-05 and LNCF-10, were investigated in this study.

Compared to the XRD patterns of the samples sintered in air, shown in Fig. 4.1a, annealing in Ar (Fig. 4.1b) did not introduce variation in the crystal structures of the three perovskites. The results indicate that synthesising the perovskite oxides in both the air and Ar produce a single phase with no impurities. XRD analysis of LNC, LNCF-05 and LNCF-10 revealed nine diffraction peaks corresponding to the [012], [110], [202], [024], [116], [214], [220], [036] and [134] planes. These peaks coincide with the expected $LaNi_{0.6}Cu_{0.4}O_3$ structure (PDF No. 04-007-9502). Furthermore, introduction of Fe shows very little change in the crystal parameters [272, 273]. The magnified XRD spectrum in the range 30° to 35° shows slight shifting of the peaks to lower 2θ values, indicative of slight lattice expansion as Fe content is increased. This expansion of interlayer spacing can assist in the diffusion of OH^- ions throughout the lattice and can lead to enhancements in ammonia oxidation reaction rates. Similar results have been observed in ternary Ni-Cu-Fe catalysts [207]. Moreover, the absence of additional peaks implies successful doping within the B-site rather than formation of a secondary phase.

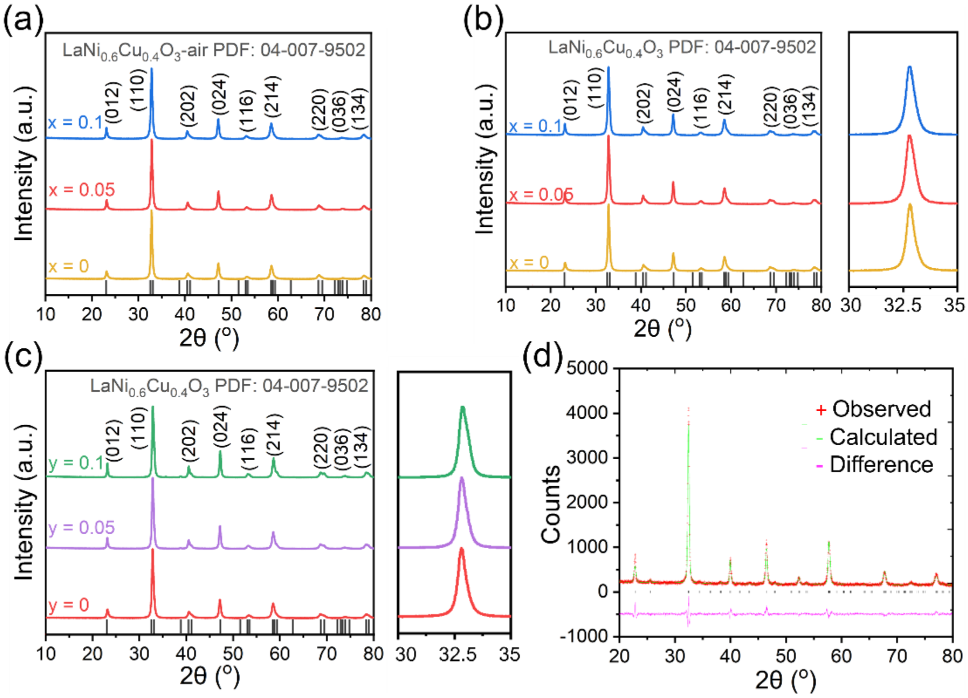

Fig. 4.1. (a) XRD analysis of synthesised $LaNi_{0.6}Cu_{0.4-x}Fe_xO_{3-\delta}$ (x = 0, 0.05, 0.1) in air [69]. (b) XRD analysis of synthesised $LaNi_{0.6}Cu_{0.4-x}Fe_xO_{3-\delta}$ (x = 0, 0.05, 0.1); XRD patterns in the 2θ range 30 to 35° (right) [69]. (c) XRD analysis of synthesised $La_yNi_{0.6}Cu_{0.35}Fe_{0.05}O_{3-\delta}$ (y = 0, 0.05, 0.1); XRD patterns in the 2θ range 30 to 35° (right) [69]. (d) Refined XRD pattern of LNCF-90 [69].

Since introduction of oxygen vacancies through annealing in Ar has proven to be a successful route towards improving AOR activity, as shown in a previous study, this concept was further explored by introducing A-site deficiencies which are known to form oxygen vacancies. Fig. 4.1c shows the XRD analysis for $La_yNi_{0.6}Cu_{0.35}Fe_{0.05}O_{3-\delta}$ (y= 0, 0.05, 0.1; denoted as LNCF-05, LNCF-95 and LNCF-90 respectively) which showed no distinctive structural changes compared to their air fired counterparts. In the presence of

A-site deficiencies, there was a shift to higher 2θ angles. A weak contraction effect on the unit cell volume appeared which agrees with the predicted effect of oxygen vacancies being formed. It is well recognised that by introducing deficiencies at the A-site, the overall positive charge of the perovskite is lowered, and this is often counterbalanced by the release of oxygen. Such release leads to the formation of oxygen vacancies inducing a contraction effect on the perovskite structure and henceforth a shift to higher 2θ angles is expected [272]. Data in Table 4.1 more closely looks at crystallite sizes and properties of the LNC based perovskites. Nonetheless, the rhombohedral structure of the parent material is retained in all A- and B-site modified samples.

Table 4.1. Structural features including crystallite sizes of A- and B-site modified LNC [69].

Sample	**Crystal system**	**Crystal size (nm)^a**
LNC	Rhombohedral	14.0
LNCF-05	Rhombohedral	14.4
LNCF-10	Rhombohedral	14.3
LNCF-95	Rhombohedral	15.7
LNCF-90	Rhombohedral	17.7

^{a} from Scherrer equation.

Rietveld refinement of the representative $La_{0.9}Ni_{0.6}Cu_{0.35}Fe_{0.05}O_{3-\delta}$ composition was carried out by GSAS and EXPGUI [252, 253]. The results indicate that $La_{0.9}Ni_{0.6}Cu_{0.35}Fe_{0.05}O_{3-\delta}$ is single phase and has a rhombohedral structure space group $R\overline{3}c$ (167) with a = 5.4555(1) Å, c = 13.2851(2) Å and V = 342.43(6) Å^3 (Table 4.2). The refined oxygen occupancy was found to be 0.798(2), reflecting the existence of a large amount of oxygen vacancies due to strategically introducing A-site deficiencies. The flexible valency of the B-site elements Ni, Cu and Fe allows for a A-site deficiencies to be accommodated for. However, it should be noted that the refined oxygen occupancy is not entirely accurate since XRD is not particularly sensitive to oxygen. Nevertheless, the stable and flexible nature of perovskite oxides allows for manipulation of the A-site and introduction of oxygen vacancies without collapsing the perovskite structure.

Table 4.2. Structure and lattice parameters of LNCF-90 [69].

Atom	**Site**	**Occupancy**	**x**	**y**	**z**	U_{iso}(Å^2)
La	6a	0.9	0	0	1/4	0.0213(4)
Ni	6b	0.6	0	0	0	0.0239(7)
Cu	6b	0.35	0	0	0	0.0239(7)
Fe	6b	0.05	0	0	0	0.0239(7)
O	18e	0.798(2)	0.4569(2)	0	0	0.019(4)

Space group *R-3c* (167); a = 5.4555(1) Å, c = 13.2851(1) Å, V = 342.43(4) Å^3, Z = 6. R_{wp} = 14.19%, R_p = 11.09%, χ^2 = 6.02.

4.3.1.2. Iodometric Titration

Iodometric titration was performed via the reduction of I_2 and the oxidation of I^- to assess the oxygen content and the results are highlighted in Table 4.3.

Table 4.3. Oxygen vacancy content of different perovskites as determined by iodometric titration [69].

Sample	**Oxygen vacancy, $V_O^{\cdot\cdot}$ (%)**
LNC	13.1
LNCF-05	13.0
LNCF-10	12.9
LNCF-95	13.9
LNCF-90	15.2

Table 4.3 shows the oxygen content of the perovskite samples. From the analysis, there was marginal change in oxygen vacancy $V_O^{\cdot\cdot}$ when the B-site was modified, however, as the A-site deficiency was introduced, the oxygen vacancy content notably increased. For example, $V_O^{\cdot\cdot}$ in stoichiometric LNCF-05 was found to be 13.0 %, which increased to 13.9 and 15.2 % as the A-site was reduced to 95 and 90 % in LNCF-95 and LNCF-90 respectively. The existence of a large amount of oxygen vacancies in $La_{0.9}Ni_{0.6}Cu_{0.35}Fe_{0.05}O_{3-\delta}$ is consistent with the Rietveld refinement analysis. This is in accordance with literature, which recognises A-site deficiencies as a route to introduce oxygen vacancies to maintain charge neutrality [29, 35, 159-161, 274]. It should be recognised that the concentration of oxygen defects near the surface is generally higher than in the bulk [151]. Therefore, the oxygen vacancy

concentration at the surface of the LNCF-90 sample is assumed to be > 15.2 %.

4.3.1.3. Scanning Electron Microscopy and Energy Dispersive X-ray Spectroscopy

SEM analysis was performed on the LNC-based perovskite. EDS was used to analyse the elemental composition and produce map sum spectra, shown in Fig. 4.2. The elemental weight (%) was taken from such spectra to show the A- to B- ratio of each sample, reported in Table 4.4. The A/B ratio varies from the expected ratio slightly but is in close proximity of what is expected [272]. It should be recognised that the summation of the La, Ni, Cu and Fe elemental weights (%) shown in this table are less than 100 % due to the presence of additional elements such as Au on the surface which is used as a coating material.

Table 4.4. Elemental weight (%) of modified A- and B-site taken from map sum spectra [69].

Sample	**Elemental weight (%)**				
	La	**Ni**	**Cu**	**Fe**	**A/B**
LNC	49.2	26.2	20.5	-	1.05 (1)
LNCF-05	49.2	26.7	19.5	3.70	0.99 (1)
LNCF-10	50.1	27.4	18.5	3.90	1.01 (1)
LNCF-95	48.5	29.0	19.8	2.65	0.94 (0.95)
LNCF-90	46.8	30.2	20.8	2.20	0.88 (0.90)

brackets indicate the expected ratio.

From the SEM images, it is revealed that the particles were uniformly dispersed and no agglomeration was observed. Introduction of the Fe dopant and A-site deficiency did not lead to significant changes in grain size or morphology. A homogenous distribution of La, Ni, Cu and Fe can be observed throughout the samples, which is in agreeance with XRD analysis and confirms the absence of any bulk impurities or secondary phases.

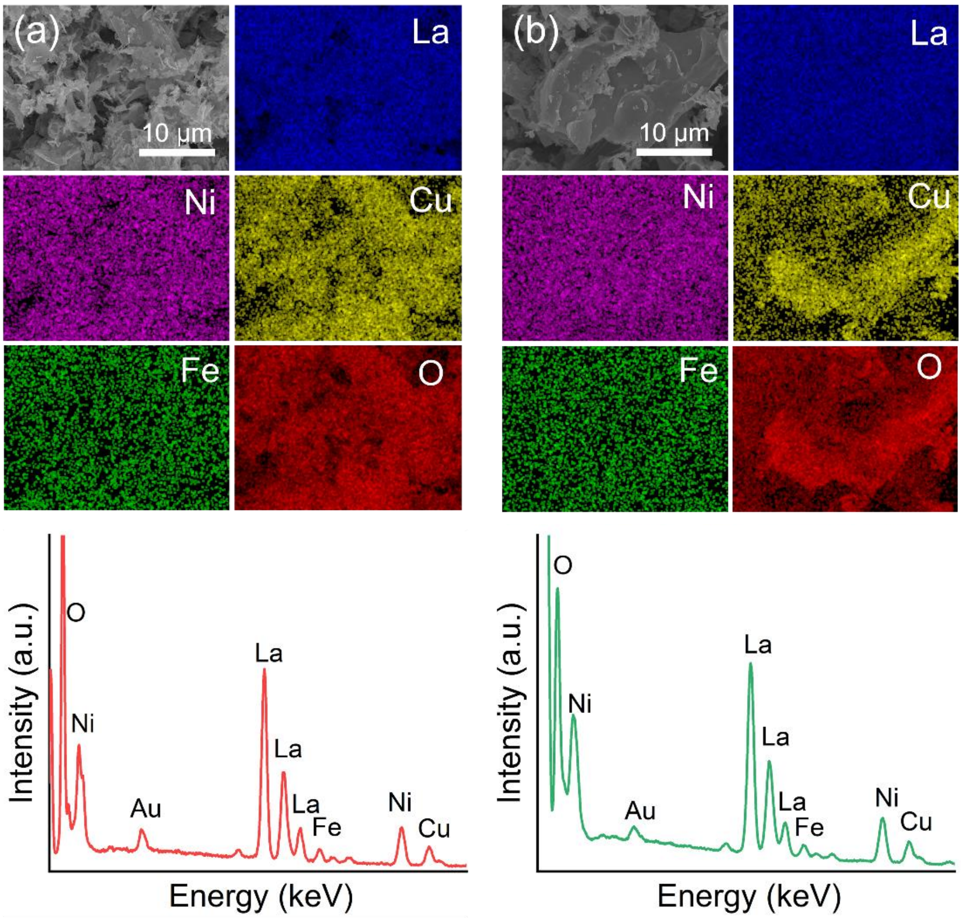

Fig. 4.2. SEM image, elemental mapping and elemental point analysis of La, Ni, Cu, Fe and O in (a) LNCF-05 and (b) LNCF-90 with gold used as coating material [69].

4.3.2. Evaluation of Ammonia Oxidation Reaction

4.3.2.1. B-site Modification

The as prepared samples were investigated for their electrochemical activity towards ammonia oxidation. In a previous study by Zhang et al, it was confirmed that the B-site is of particular interest since ammonia was found to mainly interact with these sites during the oxidation process [151, 275]. Through DFT calculations, it was noted that ammonia adsorption was more favourable in the presence of Cu in $LaNi_{1-x}Cu_xO_{3-\delta}$. The B-site composition is therefore of great importance when tailoring perovskites towards AOR activity. To further tune the properties of the B-site and investigate the effects of dual doping, Fe was introduced into the NiCu B-site to form a series of $LaNi_{0.6}Cu_{0.4-x}Fe_xO_3$ (x = 0, 0.05, 0.10, 0.15) perovskite oxides.

Fig. 4.3a shows the CV plots of the LNC, LNCF-05 and LNCF-10 perovskites in 0.5 M KOH and 55 mM NH_4Cl electrolyte. All samples obtained a similar onset potential of around ca. 0.45 V vs. Ag/AgCl, similar to literature [151, 204, 205]. The undoped LNC sample displayed an anodic current density of 47 $mAcm^{-2}$. This increased to 69 $mAcm^{-2}$ when x = 0.05, however when x was further increased to 0.10, the current dropped to 57 $mAcm^{-2}$. These results demonstrate that there is an optimum amount of Fe doping (x = 0.05) at the B-site and that LNCF-05 shows superior activity. An optimum Fe doping is not uncommon and has been reported in literature. Zhu et al. found that when investigating a ternary Ni-Cu-Fe oxyhydroxide, $Ni_{0.8}Cu_{0.4}Fe_{0.1}$ showed greater activity than undoped $Ni_{0.8}Cu_{0.4}$ and $Ni_{0.8}Cu_{0.4}Fe_{0.3}$ as well as $Ni_{0.80}Cu_{0.4}Fe_{0.4}$ [207]. In this study, the active $Ni_{0.8}Cu_{0.4}Fe_{0.1}$ has a Ni:Cu:Fe ratio of around 0.62:0.31:0.07 respectively. Here, Fe makes around 7 % of the active material, whereas in the LN—-90 perovskite, Fe is 5 % in the B-site. Despite this small variation, it can be assumed that the overall influence of Fe remains the same. Zhu et al. reported that the ammonia molecule adsorbs onto the $O_{O\text{-}Ni}$ surface of $Ni_{(1-x)}Cu_xOOH$ which is not very thermodynamically favourable due to the high Gibbs free energy of adsorption [207]. By introducing lower electronegative Fe^{3+} dopants into the $Ni\text{-}O_6$ framework, the electrons near the Fermi level of O were found to be more delocalised which increased the availability of empty orbitals to accept electrons during AOR. Since the ABO_3 perovskite structure adopts a similar $Ni\text{-}O_6$ geometry at the B site, it is logical to assume that introducing Fe into these structures would have a similar effect and therefore may explain the enhancement in AOR. Furthermore, the anodic current density of the LNCF-05 perovskite is substantially greater than that of $LaNi_{0.5}Cu_{0.5}O_{3-\delta}$ reported in previous work [151]. This indicates that fine tuning the elemental composition at the B-site is imperative for AOR activity and can provide insight into designing efficient perovskite catalysts for AOR.

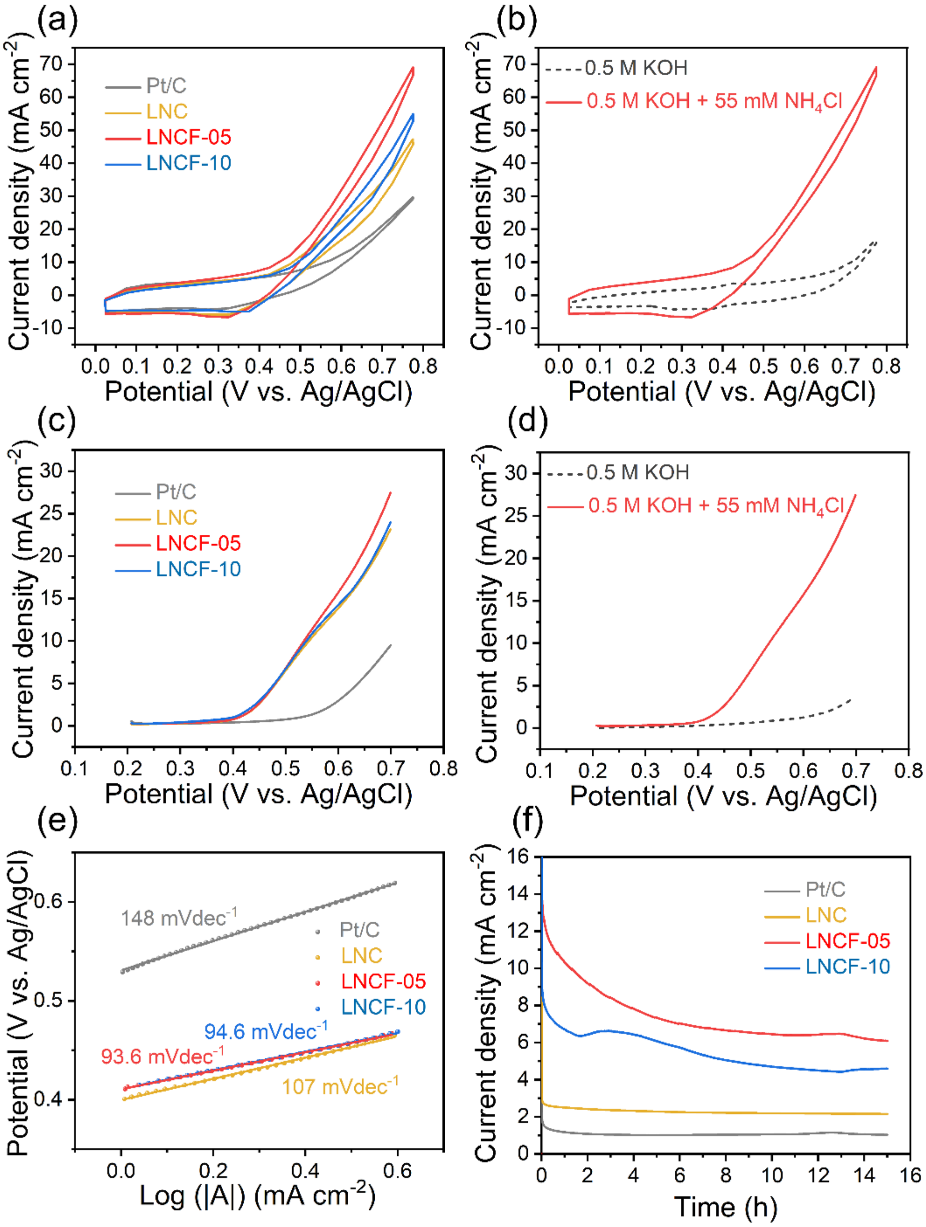

Fig. 4.3. (a) CV performances of catalysts in 0.5 M KOH + 55 mM NH_4Cl [69]. (b) CV performance of LNCF-05 in 0.5 M KOH with and without 55 Mm NH_4Cl [69]. (c) LSV performances of catalysts 0.5 M KOH + 55 mM NH_4Cl [69]. (d) LSV performance of LNCF-05 in 0.5 M KOH with and without 55 mM NH_4Cl [69].I) Tafel plots of Pt/C, LNC, LNCF-05 and LNCF-10. (f) Chronoamperometry analysis of catalysts in 0.5 M KOH + 55 mM NH_4Cl [69].

It should be noted that the current density recorded includes the combined influence of AOR and valency changes to the Ni based centre, which tend to overlap within the region scanned. To rule out the contribution of the latter, the samples were also cycled in pure 0.5 M KOH electrolyte in the absence of ammonia. Fig. 4.3b shows that anodic and cathodic peaks in the range of 0 and 0.8 V appear when the LNCF-05 perovskite is cycled in 0.5 M KOH electrolyte. These can be related to the transformation between Ni(II) and Ni(III) [151, 205]. This oxidation peak has a much lower current density than that in the presence of ammonia, with the sharp difference in current density being attributed to AOR. Interestingly, the cathodic peak does not change with the introduction of ammonia, which reinforces the Ni(III) species being liable for AOR and implies that the reaction may proceed via a direct electron transfer mechanism [210].

LSV was used to further investigate the catalytic activity of the perovskites towards ammonia electrooxidation. The applied voltage was kept below 1.1 V vs. Ag/AgCl to avoid water oxidation, the recorded current density was subsequently owed to ammonia oxidation. As shown in Fig. 4.3c, a sharp increase in ammonia oxidation current is observed above an anodic potential of 0.4 V vs. Ag/AgCl. Amongst the series of perovskites tested, LNCF-05 achieves the highest current density. The LSV results follow the same trend as those observed by CV, confirming that LNCF-05 has obvious catalytic activity towards AOR. Corresponding Tafel plots were constructed to evaluate catalytic ammonia oxidation kinetics (Fig. 4.3e). The Tafel slope of LNCF-05 (93.6 $mVdec^{-1}$) was smaller than that of LNC (107 $mVdec^{-1}$) and LNCF-10 (94.6 $mVdec^{-1}$). It can therefore be deduced that under the same applied conditions, AOR proceeds with less electrochemical polarisation and more facile electron transport on the LNCF-05 electrode. This further reinforces that the presence of Fe lowers the energy barrier towards AOR.

Stability is one of the key factors determining the quality and suitability of an electrocatalyst. Stability of the electrodes was evaluated by chronoamperometry with a fixed anode potential of 0.55 V vs. Ag/AgCl in 0.5 M KOH + 55 mM NH_4Cl. Fig. 4.3f shows chronoamperometry curves for the different electrodes recorded over a duration of 15 h. The highest current density was observed for the LNCF-05 catalyst. From the chronoamperogram, all catalysts exhibit an initial gradual drop in current density. A possible reason for the drop in current density over time may be owed to some of the active sites becoming poisoned by strong adsorption of the N* species proposed in the N+N mechanism of AOR [151, 276]. It should be noted the fluctuation shown by the LNCF-10 was due to accidentally knocking of the sample during testing. Furthermore, the current density of the Pt/C electrode was much lower than the investigated perovskite oxide catalysts which has been seen in previous work [151]. This may be associated to poisoning of the Pt surface and/or an incompatible testing potential [151, 204].

4.3.2.2. A-site Modification

Since LNCF-05 showed optimum activity, the effect of A-site deficiencies was explored using LNCF-05 as the parent catalyst. A-site deficiencies were introduced and a series of $La_{1-y}Ni_{0.6}Cu_{0.35}Fe_{0.05}O_{3-\delta}$ (y = 0, 0.05, 0.10) perovskite oxides were tested for their activity towards AOR.

In the presence of ammonia, there is a sharp increase with an onset potential of ca. 0.45 V vs. Ag/AgCl, indicating that all samples have good activity towards AOR (Fig. 4.4a) [204, 205]. For comparison, LNCF-05 obtained an anodic current of 69 $mAcm^{-1}$ at 0.8 V vs. Ag/AgCl, which increased as the A-site deficiency was introduced to 118 and 144 $mAcm^{-1}$ for LNCF-95 and LNCF-90 respectively. Furthermore, Fig. 4.4b shows that in the absence of ammonia, there are a pair of redox peaks reinforcing the transformation of the Ni(II) and Ni(III) species [151, 205].

There is an obvious increase in current density as A-site deficiencies are introduced into the perovskite oxide, which can be owed to the presence of oxygen vacancies. It is well accepted that oxygen vacancies have a significant impact on the electronic structure and surface chemistry of perovskite oxides, typically resulting in a positive effect on catalytic performance. In a previous report, oxygen vacancies were introduced into a LNCO-55-Ar sample after annealing and it was deduced that more Ni^{2+} species were created on the surface of the perovskite to maintain charge neutrality [151]. This led to a substantial enhancement in AOR performance since it is widely accepted that the Ni^{II}/Ni^{III} redox couple acts as the active site in the ammonia oxidation process[151, 205, 277]. Subsequently, it was concluded that modification of the Ni electronic structure by introduction of oxygen vacancies indirectly promotes AOR activity. This concept can be further exploited when A-site deficiencies are introduced into the perovskite since this is a promising route to establishing oxygen vacancies [29, 35, 159-161]. As the positive A-site becomes deficient, the perovskite possesses a more overall negative charge which can be subsequently counterbalanced by release of oxygen to retain charge neutrality. The above suggests that oxygen vacancies may play a key role in the stepwise oxidation of ammonia by promoting the formation of the active Ni^{2+} species for the AOR mechanism. The formation of the active redox couple is highlighted in Eq. (4.1) [278, 279].

$$Ni^{II}(OH)_2 + OH^- \leftrightarrow Ni^{III}OOH + H_2O + e^- \tag{4.1}$$

The LSV curves were collected in 0.5 M KOH and 55 mM NH_4Cl using a scan rate of 2 mVs^{-1} and are displayed in Fig. 4.4c and Fig. 4.4d. Above ca. 0.45 V vs. Ag/AgCl, there is a sharp increase amongst all three electrodes, in agreeance with CV. The corresponding Tafel plots were constructed to observe the catalytic kinetics. Fig. 4.4e shows that the Tafel slope of LNCF-90 (72.7 $mVdec^{-1}$) is lower than both LNCF-95 (92.0 $mVdec^{-1}$) and LNCF-05 (93.6 $mVdec^{-1}$). This signifies that under the same testing conditions, the ammonia oxidation reaction proceeds with greater ease and more facile electron transportation on the LNCF-90 surface. Again, this indicates the importance of oxygen vacancies in indirectly facilitating AOR [151].

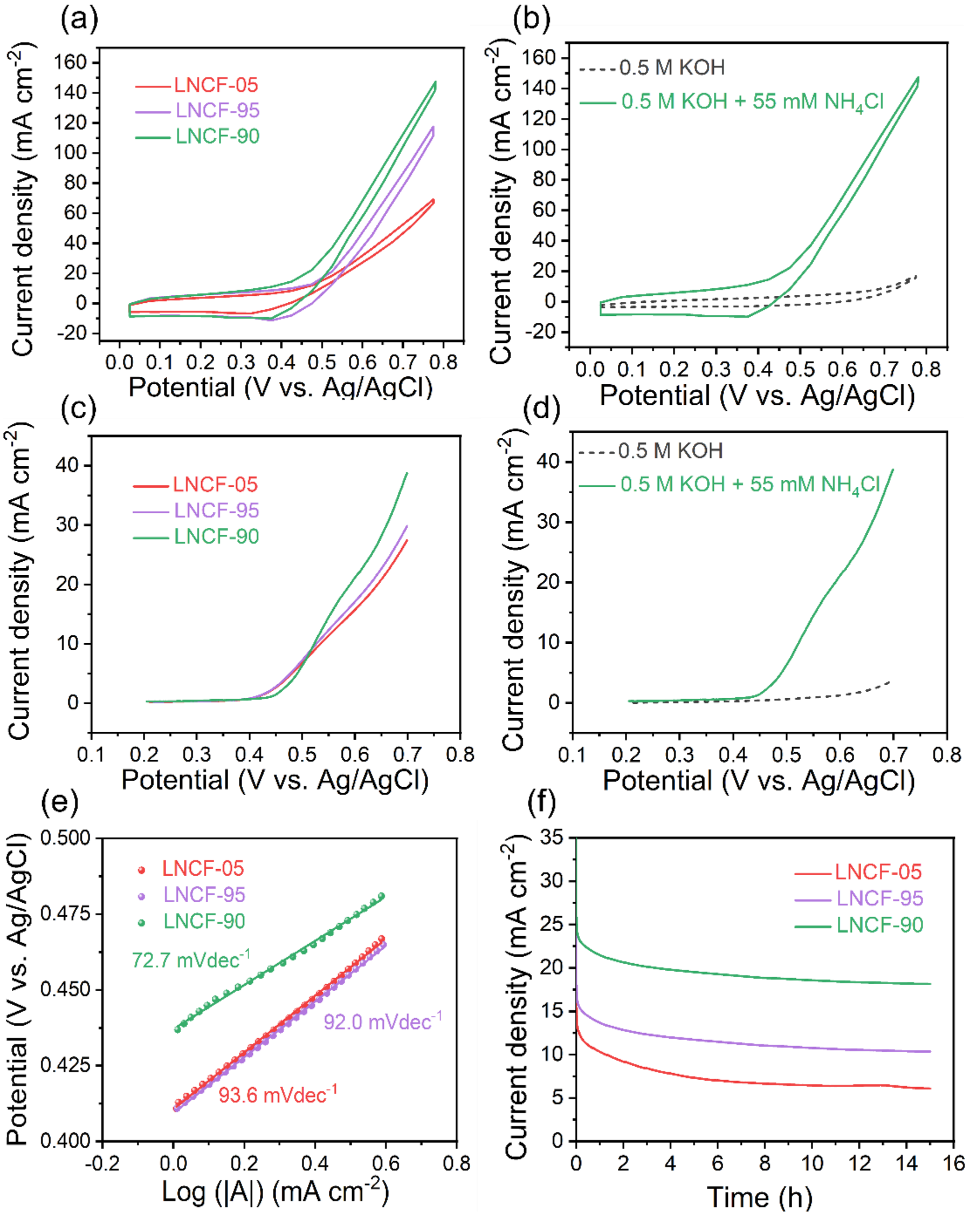

Fig. 4.4. (a) CV performances of catalysts in 0.5 M KOH + 55 mM NH_4Cl [69]. (b) CV performance of LNCF-90 in 0.5 M KOH with and without 55 Mm NH_4Cl [69]. (c) LSV performances of catalysts in 0.5 M KOH + 55 mM NH_4Cl [69]. (d) LSV performance of LNCF-90 in 0.5 M KOH with and without 55 mM NH_4Cl [69]. (e) Tafel plots of LNCF-05, LNCF-95 and LNCF-90 [69]. (f) Chronoamperometry analysis of catalysts in 0.5 M KOH + 55 mM NH_4Cl [69].

The key parameters of similar reported AOR electrocatalysts are displaIed in Table 4.5 for comparison. Compared to both bimetallic NiCu, which shows a current density of 35 mAcm^{-2} at 0.55 V vs. Ag/AgCl, and single doped, stoichiometric $LaNi_{0.5}Cu_{0.5}O_{3-\delta}$-Ar, which shows a current density of around

10 mAcm^{-2} at 0.55 V vs. Ag/AgCl, $La_{0.9}Ni_{0.6}Cu_{0.35}Fe_{0.05}O_{3-\delta}$ shows an improved current density of around 50 mAcm^{-2} at 0.55 V vs. Ag/AgCl under similar testing conditions [151, 204]. Therefore, amongst the list of catalysts, in particular those based on non-precious metal groups, LNCF-90 demonstrates superb AOR activity.

Table 4.5. Performance of AOR on different electrocatalysts [69].

Catalyst	**Fuel**	**Scan rate (mV/s)**	**E_p (V)**	**Standard E_p (V)**	**Current density (mAcm^{-2})**	**Ref**
$Ni(OH)_2$	0.5 M NaOH + 55 mM NH_4Cl	25	0.55 V vs. Ag/AgCl	1.57 V vs. RHE [a]	5	[204]
NiCu					35	
NiMn			0.50 V vs. Ag/AgCl	1.52 V vs. RHE [a]	20	
NiFe					25	
a-NiCu	0.5 M NaOH + 55 mM NH_4Cl	20	0.70 V vs. SCE	1.77 V vs. RHE [a]	30	[207]
a-NiCuFe					60	
$Ni_{93}Pd_7$	0.5 M $NaNO_3$ + 200 mM NH_4NO_3	50	1.25 V vs. HgO/Hg	2.07 V vs. RHE	60 (A g^{-1})	[280]
$Ni_{98}Pd_2$					150 (A g^{-1})	
NiCu	0.5 M NaOH + 55 mM NH_4Cl	50	0.70 V vs. Ag/AgCl	1.72 V vs. RHE [a]	52	[205]
NiCu	1 M KOH + 0.5 M NH_3	50	0.65 V vs. HgO/Hg	1.68 V vs. RHE [a]	110.4	[281]
PtNi	1 M KOH + 0.1 M NH_3	10	0.69 V vs. RHE	0.69 V vs. RHE	75.32 (Ag^{-1})	[282]
Ni	0.33 mM NH_4^+ + 0.5 M KOH	120	0.45 V vs. HgO/Hg	1.48 V vs. RHE [a]	~9	[283]
Co_{10}/Ni			0.38 V vs. HgO/Hg	1.41 V vs. RHE [a]	8.5	
NiO	200 mM NH_4OH + 100 mM	100	1.28 V vs. HgO/Hg		2.93	[284]
NiO-TiO_2				2.31 V vs. RHE [a]	3.01	

	$NaNO_3$ (+3 M NaOH)					
Pt	1 M KOH + 0.1 M NH_3	50	-0.25 V vs. Ag/AgCl	0.77 V vs. RHE [a]	1.63	[285]
PtNi					2.39	
PtNiO					2.72	
PtIr	1 M KOH + 0.1 M NH_3	5	~0.65 V vs. RHE	~0.65 V vs. RHE	25.1 (Ag^{-1})	[286]
$PtIr/SiO_2$-CNT-COOH			~0.70 V vs. RHE	~0.70 V vs. RHE	90.6 (Ag^{-1})	
$PtIrNi/SiO_2$-CNT-COOH					124.0 (Ag^{-1})	
Pt	1 M KOH + 0.5 M NH_3	20	-0.20 V vs. Hg/HgO	0.83 V vs. RHE [a]	~0.34	[287]
Pt 100					~0.95	
$PtSnO_2$					~0.50	
$PtSnO_2$ 100					~0.75	
Pt	0.05 M KOH + 100 mM NH_3	50	0.70 V vs. RHE	0.70 V vs. RHE	~0.42	[288]
Pt plate	1 M KOH + 1 M NH_3	10	-0.23 V vs. HgO/Hg	0.80 V vs. RHE [a]	1.7	[289]
Pt-black					20	
Pt-CNT (160 °C)			~-0.19 V vs. HgO/Hg	~-0.84 V vs. RHE [a]	~58	
Pt NC	0.1 M KOH + 0.1 M NH_3	50	~0.78 V vs. RHE	~0.78 V vs. RHE	0.58	[290]
Ir and $Ni(OH)_2$-decorated			0.82 V vs. RHE	0.82 V vs. RHE	0.72	
Pt NC Ir-decorated Pt NC			0.75 V vs. RHE	0.75 V vs. RHE	1.25	
$LaNi_{0.5}Cu_{0.5}O_{3-\delta}$-Ar	0.5 M KOH + 55 mM NH_4Cl	25	0.55 V vs. Ag/AgCl	1.57 V vs. RHE [a]	~10	[151]
$LaNi_{0.6}Cu_{0.35}Fe_{0.05}O_{3-\delta}$	0.5 M KOH + 55 mM NH_4Cl	25	0.55 V vs. Ag/AgCl	1.57 V vs. RHE [a]	~20	This work [69]
$La_{0.9}Ni_{0.6}Cu_{0.35}Fe_{0.05}O_{3-\delta}$					~50	

[a] potentials estimated assuming very alkaline environment (pH = 14).

Stability of the LNCF-05, LNCF-95 and LNCF-90 electrodes were examined via chronoamperometry with a fixed anode potential of 0.55 V vs. Ag/AgCl in 0.5 M KOH and 55 mM NH_4Cl. Fig. 4.4f shows the stability of the electrodes tested over a duration of 15 h. For the stoichiometric LNCF-05 electrode, the stability slowly decreases over the testing duration reaching around 7.5 mAcm^{-2} after 3 h and eventually plateauing after 6 h. This drop is less pronounced in the LNCF-95 sample, with a value of around 12.5 mAcm^{-2} after testing. The LNCF-90 electrode shows much more stable activity, with an initial minor dro116hould116urrent density which then stabilises and is maintained around 22 mAcm^{-2}. These results indicate that introducing A-site deficiencies improves both stability and catalytic activity of the LNCF based perovskites.

4.3.3. Ammonia Electrolysis

Making use of ammonia in clean energy applications is especially interesting due to the high volumetric energy density of ammonia (12.9 MJL^{-1}) [25, 45, 207, 291-293]. This is relatively high compared to other conventional fuels such as hydrogen, methanol and ethanol [207, 294]. Recently, electrooxidation of ammonia has surfaced as an effective technique to remove ammonia which involves simple operation in the absence of poisonous products [204, 205, 295-297]. Ammonia electrolysers utilise AOR at the anode site (Eq. (4.2)) and a subsequent series of electrochemical reactions can effectively convert ammonia into nitrogen and hydrogen gas through a three-electron oxidation reaction [206, 298].

$$NH_3 + 3OH^- \rightarrow \frac{1}{2}N_2 + 3H_2O + 3e^- \qquad E^o = -0.77\,V\,vs.SHE \tag{4.2}$$

$$3H_2O + 3e^- \rightarrow \frac{3}{2}H_2 + 3OH^- \qquad E^o = -0.83\,V\,vs.SHE \tag{4.3}$$

$$Overall: NH_3 \rightarrow \frac{1}{2}N_2 + 3H_2O + \frac{3}{2}H_2 \qquad E_{cell} = 0.06\,V \tag{4.4}$$

This electrochemical technique not only removes unwanted ammonia from aqueous solution but can also be used as indirect hydrogen storage to produce power via combustion methods and fuel cells [25, 64, 205, 299-301]. This provides a potential solution for the on-board hydrogen supply in applications such as fuel cell vehicles [25, 302, 303]. Interestingly, a recent publication revealed that high-purity hydrogen was produced by the electrolysis of ammonia at intermediate temperatures [304]. Furthermore, the theoretical energy consumption of ammonia electrolysis to produce hydrogen is around 95 % less than that of water electrolysis.

Interestingly, wastewater contains a large amount of ammonia, which poses a great hazard to the quality of water resources and can have a substantial effect on environmental and human health [305]. The treatment of wastewater has become a growing topic of interest due to the development of industrial and human activities leading to large amounts of commercial and domestic waste [306, 307]. Use of such water as an electrolyte in ammonia electrolysers may be a useful method to remove the high concentrations of ammonia and simultaneously treating wastewater. To test the viability of the catalyst as an anode in an ammonia electrolyser under such conditions, the LNCF-90 perovskite material was first tested for its activity towards AOR in both simulated and real landfill leachate. Landfill leachate was collected and characterised using a UV-Vis and pH-meter to determine the concentration of ammonia and the pH of the sample respectively. It is important to determine the pH value of the wastewater since the reaction is highly pH dependent and alkalinity of the electrolyte solution plays a key role in AOR [210].

In the present study, the ammonia concentration in a batch of a landfill leachate sample was found to be 2000 ppm and the pH ~8 was weakly alkaline, similar to values reported in literature [151, 308]. A simulated wastewater sample was prepared using these parameters to investigate the activity of the perovskite in pure ammonia solution. Based on the aforementioned performance, LNCF-90 was chosen as the working electrode and tested via CV in both simulated and real wastewater. Fig. 4.5a shows the CV plots of LNCF-90 in simulated wastewater (2000 pm NH_4Cl, with an appropriate amount of KOH added to bring the pH to 8), real wastewater

(2000 ppm ammonia, pH 8) and both the simulated and real wastewater with the addition of 0.5 M KOH to make the environment extremely alkaline.

In the absence of an alkaline environment, the simulated and real wastewater show negligible activity towards AOR. However, on addition of 0.5 M KOH, both the simulated and real wastewater show substantial activity above an onset potential ca. 0.45 V vs. Ag/AgCl. These findings support the fact that the AOR mechanism is pH dependent as has been found in literature and proceeds in a highly alkaline condition [210]. Notably, the anodic current density reaches around 112 mAcm^{-2} in simulated wastewater with addition of 0.5 M KOH, which is nearly double that in real wastewater at around 60 mAcm^{-2}. It is recognised that organic oxidation at the anode surface is common in landfill leachate solutions [309]. This oxidation process could possibly compete with ammonia oxidation at the anode surface and may partially explain the lower polarisation performance seen when testing in real landfill leachate as opposed to simulated landfill leachate. Moreover, Zeng et al. found that the biodegradation of organic matter could possibly have a negative impact on ammonia oxidation [310]. A similar adverse impact on the electrooxidation of ammonia may oIcur in the presence of inorganic and organic matter found in the real landfill leachate under investigation. Identification of some ions on the surface of the electrode surface after exposure to real landfill leachate are discussed in greater detail in the following section. Nevertheless, it is reasonable to assume that impurities within the real wastewater may affect and interfere with the performance of the electrode, as is reflected by the differences in LSV measurements shown in Fig. 4.5b.

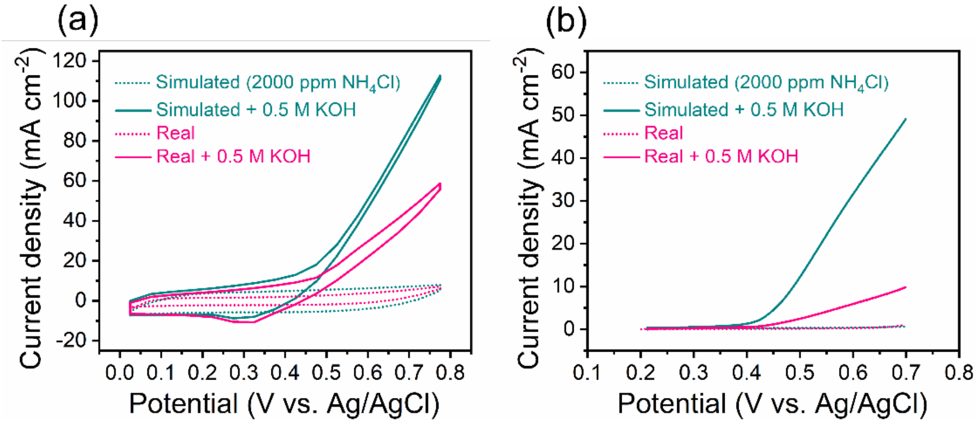

Fig. 4.5. (a) CV and (b) LSV of LNCF-90 in simulated and real wastewater with and without 0.5 M KOH [69].

It should be noted that although the ammonia concentration of the simulated wastewater was prepared at 2000 ppm NH_4Cl (~120 mM), which is double that of the AOR tests above (55 mM), the current density does not double and scale in a similar way. Despite nearly doubling the ammonia concentration, the current density remains somewhat similar in both scenarios, probably due to saturation of the active sites on the electrode surface. This phenomenon has also been observed in a previous report [210].

Electrolysis of simulated wastewater using LNCF-90 as the working electrode was examined and the current density of the cell was recorded in Fig. 4.6. Pt mesh was chosen as the counter electrode and Ag/AgCl as the reference electrode in a three-electrode cell set up. A long-time ammonia electrolysis test was carried out in 25 mL of both real and simulated wastewater for comparative purposes, with the addition of 0.5 M KOH. Since it has been verified that the ammonia oxidation process favours alkaline conditions, the electrolyte solutions will hereby be simply referred to as simulated and real wastewater (as it is implied that the addition of KOH is constant). A fixed anodic potential of 0.55 V vs. Ag/AgCl was applied to avoid unfavourable reactions such as oxygen evolution which may become more prominent under higher applied potentials and result in high energy consumption [207]. Over the entire testing duration, the current density drops to around 3 mAcm^{-2}. It should be noted that the removal efficiency reaches around 95.7 % at 100 hr, which implies a small amount of ammonia remains in solution and is responsible for generating this small current.

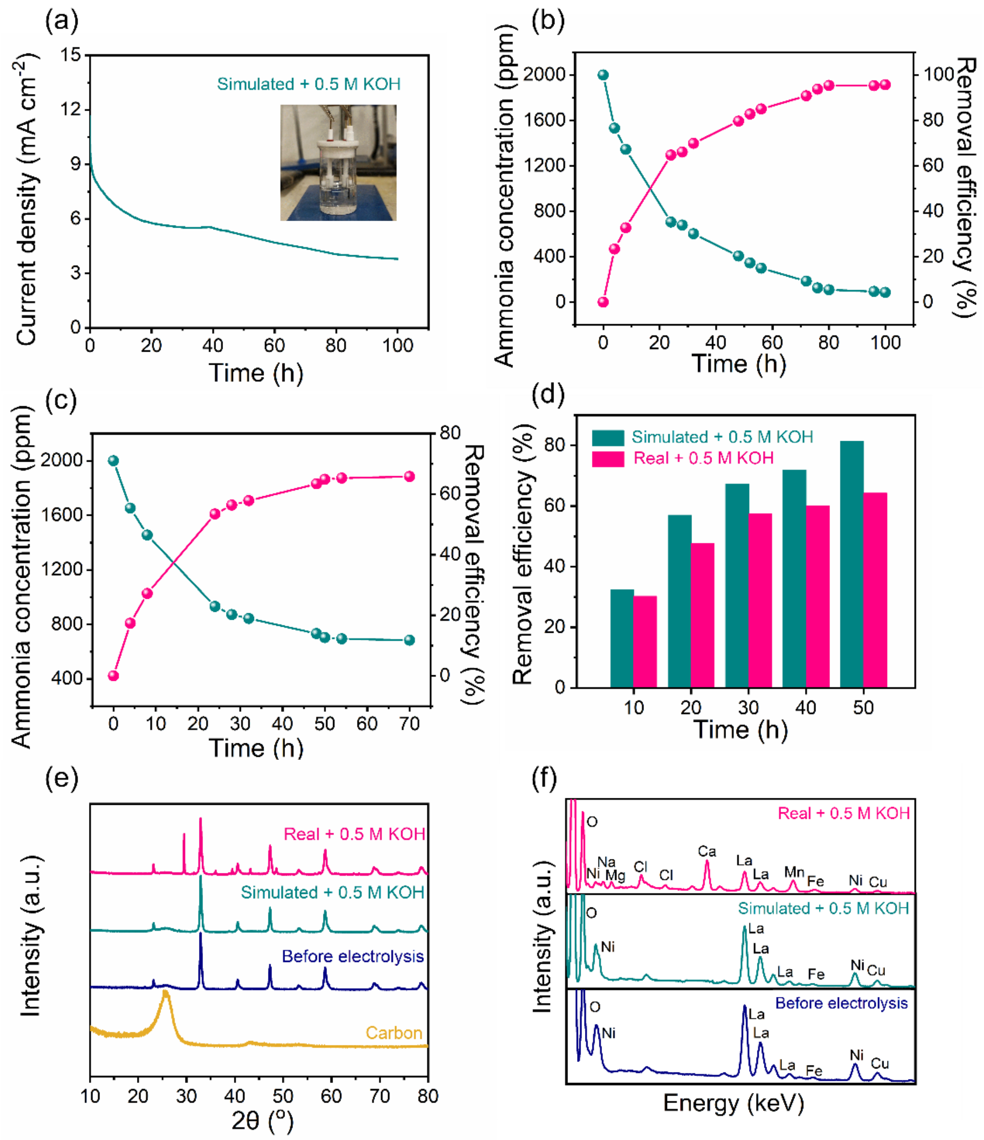

Fig. 4.6. (a) Electrolysis profile of LNCF-90 in simulated wastewater with the addition of 0.5 M KOH, insert of electrolysis cell [69]. (b) Ammonia concentration and removal efficiency of LNCF-90 in simulated wastewater in 0.5 M KOH [69]. (c) Ammonia concentration and removal efficiency of LNCF-90 in real wastewater in 0.5 M KOH [69]. (d) Removal efficiency profiles of LNCF-90 in simulated and real wastewater with the addition of 0.5 M KOH [69]. (e) XRD analysis of LNCF-90 electrode before and after electrolysis test [69]. (f) EDS point analysis of LNCF-90 electrode before and after electrolysis test [69].

In a 100 h test, the current density of the cell employing simulated wastewater electrolyte was initially high and then decreased against time due to the consumption of ammonia within the electrolyte solution. During the initial testing period, the ammonia concentration continued to decrease over time and a removal efficiency of 95.4 % was achieved after 80 h operation (Fig. 4.6b). Beyond 80 h, the removal efficiency showed minimal change, reaching 95.7 % after 100 h. The results signify that LNCF-90 is a good electrode for use within an ammonia electrolyser, with the ability to reduce ammonia concentration making it an ideal candidate for ammonia-containing wastewater treatment.

It should be noted that the pathway and exact intermediates formed throughout the ammonia oxidation process is complex and complete oxidation to N_2 may be hindered by the formation of intermediates [311]. Some studies suggest that ammonia undergoes deprotonation to form N_{ads} which can either be coupled to form N_2 or oxidised to form NO_x species [206, 311, 312]. It has also been suggested that the formation of N_2 may occur via dimerization of partially dehydrogenated $^*NH_x$ species [207, 311, 313]. The possibility of NO_x formation is also viable through this mechanism since NH_3 can be oxidised to NH_2OH, which can then be further oxidised to form NO_x species [311, 314]. Selective catalytic oxidation of ammonia and complete removal of ammonia nitrogen is ideal for wastewater treatment [311]. High NH_3 conversion at temperatures less than 180^{o}C can be obtained on supported noble metals such as Ag/Al_2O_3, CuO/RuO_2, $Pt/CuO/Al_2O_3$ and Ir, but selectivity towards N_2 needs to be significantly improved [315-319]. To identify the possible presence of nitrate ions, a standard 'brown-ring' test was conducted on the simulated wastewater solution after electrolysis and the formation of the $[Fe(H_2O)_5(NO)]^{2+}$ ion gave the expected brown ring result [320]. The test therefore confirmed the presence of nitrate ions at detectable levels after the electrolysis of simulated wastewater. Although the complete removal of ammonia nitrogen is ideal for wastewater, many works report the presence of NO_x, particularly on nickel hydroxide anodes [205, 277, 311]. A possible route of formation for the nitrate species on nickel hydroxide surfaces has been proposed in previous studies and is as follows [277]:

$$Ni^{III}OOH - NH_{3(ads)} + 9OH^{-} \rightarrow Ni^{III}OOH + NO_3^{-}\ 6H_2O +\ 8e^{-} \qquad (4.5)$$

To further validate the use of the LNCF-90 electrode in a practical setting, real wastewater was also used as an electrolyte. The ammonia concentration profile shown in Fig. 4.6c shows that the removal efficiency reached 65.8 % after a 70 h operation in real wastewater. It should be noted that this concentration profile shows a steady decrease over time for the first 50 h and then begins to plateau, with only a marginal reduction in ammonia between 50 and 70 h (64.9 and 65.8 % respectively). This is unlike the simulated wastewater solution, which continues to remove ammonia until 96.7%, showing that the process in real wastewater differs. The results imply that past a certain point, the catalyst ability to remove ammonia is limited, most likely due to contamination of the electrode surface by impurities in real wastewater.

For comparative purposes, the ammonia removal efficiencies in both simulated and real wastewater over a duration of 50 h is provided in Fig. 4.6d. Within the first 10 h, there is a small difference in removal efficiencies, however, as time progresses, the difference in removal efficiencies between the simulated and real wastewater becomes more evident. This may be owed to secondary ions and impurities present within real wastewater which may deposit onto the electrode and interfere with AOR at the catalytic surface, hindering the process and causing a lower removal efficiency to be observed. This is investigated in further detail below. Nonetheless, the removal efficiency of $La_{0.9}Ni_{0.6}Cu_{0.35}Fe_{0.05}O_{3-\delta}$ in real wastewater is still comparable to the removal of ammonia in pure ammonia solutions (~40-70 %) where Ni and $Ni(OH)_2$ based materials are used as AOR catalysts [204, 205, 207-210].

Fig. 4.6e shows XRD diffractograms of the LNCF-90 electrode before and after electrolysis testing. There is no apparent change in the crystal structure after testing in simulated wastewater, indicating the robust and stable nature of the perovskite oxide. After testing in real wastewater, although the predominant perovskite peaks remain present, there are some additional peaks which may be correlated to deposition of impurities or additional ions on the surface of the electrode from real wastewater.

To further explore the existence of such ions, SEM and EDS analysis was carried out. Fig. 4.7 shows the SEM and EDS analysis of the LNCF-90 electrode after electrolysis in real wastewater. The elements remain uniformly distributed; however, the point analysis reveals the presence of other ions on the electrode surface after testing in real wastewater.

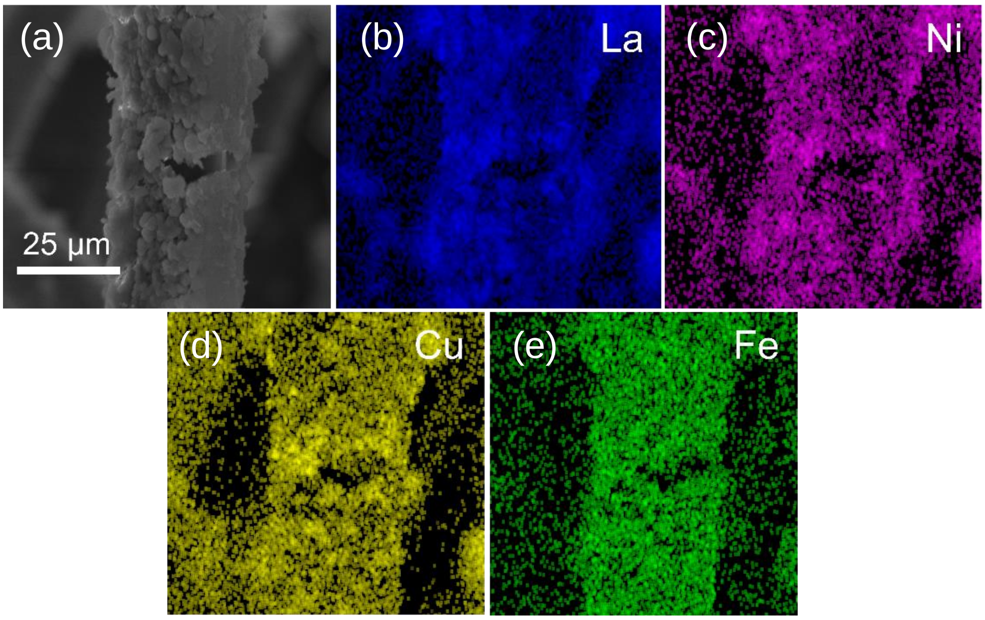

Fig. 4.7. (a) SEM of LNCF-90 electrode after test in real wastewater scaled to 25 µm bar. EDS of elements (b) La (c) Ni (d) CInd (e) Fe [69].

Hardness-causing elements such as Na, Mg, Ca and Cl were identified on the electrode surface which are commonly reported in real wastewater and landfill leachate. These may form an insulating layer on the surface of electrodes [321-325]. The distribution of such elements is mapped in Fig. 4.8 and reveals quite intense and homogenous dispersion across the electrode surface after testing in real wastewater. This indicates that the lower performance in real wastewater may be due to the presence of secondary ions which can lead to an insulating layer on the catalyst surface. If such an electrode were to be used for the removal of ammonia and treatment of real wastewater, cleaning procedures of the electrode or slight pre-treatment of hard ions in the water should be considered.

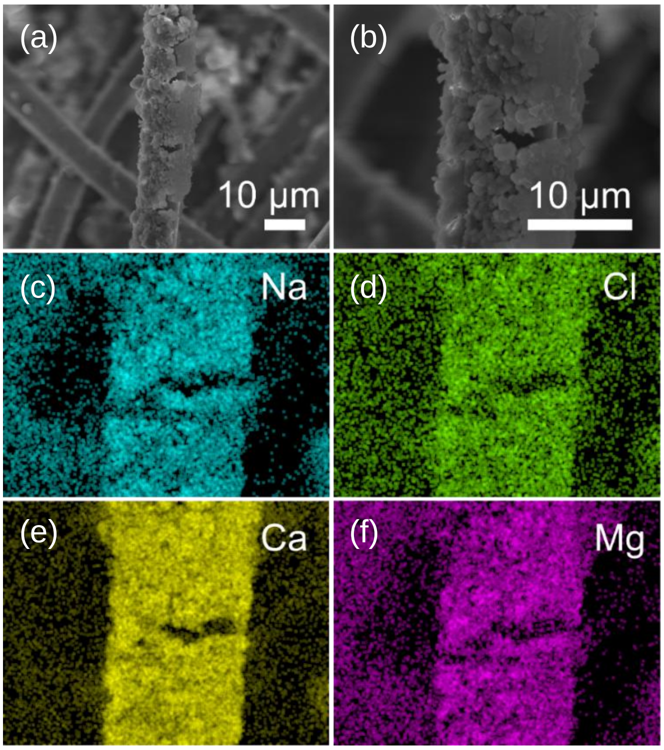

Fig. 4.8. (a) SEM imaging of LNCF-90 electrode after electrolysis test in real wastewater. (b) SEM imaging of LNCF-90 electrode after electrolysis test in real wastewater. EDS imaging of elements (c) Na (ICl (e) Ca and (f) Mg after electrolysis test of LNCF-90 in real wastewater [69].

It should be noted that ammonia can be removed by (i) direct oxidation and/or (ii) indirect oxidation of ammonia mediated by electro-generated active chlorine species [326]. Direct ammonia oxidation requires adjustment of wastewater pH to values greater than the pK_a of the NH_4^+/NH_3 acid-base pair ($pH > 9.25$) as NH_4^+ cannot be directly oxidised at the anode [326, 327]. This approach has been adopted in this paper due to ammonia oxidation reaction requiring alkaline environments [210]. However, it is often accepted that ammonia can undergo indirect oxidation which takes advantage of in situ active chlorine species in wastewater. A series of electrochemical reactions convert chloride ions present in solution into chloride radicals which then undergo a Volmer-Heyrovsky type reaction to form chlorine. Hydrolysis of chlorine leads to the formation of hypochlorous acid (HOCl) which is an effective oxidant and can react with ammonium ions to form N_2 or NO_3 ions [326, 328, 329]. The efficiency of the indirect mechanism is highly dependent on the pH of the electrolyte solution, with both highly acidic and highly alkaline environments adversely affecting HOCl formation [309]. Zhou et al. studied the effect of acidic, neutral and alkaline pH environments (5.16, 7.02 and 10 respectively) on treatment performances and the highest removal of NH_4^+ was obtained at pH 5.16 due to the presence of HOCl [330]. However, since the pH of the wastewater investigated within this study was adjusted to give very alkaline environments, the extent of hypochlorous acid and ammonium formation is considered to be reasonably low [309]. It is therefore assumed that the dominate oxidation pathway for the simulated and real wastewater samples tested in this study occur through a direct mechanism.

4.4. Perspective of Perovskites as Anodes

The above sections show how non-PGM-based electrocatalysts, like perovskite oxides, have been utilised to assist AOR, specifically in the context of ammonia electrolysers. Even though this material has not explicitly been implemented into a working DAFC, it shows great potential to alleviate PGMs at the anode site of such devices. Since the anode electrodes of both ammonia fed electrolysers and DAFCs rely on the ammonia oxidation reaction, it can be reasonably assumed that the catalysts utilised within these systems may be interchangeable.

Furthermore, this study demonstrates how perovskite oxides may be useful in wastewater treatment, making use of the high amount of ammonia content within landfill leachate. This paves way for potential applications of DAFCs in the wastewater treatment industry, where landfill leachate may be used as a suitable anodic fuel, converting energy from waste. The possibility of doing so has briefly been investigated by Zhang et al., who explored electricity generation from ammonia in landfill leachate using a DAFC and precious-metal-free electrodes [305]. This subsequently widens the scope of DAFCs, and this study highlights the potential use of perovskite oxides as catalysts for these applications.

Implementation of perovskite oxides into anode electrodes of DAFCs, however, requires further optimisation. As will be highlighted later in this thesis, proper catalyst layer design is important to truly optimise electrode-electrolyte interactions. This indicates that not only must the anode catalyst layer be active towards AOR, but must also possess adequate: (i) electronic conductivity, (ii) ionic conductivity and (iii) good chemical and mechanical stability.

Furthermore, it is important to recognise that the results presented in 4.3.2 show that the LNCF-90 perovskite oxide is active towards AOR in a batch testing environment of 0.5 M KOH + 55 mM NH_4Cl. These conditions are common for testing AOR activity, however, may not truly reflect activity of the catalyst in a working DAFC where the conditions vary. The latter typically employs highly concentrated ammonia solution at varying flow rates and backpressure. For example, the parameters used for the DAFCs in this study involve 7 M NH_4OH + 1 M KOH at a flow rate of 2 $mLmin^{-1}$ and backpressure of 3 bar. This may influence the electrocatalytic ability and stability, especially in the presence of additional impurities.

4.5. Conclusion

Although the content of this thesis predominantly focuses on the design and optimisation of DAFCs cathodes due to sluggish ORR kinetics, the role of AOR at the anode on overall cell performance must also be recognised. This chapter therefore provides insight into how perovskite oxides can be tailored to favour AOR and lays foundation for future work regarding implementation of such catalysts into working DAFC anodes. The key findings from this chapter are as follows:

(i) A series of A- and B-site modified $La_{1-y}Ni_{0.6}Cu_{0.4-x}Fe_xO_{3-\delta}$ (x = 0, 0.05 and 0.10; y = 0, 0.05 and 0.10) perovskite oxides were prepared by a Pechini method and tested towards ammonia oxidation.

(ii) An optimum Fe doping of x = 0.05 (LNCF-05) showed superior activity compared to its counterparts.

(iii) When A-site deficiencies were introduced into the catalyst, further enhanced oxidation performance and stability was achieved when y = 0.10 (LNCF-90) due to presence of oxygen vacancies.

(iv) The perovskite may be considered as a suitable alternative to PGM electrodes such as Pt/C.

(v) The catalyst was able to perform well in an ammonia electrolyser using both simulated and real wastewater, achieving a maximum removal rate of 95.7 % after 100 h operation in simulated waste.

(vi) The perovskite demonstrates AOR activity and shows efficiency in an electrolyser. Since the anodes of ammonia fed electrolysers and DAFCs both rely on AOR, the results imply that the perovskite has potential to act as an anode in DAFCs.

An efficient catalyst for ammonia oxidation was identified and this chapter paves the direction for future work in tailoring perovskite oxides, particularly those possessing an A-site deficiency, towards AOR. The influence of introducing Fe into the B-site and a slight A-site deficiency can be appreciated when comparing to similar materials found in literature. Zhang et al. found that when using $LaNi_{0.5}Cu_{0.5}O_{3-\delta}$, a current density of ~10 $mAcm^{-2}$ was achieved at 0.55 V vs. Ag/AgCl [151]. In this study, a current density of ~20 and ~50 $mAcm^{-2}$ was achieved when using $LaNi_{0.6}Cu_{0.35}Fe_{0.05}O_{3-\delta}$ and $La_{0.9}Ni_{0.6}Cu_{0.35}Fe_{0.05}O_{3-\delta}$ respectively under the same operating conditions, highlighting improved performance. Further investigation, however, is necessary before implementing such catalysts into real working DAFC anodes.

CHAPTER 5 Fuel Cell Design and Assembly

5.1. Background

Although electrode-electrolyte interactions are at the heart of fuel cell devices, the hardware components need to be properly assessed to ensure such interactions are not overshadowed by improper construction of the cell.

Currently, there is scarce literature regarding the precise nature and design of components used within fuel cell assemblies. These components play an important role in the overall durability, performance and cost of the device and are particularly important in DAFCs where compatibility with ammonia may be an issue. This extends to the entire balance of plant, where for example, pressure gauges commonly include brass, which is easily corroded and becomes brittle in the presence of ammonia. The choice of such materials used within DAFCs, such as current collectors, FFPs and interconnectors, can contribute to overpotential in the form of electron resistance as mentioned in Chapter 1. To truly exploit and optimise performance, proper design of the entire fuel cell must subsequently be considered.

The commercialisation of fuel cells remains limited due to challenges such as cost reduction, long-term durability and reactant delivery to the active sites [331, 332]. The latter is often a consequence of poor reactant mass transport to the reaction zone and plays a key role in the overpotential observed at high current density regimes of polarisation curves [331-334]. Non-uniform flow of fuel within flow channels can result in local starvation of reactants at the active sites of catalyst layers, which directly impacts cell efficiency and performance [333]. Enhanced mass transport is therefore imperative for even current density distribution, high power density and better fuel utilisation [331, 333-338]. An effective flow field design is consequently also crucial for fuel cell performance in terms of its concentration overpotential, and can alter its overall commercialisation process [333].

Several types of FFP designs such as parallel, serpentine and interdigitated channels have been proposed and developed over the past few decades, each of which have merits and shortcomings [331, 333, 336, 339, 340]. Parallel flow channels offer an easy and convenient design in terms of manufacturing. An illustration of parallel, serpentine and interdigitated flow fields are shown in Fig. 5.1. However, conventional straight parallel flow channels endure an uneven distribution of fluid [333, 339-341]. In the case of serpentine channels, however, the flow is forced to move through meandering paths that cover the entire active site and eliminates areas of stagnant flow [331]. Despite popularity, the pressure drop in single serpentine flow is high due to long path lengths as well as the likelihood of blockages and formation of slug and plug flows [333, 339, 342]. This may result in lowering the total efficiency of fuel cells and an increase in mechanical stress due to the high-pressure gradients between the inlet and outlet [333, 339, 343].

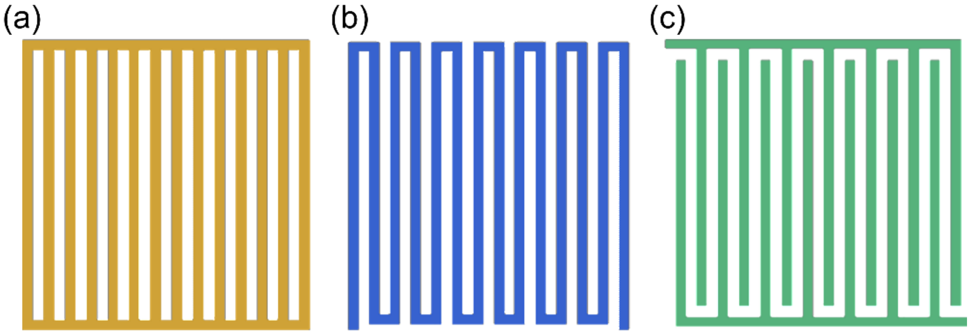

Fig. 5.1. Illustration of (a) parallel (b) serpentine and (c) interdigitated flow field patterns.

An effective method to improve fluidic distribution to the catalyst layer surface and promote uniform current density across the active area has involved tapering of channels and manifolds in FFPs [333-338]. However, these studies are often concerned with tapering in a single dimension, ignoring the effects of two-dimensional tapering which can provide efficient utilisation of space across the active area. Moreover, most studies focus on FFP designs suited towards PEMFCs where reactants are in gaseous phase, with current devices employing liquids simply utilising FFP configurations from PEMFC designs despite differences between gas and liquid properties such as viscosity [331, 333-338, 343, 344]. However, with growing interest in alternative fuel cells such as DAFCs, it is attractive to explore how FFPs are also suited towards liquid delivery [53, 58-62, 64, 76, 77]. The importance of mass transport therefore cannot be neglected and should be considered for efficient performance of DAFCs.

This chapter aims to explore and optimise the choice and design of fuel cell components to minimise their effects towards polarisation losses in the fuel cell and to provide a compatible and robust device. To truly exploit the intrinsic activity of catalysts and ensure that their performance is not overshadowed by poor mass transport to the active sites, this chapter also investigates the fluidic distribution of both gas and liquid across FFPs. The present work therefore establishes a route to an efficient fuel cell assembly.

5.2. Material Consideration

As mentioned above, the components of a fuel cell play a key role in its overall operation and stability. The devices therefore require a strong and robust build. For example, incorrect gasket thickness and end plate compaction can result in fuel leaks and insufficient fuel cell compression respectively. Proper design and assembly of fuel cell components is subsequently extremely important. The individual components are shown in Fig. 5.2 and will be carefully assessed and chosen based on their suitability, cost and compatibility with operating conditions.

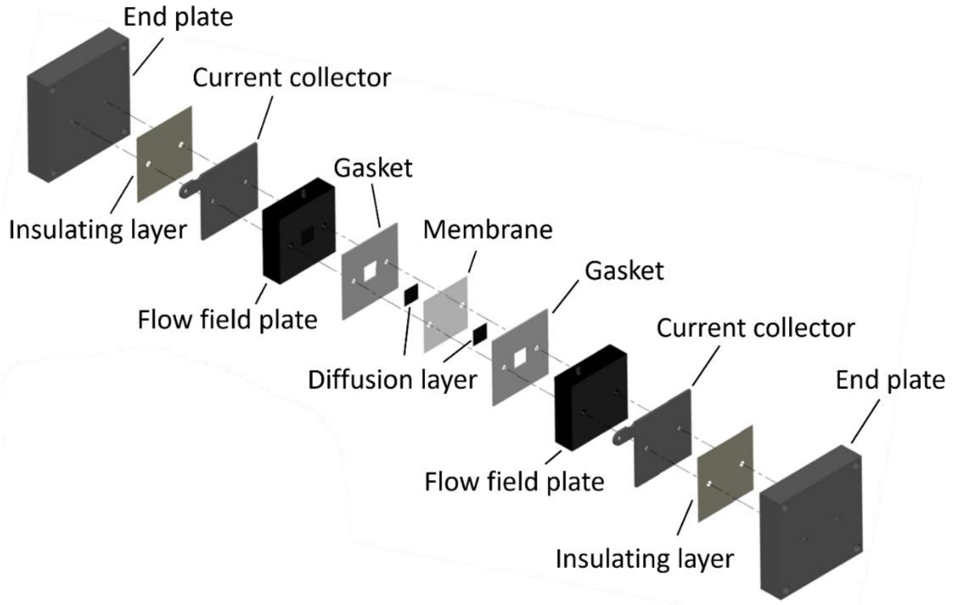

Fig. 5.2. Schematic illustrating individual components of a typical DAFC assembly.

As mentioned in Chapter 1, each conductive material has an intrinsic resistance ($\boldsymbol{R}$) to charge, exposing all electrochemical cells to ohmic overpotential ($\boldsymbol{\eta_o}$). Electrical resistances that arise from cell components like the electrolyte, catalyst layers, GDLs, FFPs, current collectors and interface contacts therefore have an effect on the overpotential [13, 15]. Subsequently, the entirety of the fuel cell build plays a role in cell performance. Henceforth, materials used within the DAFC must be carefully chosen.

5.2.1. End Plates

An uneven pressure distribution across the membrane electrode assembly (MEA) can lead to increased electrical contact resistance, non-uniform current density and uneven heat generation which can result in hot spot formation within the MEA [345, 346]. Mechanical compaction of end plates are consequently used for MEA compression and proper sealing of the cell. The main method to hold the fuel cell fixture in place tends to rely on bolts at the end plates which are torqued to a pre-set value that establishes a desired compression on the MEA without causing deformations [347].

Thick end plates are generally used to avoid an uneven pressure distribution, where the clamping pressure is adjusted to apply an appropriate pressure across the area [346-348]. There have been studies regarding the effect of clamping on parameters such as interfacial contact resistance and ohmic resistance [346, 349-353]. It has been recognised that large power losses within a PEMFC may be owed to contact resistance between FFPs and GDLs [354]. Increasing the applied pressure via end plate compaction can therefore increase the contact area between the FFP and diffusion layer media and decrease the overall contact resistance. However, it should be noted that excessive pressure may cause the diffusion layer, which is typically composed of carbon fibres that are soft and brittle, to become over-compressed which would result in decreased porosity within the layer [346, 354]. A similar concept can be applied to DAFCs, signifying the importance of end plates. Correct adjustment of the applied pressure via end plates is particularly interesting in DAFCs, since an extreme amount of compaction may lead to puncturing of the thin membranes that are often used in these devices.

Ultimately, end plates should be designed in such a way that they satisfy fuel cell conditions and provide sufficient clamping pressure. Metallic plates such as stainless steel and aluminium are most commonly applied as end plates [346]. Due to the highly corrosive nature of ammonia, stainless steel, of appropriate thickness, was chosen as the end plate material within this study, largely owed to its high chemical resistance.

5.2.2. Current Collectors

The choice of current collector material is particularly important since this component can contribute to ohmic resistances due to electron resistances present within the conductive material, affecting the middle regime of polarisation curves. An ideal current collector should possess high electrical and thermal conductivity, high mechanical strength and corrosion resistance, low contact resistance, and be both easily manufactured as well as low costing. Based on the above criteria, current collectors are generally categorised into metallic and non-metallic materials. Amongst the choice of non-metallic materials, graphite has proven to be a good candidate owed to its high electrical and thermal conductivity, high corrosion resistance and low contact resistance. However, its poor mechanical strength often hinders its machining process, and its brittle nature limits its thickness to the order of several millimetres, increasing the size and weight of the material as well as the machining cost [356-359].

In order to overcome these limitations, metallic materials are often used. Unlike graphite, these materials maintain high mechanical strength, allowing for greater ease of machining and thinner plates to be used, reducing plate size, weight and cost. Metallic current collector materials include stainless steel, titanium and aluminium [359-361]. Amongst these, stainless steel is a popular candidate [356-359]. It should be noted, however, that long testing times often leads to corrosion of stainless steel which can increase the contact resistance. To avoid this, stainless steel can be coated with a highly conductive metal such as platinum or gold, but this significantly increases costs [356, 357, 359].

For the purpose of low cost, the current collector used within this study was a thin stainless-steel sheet. The current collector is sandwiched between the end plate and the FFP as shown in Fig. 5.2. To avoid electrical contribution from the metal end plates which may interfere with performance, a thin mica sheet was placed between the end plate and current collector to provide electrical insulation.

5.2.3. Flow Field Plates

FFPs are a crucial component of a fuel cell since they supply fuel to the MEA. Their design is therefore imperative since it contributes to both ohmic and concentration overpotentials, affecting the middle and high current density region of fuel cell polarisation curves as mentioned in Chapter 1. The MEA is sandwiched between two FFPs with good alignment and orientation, as seen in Fig. 5.2 [362]. These plates contain channels embedded within their fixtures that allow for easy exposure of fuel to the diffusion layer, which can then diffuse through and reach the catalytic sites for the relevant reactions to occur at the electrode-electrolyte interface. These plates must be sufficiently strong to withstand assembly and be fabricated from a good electronic conductor such as graphite or stainless steel. They must also satisfy various requirements such as gas and liquid permeability, electrical and thermal conductivity, mechanical strength, corrosion resistance, ease of manufacturing and low cost [362].

For this study, graphite was used as the FFP material since it is highly popular and possesses relatively high thermal conductivity which is important when testing at elevated temperatures. Channel design on even fluidic distribution across the active area, which in the case of fuel cells is the CL, has been investigated and is discussed in greater detail in section 5.3 of this chapter.

5.2.4. Gaskets

Fuel leakage can result in unused reactant and reduced fuel cell performance due to loss of reactant or fuel cross over. Leak tightness is therefore essential and can be improved by compression of the cell along with use of a good gasketing material. Many types of gasketing materials have been proposed for use within fuel cells. Several requirements such as long-term chemical and thermal stability, electrical insulation between components, excellent sealing capacity, prevention of fuel mixing, vibration and shock resistance and low cost must be considered [363]. These parameters are often difficult to satisfy simultaneously and common gasket materials for low temperature fuel cells generally fall under two main categories: compressible, such as ethylene propylene diene terpolymer (EPDM) rubber, and incompressible, such as silicone and PTFE [347, 363].

Compared to PTFE, silicon and EPDM provide good compressibility and subsequent tightness. These materials are often cheap to source and easy to shape into the desired gasket [363]. Often, the choice between EDPM and silicone as a gasketing material is based on user discretion and studies have been conducted on the degradation of gasketing materials where impurities may contaminate the MEA [347, 364-368]. EPDM is generally considered best for gas tightness; however thin sheets may not be readily available. In smaller cells at ambient pressure, soft gasketing materials such as silicon work well for sealing. In larger pressurised cells, however, such material can become deformed under compression and potentially block flow. To overcome this, the use of more rigid gasket materials, use of bridging pieces to cover flow channels, or machining flow channels with a deeper width and depth may be useful [363].

Apart from material choice, the thickness of the gasket also plays a key role in fuel cell build [347]. The gasket thickness ultimately decides how much the FFPs can pinch into the electrode. To ensure good contact and consequently low resistance, it is imperative that the gasket thickness is chosen such that it is equal to the individual electrode thickness minus the desired pinch.

For this research, silicone rubber was chosen as the gasket material since relatively thin sheets are obtainable and the work within this project focuses on smaller cells where silicone works well. As well as providing the correct thickness required for this study, it is cheap, readily available, and chemically resistant to ammonia solution.

5.3. Numerical Methodology

As mentioned in Chapter 1, concentration overpotential ($\boldsymbol{\eta_c}$) is caused by the concentration gradient profile that develops between the bulk electrolyte and electrode surface due to slowness in the mass transport mechanisms [11]. Due to such limitations in mass transport, reactants and products cannot efficiently flow to and from reaction sites respectively [11, 12]. These concentration losses can be minimised by optimising mass transport within fuel cell electrodes, where the flow structures can provide sufficient pathways for reactants and/or products to diffuse to/from the electrode surface [13]. Subsequently, the precise design of FFPs, which are the physical structures that supply fuel to and from the active sites, are particularly important for efficient cell operation and must be considered. Section 5.2. identified graphite as a promising material for FFPs and allows for ease in machining. The following section therefore looks at how to manipulate the flow structure that is embedded in such graphite FFPs and uses both theoretical and practical approaches to validate the design.

5.3.1. Numerical Procedure

COMSOL Multiphysics 5.3 was used to model the three-dimensional FFPs. Navier-Stokes equations were solved for the boundary conditions of the inlet, outlet and walls. A tetrahedral meshing was used. The x, y and z directions were along the manifold, channels and vertical to the active area respectively.

The boundary conditions applied to the numerical model involves uniform velocity of incoming fluid and a laminar flow profile being established before interaction with the structural elements of the model.

Due to the complexity of the modelling software and the prerequired knowledge to run theoretical simulations, the matrix and models were prepared by Professor Andre van Veen. My contribution to this section of work involved adjusting parameters such as the nature of the fluid, flow rates and tapering ratios of the manifolds as well as image processing and interpreting data.

5.3.2. Governing Equations

The mathematical model developed in this study assumes that (i) the reactant fluid is incompressible, (ii) no slip boundary conditions are imposed to the flow field walls and (iii) laminar flow is established.

Based on the above, fluidic flow through the channels was simulated by solving Navier-stokes equations. The relevant conservation equations are described below.

The mass conservation equation is expressed as follows:

$$\frac{\partial \rho}{\partial t} + \nabla \cdot \rho\left(\vec{V}\right) = 0 \qquad (5.1)$$

Where ρ is the density, t is time, ∇ is the gradient operator and $\vec{V}$ is the velocity of the fluid.

The momentum conservation equation is expressed below. Since the density of the fluid remains constant, the equation can be simplified for incompressible three-dimensional flow:

$$\rho \frac{\partial V}{\partial t} = \rho g - \nabla p + \mu \nabla^2 V \qquad (5.2)$$

Where g is the gravitational acceleration, p is an unknown and μ is the viscosity coefficient.

It should be noted that the above time dependent components convert to zero in the simulations as steady state is assumed.

By tapering the FFP manifolds in both height and width, a constant change in cross-sectional area with respect to length can be implied. The geometry of the manifolds can therefore be assumed to behave similarly to that of a cone, where the cone can be considered as a series of cylindrical pipes with varying radii as shown in Fig. 5.3.

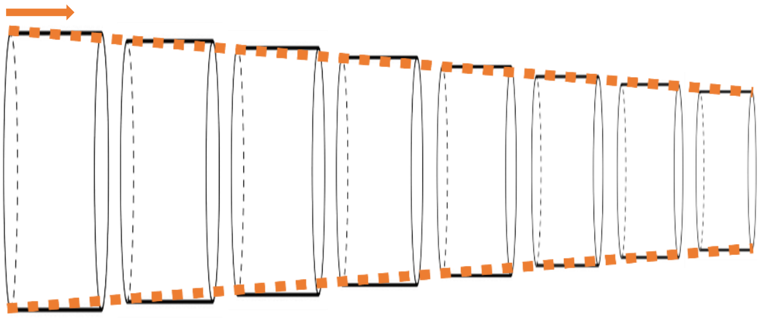

Fig. 5.3. Illustration demonstrating how a cone can be considered as a series of cylindrical pipes with varying radii and an arrow to illustrate direction of flow.

Considering the geometry as a cylindrical pipe, the Navier-Stokes equations can be exploited to derive the Hagen-Poiseuille equation which provides insight into the pressure drop through a cylindrical pipe of constant cross section [369]. The equations governing Hagen-Poiseuille flow assume that: (i) the flow is steady, (ii) the radial and azimuthal components of the fluid velocity are zero, (iii) the flow is axisymmetric, and (iv) the flow is fully developed. The Hagen-Poiseuille equation is expressed as follows:

$$\Delta p = \frac{8\mu L Q}{\pi R^4} = \frac{8\pi\mu L Q}{A^2} \tag{5.3}$$

Where Δp is the pressure difference between two points along the pipe, μ is the dynamic viscosity of the liquid, L is the length of the pipe, Q is the volumetric flow rate, R is the pipe radius and A is the cross section of the pipe.

In a cone geometry, a dead end would result in ideal fluidic distribution to any subchannels along the length of the cone. However, an infinitesimally small cross-sectional area would introduce practical limitations to and would ultimately restrict flow at the end. The design and size of the upper and lower regions of the cone must be scaled according to the scenario. This is discussed in further detail in section 5.4.

5.3.3. Material Selection

Based on section 5.2, material selection for the individual cell components was carefully considered for this study. The components and their respective parameters are listed in Table 5.1.

Table 5.1. Properties of fuel cell components.

Component	Parameter	Value	Unit
Endplate	Thickness	18	mm
Insulating layer	Thickness	0.2	mm
Current collector	Thickness	2	mm
	Electrical conductivity	1.33×10^6	$S\ m^{-1}$
	Thermal conductivity	15	$W\ m^{-1}\ K^{-1}$
Flow field plate	Thickness	18	mm
	Electrical conductivity	1×10^6	$S\ m^{-1}$
	Thermal conductivity	85	$W\ m^{-1}\ K^{-1}$
Gasket	Thickness	1	mm

These were inputted into the simulation software to model the parameters of a realistic fuel cell.

5.3.4. Computational Domain

According to literature, enhancing flow uniformity in the channels of parallel FFPs leads to an increase in power and lowering of resistances owed to pressure gradients. Many techniques have been proposed to do so including the modification of channels, manipulating the inlet and outlet manifolds and embedding baffles into the flow field [333]. It should be noted that these studies exploit a readily available package that can simulate the relationship between fluidic distribution and the current densities obtained in PEMFCs due to the large amount of data available on PEMFCs. Such a package, however, is not available for DAFCs, since they operate under different parameters and catalysts. Simulations regarding the corresponding current densities obtained within these systems would therefore be challenging and outside the scope of this study. It can be logically assumed, however, that efficient delivery of reactants in a uniform manner would also lead to improved current densities and cell performances in DAFCs, as this is based on fundamental concepts such as mass transport.

This study exploits the simplicity of parallel FFPs (PFFPs) and tapers the inlet and outlet manifolds in both height and width to provide a more uniform flow, whilst effectively utilising space across the active area. The active area includes the tapered inlet and outlet manifolds as well as the sub channels. This arrangement maintains a constant active area size in all scenarios discussed in the study, allowing for easy comparisons. Three different PFFP designs were explored: (i) a conventional parallel flow field plate with no manifold tapering simply denoted as PFFP, (ii) manifold tapering in one (width) dimension (PFFP-1D) and (iii) manifold tapering in two (height and width) dimensions (PFFP-2D).

The domains of three-dimensional PFFP models used within this study consist of a graphite block with inlet and outlet feeds connecting to the central flow design. The block was modelled with dimensions of 5 x 5 x 2 cm with an active flow field area of 5 cm^2. The width and depth of each channel and the width of each rib was 1.13 cm in all flow field designs.

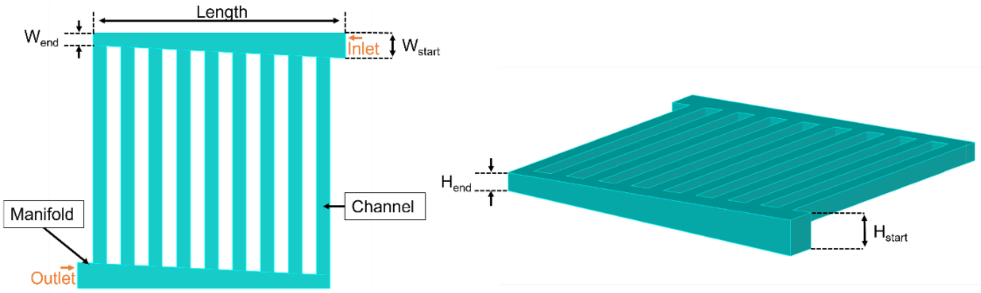

Fig. 5.4. Schematic view of PFFP-2D illustrating parameters described in the study.

The manifolds were tapered to improve uniformity of fluidic distribution over the active area. The start width of the manifold was two times larger than that of the end for the PFFP-1D model. For the PFFP-2D scenario, both the start height and width of the manifold was two times larger than that of the end. Precise details of the PFFPs are tabulated in Table 5.2.

Table 5.2. Dimensions of the flow fields.

Parameter	Value (mm)	Unit
Length	22.5	mm
Channel height	1.13	mm
Channel width	1.13	mm
Rib width	1.13	mm
W_{start} (PFFP)	1.13	mm
W_{start} (PFFP-1D)	2.25	mm
W_{start} (PFFP-2D)	2.25	mm
W_{end} (PFFP)	1.13	mm
W_{end} (PFFP-1D)	1.13	mm
W_{end} (PFFP-2D)	1.13	mm
H_{start} (PFFP)	1.13	mm
H_{start} (PFFP-1D)	1.13	mm
H_{start} (PFFP-2D)	2.25	mm
W_{end} (PFFP)	1.13	mm
W_{end} (PFFP-1D)	1.13	mm
W_{end} (PFFP-2D)	1.13	mm

The above is a preliminary model which is useful to observe the effects of tapering manifolds on the fluidic distribution as it provides a relatively large active area to examine. However, since the final project under investigation is concerned with laboratory scale, simulations regarding a smaller active area were also run to confirm that the observed phenomena also hold for laboratory scale experiments. Smaller active areas of around 1 cm^2 are logical for laboratory scale experiments as they promote less waste of catalytic materials in the initial testing stage before scale up. For these laboratory scale simulations, models with dimensions of 5 x 5 x 1.8 cm were used, with active areas of 1 cm^2. The width and depth of each channel and the width of each rib was 0.5 mm in all flow field designs. Other parameters for the PFFPs in these cases were rescaled appropriately based on Table 5.2.

5.3.5. Physical Assumptions

All simulations had the same operating conditions. The temperature was set to 293.15 K and the absolute ambient pressure at 1 atm. Water was used to represent the liquid fluid since ammonia solution for real DAFCs is dissolved in water. This can therefore be assumed to be reasonable. Air was used as the gas in the study since this is the oxidant for the final DAFC. Other parameters are listed in Table 5.3.

Table 5.3. Physical properties used in the simulations.

Parameter	Value	Unit
Air density	1.204	kg m^{-3}
Air dynamic viscosity	18.5	μPa s
Air flow	100	mL min^{-1}
Water density	0.997	kg m^{-3}
Water dynamic viscosity	1	mPa s
Water flow	5	mL min^{-1}
Ambient temperature	293.15	K
Absolute ambient pressure	1	atm

For the laboratory scale simulations, the parameters were adjusted to closely match those which would be later used in real experiments. The flow rates at the inlets of the anode and cathode were 2 mL min^{-1} and 180 mL min^{-1} respectively. The remaining parameters in Table 5.3 were kept constant.

It should also be noted that although this study makes use of flow field design methods from PEMFCs, PEMFCs and DAFCs are based on different chemistry. Use of the latter alleviates some of the problems associated with PEMFCs. PEMFCs often experience difficulties associated with flooding and water management due to the formation of water that occurs on the reaction of hydrogen and oxygen. Water droplet formation and two-phase flow regimes are therefore frequently explored for the performance of these systems [333, 370, 371]. In DAFCs, however, the anodic stream is ammonia solution, so water management is not an issue as the site is already submerged in an aqueous environment. Furthermore, the oxidant is humidified air or oxygen since cathode depends on the reaction between oxygen and water (as seen in Eq. (1.4)). Since the oxygen is introduced into the cell humidified, it can be assumed that the presence of water droplets at the cathode is negligible. Thus, it is reasonable to consider single phase regimes in these models.

5.3.6. Experimental Validation

To verify the predicted fluidic distribution, experiments were conducted on 3D printed models based upon the parameters of the PFFP, PFFP-1D and PFFP-2D designs used in the simulation section. Fluorescein disodium salt solution was used as a dye to visually monitor the fluidic distribution and fed through the channels at a flow rate of 5 mL min^{-1} using a HPLC pump. The effect of the dye on water viscosity was assumed to be negligible. Water was used to flush the channels at a flow rate of 5 mL min^{-1} using a peristaltic pump. The larger 5 cm^2 active area designs were used for the 3D printed models for visual ease. A photograph of the setup is shown in Fig. 5.5.

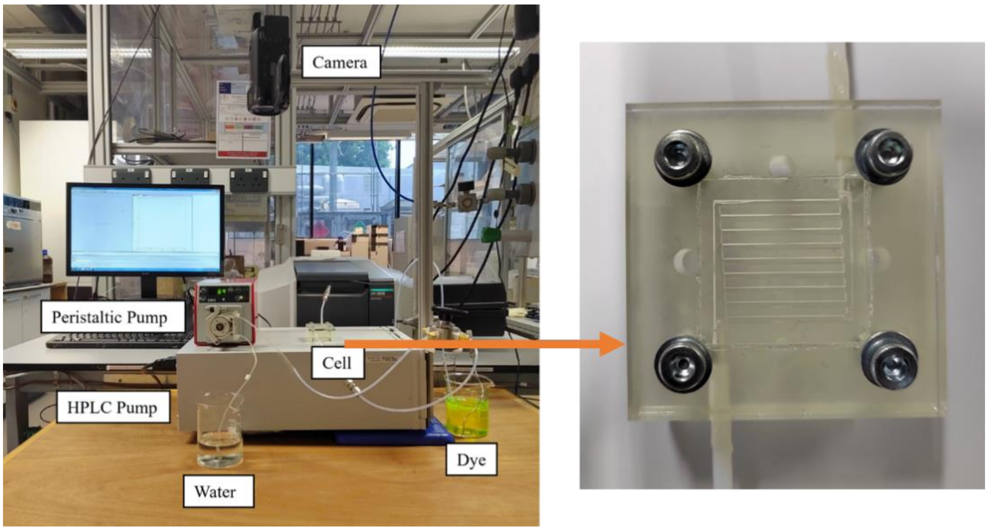

Fig. 5.5. Experimental set up (left) and PFF-2D acrylic cell (right).

To prevent leaking, silicone sealant was used to sandwich the block and a laser-cut acrylic sheet of 6 mm acted as an endplate. This allowed for the PFFP designs to be observed through a transparent endplate. The cells were photographed by a digital camera (Panasonic HC-V770) to capture the flow patterns.

5.4. Result and Discussion

The study investigates how PFPP patterns influence fluidic distribution at the active sites of fuel cell devices, particularly DAFCs, which is especially important to reduce concentration overpotential and reduce mass transport resistances. The following section looks at how tapering of the manifold in such PFFPs can be used as a powerful design tool for uniform flow. Although tapering manifolds in one dimension has been reported in literature, the effects of tapering in two dimensions (both height and width) have not been explored. The pressure contours and velocity field profiles for all models (PFFP, PFFP-1D and PFFP-2D) will be presented below. Investigation into the scale factor applied when tapering manifolds will also be shown to further refine the design. Then, a visual experiment of the flow distribution will be given to verify theoretical results.

5.4.1. Effects of Manifold Tapering

The pressure contours for the PFFP, PFFP-1D and PFFP-2D models fed with air are shown in Figs. 5.6a-c. Fig. 5.6a demonstrates that for the PFFP model, an overall pressure gradient of approximately 10 Pa over the active area is observed. This is reduced 50 % in the PFFP-1D model, and further reduced by approximately 75 % in PFFP-2D, with a difference of around 3 Pa between the pressure between the inlet and outlet manifold feeds.

The results highlight the impact of efficient tapering design on pressure gradients across the flow field area. In the context of fuel cells, lowering the pressure gradients between the inlet and outlet feeds reduces mechanical stresses experienced by the MEA [333, 339, 343]. This is particularly important for DAFC which employ thin (μm) polymeric membranes and may be susceptible to puncturing under high pressure gradients. Notably, there is a diagonal pattern of pressure drop across the entire active area for the PFFP-2D model, this is indicative of even flow distribution.

Figs. 5.6d-f shows the velocity distribution for the PFFP, PFFP-1D and PFFP-2D models fed with air. In agreeance with literature, the conventional PFFP model shows a non-uniform distribution across the channels of the CL, reinforcing that this phenomenon is dominant and limits the application of traditional parallel flow field patterns. There is a strong tendency for the fluid to initially flow down the end channel. In Fig. 5.6e, the PFFP-1D design shows great improvement in flow distribution. This agrees with previous studies that have investigated the effects of tapering in one-dimension and reinforces the concept of tapering manifolds as a useful way to manipulate fluidic flow within these systems [372]. Despite the velocity profile demonstrating greater homogeneity, the relative flow velocities at the end channels remain greater than those along the middle channels, exposing areas of design improvement. When tapering in two-dimension, Fig. 5.6f reveals that the PFFP-2D design shows substantial improvement in flow uniformity across all channel paths. The simulations therefore suggest that PFFP-2D demonstrates superior design in terms of pressure and velocity profiles.

Uniform fluidic distribution offered by the PFFP-2D design is significant for fuel cell performance as it indicates an even supply of reactant to the active sites of the catalyst surface, which influences interactions at the electrode-electrolyte interface of DAFCs. This is imperative for reducing mass transport limitations and signifies that the above is an important design element for better fuel cell performance.

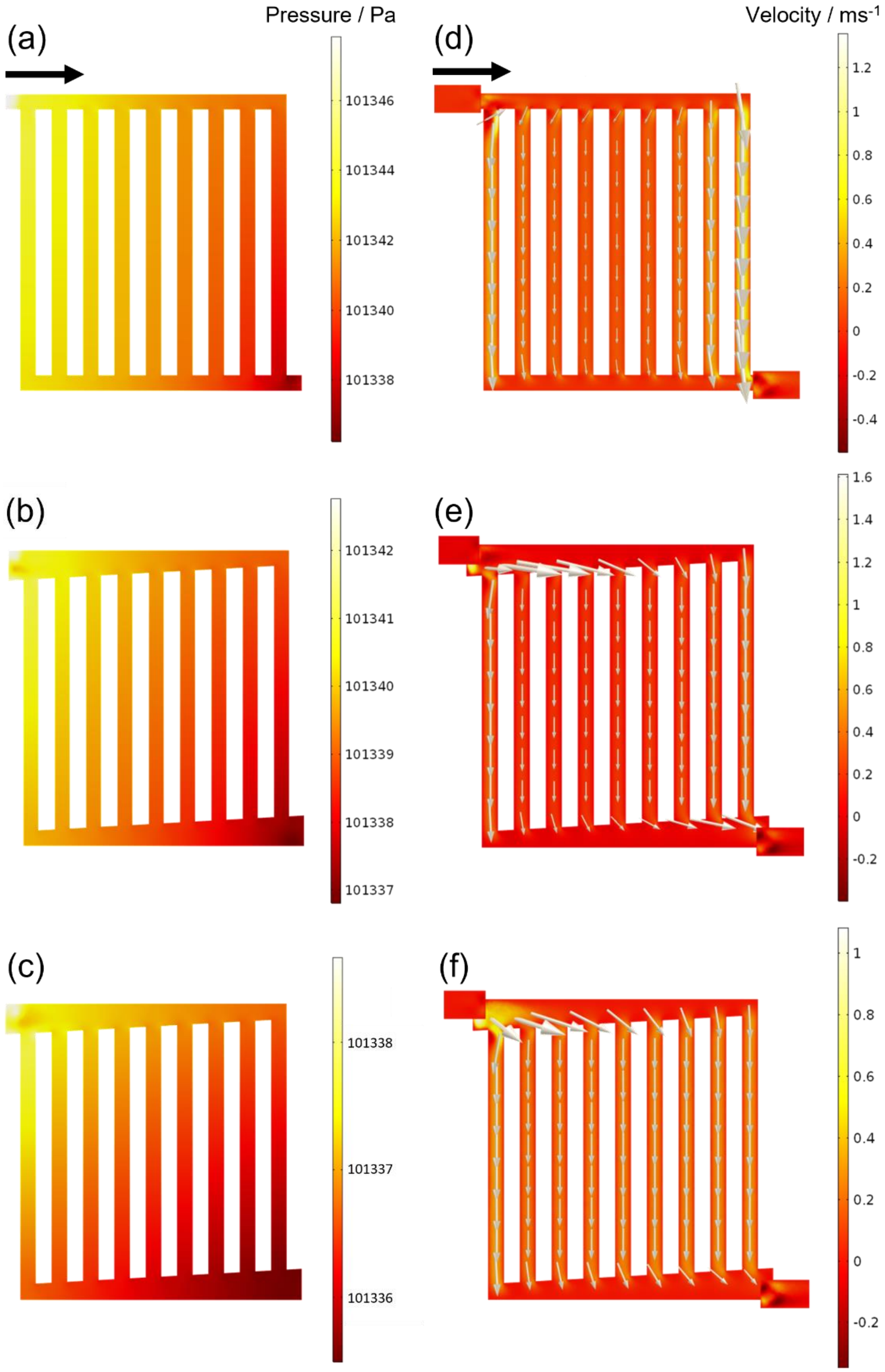

Fig. 5.6. Pressure contours for different FFPs fed with air at the cathodic site: (a) conventional PFFP, (b) PFFP-1D and (c) PFFP-2D. Velocity fields for different FFPs fed with air at the cathodic site: (d) conventional PFFP, (e) PFFP-1D and (f) PFFP-2D. The arrow represents the direction of flow.

Unlike traditional studies on FFP design which are based on conventional PEMFCs, DAFCs employ liquid ammonia rather than gaseous hydrogen as the anodic fuel. To investigate the differences in behaviour when liquid is employed as the fluid, simulations were also run with water being introduced at the inlet. The pressure contours for the PFFP, PFFP-1D and PFFP-2D models fed with water are shown in Figs. 5.7a-c.

Fig. 5.7a demonstrates that for the PFFP model, a pressure drop of 22 Pa over the active area is observed. This is reduced to 11 Pa in the PFFP-1D model, and further reduced to 6 Pa in PFFP-2D. The results reveal that in a PFFP design where two-dimensional tapering is introduced, there is a pressure drop around 70 % less than that of a simple PFFP with no tapering.

Although the absolute pressures observed within the liquid and gas fed simulations differ, the overall trend in both cases remains consistent such that there is a clear drop in pressure gradient (~ 70 %) across the entire active area when the PFFP-2D model is implemented. Again, this is particularly useful for DAFCs and provides insight into the configuration of FFPs in the final cell assembly. The results suggest that the FFPs should be placed in such a way that the liquid and gas streams run parallel but opposite to one another, to balance the pressure gradients and reduce stress on the membrane.

The velocity distribution for the PFFP, PFFP-1D and PFFP-2D models fed with water are shown in Figs. 5.7d-f. Like above, the absolute velocity values deviate between the gas and liquid fed simulations, however the same overall trend remains. In the conventional PFFP case, there is a strong tendency for water to flow down the end channel. When tapering in one-dimension, this effect is improved, and is further improved when two-dimensional tapering is introduced.

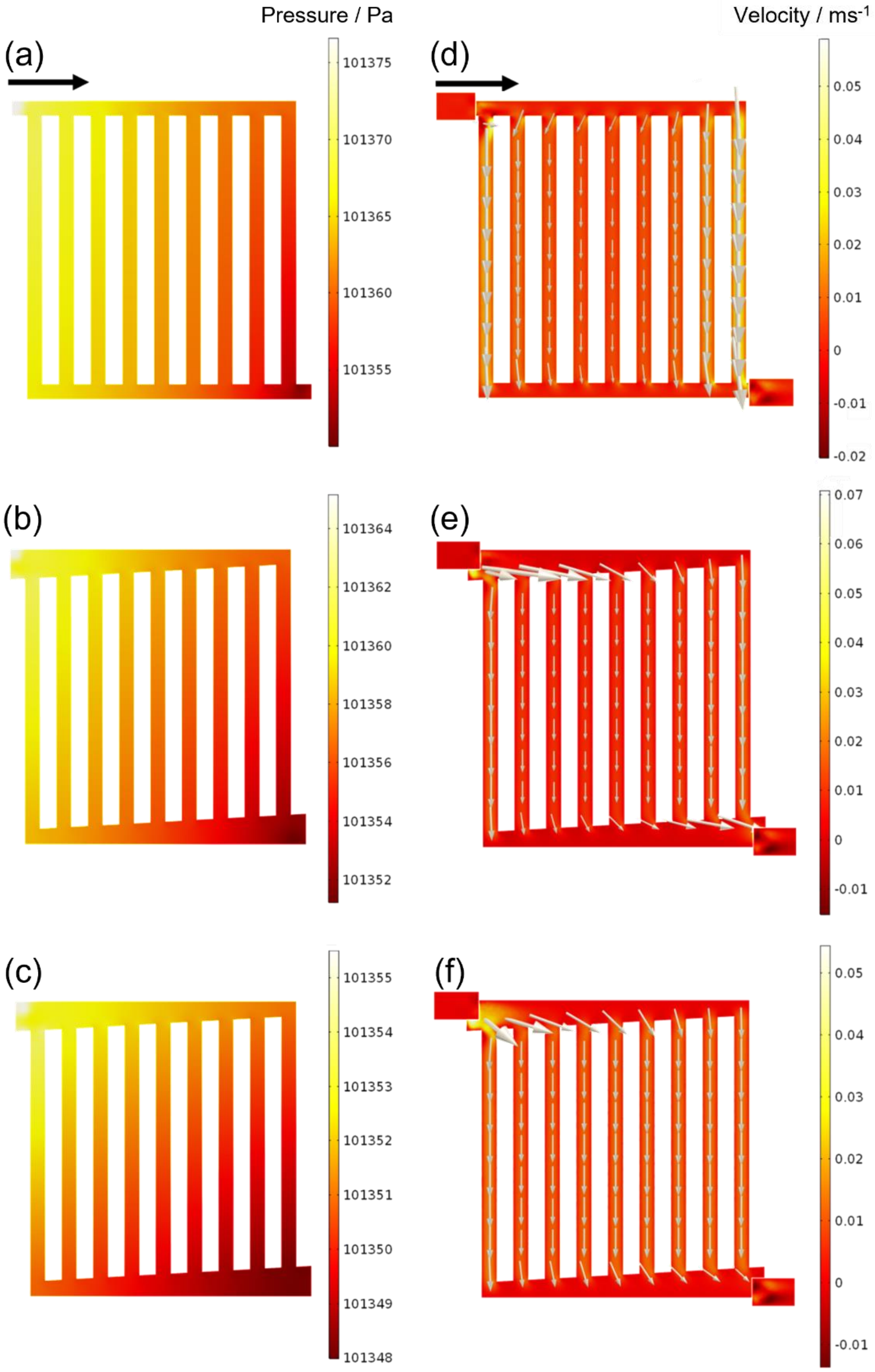

Fig. 5.7. Pressure contours for different FFPs fed with water at the anodic site: (a) conventional PFFP, (b) PFFP-1D and (c) PFFP-2D. Velocity fields for different FFPs fed with water at the anodic site: (d) conventional PFFP, (e) PFFP-1D and (f) PFFP-2D. The arrow represents the direction of flow.

The results suggest that regardless of the fluid properties, tapering the manifolds of PFFPs in two-dimensions significantly improves fluidic distribution over the area specified and is predicted to be a powerful route to manipulate the delivery of reactants to the active sites of electrode-electrolyte interfaces. Since an increase in reactant transfer and uniform distribution to the electrode catalyst surface has been noted to improve current densities and power densities of fuel cells, PFFP-2D can be assumed to play a significant role towards enhancing DAFC perform.

5.4.2. Extent of Manifold Tapering

Since the effects of tapering in both width and height has shown to display superior activity, the extent of tapering should also be regarded. Currently, the simulations consider an arbitrary scaling of 2:1 between the inlet and outlet feeds respectively. However, other ratios have not yet been considered and are necessary for the design process. Since the flow trends between the gas and liquid fluids remain similar, the following simulations and experiments simply consider liquid as the fluid. The same conditions as those used in section 5.4.1 are applied here.

As mentioned earlier, the tapered manifold can be theorised to behaviour similarly to a cone, in which case a dead end would obtain ideal fluidic distribution to the connecting channels along the length of the cone. However, an infinitesimally small cross-sectional area at the end introduces physical limitations to the design and would ultimately restrict flow at the end. The lower boundary of the manifold dimension is therefore fixed to the size of the channel feed, in this case, 1.13 mm. This implies that the upper boundary of the tapered manifold can be manipulated and scaled accordingly. To investigate the scaling ratio, three scenarios are presented below. Scale factors between the upper and lower boundaries of 1.5:1, 2:1 and 3:1 were implemented and the simulations are shown Fig. 5.8.

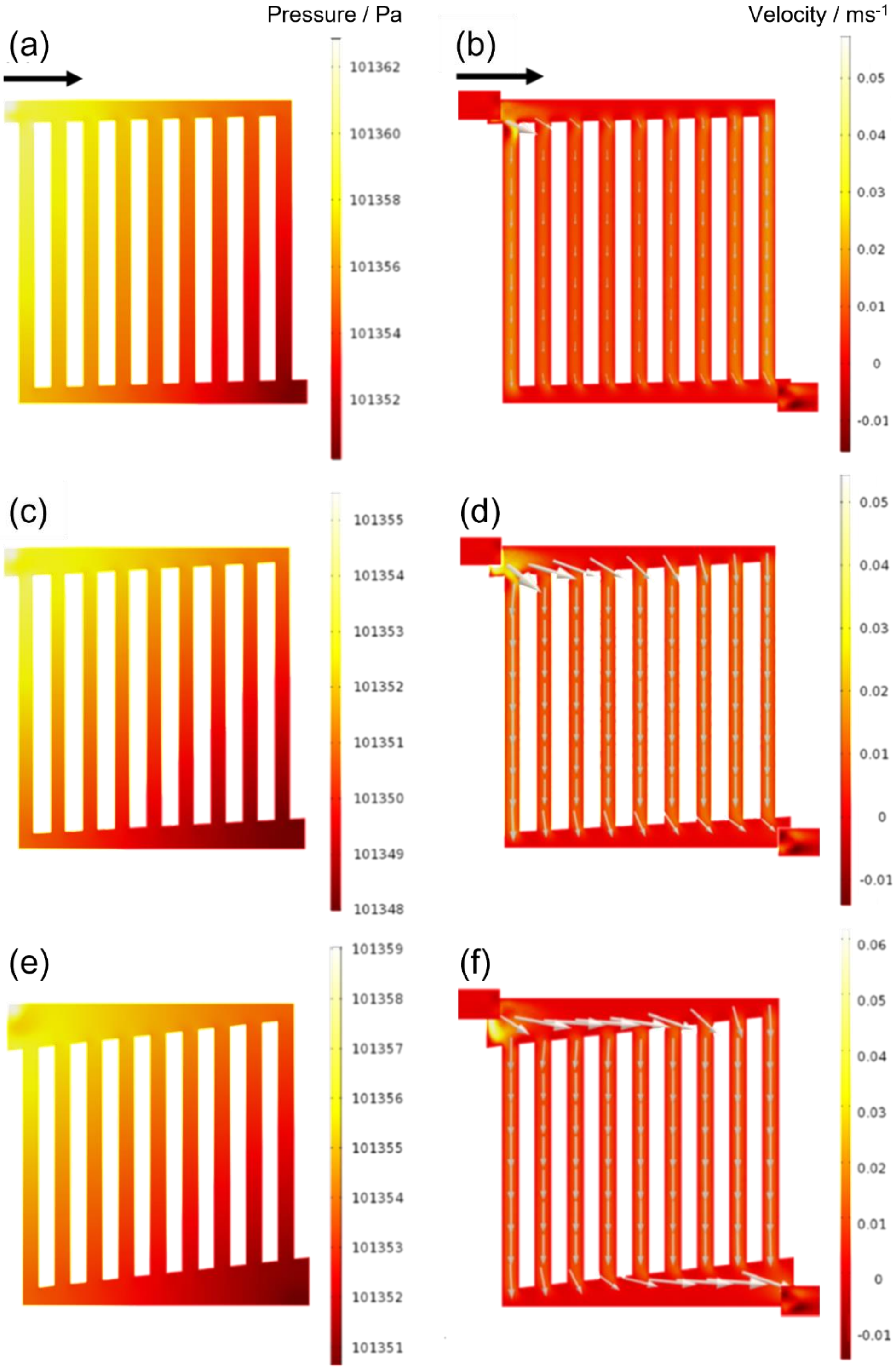

Fig. 5.8. Pressure contours (a) and velocity profile (b) for PFFP-2D with tapering scale factor of 1.5:1. Pressure contours (c) and velocity profile (d) for PFFP-2D with tapering scale factor of 2:1. Pressure contours (e) and velocity profile (f) for PFFP-2D with tapering scale factor of 3:1. The arrow represents the direction of flow.

When the scale factor is fixed to 1.5:1, the pressure gradient and velocity profiles show minimal improvement and mostly resemble behaviour that is similar to that of the conventional PFFP. The velocity field reveals that the fluid again prefers the route of the end channels compared to the middle channels, highlighting an uneven fluidic distribution. This demonstrates that a relatively small tapering scale factor is not sufficient to greatly deviate flow behaviour from a simple PFFP.

It can be reasonably assumed that by further increasing the scale factor, the above effects would be less prominent. As the scale factor increases to 2:1, there is notable difference in the pressure contour map and velocity profile. As discussed in section 5.4.1, there is significant improvement in the fluidic distribution, signifying that the extent of manifold tapering also plays a key role in the flow path.

When the scale factor is further increased to 3:1, there is further improvement in the pressure gradient and velocity field profiles. The results demonstrate that as the scale factor between the upper and lower boundary increases, the performance improves. However, the change between that of 3:1 and 2:1 can be considered minimal, with both scenarios offering considerably uniform distribution across the CL.

Since the difference between uniform distribution in the latter two models is minimal, a trade-off between the fluidic behaviour and practicality of the design must be acknowledged. When a scale factor of 3:1 is employed, the manifold fills a considerable fraction of the active site. For this reason, a greater manifold tapering can be considered inefficient in terms of space utilisation. Subsequently, a 2:1 scale ratio is satisfactory in providing both uniform distribution and a compact design without compromising flow.

5.4.3. Testing in 3D models

To bridge the gap between theoretically and experimentally obtained results, 3D models of the PFFP, PFFP-1D and PFFP-2D designs were printed based on the simulation parameters. A series of experiments were conducted to visually observe the flow pathways in the designed PFPPs. A bright fluorescent dye, fluorescein disodium salt solution, was used to aid in tracing of the fluid. Since the simulations employ an active area of 5 cm^2, the same active area size was used in the 3D printed model, as this allows for easy visualisation and tracking of the distribution pathway. The flow rate was also kept consistent with the simulation parameters.

Fig. 5.9 displays the flow patterns of fluorescein disodium salt solution in the 3D printed PFFP, PFFP-1 and PFFP-2D models. Each still image is taken at the same timeframe for consistency and easy comparison between the individual scenarios.

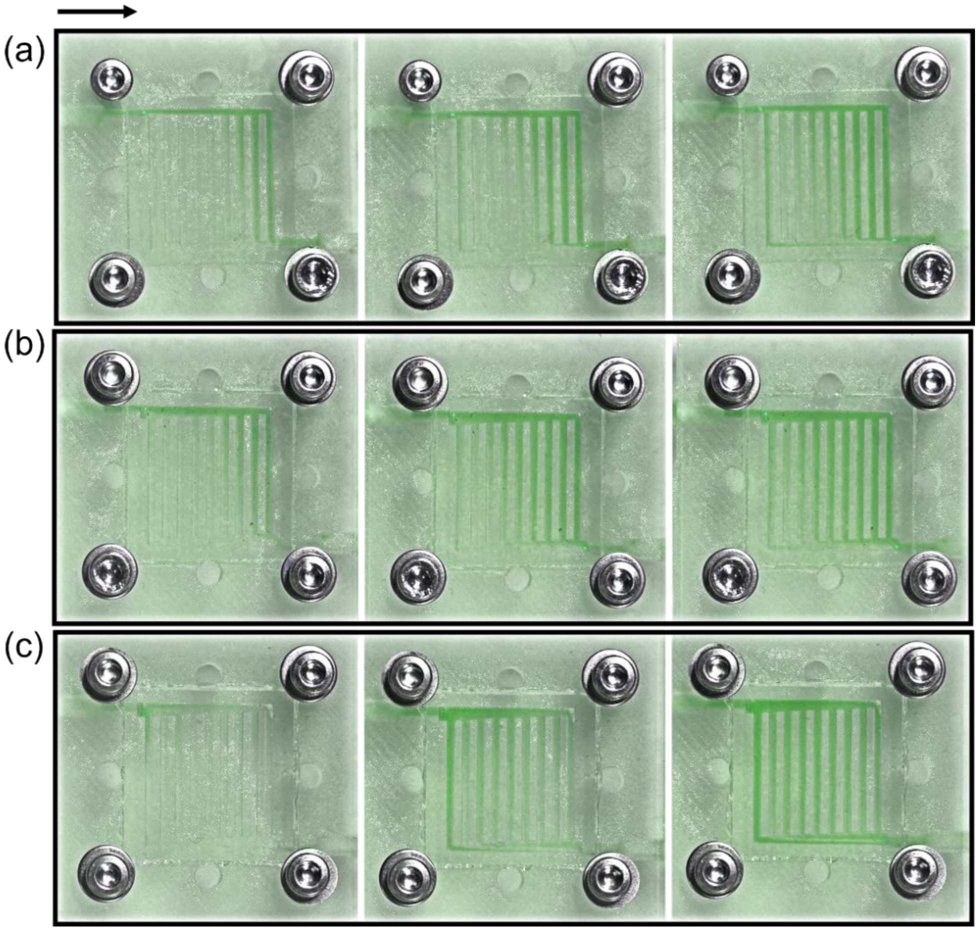

Fig. 5.9. Flow patterns of fluorescein disodium salt solution through the 3D printed (a) PFFP, (b) PFFP-1 and (c) PFFP-2D models. The arrow represents the direction of flow.

Flow distribution of the dye through the simple PFFP model reveals that the dye had an initial tendency to flow down the end channel. The second photograph shows that the fluid then takes the path of the channel closest to the inlet before slowly filling the middle channels. This is in agreeance with the results obtained from the simulations in section 5.4.1. Subsequently, in the middle region, particularly towards the inlet feed, there is scarce fluid delivery compared other zones of the active area. In context of fuel cell performance, these findings reinforce that there is poor reactant mass transport across the entirety of the reaction zone which can give rise to local starvation of reactants at the active sites of catalyst layers [331-334].

Although to a lesser extent, the flow in the PFFP-1D model follows the same overall trend, with the end channel being the preferred path. This also agrees with the findings acquired through the simulations above and shows that although uniformity in fluid distribution remains tricky, there is an improvement evidenced by the smaller fraction of undelivered dye.

In large contrast, Fig. 5.9c highlights that the dye follows a different path when the manifolds are tapered in two-dimensions. Instead of showing a strong preference to flow down the end channel, as was seen in the former two models, the flow begins diagonally filling across the channels and provides a more even distribution. At the same timeframes captured between the three designs, the PFFP-2D 3D printed model shows that the fluid is not only more evenly distributed, but also fills the entire active area quicker. The experimental analysis shows strong agreement with the predictions of the simulated models, reinforcing the advantages of two-dimensional manifold tapering in flow field designs.

It should be noted however, that these experiments illustrate the flow of fluid when the flow field plate is placed horizontally. However, different behaviour may be expected in the working final fuel cell configuration since such cells are placed in a vertical configuration. This may influence the behaviour of fluidic flow and is difficult to predict. Yang et al. for example, explored anode flow fields of direct methanol fuel cells placed in different orientations and found that in a vertical configuration, cell performance was greatly enhanced compared to horizontal configuration [373]. This was owed to the reduced average size and number of CO_2 gas slugs that flow across the channels and form on reaction of methanol with water. However, in this model, two phase flow is assumed to be negligible. In real working conditions, a highly efficient anode could possibly lead to formation of nitrogen where such two phase flow becomes important. The influence of gas slugs may therefore be more critical in such orientations and to avoid complications, it may be useful to place cells vertically in such a way that the anode exhaust is at the top to help the release of bubbles. Nevertheless, a vertical configuration and the formation of two-phase flow requires a new model. The contributions of gravity must also be acknowledged in such scenarios.

5.4.4. Laboratory Scale

For practical laboratory scale experiments, a smaller active area is valuable to avoid waste of material, especially during initial trails of finding electrode and catalytic materials. For such trials, a relatively small reaction zone is ideal before scaling up can be implemented. An active area of 1 cm^2 more closely resembles a fuel cell for laboratory scale use and for exploitation in preliminary testing stages of the cell. The above designs must therefore be tailored towards real build.

For this reason, the simulations were performed once again, with the active sites being scaled down to 1 cm^2 to ensure that the phenomena observed is applicable to all active area sizes. Simulations rather than experimental studies were carried out since the flow of dye would be harder to visually track in an active area of 1 cm^2. Nevertheless, the above subsections show that the theoretical and experimental results are in good correlation. Simulation studies should therefore be sufficient to judge whether the overall behaviour remains the same in a smaller active area. For these simulations, liquid was chosen as the fluid feed, introduced at a rate of 2 mL min^{-1} to represent laboratory conditions more accurately.

Fig. 5.10 shows the velocity profiles along each channel of the different models. Eight cross sectional planes were placed along each channel to investigate the flow profile more closely. In all scenarios, the walls of each channel experiences zero velocity, indicative of the no slip boundary conditions being implemented. The laminar flow profile builds towards the centre of each channel where the maximum velocities are observed.

Consequently, the parabolic profiles characteristic of laminar flow can be seen in each channel.

Fig. 5.10a shows the velocity contour profile over the active area of the conventional PFFP design. The outer channels experience flow with greater velocity compared to the middle channels, evidenced by a clear colour change. This phenomenon is also represented by the graph shown to the right of the velocity contour profile, where a parabolic-type trend is observed. Channel 1 followed by channel 10 experience the greatest flow velocity and the middle channels considerably less, highlighting an obvious non-uniform distribution over the active area. Moreover, the result follows the same trend as was seen in both the larger simulated models and 3D printed experiments.

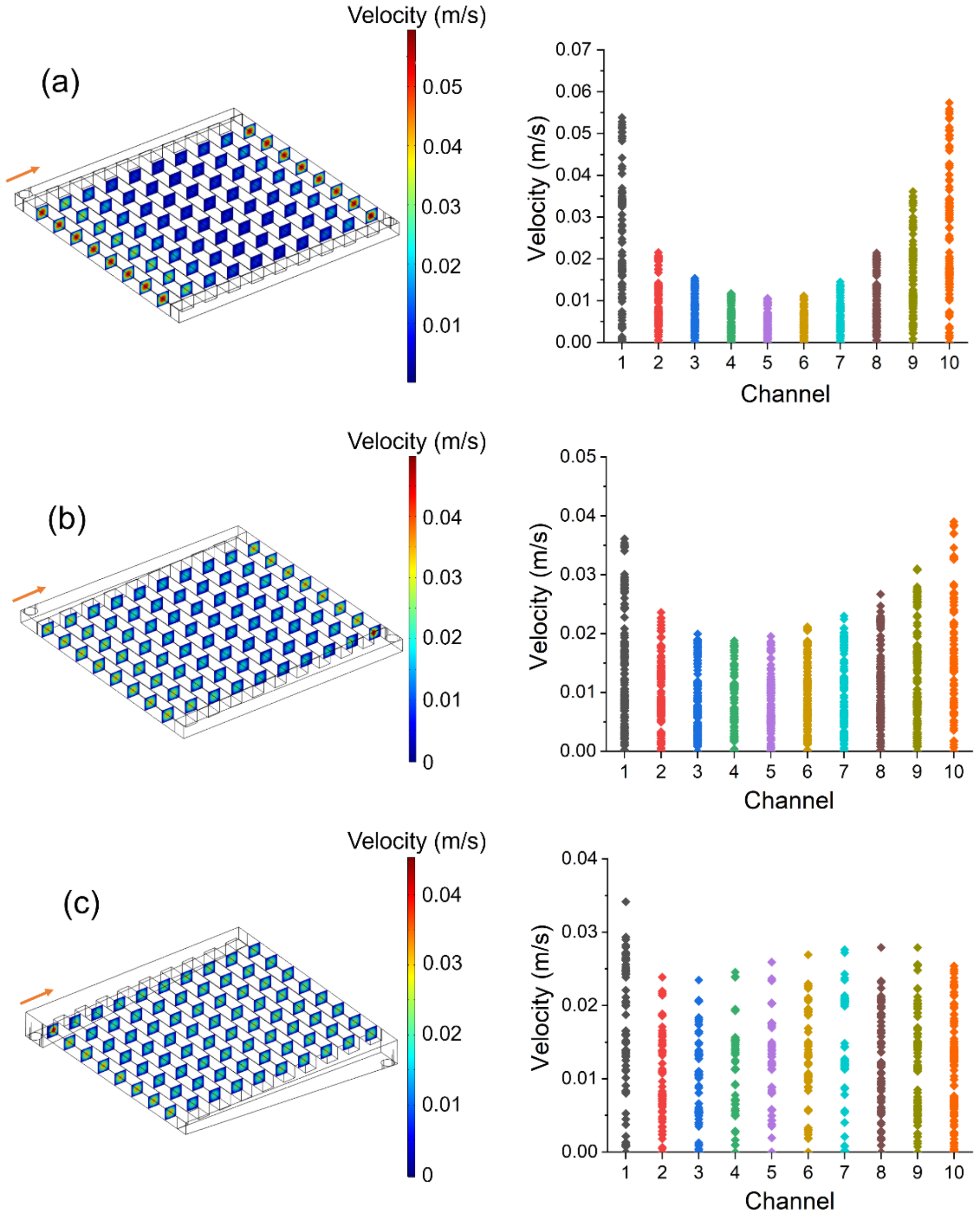

Fig. 5.10. Velocity profile along each channel (left) with arrows showing the direction of flow, and velocity values mapped along each channel (right) for (a) PFFP, (b) PFFP-1D and (c) PFFP-2D design with an active area of 1cm^2.

Fig. 5.10b shows the respective velocity contour profile over an active area utilising the PFFP-1D design. Again, the outer most channels, channel 1 and channel 10, experience a higher flow velocity compared to the central channel streams. However, the trend is less prominent than the former simple PFFP design. This can be seen more clearly on the plot to the right. In comparison with Fig. 5.10a, the data in Fig. 5.10b shows that the difference in flow velocity between the outer and central channel streams is far less. Although a notable improvement can be seen, the overall parabolic-type trend is still observed.

From the velocity contour map shown in Fig. 5.10c, flow over the area employing the PFFP-2D design shows very different behaviour compared to the previous two cases. Colour change between the different channels is less apparent, implying a more even flow velocity is experienced over the entirety of the active area. This is more easily distinguished by the plot given to the right. Here, unlike the previous two cases, where channel 1 and channel 10 observe relatively higher flow velocities, a much more even flow velocity is experienced amongst channel 2 to channel 10. Notably, channel 1 experiences a relatively higher flow velocity which coincides with what was observed experimentally by the 3D printed models. However, the difference between the flow velocity in this channel compared to the remaining channels is far less prominent than the gradient observed in Fig. 5.10a and Fig. 5.10b.

When considering the average velocity of each channel more closely, the extent of non-uniformity can be quantitatively assessed in each situation presented in Figs. 5.10a-c. In a uniform situation, the fluid velocity of each channel should be equal, meaning the variance should be null. In the PFFP, PFFP-1D and PFFP-2D models, there is a decrease in calculated variance from 4.32 x 10^{-5} ms^{-1} to 6.35 x 10^{-6} ms^{-1} to 2.81 x 10^{-6} ms^{-1} respectively. The values highlight that variation of velocity in each channel is smallest in the PFFP-2D model. Such increase in uniform distribution is known to directly influence current densities and power densities of fuel cells [333].

The data shows that regardless of active area size and fluid flow rates, the same overall trends are observed with the previous subsection. This reinforces that the theory behind the PFFP-2D design holds for different scenarios.

Since reaction rates are strongly influenced by mass transfer limitations, they may shadow the intrinsic performance of the catalyst in electrochemical reactions, such as those that take place at the anode and cathode sites of DAFCs. The potential of the catalytic material may therefore not be truly reflected and may subsequently be overlooked. This emphasises the importance of proper FFP design on the overall performance of the cell. The section presented illustrates a route to successfully manipulating FFP designs to improve flow distribution across the active area, which essentially resembles the catalyst layer of a DAFC. In doing so, it can be assumed that mass transfer influences arising from the FPPs are minimised to some extent, allowing interactions at the electrode-electrolyte interface to proceed with greater ease and improve overall output of fuel cell.

5.5. Fuel Cell Build

Considering the findings throughout this chapter, a real fuel cell device was built for conducting laboratory experiments (discussed in later chapters). The design of the fuel cell in terms of materials and FFP pattern were chosen based on the results obtained.

Fig. 5.11 shows the individual components that were purchased and machined to be used in the DAFC assembly. The end plates, insulating layers, current collectors, FFPs and gaskets were made from stainless steel, mica sheets, stainless steel, graphite and silicone rubber respectively (as chosen in section 5.2). The dimensions of the components are the same as those used within the simulations.

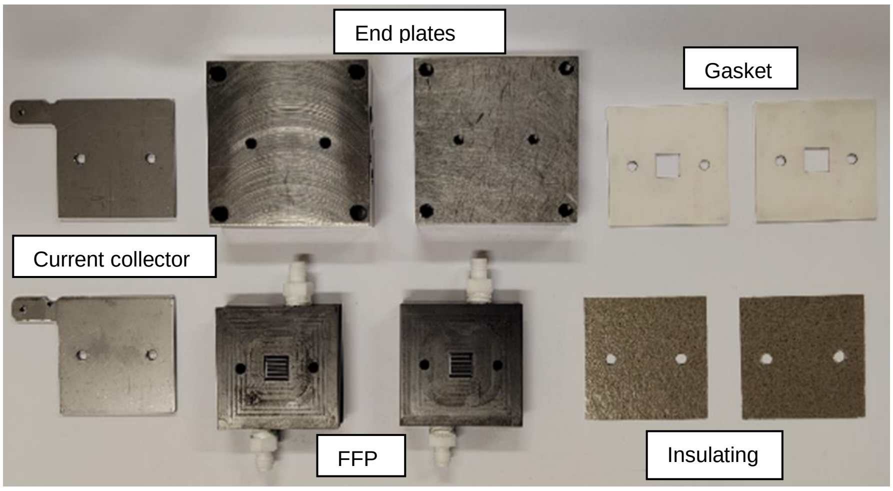

Fig. 5.11. Individual components of DAFC.

The precise arrangement of the components to assemble a working DAFC is shown in Fig. 5.12. Fig. 5.12a shows an AutoCAD 3D drawing used to conceptualise the prototype and Fig. 5.12b shows the real DAFC build. The FFP pattern is highlighted in both cases and shows that the PFFP-2D design is implemented.

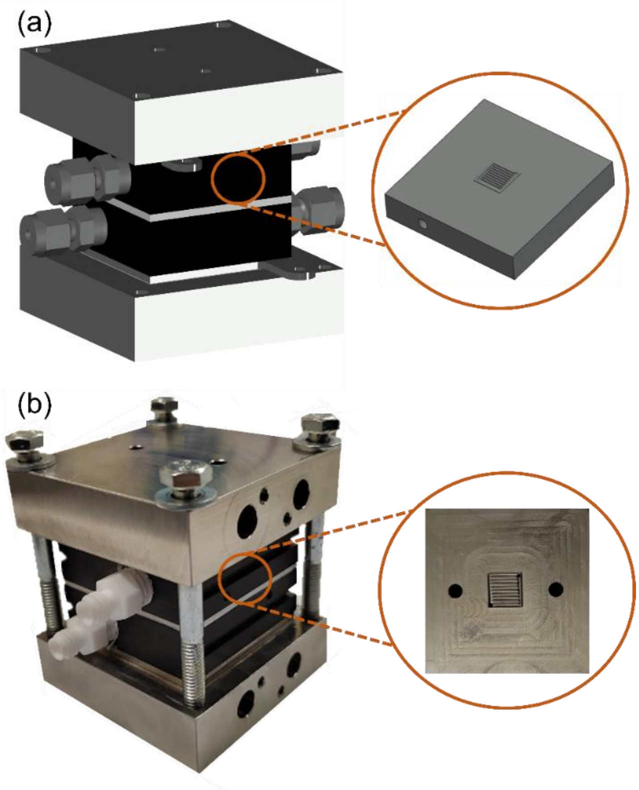

Fig. 5.12. Illustration of assembled DAFC with zoom of FFP employing PFFP-2D design.

It should be noted that the FFPs are connected to the main feeds in such a way that the air and ammonia solution are introduced in parallel but opposite direction. As mentioned above, this helps alleviate deviations in pressure distribution over the MEA and reduces mechanical stress on the membrane, which is extremely important in DAFCs. In this study, a poly(aryl piperidinium) membrane of 20 µm thickness was employed so the assembly of the cell, and in turn, the pressure distribution, is particularly important not to puncture such a thin membrane. Furthermore, PTFE connectors were fitted into the FFPs due to the malleable nature of graphite. These were then connected to the anodic/cathodic inlet and outlet streams as discussed in Chapter 3.

In the above section, it is noted that the mechanical compaction of end plates is necessary for efficient MEA compression, which is crucial for reducing contact resistances. Furthermore, compaction of end plates is essential for proper sealing of the cell and to avoid loss of reactant fluid. Fig. 5.13 shows that the fuel cell fixture is held in place with bolts that are torqued to a pre-set value which establishes a desired compression on the MEA. To explore this torque value, pressure paper (extreme low pressure film 0.05-0.2 Mpa, Fujifilm, Instruments Direct (Services) Limited) was placed in the middle of the cell assembly (to resemble the MEA) and used to judge the extent of contact and compression that would be exerted on the MEA (Fig. 5.13). This is an insightful tool to visually understand the nature of contact resistances and allows for a simple pressure test to be conducted.

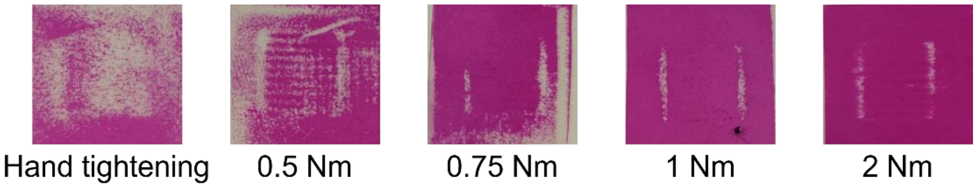
Hand tightening 0.5 Nm 0.75 Nm 1 Nm 2 Nm

Fig. 5.13. Pressure paper results obtained from applying different torques to the assembled DAFC.

Fig. 5.12 shows that hand tightening of the bolts would provide inefficient contact at the MEA, evidenced by the lack in colour across the FFP active area. This would thus lead to inadequate contact between the electrode and electrolyte as well as between the electrodes and membrane. Consequently, this would contribute to polarisation losses and show underperformance of the DAFC. When 0.5 Nm torque is applied, there is a notable change in the pressure paper results. The FFP pattern is shown embedded on the paper and demonstrates better contact at the MEA. There are, however, still regions where contact remains somewhat inefficient, implying that a higher torque is to be applied. As the applied torque is increased, there is substantial improvement, with 1-2 Nm showing optimum contact. Since the results obtained by using 1 and 2 Nm show minimal difference, it can be assumed that at most 2 Nm is required to provide good contact in this DAFC.

It should be noted that the exact torque to apply must (i) consider the thickness of the electrodes and the MEA assembly and (ii) not be too high such that there is deformation of the MEA. This is therefore subject to practice.

Moreover, the tests demonstrate that the individual components can withstand the applied torque and demonstrate good mechanical strength due to the absence of deformities and cracks in the materials. This implies a good choice of materials was chosen and are suitable for fuel cell build.

5.6. Conclusion

To truly exploit the performance of fuel cells, it is attractive to optimise the structure of such devices. This chapter aimed to explore the choice and design of fuel cell components to minimise their effect towards polarisation losses in the fuel cell.

Currently much research into fuel cell design has been focused on PEMFCs and the optimisation of gaseous delivery to the active sites. There is scarce literature regarding material consideration specific for DAFCs, which have additional requirements such as compatibility with ammonia. The route to model and build an efficient fuel cell was therefore considered within the context of this study. Flow field design on the effects of liquid ammonia delivery was also investigated using both simulated and experimental models to represent flow in DAFCs more accurately. The above was used to construct a working DAFC for use in later experiments within this thesis. The key findings of this study are as follows:

(i) The individual components of a DAFC were carefully selected and their criteria was based on strength, availability, cost and compatibility.

(ii) 3D simulations were presented using COMSOL Multiphysics where a conventional parallel flow field plate (PFFP) with no manifold tapering, one-dimensional tapering (PFFP-1D) and two-dimensional tapering (PFFP-2D) design was modelled to see the effects of gas and liquid delivery across the active site.

(iii) The results reveal that the overall flow trends for both gas and liquid fluids remain similar.

(iv) In PFFP, there is non-uniform distribution of fluid and a notable pressure drop along each channel of the design. There is great tendency for the fluid to flow along the end channel before flowing along the middle channels.

(v) In PFFP-1D, which included tapering the manifolds solely in width, the flow distribution improves, however the overall trend remains similar to PFFP and leaves room for further design improvement.

(vi) When the manifolds were tapered in both height and width, PFFP-2D showed notable improvement in fluidic distribution, with highly uniform flow and a smaller pressure gradient across the entire active site.

(vii) When exploring the scale factor between the upper and lower boundaries of manifold tapering, a compromise between the fluidic behaviour and practicality of the design must be acknowledged. A scale factor ratio of 2:1 is satisfactory to provide both uniform distribution and a compact design.

(viii) Simulations were validated by conducting experiments on 3D printed models using a fluorescent dye to visually track flow across the active site.

(ix) The models were rescaled to satisfy laboratory scale experiments and remained in good agreement with the previous simulated and experimental data, revealing that the design holds for various scaling factors and flow rates.

(x) A real fuel cell was built using the findings of the study and the device was constructed with sufficient torque and assembly.

The results of this chapter highlight the significance of proper fuel cell design. The content provides a good foundation for the strategy and optimisation of fuel cell construction, particularly for DAFCs. It should be acknowledged however, that the tests carried out in this chapter rely on the flow field plate being plated horizontally but in real fuel cell configurations, the cell is placed vertically. This may lead to different behaviours of fluid flow, although difficult to predict. Future work may therefore focus on any differences observed between horizontal and vertical configurations of the flow field.

CHAPTER 6 Perovskite Oxides for Oxygen Reduction Reaction

The works in this chapter form part of a publication by the author in Applied Catalysis B: Environmental [68].

6.1. Background

Although perovskite oxides have been extensively exploited in various electrochemical reactions and applications, their use as catalysts in DAFCs has not been widely implemented [35]. Given that such materials have been greatly recognised for their superb oxygen reduction activity, as discussed in Chapter 2, perovskite oxides possess excellent potential to assist ORR at the cathodic site of DAFCs.

Suntivich et al. importantly established that perovskite oxides with near unity e_g orbital occupancy exhibited optimum ORR activity, since this, much work has been devoted towards manipulation of e_g-filling [31, 104]. Partial substitution at the B-site in particular, has widely been used to modify the e_g-filling and bring it closer to near unity. Based on this method, many works have led to the discovery of highly active ORR perovskite oxides catalysts [99, 124-126, 140-146]. The effects of structural changes and calcination temperatures have also shown to have an impact on e_g-filling and ORR activity [38]. Such materials can therefore be considered promising and easily designed to satisfy the requirements of cathodic catalysts in low temperature DAFCs.

Recently, the use of $SrFe_{0.8}Cu_{0.1}Nb_{0.1}O_3$ and $SrCo_{0.8}Cu_{0.1}Fe_{0.1}O_3$ as cathodes was investigated in a DAFC and power densities of around 0.30 and 0.25 $mWcm^{-2}$ were achieved respectively in 35 wt. % NH_3H_2O and 1 M NaOH. The half-cell electrochemical reaction, however, was not studied and subsequently the true extent of these perovskite oxides to assist ORR was unclear. Thus, much room for improvement and exploration regarding utilisation of perovskite oxides to assist the cathodic reaction remains.

Despite the significant body of work described above, certain approaches influencing the electrocatalytic performance of perovskite oxides towards ORR, such as the effects of introducing two dopants at the B-site, have not been as widely explored. In the present work, a series of B-site substituted $LaCoO_{3-\delta}$ (LCO) perovskite oxides, including $LaCr_{0.5}Co_{0.5}O_{3-\delta}$ (LCCO), $LaFe_{0.5}Co_{0.5}O_{3-\delta}$ (LFCO) and $LaCr_{0.25}Fe_{0.25}Co_{0.5}O_{3-\delta}$ (LCFCO), were synthesised via a conventional Pechini method and their activity towards ORR in O_2-saturated 0.1 M KOH solution was studied using a RDE technique. Thorough investigation into the extrinsic (surface area and particle size) and intrinsic (formation of oxygen vacancies, oxidation states, occupancy of e_g levels) properties of electrocatalysts were conducted to explore the synergetic effects of doping both Cr and Fe at the B-site of LCO. The effects of strategically introducing two dopants into the B-site of LCO on oxygen reduction activity has not been explored previously but is feasible to explore the true flexibility of these materials. The second part of this study looks at optimising the LCFCO synthesis method by exploring different calcination temperatures.

Through proper optimisation, this chapter aims to tailor a novel perovskite oxide towards ORR in alkaline media and demonstrate a viable strategy that will pave way for future design of cheap and readily available materials for devices such as fuel cells, alleviating reliance on PGMs. The applicability of such a catalyst for ORR at the cathodic site of a working DAFC will be explored in later chapters.

6.2. Experimental

6.2.1. Materials

$La(NO_3)_3{\cdot}6H_2O$ (98+ wt. %, Fisher Scientific), $Co(NO_3)_2{\cdot}6H_2O$ 99 wt. %, Fisher Scientific), $Cr(NO_3)_2{\cdot}6H_2O$ (99 wt. %, Fisher Scientific) and $Fe(NO_3)_3{\cdot}9H_2O$ (99+ wt. %, Fisher Scientific) were used as metal precursors with no further purification. Citric acid (99+ wt. %) and ethylene glycol were purchased from Alfa Aesar and Fisher Scientific respectively. Carbon black (Vulcan XC-72R, Fuel Cell Store) and Nafion solution (5 wt. %, Sigma Aldrich) were added to prepare an ink for the RDE tests. Pt/C was commercially purchased (platinum nominally 20 % on surable carbon support, Alfa Aesar). Other chemicals such as isopropanol and potassium hydroxide (KOH) were all analytical reagents purchased from Alfa Aesar.

6.2.2. Synthesis of Perovskite Oxide Powders

The perovskite oxide powders were synthesised using a conventional Pechini method [374]. In brief, appropriate amounts of the metal nitrate precursors were dissolved in an aqueous solution at room temperature. Citric acid was added in a molar ratio of 1:1.2:1.2 of total metal ions:citric acid:ethylene glycol. The resultant solution was stirred and heated to 120 ^oC. After the evaporation of water, the sample was heated to 410 ^oC to form an ash which was finely ground using an agate mortar and pestle. The powder was calcinated in air at 500 ^oC for 2 h with a heating/cooling rate of 5 $^oCmin^{-1}$ before being reground and further calcinated at 1000 ^oC for 4 h with a heating/cooling rate of 3 $^oCmin^{-1}$ to obtain the final perovskite phase. The collected $LaCoO_{3-\delta}$, $LaCr_{0.5}Co_{0.5}O_{3-\delta}$, $LaFe_{0.5}Co_{0.5}O_{3-\delta}$ and $LaCr_{0.25}Fe_{0.25}Co_{0.5}O_{3-\delta}$ samples were labelled LCO, LCCO, LFCO and LCFCO respectively. The synthesis of LCFCO was further explored by adjusting the final calcinating temperature to 600, 700, 800 and 900 ^oC, hereby referred to as LCFCO-600, LCFCO-700, LCFCO-800 and LCFCO-900 respectively.

6.2.3. Physicochemical Characterisation

XRD analysis was used to examine the phase and purity of the perovskite oxide powders. Measurements were carried out at room temperature on a PANalytical X'Pert Pro diffractometer (Cu Kα source, 1.5405 Å) and collected in the 2θ range of 10-80° with a step of 0.0167°. Phase analysis and identification was conducted via the HighScore software. It should be noted that particle size can affect intrinsic ORR activity, consequently, to gain insight into structure-property relationship, crystallite sizes were calculated using data extracted from the XRD patterns by use of the Scherrer equation.

Due to complexity, Rietveld refinement was carried by Professor Shanwen Tao using GSAS and EXPGUI [252, 253].

The above methods give an average value of crystalline sizes; however, real samples usually consist of grains with different domains. To evaluate the distribution of grain sizes and account for non-coherent domains, SEM images were taken. SEM was used to examine the morphology of the catalyst at the surface using a Zeiss SUPRA 55-VP machine, equipped with an EDS spectrometer for elemental analysis. Specimens were prepared prior to testing by depositing small amounts of the powder and coated with Au.

Raman spectroscopy was used to explore bonding modes and was conducted using a Renishaw InVia Raman Microscope with an exciting wavelength of 532 nm.

XPS was utilised to study elemental oxidation states and was measured using a monochromated Al K_α X-ray source on a Kratos Axis Ultra DLD spectrometer (Kratos Analytical, Manchester, UK). The data was collected at a take-off angle of 90° to the surface plane and analysed using the Casa XPS package. To prevent the surfaces becoming positively charged, charge neutralization was employed and the spectra were later referenced to the C-C peak at 285.5 eV during analysis.

Textural properties were assessed via N_2 adsorption-desorption isotherms of the perovskite oxide powders recorded at liquid N_2 temperature using a Micromeritics ASAP 2020 apparatus. Samples were degassed at 300 ^{o}C for 1 h. Specific surface areas (SSA) were determined by applying the BET method.

6.2.4. Electrochemical Characterisation

The electrochemical activity of the samples towards ORR were measured via a RDE technique in O_2-saturated 0.1 M KOH solution at room temperature (ca. 20 ^{o}C). An ink was prepared by mixing the perovskite oxide catalyst powder and carbon black (Vulcan XC-72R) in a 5:1 mass ratio respectively. The oxide was physically mixed with high surface area carbon black (Vulcan XC-72R, specific surface area 216 m^2g^{-1}) to facilitate electrical contact between the oxide particles and help eliminate issues relating to electronic conductivity, favouring complete utilisation of the perovskite surface [185]. The resulting powders were dispersed and sonicated in ethanol and Nafion solution, which was used as a binding agent, before being pipetted onto a glassy carbon (GC) disk electrode (PINE research, AFE2M050GC) and dried at room temperature to form a thin film. The geometric surface area of the GC electrode was 0.196 cm^2. The catalyst coated CG electrode was mounted onto a RDE shaft (AFE6MB) attached to a modulated speed regulator (PINE research, MSR) and used as the working electrode in a typical three-electrode set up contained in an electrochemical cell kit (PINE research, AKCELL2). Pt mesh and Ag/AgCl (saturated KCl) were used as the counter and reference electrodes respectively.

To assess ORR activity, electrochemical characterization was determined by recording polarisation curves on a Solartron 1470E multichannel cell test system. Tests were conducted in O_2-saturated 0.1 M KOH solution using the potential range of -0.6 to 0.1 V vs. Ag/AgCl (0.36 to 1.06 V RHE) at a scan rate of 10 mVs^{-1} and various rotation rates (100, 400, 900, 1600 rpm) of the RDE. Chronopotentiometry tests were conducted in 0.1 M KOH at room temperature under a fixed potential of -0.4 V vs. Ag/AgCl. From analysis of the ORR polarisation curves, Koutecky-Levich (K-L) plots were exploited to calculate the electron transfer number for all electrocatalysts using the following equations [99, 375]:

$$\frac{1}{I} = \frac{1}{I_L} + \frac{1}{I_k} = \frac{1}{B\omega^{1/2}} + \frac{1}{I_k} \tag{6.1}$$

$$B = 0.62nFC_0D_0^{2/3}V^{-1/6} \tag{6.2}$$

where I is the measured current density, I_K and I_L are the kinetic and limiting current density respectively, ω is the angular velocity of the disk, n is the electron transfer number, F is the Faraday constant (96485 C mol^{-1}), C_0 is the bulk concentration of O_2 (1.2×10^{-6} mol cm^{-3}), D_0 is the diffusion coefficient of O_2 in 0.1 M KOH (1.9×10^{-5} cm^2 s^{-1}), and V is the kinematic viscosity of the electrolyte (0.01 cm^2 s^{-1}).

6.3. Results and Discussion

6.3.1. Sample Characterisation

6.3.1.1. Varying B-site Configuration

The room temperature XRD patterns of the parent LCO sample as well as the singly and doubly doped counterparts are compared in Fig. 6.1b. The detailed lattice parameters are listed in Table 6.1. XRD analysis reveals that the intense reflections of the LCO perovskite were well indexed to the rhombohedral crystal system (PDF 00-048-0123) and agrees well with literature [376, 377]. The perovskite phase is successfully formed in all samples with no indications of any structural or phase changes, demonstrating that Cr and Fe are successfully introduced into the B-site with no secondary phases or impurities.

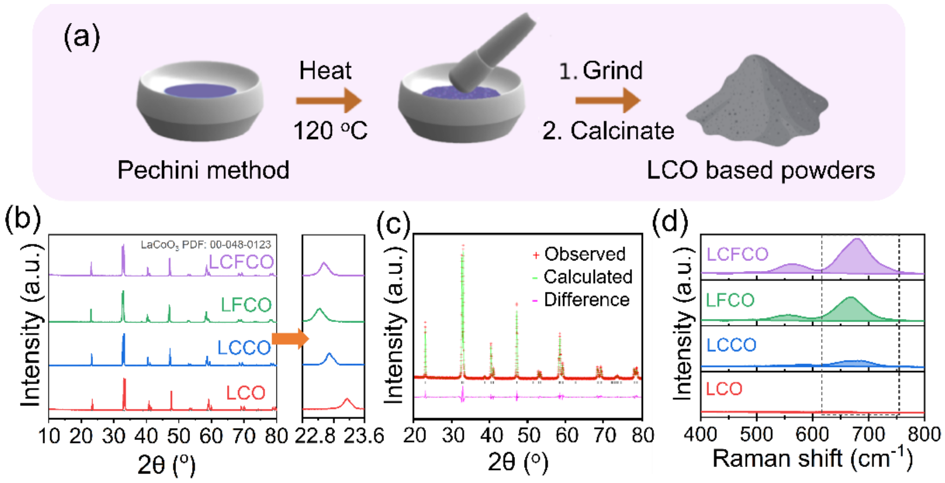

Fig. 6.1. (a) Schematic illustration of the preparation process of LCO-based perovskite oxide powders by a Pechini method [68]. (b) XRD patterns of the prepared LCO, LCCO, LFCO and LCFCO perovskite oxide powders; XRD patterns in the 2θ range 22.8 to 23.6° (right) [68]. (c) Rietveld refinement pattern of synthesised LCFCO [68]. (d) Raman spectra of LCO, LCCO, LFCO and LCFCO [68].

There is a clear gradual shift in diffraction peaks to lower 2θ values on doping of Cr and/or Fe which indicates expansion of the unit cell. In Table 6.1, the cell volumes concur with this observation. If expansion is assumed to be isotropic and the same in all directions of the cell, the magnitude of expansion can be inferred by these changes in cell volume. Compared to LCO, LCCO shows a 1.98 % cell volume increase, and this is further increased to 2.84 % in LFCO. In LCFCO, the cell volume increase is found to be 2.55 % compared to LCO. The presence of Fe has notably been linked to lattice expansion in literature where Ivanova et al. demonstrated lattice expansion when Fe was introduced into $LaFe_xCo_{1-x}O_3$ due to the larger ionic radius of high spin Fe^{3+} ions [378].

On introduction of Cr into the B-site of the LCO perovskite oxide, the peaks shift to lower 2θ angles with respect to the parent structure. This can be seen with the [100] peak highlighted in Fig. 6.1b (right). This shift can be attributed to the larger crystal radius of Cr^{3+} (0.755 Å), compared to intermediate spin (IS) Co^{3+} ions, which is logically presumed to be between that of low spin

(LS) (0.685 Å) and HS (0.750 Å) Co^{3+} [99, 379-381]. Upon introduction of Fe at the B-site, there is a further obvious shift in diffraction peaks towards lower 2θ angles. This can be owed to the larger crystal radius of high spin (HS) Fe^{3+} ions compared to that of both Cr^{3+} and Co^{3+}, henceforth a greater expansion of the lattice can be expected to accommodate for the larger crystal radius [99, 379-381].

When the B-site is dual substituted with both Cr and Fe, the peaks are found to be situated in-between that of LFCO and LCCO. This is expected due to the lower Fe ratio and the smaller ionic radius of Cr^{3+} in comparison to Fe^{3+}. Safakas et al. found a similar trend when the relative amount of Fe^{3+} in $LaCo_xFe_{1-x}O_{3-\delta}$ was decreased and found that a contraction effect on the unit cell was present due to the lower Fe^{3+}:Co^{3+}ratio [99]. These corresponding shifts reinforce the successful substitution of both dopants into the B-site. Moreover, the decrease in crystalline sizes on substitution can be related to the decrease in the unit cell volume and micro-strain [379].

Table 6.1. Structural features of synthesised perovskite oxides [68].

Sample	a (Å)	c (Å)	Cell volume ($Å^3$)	Crystal size (nm) [b]
LCO	5.4364(4)	13.0822(3)	334.83	44.5
LCCO	5.4717(5)	13.1696(9)	341.47	41.6
LFCO	5.4825(9)	13.2286(8)	344.35	29.2
LCFCO	5.4786(1)[a]	13.2100(2) [a]	343.378(6) [a]	36.4

[a] lattice parameter and unit cell volume calculated from Rietveld refinement method.

[b] crystal size was calculated by Scherrer equation.

Rietveld refinement of the LCFCO composition was carried out by GSAS and EXPGUI [252, 253]. The refined XRD pattern is shown in Fig. 6.1c, with the lattice parameters listed in Table 6.2. It is confirmed that LCFCO exhibits a space group R-3c (167); a = 5.4786(1) Å, c = 13.2100(2) Å and V = 343.378(6) $Å^3$. It should be noted that all lattice parameters are within a similar range to the parent structure and as expected, the unit cell volume of

LCFCO (343.378(6) Å^3) is between that of LFCO (344.35 Å^3) and LCCO (341.47 Å^3). The refined parameters therefore support the above analysis indicating successful substitution into the B-site.

Table 6.2. Structure and lattice parameters of LCFCO determined by Reitveld refinement [68].

Atom	Site	Occupancy	x	y	z	U_{iso}(Å^2)
La	6a	1	0	0	1/4	0.0154(3)
Cr	6b	0.25	0	0	0	0.0132(5)
Fe	6b	0.25	0	0	0	0.0132(5)
Co	6b	0.5	0	0	0	0.0132(5)
O	18e	0.984(6)	0.4465(4)	0	0	0.0186(14)

Space group *R-3c* (167); *a* = 5.4786(1) Å, *c* = 13.2100(2) Å, *V* = 343.378(6) Å^3, *Z* = 6. R_{wp} = 9.84%, R_p = 7.84%, χ^2 = 2.495.

Raman spectroscopy was used to gain greater insight into the M-O bond strength for the various perovskite oxides. The four distinguishable bands present for $LaCoO_3$ in Fig. 6.1d coincide with those stated in literature [377, 382, 383]. The band that appears at the lowest Raman shift value is associated with the E_g La stretching vibration [383]. There is minimal shift in this band on substitution at the B-site which indicates that the introduction of Cr and Fe dopants do not interact with the A-site but instead engage at the B-site as expected. The second and third bands are due to the E_g bending and E_g quadrupole vibrations respectively. The highest energy band is attributed to the A_{2g} breathing mode of the oxygen ion cage with respect to the CoO_6 (BO_6) octahedron [383]. These latter bands associated with CoO_6 vibrations are shown to be more sensitive to substitution as expected.

The A_{2g} band in LCO has the lowest Raman energy (642 cm^{-1}). In the presence of B-site substitution, the A_{2g} band shifts to higher Raman energies in LCCO and LFCO (681 cm^{-1} and 667 cm^{-1} respectively). The A_{2g} band in LCFCO is found in-between that of the abovementioned, with a Raman energy of 678 cm^{-1}, revealing that the Co B-site interacts with both Cr and Fe. The absence of additional bands and the respective shifting of the A_{2g} band indicates that the dopants are successfully introduced into the BO_6 octahedron, in agreeance with XRD.

The morphologies of the prepared perovskite oxide powders were characterised by SEM. The images in Figs. 6.2a-d reveal globular grains are formed for all compositions which are relatively uniform in size. It should also be noted that an obvious reduction in grain size is observable as Fe is introduced into the sample. This has been reported in literature where the presence of Fe reduces the extent of particle agglomeration [378]. Subsequently, the samples containing Fe (LFCO and LCFCO) show an obvious reduction in grain size.

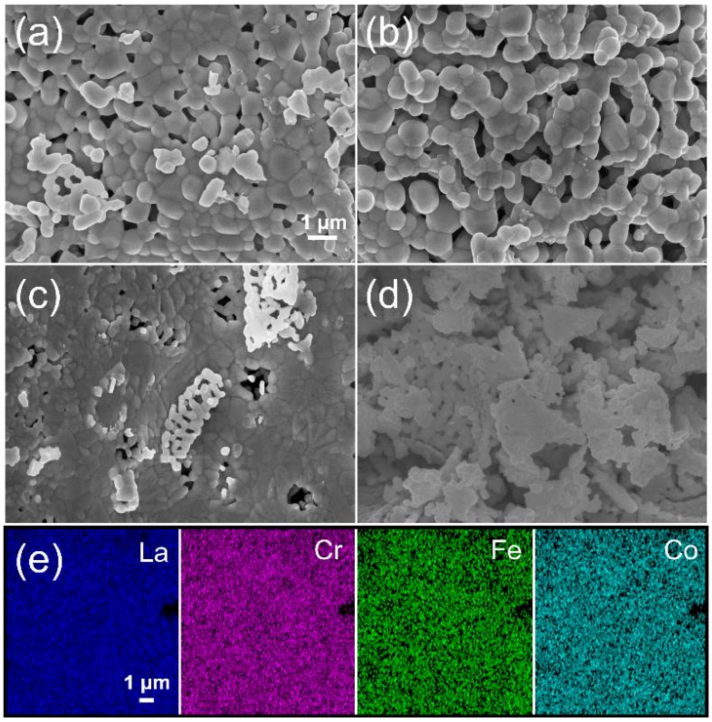

Fig. 6.2. SEM images of (a) LCO (b) LCCO (c) LFCO and (d) LCFCO. (e) Corresponding EDS elemental mapping of La, Cr, Fe and Co in LCFCO [68].

EDS was used to explore the different elemental compositions and a detailed analysis is reported in Table 6.3. Elemental mapping of the LCFCO perovskite is also provided to demonstrate visual distribution of the elements against the scale bar given in Fig. 6.2e. The elements of La, Cr, Fe and Co are homogenously dispersed with no apparent areas of agglomeration, indicating that no secondary phases or impurities are present. The lack of agglomeration may indicate little or no presence of other oxide phases being present. This is in agreeance with the formation of a single-phase perovskite oxide as determined by XRD and Raman spectroscopy. Furthermore, the elemental analysis reveals that the atomic composition between the A and B site remains 1:1 regardless of the doping nature and concentration, satisfying the ABO_3 composition.

Table 6.3. Elemental analysis of synthesised perovskite oxides [68].

Sample	**Atomic composition (%)**				
	La	**Co**	**Cr**	**Fe**	**A/B**
LCO	54.1	46.9	-	-	1.15 (1)
LCCO	53.9	24.2	22.8	-	1.15 (1)
LFCO	53.5	24.8	-	22.6	1.13 (1)
LCFCO	54.8	23.6	12.0	10.7	1.18 (1)

brackets indicate the expected ratio.

The nature and surface composition of the samples were studied by XPS. The corresponding spectra of LCO, LCCO, LFCO and LCFCO are provided in Fig. 6.3, Fig. 6.4, Fig. 6.5 and Fig. 6.6 respectively. Since the data can be fitted well to the La_2O_3 spectra, the La species presented at the A-sites are reasonably assumed to be in the +3 oxidation state as expected, satisfying the ABO_3 composition. The deconvoluted spectra can be fitted to peaks arising from La $4d_{5/2}$ and La $4d_{3/2}$ [269]. The Co $2p_{3/2}$ peaks of all samples can be fitted well to the Co_3O_4 spectra [384]. It is stated in literature that for Co_3O_4, where Co(II/III) exists in the +2 and +3 oxidation states, the Co $2p_{3/2}$ peak corresponding to binding energies (BE) around 780 eV can be assigned to octahedral Co^{3+}, whereas the Co $2p_{3/2}$ signal at higher BE, at around 781 eV, together with the shake-up satellite signals are indicative of surface Co^{2+} [385-387]. The results therefore suggest the presence of Co in both the +2 and +3 oxidation states in all samples. Furthermore, the Co $2p_{3/2}$ peak observed at higher BE may be closely related to the CoO species where Co is in the +2 oxidation state [384]. The peak with lowest BE in all spectra can therefore be associated with Co in the 3+ oxidation state whilst the latter two peaks at higher BE may be assigned to the 2+ oxidation state.

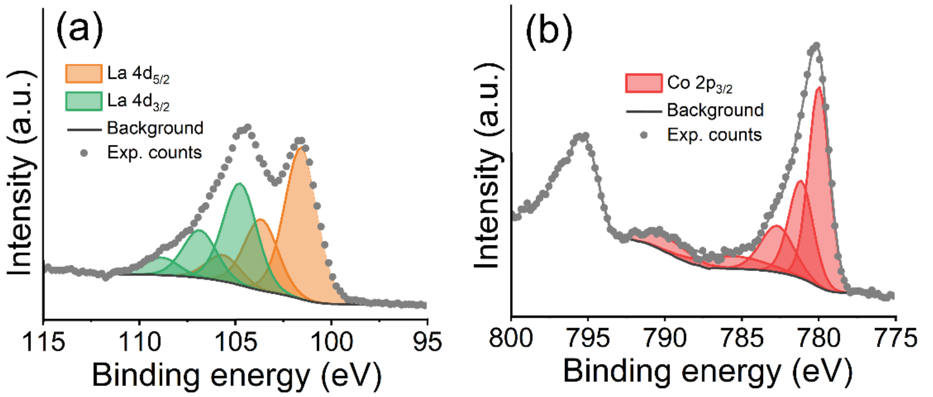

Fig. 6.3. XPS analysis of LCO demonstrating (a) La and (b) Co spectra [68].

Table 6.4. The BE and relative proportion (%) of Co^{2+}/Co^{3+} from Co $2p_{3/2}$ XPS data [68].

Sample		**Co $2p_{3/2}$**		
		Co^{2+}		**Co^{3+}**
LCO	BE (eV)	781.15	782.75	779.95
	(%)	52.8		47.2
LCCO	BE (eV)	781.18	782.29	781.19
	(%)	49.0		51.0
LFCO	BE (eV)	780.87	782.47	779.67
	(%)	51.4		48.6
LCFCO	BE (eV)	780.97	782.57	779.97
	(%)	48.3		51.7

The deconvoluted Cr $2p_{3/2}$ spectra in LCCO and LCFCO are characteristic of Cr^{6+} and Cr^{3+} species [385]. The fractional percentage of Cr in the 3+ oxidation state is calculated to be around 56.9 % in LCFCO, which is similar to that of LCCO (61.9 %) (Table 6.5). This demonstrates that the fraction of Cr^{3+} species within the sample remains relatively unchanged in the presence of additional dopants. Furthermore, the Fe $2p_{3/2}$ and $2p_{1/2}$ spectra can be fitted to peaks corresponding to Fe_2O_3 where Fe is in the +3 oxidation state. On introduction of Cr into LCO, there is a clear shift of the Co $2p_{3/2}$ peak position towards higher binding energies from 779.7 eV to 780.4 eV, as well as an obvious increase in satellite signal intensity, both of which are indications of strong interactions between Cr and Co [385].

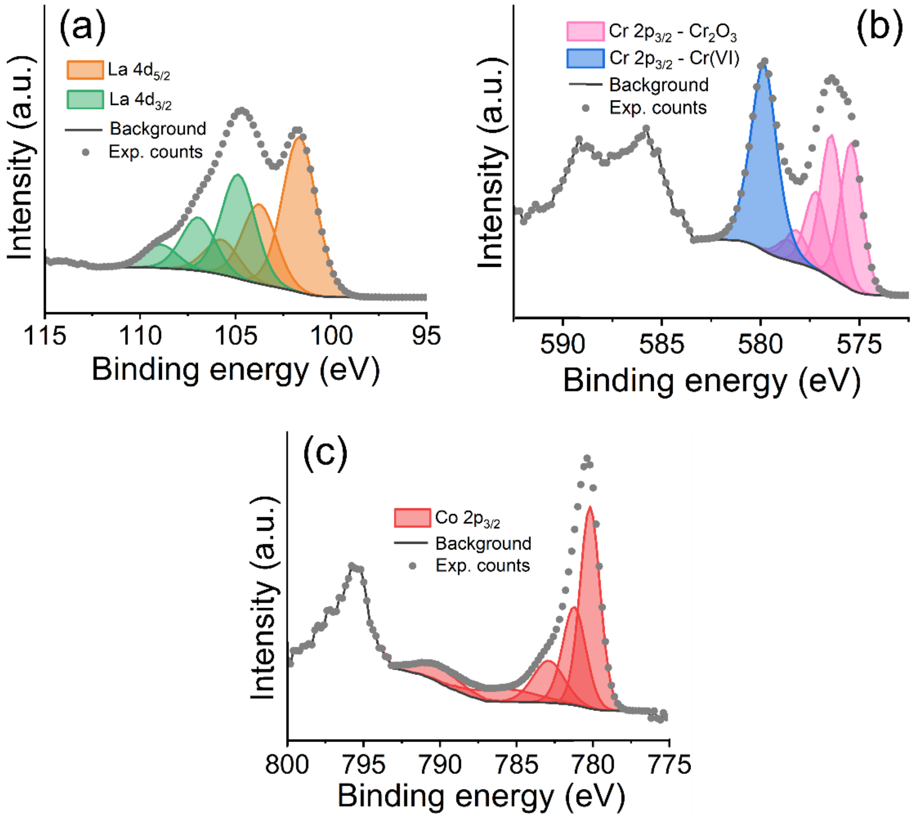

Fig. 6.4. XPS analysis of LCCO demonstrating (a) La, (b) Cr and (c) Co spectra [68].

Table 6.5. The BE and relative proportion (%) of Cr^{3+}/Cr^{6+} from Cr $2p_{3/2}$ XPS data [68].

Sample		**Cr 2p3/2**					
		Cr^{3+}					**Cr^{6+}**
LCO	BE (eV)	-	-	-	-	-	-
	(%)	-					-
LCCO	BE (eV)	575.39	576.39	577.19	578.19	578.65	579.79
	(%)	38.1					61.9
LFCO	BE (eV)	-	-	-	-	-	-
	(%)	-					-
LCFCO	BE (eV)	575.37	576.37	577.17	578.17	578.56	579.77
	(%)	43.1					56.9

The Fe $2p_{3/2}$ and $2p_{1/2}$ spectra in both LFCO and LCFCO can be fitted to peaks corresponding to Fe^{3+}. There is also an increase in binding energy of the Co $2p_{3/2}$ profile when Fe is introduced into LCO to form LFCO (779.9 eV), however, this is slightly less pronounced and indicates that Cr may interact more strongly with the Co centre.

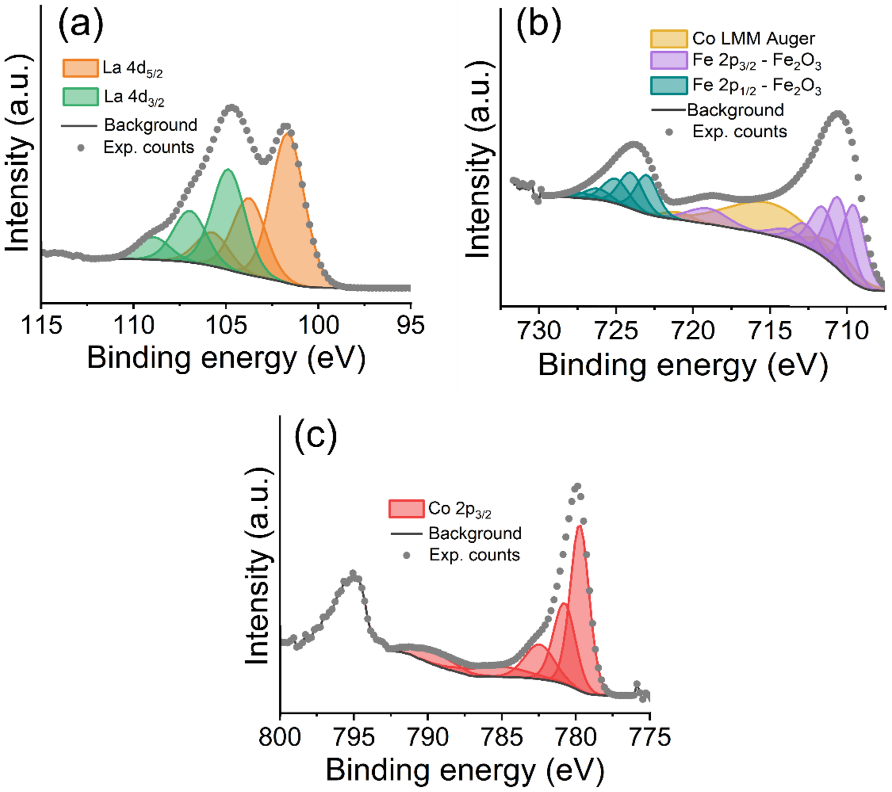

Fig. 6.5. XPS analysis of LFCO demonstrating (a) La, (b) Fe and (c) Co spectra [68].

When both Fe and Cr are introduced, LCFCO also demonstrates a shift in the Co $2p_{3/2}$ peak position towards a binding energy of 780.0 eV. These results demonstrate that in the presence of both dopants, the surface species do not change and there are no further variations in oxidation states. Through slight changes in binding energy however, it can be deduced that these ions interact at the B-site which may lead to synergistic effects.

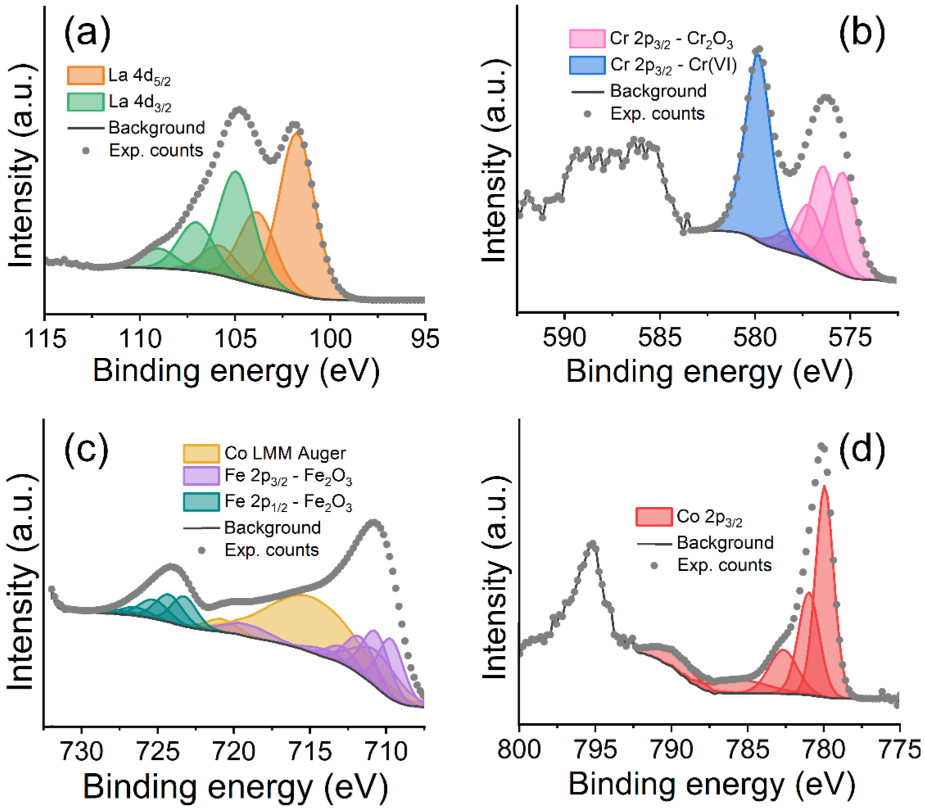

Fig. 6.6. XPS analysis of LCFCO demonstrating (a) La (b) Cr (c) Fe and (d) Co spectra [68].

The oxygen species at the surface of the perovskite oxide powders were also investigated by XPS (Fig. 6.7). The spectra can be fitted into four subpeaks that can be assigned to lattice oxygen species (O^{2-}), highly oxidative oxygen species (O_2^{2-}/O^-), surface-adsorbed oxygen species or hydroxyl groups (-OH) and surface adsorbed water (H_2O), herein labelled as O1, O2, O3 and O4 respectively [125, 388]. The relative concentration of each oxygen-containing species is listed in Table 6.6. According to literature, the highly oxidative oxygen species (O_2^{2-}/O^-) is closely related to surface oxygen vacancies and defects [125, 142, 159, 388]. Compared to LCO, incorporation of Cr in LCCO results in an obvious increase of the O2 peak, indicating an enrichment in surface oxygen vacancies. When Fe is introduced however, this is much less pronounced. LCFCO also shows a relative increase in surface oxygen vacancies, presumably due to the presence of Cr.

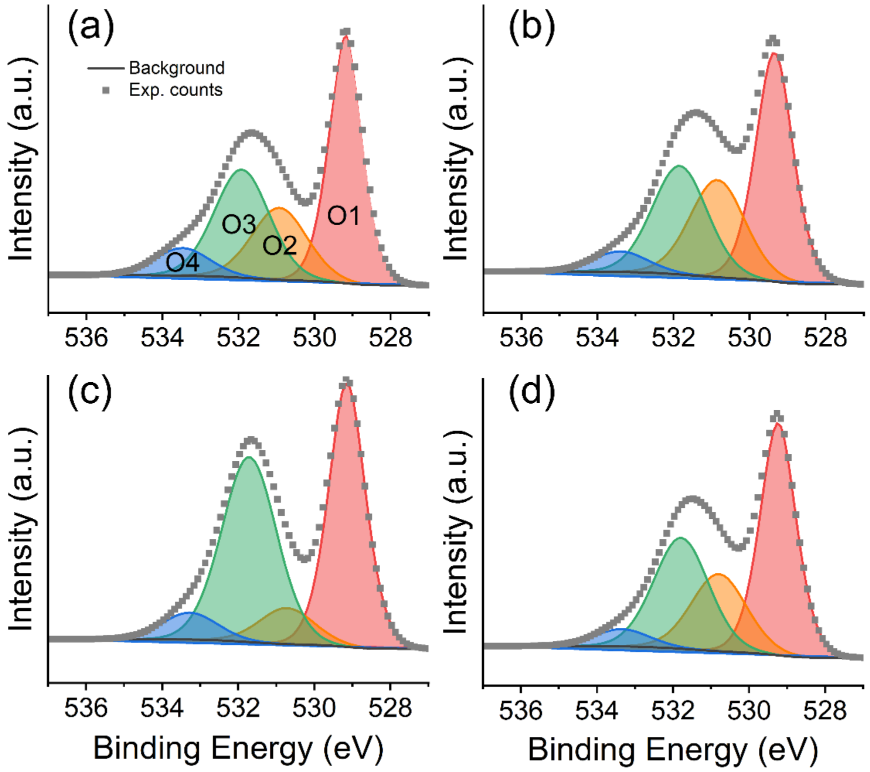

Fig. 6.7. Deconvoluted O 1s spectra for the LCO, LCCO, LFCO and LCFCO perovskite powders [68].

Table 6.6. The BE and relative concentration of oxygen species from the deconvoluted O 1s XPS peak [68].

Sample		**O 1s**				**Area ratio O2/(O1+ O3+O4)**
		O1	**O2**	**O3**	**O4**	
LCO	BE (eV)	529.00	530.95	531.95	533.45	0.24
	(%)	40.44	19.56	30.23	9.77	
LCCO	BE (eV)	529.39	530.90	531.90	533.39	0.34
	(%)	38.78	25.23	29.23	6.76	
LFCO	BE (eV)	529.17	530.67	531.67	533.27	0.09
	(%)	40.84	8.51	43.45	7.20	
LCFCO	BE (eV)	529.27	530.77	530.77	533.37	0.27
	(%)	41.08	21.49	31.08	6.35	

6.3.1.2. Varying Final Calcinating Temperature

Since LCFCO is a novel perovskite oxide, its synthesis has not been widely explored. The synthesis method of LCFCO was therefore studied to assess the limits and properties of the perovskite oxide at varying final calcinating temperatures. LCFCO was prepared at different temperatures of 600, 700, 800 and 900 ^{o}C labelled as LCFCO-600, LCFCO-700, LCFCO-800 and LCFCO-900 respectively. The corresponding XRD analysis for these powders is shown in Fig. 6.8. For comparison, the parent LCFCO (LCFCO prepared at 1000 ^{o}C) perovskite sample is also displayed.

The major differences revealed by XRD analysis between the samples are: (i) as the final calcinating temperature is lowered, the powders display broader peaks indicating smaller particle size and (ii) LCFCO-600 contains a secondary phase which is reflected by an additional reflection at a 2θ value of 28.4^{o} belonging to the [040] plane of La_2CoO_4 (PDF 04-008-9324), whereas LCFCO-700, LCFCO-800 and LCFCO-900 are single phase. Referring to the former observation, Retuerto et al. reported similar findings when exploring the extrinsic effects of $LaNiO_3$ at different temperatures. It was found that amongst $LaNiO_3$ prepared at 700, 800 and 900 ^{o}C, powder neutron diffraction and XRD revealed that 700-$LaNiO_3$ had the smallest particle size [38]. The smaller particle size at lower calcinating temperatures is therefore expected. Secondly, when calcinating temperature is below 700 ^{o}C, the sample shows a quasi-crystalline phase. The main peaks of LCFCO-600 are similar to that of the parent perovskite oxide; however, the peaks are shifted to lower diffraction angles. Furthermore, the presence of La_2CoO_4 shows an intermediate may be formed if temperatures are not sufficient. The result of an intermediate at temperatures lower than those to form a pure single perovskite phase is not uncommon and has been reported in literature [389]. The results indicate that LCFCO with a pure perovskite structure requires temperatures of at least 700 ^{o}C. For this reason, only LCFCO-700, LCFCO-800 and LCFCO-900 are considered towards ORR activity in later sections. Moreover, as calcinating temperatures increase, the peak intensity does not change significantly, implying that the crystalline phase does not undergo any further changes on increasing temperatures [389].

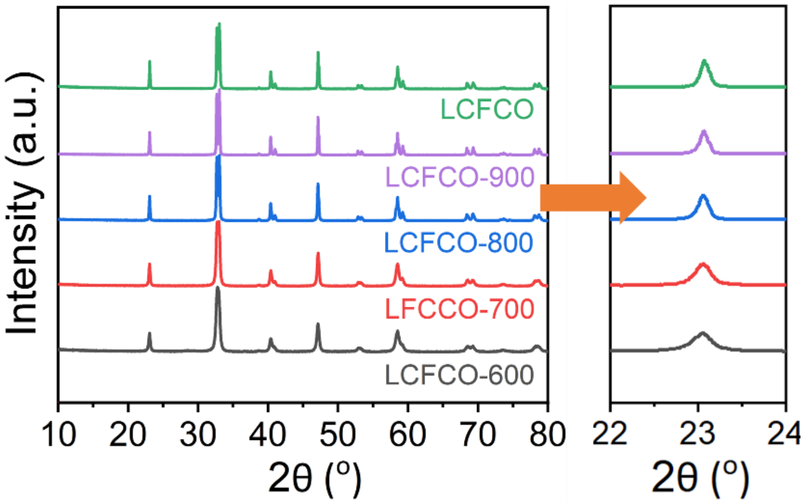

Fig. 6.8. (a) XRD patterns of the prepared LCFCO-600, LCFCO-700, LCFCO-800, LCFCO-900 and LCFCO perovskite powders [68].

To get a better idea of size-activity relationship, it is important to explore the crystal sizes of the LCFCO samples. Table 6.7 shows the crystallite domains for the LCFCO-700, LCFCO-800, LCFCO-900 and parent LCFCO perovskite oxide samples calculated from the Scherrer equation. The data reveals that there is a reduction in crystalline size as calcinating temperature is reduced as expected. These results coincide with literature [38].

The methods above give an average value of crystalline domain sizes; however, real samples tend to have grains with different domains. To assess the distribution of different grain sizes and explore the morphologies of the prepared powders, SEM characterisation was used. The images in Figs. 6.9a-d reveal a reduction in grain size as calcinating temperature is reduced, with LCFCO-700 showing a distinctively small grain size. This coincides with the analysis obtained from XRD. The shape of the grains remains fairly consistent as the temperature is reduced, with all samples demonstrating globular shaped grains of uniform shape and size throughout.

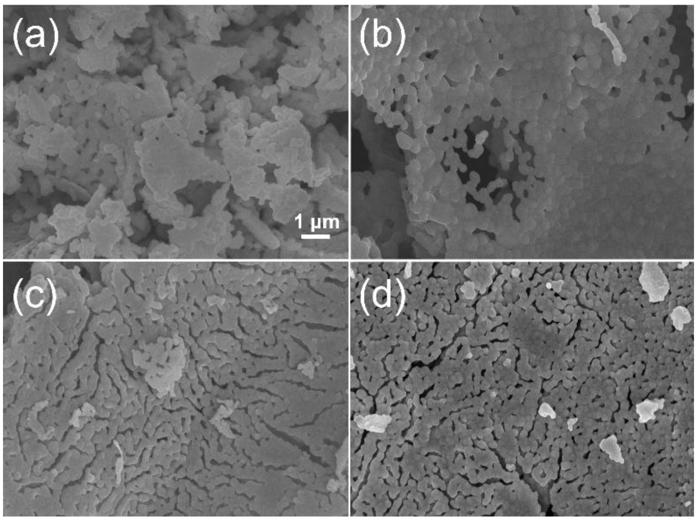

Fig. 6.9. SEM images of (a) LCFCO, (b) LCFCO-900, (c) LCFCO-800 and (d) LCFCO-700 [68].

The measured SSA of the synthesised perovskite oxide powders ranged from 1.0 to 5.2 m^2g^{-1} as shown in Table 6.7. Such SSA values are typical for perovskites due to the relatively high temperature treatment required for perovskite phase formation [38, 99].

Table 6.7. Particle sizes and SSA of the synthesised perovskite oxides [68].

Sample	**Crystal system**	**Crystal size (nm)** [a]	**SSA (m^2g^{-1})**
LCFCO	Rhombohedral	36.4	1.0
LCFCO-900	Rhombohedral	34.2	1.2
LCFCO-800	Rhombohedral	29.49	2.1
LCFCO-700	Rhombohedral	24.6	5.2

[a] crystal size was calculated by Scherrer equation.

There is a clear increase in SSA as calcining temperature is reduced, which is in accordance to literature [38, 390]. The findings can be rationalised due to higher calcining temperatures resulting in the agglomeration of particles and consequently smaller exposed surface areas. The development of synthesis methods leading to reduced particle sizes, and therefore an increased SSA, is subsequently interesting as it could allow for the same ORR performance to be obtained at a lower loading. This indicates that a smaller cathode layer thickness can be utilised and lead to reduced voltage losses due to mass transport resistances [99, 173].

6.3.2. Evaluation of Oxygen Reduction Reaction

6.3.2.1. Effects of B-site Configuration

The electrocatalytic performance of the LCO, LFCO, LCCO and LCFCO perovskite oxide samples towards ORR were evaluated in O_2-saturated 0.1 M KOH solution between -0.6 and 0.1 V vs. Ag/AgCl (0.36 to 1.06 V vs. RHE) at a scan rate of 10 mVs^{-1}. The potential range was chosen to avoid possible irreversible reduction of the perovskite catalysts by avoiding more cathodic potentials being applied. For comparison, the polarisation curve for the Pt/C electrocatalyst was also collected under similar conditions.

Fig. 6.10a shows an illustration of the RDE technique and the reaction that occurs on the surface of the deposited perovskite powders. The current densities (normalised to the geometric surface area of the electrode disk) vs. potential for the different electrocatalysts at varying rotation rates of the RDE equal to 100, 400, 900 and 1600 rpm are shown in Figs. 6.10b-e. Furthermore, a comparison of the polarisation curves for the electrocatalysts fixed at a rotation rate of the RDE equal to 1600 rpm is shown in Fig. 6.10f.

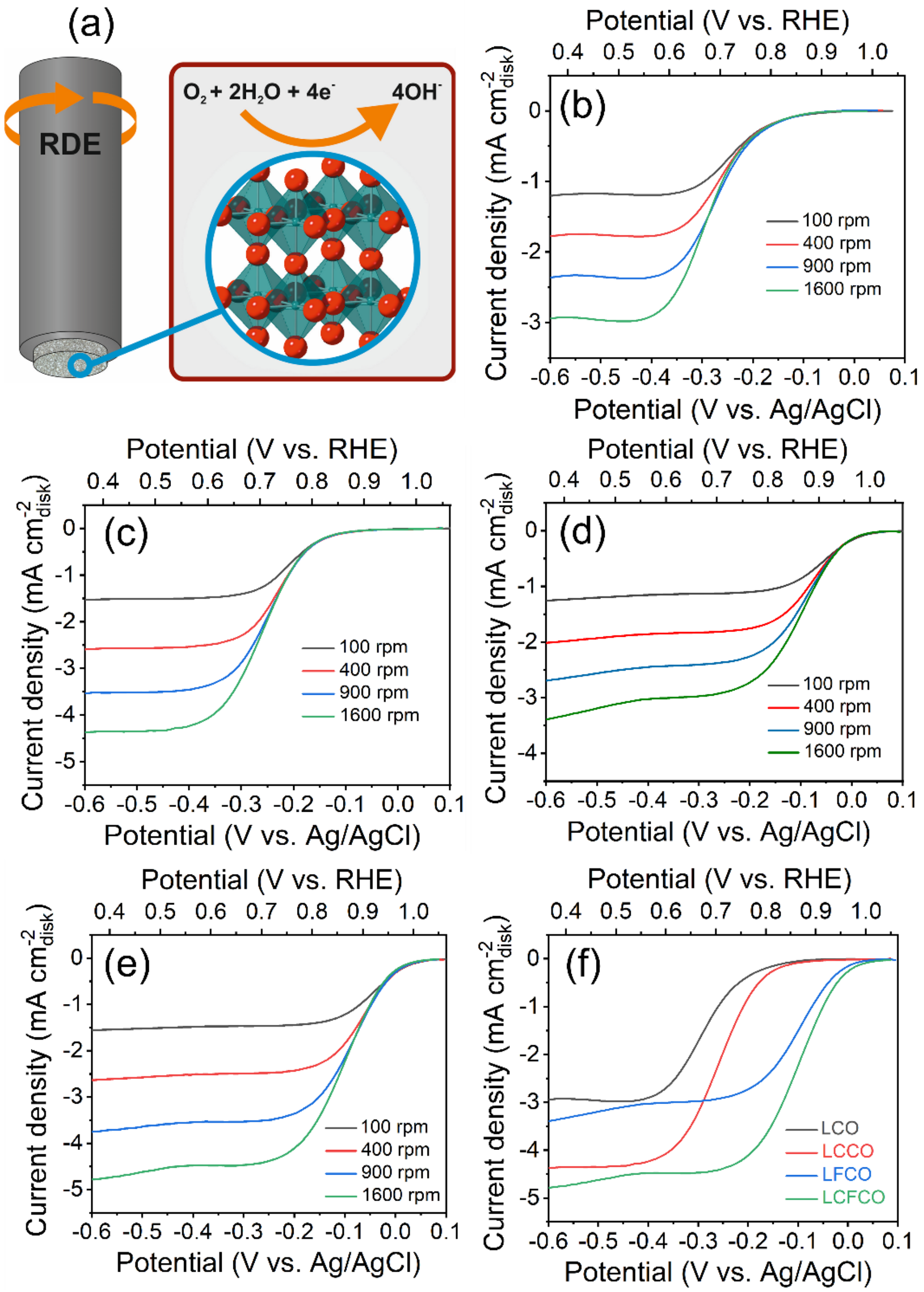

Fig. 6.10. (a) Illustration of RDE technique used for testing ORR activity of different perovskite oxide materials [68]. Polarisation curves obtained for the (b) LCO, (c) LCCO, (d) LFCO and (e) LCFCO perovskite oxides in O_2-saturated 0.1 M KOH solution: RDE rotation rates of 100, 400, 900 and 1600 rpm [68]. (f) Comparison of polarisation curves of the perovskite oxides in O_2-saturated 0.1 M KOH solution at RDE rotation rates of 1600 rpm [68].

Over the entire potential range, the current density at the same potential increases upon doping at the B-site, indicating an increase in ORR activity. Though, it is difficult to draw definite conclusions without further analysis since the reduction reaction depends on several factors. These are more closely examined in the upcoming sections.

An overview of the intrinsic ORR activity for electrocatalysts can be inferred from their onset potentials [28, 99]. The onset potentials (E_{onset}) of the perovskite oxides were determined by intersection of the current baseline with a tangent line drawn from the polarisation curve at the end of the kinetic control region (Fig. 6.11a) [99]. On this basis, the onset potentials of the electrocatalysts follows the descending order LCFCO > LFCO > LCCO > LCO with E_{onset} values of 0.97 > 0.95 > 0.83 > 0.80 V vs. RHE respectively. This is graphically demonstrated in Fig. 6.11b. Interestingly, the onset potential of LCFCO shows similar performance to the Pt/C electrocatalyst (0.96 V vs. RHE) (Fig. 6.11c). This value is similar to that of PGM-based electrocatalysts reported in literature, whereby ORR onset potentials more positive than 0.93 V vs. RHE have been recorded for both Pt/C (20 wt.%) and Pd/C (20 wt.%) in alkaline medium [28, 391, 392]. Notably, the onset potential of the LCFCO electrocatalyst can be considered as being heavily influenced by the presence of Fe, since LFCO shows a similar positive shift in onset potential compared to undoped LCO. A similar positive shift in ORR onset potential when Fe is introduced into electrocatalysts has been reported in literature [391, 392]. Introduction of Cr to form LCCO however, shows a much less pronounced shift in onset potential.

One of the most common methods for evaluating catalyst performance is to compare half-wave potentials ($E_{1/2}$). This is particularly useful as it allows for PGM-free electrocatalysts to be compared with Pt catalysts in terms of their half-wave potential [393]. The $E_{1/2}$ values of the perovskite oxides were determined by the potential recorded at the midpoint of the polarisation curves; the point at which the reduction current begins rapidly increasing and saturation in the limiting region (Fig. 6.11d). On this basis, the half-wave potential of the electrocatalysts follows the descending order LFCO > LCFCO > LCCO > LCO with $E_{1/2}$ values of 0.87 > 0.86 > 0.71 > 0.68 V vs. RHE. Despite the $E_{1/2}$ value for LFCO being slightly greater than that of LCFCO, the change is minimal, and both show a substantial difference compared to the undoped LCO. Again, it can be logically assumed that the half-wave potential of LCFCO is heavily influenced by the presence of Fe due to the similarities between LCFCO and LFCO. The presence of Cr plays a smaller contribution in this regard. Importantly, the half-wave potential value of LCFCO is comparative to Pt/C and other PGM-free electrocatalysts reported in literature, which fall in the range between 0.53 to 0.87 V vs. RHE [391, 393-398]. Pt/C in this study showed a slightly lower half-wave potential of 0.85 V vs. RHE (Fig 6.11e). Tran et al. recorded a similar $E_{1/2}$ of 0.84 V vs. RHE for Pt/C in O_2-saturated 0.1 M KOH solution with a RDE rotation rate of 1600 rpm [391]. This illustrates the great potential of LCFCO as a PGM-free electrocatalyst for ORR.

To gain further insight into the ORR kinetics, Tafel plots were constructed and fitted for the perovskite electrocatalysts (Fig. 6.11f). The polarisation curves were extracted and plotted between the potential verses the logarithm of current density (log I). In doing so, Tafel slopes can be regarded as an effective method for kinetic assessment and provide insight into the kinetics of the ORR activity for the individual electrocatalysts [399-401]. The results reveal that the Tafel slope for LCFCO (93 $mVdec^{-1}$) was smaller than LFCO, LCCO and LCO (99, 101 and 133 $mVdec^{-1}$ respectively), indicating that the incorporation of the Cr and Fe dopants into LCO induces faster electrokinetics.

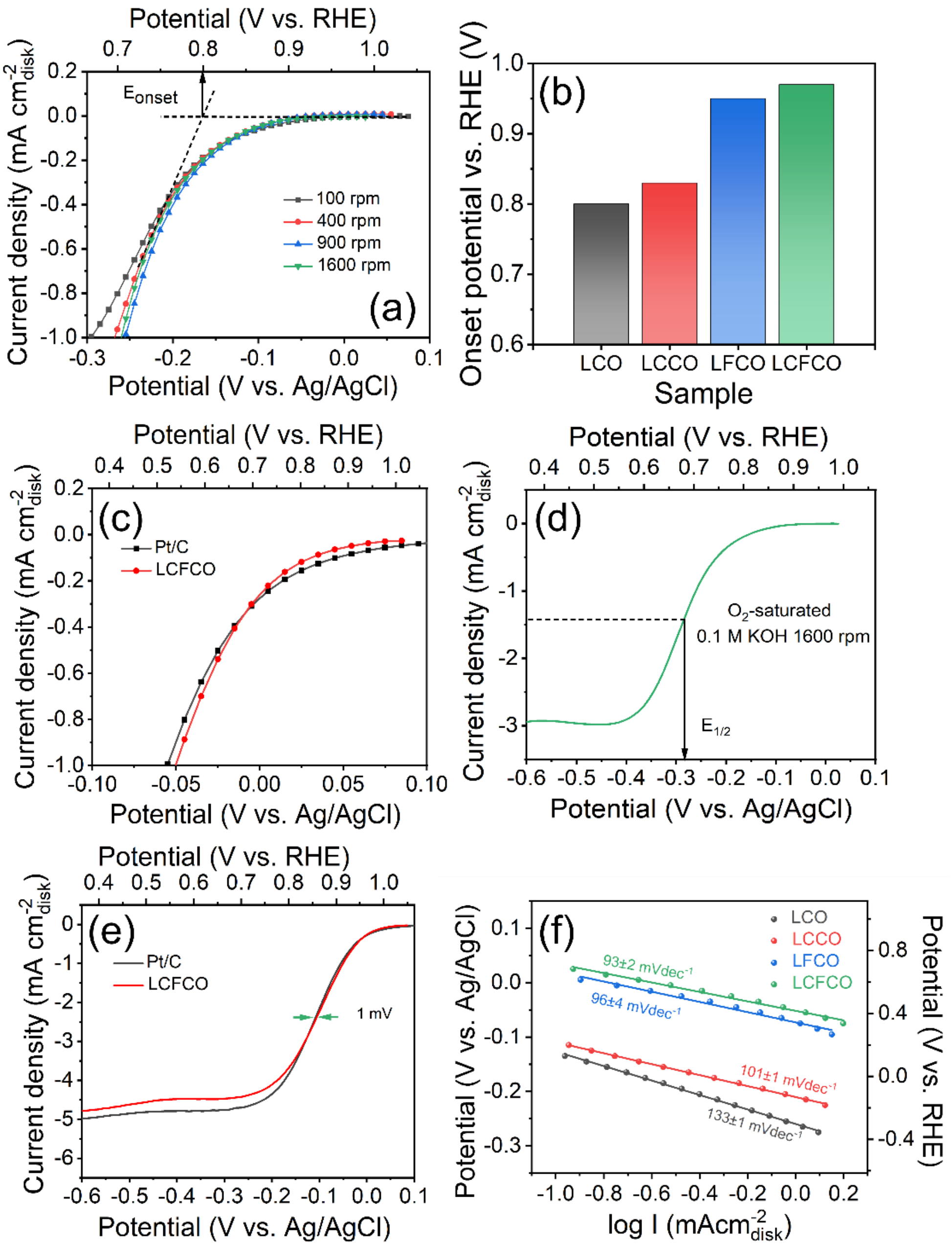

Fig. 6.11. (a) Example determination of E$_{onset}$ for the LCO electrocatalyst in O_2-saturated 0.1 M KOH solution [68]. (b) Onset potential values for the tested electrocatalysts in O_2-saturated 0.1 M KOH solution and room temperature; RDE rotation rate of 1600 rpm [68]. (c) Zoomed comparison of E$_{onset}$ between the Pt/C and LCFCO in O_2-saturated 0.1 M KOH solution [68]. (d) Example determination of $E_{1/2}$ for the LCO electrocatalyst in O_2-saturated 0.1 M KOH solution [68]. (e) Polarisation curves of Pt/C and LCFCO electrocatalysts with $E_{1/2}$ difference noted in O_2-saturated 0.1 M KOH solution: RDE rotation rate of 1600 rpm [68]. (f) Corresponding Tafel plots for perovskite oxides in O_2-saturated 0.1 M KOH solution [68].

As well as improved E_{onset} and $E_{1/2}$ values, the LCFCO electrocatalyst also shows an enhanced current density at the same potential over the same range compared to the undoped and singly doped counterparts (Fig. 6.12a). The enhanced ORR activity cannot therefore be merely described by differences in onset potential and half-wave potential.

Fig. 6.12b shows K-L plots for the electrocatalysts at an applied potential of -0.55 V vs. Ag/AgCl (0.41 V vs. RHE) using polarisation data obtained in Figs. 6.8b-e and the application of Eqs. (6.1-6.2). The K-L plots show that the diffusion currents for all samples linearly scale with $\omega^{1/2}$. The linearity of the data indicates that Eq. (6.1) is satisfied. From the slope of the lines and rearrangement of Eq. (6.2), the number of transferred electrons n per reduced oxygen molecule can be calculated. The results of this calculation are visually presented in Fig. 6.12c.

The results reveal that the number of electrons involved in the ORR mechanism changes on introduction of dopants indicating a change in the ORR pathway for the different electrocatalysts. The calculated average number of transferred electrons n follows the descending order of 4.0 > 3.8 > 3.4 > 3.2 for LCFCO > LCCO > LFCO > LCO. Based on this, it is evident that the presence of Cr plays a key role in increasing the number of electrons involved in the ORR mechanism and therefore plays a key role in the enhanced current density observed by LCFCO compared to LCO. This may be partly attributed to the oxygen species present on the surface of the perovskite [392].

Oxygen vacancy formation at the perovskite oxide surface has been reported to promote oxygen adsorption and charge transfer [29, 99, 159]. Although the exact $4e^-$ mechanism for ORR remains ambiguous, there are generally three proposed mechanisms based on the orientation of oxygen adsorption: (i) end-on (ii) side-on and (iii) bidentate absorption. The latter involves participation of oxygen vacancies and the B-site element [127]. This is discussed in greater detail in Chapter 2 but ultimately, oxygen vacancies have been recognised as an activity descriptor for ORR and have been found to have a profound effect on electrochemical activity of perovskite oxides [29]. Subsequently, several studies have reported the beneficial effects of surface oxygen vacancies on the ORR activity of perovskites as well as selectivity to the 4e$^-$ reduction pathway [29, 99, 159, 161, 162, 177, 402].

XPS analysis in Fig. 6.7 revealed that the mass percent of O_2^{2-}/O^- (O2) is higher in both LCCO and LCFCO than in LCO. As mentioned above, literature shows that this highly oxidative oxygen species (O_2^{2-}/O^-) is closely related to surface oxygen vacancies and defects [125, 142, 159, 388]. This can therefore be used as an indication of oxygen vacancy content present within the samples studied. The respective ratio of O2/(O1+O3+O4) was subsequently calculated to give an estimated oxygen vacancy ratio and is visually displayed in Fig. 6.12d [125, 142, 388].

On introduction of Cr, LCCO shows a large increase in oxygen vacancy ratio (34 %) and current density at the same potential over the same potential range compared to LCO (24 %). The results imply that oxygen vacancy formation can largely contribute to improved current density and that Cr plays a key role in doing so. Gao similarly reported that when introducing Cr doping, the $LaCr_{0.25}Fe_{0.25}O_3$ perovskite oxide possessed a higher ratio of oxygen defects, O2 (48.4 %), than other samples studied [142]. It was deduced that the presence of the Cr introduced more oxygen defects, in turn enhancing OER activity and the interaction of adsorbed oxygen-containing species. It is therefore established that Cr doping can lead to oxygen vacancy formation which increases ORR activity since oxygen vacancies have been found to improve selectivity towards the 4e$^-$ reduction pathway [159].

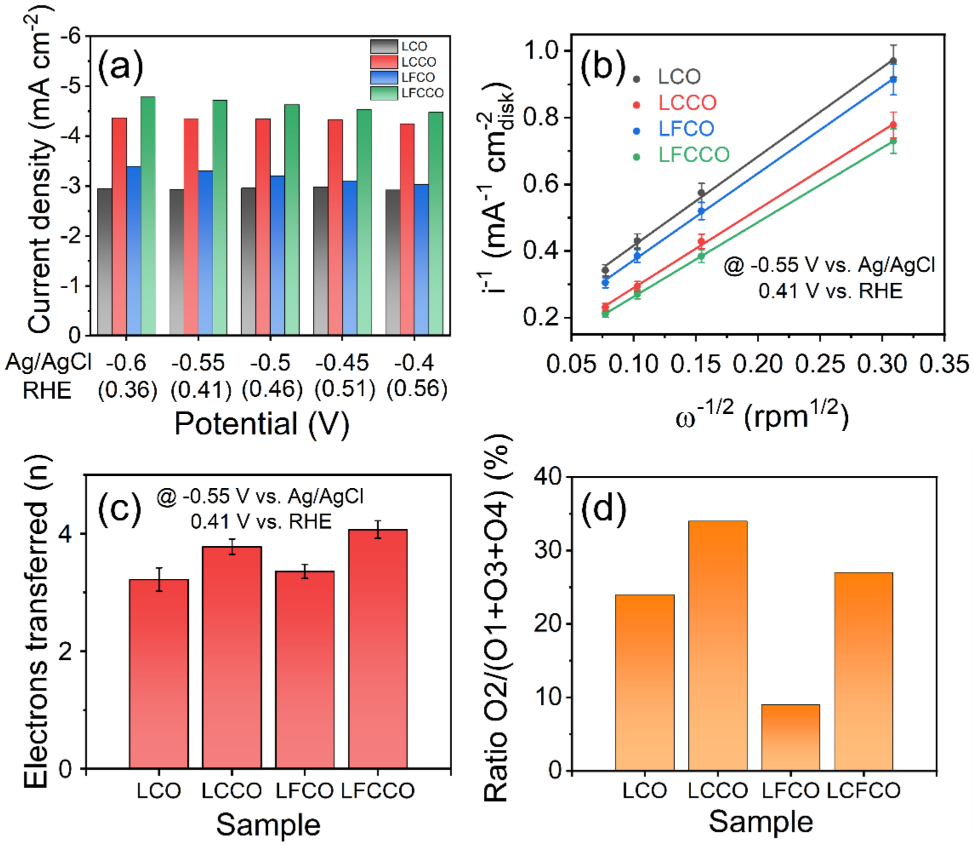

Fig. 6.12. (a) Bar graphs showing the tested LCO, LCCO, LFCO and LCFCO electrocatalyst current density responses at selected potentials [68]. (b) K-L plots for the LCO, LCCO, LFCO and LCFCO perovskites at a potential of -0.55 V vs. Ag/AgCl (0.41 V vs. RHE) [68]. (c) Calculated electron transfer number n for ORR using K-L slopes [68]. (d) Area ratio O2/(O1+O3+O4) in the tested electrocatalysts as deduced from XPS analysis [68].

The results of this study therefore correspond well with literature since the samples containing Cr (LCCO and LCFCO) have (i) the number of electrons transferred in the reaction mechanism being close to 4 which (ii) is owed to the enrichment of oxygen vacancies and (iii) is known to improve current density. It is reasonable to therefore assume that the oxygen vacancy content at the LCFCO surface (27 %) is heavily influenced by the presence of Cr and this species subsequently largely contributes to the enhanced current density observed.

On introduction of Fe, however, LFCO displays a lower ratio (9 %), which is indicative of a lower oxygen vacancy ratio, and minimal change in current density at the same potential over the same potential range compared to LCO. Similar trends in oxygen vacancy formation have been observed in literature [29, 99, 403]. Garcia-Lopez et al. for example, found a decrease in oxygen vacancy ratio with increasing substitution of Co by Fe in $La_{0.6}Sr_{0.4}Co_xFe_{1-x}O_{3-\delta}$ [403].

Apart from electrocatalytic activity, stability is another important factor for advanced electrocatalysts. The long-term stability of the LCFCO was confirmed by chronopotentiometry tests in O_2-saturated 0.1 M KOH solution at a fixed potential of -0.4 V vs. Ag/AgCl with a RDE rotation rate of 1600 rpm. As shown in Fig. 6.13a, LCO shows a decrease in stability over the testing duration. However, with the doped perovskite oxides and particularly the LCFCO electrocatalyst, there is an initial slight decrease during testing which then stabilises over the duration. The relative current density of LCFCO reaches around 94.5 % throughout the testing period, indicating that the electrocatalyst remains stable over an extended period. Notably, the stability of LCFCO is slightly higher than that of Pt/C (92.7 %) over the same testing duration and conditions (Fig. 6.13b). Similar stability of Pt/C (20 wt. %) electrocatalysts has been observed in literature, where a retention of 93.5 % was observed after 10000 s in O_2-saturated 0.1 M KOH solution with a RDE rotation rate of 1600 rpm [392]. The results signify that LCFCO is a highly active and stable electrocatalyst towards ORR.

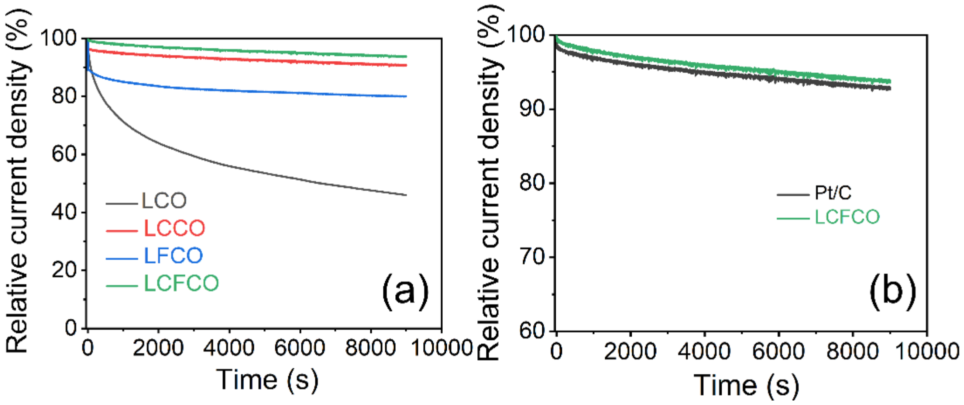

Fig. 6.13. (a) Chronopotentiometry analysis of the LCO, LCCO, LFCO and LCFCO perovskites held at a fixed potential of -0.4 V vs. Ag/AgCl in O_2-saturated 0.1 M KOH solution: RDE rotation rate of 1600 rpm [68]. (b)

Chronopotentiometry analysis of the Pt/C and LCFCO electrocatalysts held at a fixed potential of -0.4 V vs. Ag/AgCl in O_2-saturated 0.1 M KOH solution [68].

As mentioned in previous literature, ORR on perovskite oxides in alkaline media is complicated and the reaction depends on several factors such as intrinsic activity, conductivity and surface adsorption properties, all of which should not be considered independently [28, 99]. As proposed in earlier studies, changes in electronic structure can affect the rate determining steps and the overall ORR performance, with an optimum activity being observed when the e_g-filling is close to 1 [31, 104, 125, 126, 143-145].

Since the exact spin states of the transition metals in $LaCr_{0.25}Fe_{0.25}Co_{0.5}O_{3-\delta}$ have not been determined prior to this study, an approximation of the e_g-filling based on literature and XPS data provided in Table 6.4 and 6.5 has been made. Given that the B-site metal exhibits different valence states, the electronic filling of the e_g orbital becomes complex. It is often widely accepted that Co^{2+} (d^7) ions exist in high spin states ($e_g = 2$), whereas the spin state of Co^{3+} in $LaCoO_3$ has proven to be more difficult to determine. It is often accepted that that Co^{3+} exists in an IS state at temperatures above 70-90 K, rather than the Hund's predicted HS state ($t_{2g}^4e_g^2$) [377, 404, 405]. It is due to this phenomenon that Co^{3+} in $LaCoO_3$ is assumed to have unique electronic properties where the e_g occupancy is ~1 and explains its activity towards ORR. Although there is still extensive debate over the exact Co spin state, Co^{3+} is assumed to exist in an intermediate spin state (e_g ~1) for the simplicity of the calculations in this study [404-408]. Based on literature, Fe^{3+} tends to favour high spin configuration ($t_{2g}^3e_g^2$), leading to an e_g-filling of 2. Furthermore, XPS data also reveals that Cr in LCCO and LCFCO exists in the +6 and +3 oxidation state, with the latter being dominant. For e_g calculations, the effect of Cr^{6+} are neglected since there are no d electron orbitals and only Cr^{3+} ($t_{2g}^3e_g^0$) is considered, leading to an e_g-filling of 0. The average filling of electrons in the e_g orbital ($\bar{n}$) can be calculated based on Eq. (6.3) [125].

To find the average e_g-filling at the B-site, the following equation was [125]:

$$\bar{n} = \frac{1}{m} \sum_{Cr,Fe,Co} e_g^d p \tag{6.3}$$

Where $\bar{n}$ represents the average filling of electrons in the e_g orbital at the B-site, m represents the number of species occupying the B-site, e_g^d represents the number of electrons in the e_g orbitals of ions at different valency and P represents the percentage of ions at different valence states.

In LCO:

$$\bar{n} = \frac{1}{1}(2{\cdot}52.8\% + 1{\cdot}47.2\%)$$
$$= 1.5$$

In LCCO:

$$\bar{n} = \frac{1}{2}(2{\cdot}49.0\% + 1{\cdot}51.0\% + 0{\cdot}38.1\%)$$
$$= 0.75$$

In LFCO:

$$\bar{n} = \frac{1}{2}(2{\cdot}51.4\% + 1{\cdot}48.6\% + 2{\cdot}1\%)$$
$$= 1.76$$

In LCFCO:

$$\bar{n} = \frac{1}{3}(2{\cdot}48.3\% + 1{\cdot}51.7\% + 2{\cdot}1\% + 0{\cdot}38.1\%)$$
$$= 1.16$$

From the calculations, it can be seen that the e_g-filling of LCO was around 1.5 and approaches closer to unity when doped by both Cr and Fe in LCFCO where $e_g = 1.16$. The near unity e_g-filling found in LCFCO may also partially explain the enhanced ORR activity compared to its undoped and singly doped counterparts.

6.3.2.2. Effects of Final Calcinating Temperature

Since the lowest calcination temperature that the pure perovskite oxide phase could be formed at was 700 ^oC, the electrocatalytic performance of the LCFCO-700 towards ORR were evaluated in O_2-saturated 0.1 M KOH solution between -0.6 and 0.1 V vs. Ag/AgCl (0.36 to 1.06 V vs. RHE) at a scan rate of 10 mVs^{-1} was studied. The current densities (normalised to the geometric surface area of the electrode disk) vs. potential for the LCFCO-700 electrocatalyst at varying rotation rates of the RDE equal to 100, 400, 900 and 1600 rpm are shown in Fig. 6.14a. The potential range was chosen to avoid possible irreversible reduction of the perovskite catalysts by avoiding more cathodic potentials being applied. For comparison, the polarisation curves for the parent LCFCO perovskite sample and Pt/C electrocatalyst are also displayed in Fig. 6.14b and Fig. 6.14c respectively.

As expected, the current density increases with increasing rotation rate of the RDE. Fig. 6.14b illustrates the comparative current density vs. potential for the LCFCO-700 and LCFCO electrocatalysts with a rotation rate of the RDE equal to 1600 rpm. The key differences between the samples are: (i) LCFCO-700 shows a more positive E_{onset} potential compared to LCFCO, (ii) LCFCO shows a more positive $E_{1/2}$ potential (0.88 V vs. RHE) compared to LCFCO (0.86 V vs. RHE) and (iii) LCFCO-700 shows a slight increase in current density (-4.85 $mAcm^{-2}_{disk}$) compared to LCFCO (-4.77 $mAcm^{-2}_{disk}$) at a reducing potential of -0.6 V vs. Ag/AgCl (0.36 V vs. RHE). These improvements in performance may be attributed to the enhancement in the number of exposed active sites due to a higher SSA (Table 6.7). Similar trends have been seen by Retuerto et al. who found that the perovskite catalysts 700-$LaNiO_3$ and 800-$LaNiO_3$, which were calcinated at 700 and 800 ^oC respectively, showed more positive E_{onset} potentials than 900-$LaNiO_3$ and 1000-$LaNiO_3$, which were calcinated at 900 and 1000 ^oC respectively [38].

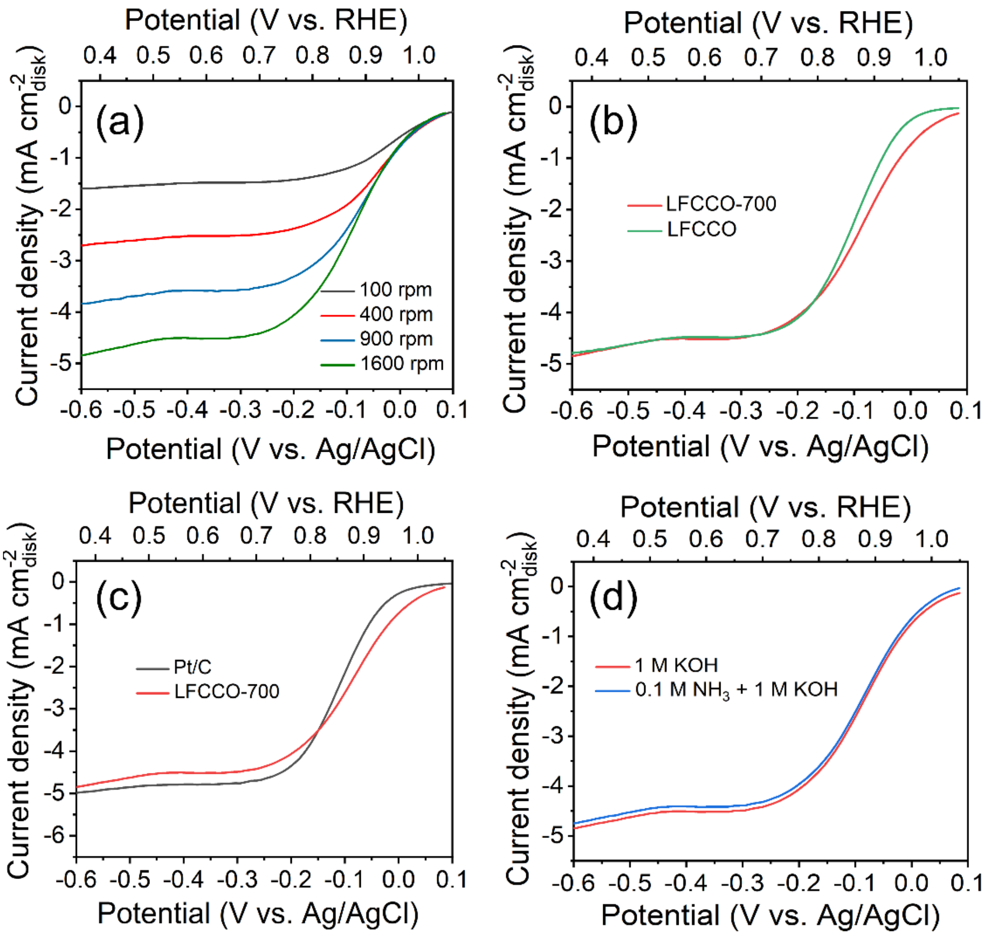

Fig. 6.14. (a) Polarisation curves of the LCFCO-700 perovskite in O_2-saturated 0.1 M KOH solution; RDE rotation rates of 100, 400, 900 and 1600 rpm [68]. (b) Polarisation curves obtained for the LCFCO-700 and LCFCO perovskites in O_2-saturated 0.1 M KOH solution: RDE rotation rate of 1600 rpm [68]. (c) Polarisation curves of Pt/C and LCFCO-700 electrocatalysts in O_2-saturated 0.1 M KOH solution; RDE rotation rate of 1600 rpm [68]. (d) Polarisation curves obtained for the LCFCO-700 in O_2-saturated 0.1 M KOH solution with and without 0.1 M NH_3: RDE rotation rate of 1600 rpm [68].

Moreover, Fig. 6.14c shows that LCFCO-700 has similar enhancement in E_{onset} and $E_{1/2}$ potentials compared to commercial Pt/C. Furthermore, the current density value is remarkably similar to the commercial Pt/C electrocatalyst, illustrating that LCFCO-700 is a promising candidate for ORR.

To assess applicability of the perovskite oxide as a cathode catalyst in DAFCs, certain conditions must be satisfied to transition the ORR electrocatalyst into a practical application. The choice of a cathode catalyst for DAFCs has been directed by: (i) the desire to reduce use of PGMs and (ii) a minimal impact on ORR activity in the presence of ammonia [77]. The latter stems from the acknowledgement that ammonia crossover to the cathode is common in existing in DAFCs [77]. This is largely due to the membrane thicknesses employed within these devices. Since membrane related ohmic losses within the DAFCs are a great limitation, thinner membranes are favourable to decrease OH^- diffusion and mass transfer. Reducing membrane thickness however, is known to lead to fuel permeation across the membrane, resulting in fuel crossover and flooding of the cathode [59]. This has been observed in cases which have led to a reduced OCV and overall fuel cell efficiency [89]. Suzuki et al. for example, obtained an OCV of 0.370 V whilst using Pt-based electrocatalysts at 20 ^{o}C, much lower than the expected theoretical value of 1.17 V due to ammonia cross over to the cathode [89]. Lee et al. displayed a similarly low OCV value of 0.360 V when using Pt-based electrocatalysts in an ammonia-fuelled AMFC [409]. Ishiyama et al. also exhibited a lower OCV than expected, with 0.45 V at 50 ^{o}C, [75].

This study has shown how the first directive mentioned above, the desire to reduce use of PGMs, is satisfied; there is a reduced reliance on PGMs and the study makes use of a more readily available and cost efficient LCFCO-700 perovskite oxide that shows comparable ORR activity to commercial Pt/C. To satisfy the second requirement, that being a minimal impact on ORR activity in the presence of ammonia, the LCFCO-700 perovskite oxide was tested in O_2-saturated 0.1 M KOH solution with and without the presence of 0.1 M NH_3 to mimic the effects of ammonia fuel cross over in a DAFC. Fig. 6.14d shows that on introduction of 0.1 M NH_3, there is negligible change in ORR activity for the LCFCO-700 perovskite oxide, indicating that the ORR activity is not affected by the presence of a small amount of ammonia. It can therefore be reasonably assumed that there will be minimal negative effect of ammonia cross-over if LFCCO-700 were to be employed as a cathode in a DAFC, making it a suitable and promising candidate.

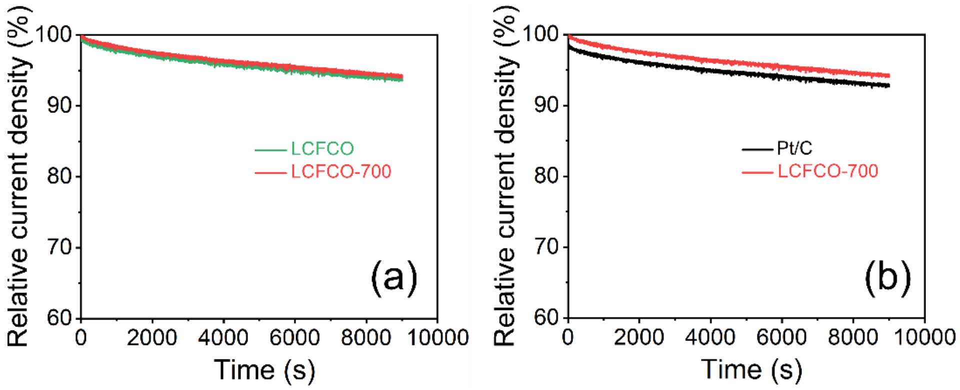

Fig. 6.15. (a) Chronopotentiometry analysis of LCFCO and LCFCO-700 perovskites held at a fixed potential of -0.4 V vs. Ag/AgCl in O_2-saturated 0.1 M KOH solution: RDE rotation rate of 1600 rpm [68]. (b) Chronopotentiometry analysis of the Pt/C and LCFCO-700 electrocatalysts held at a fixed potential of -0.4 V vs. Ag/AgCl in O_2-saturated 0.1 M KOH solution [68].

Furthermore, the long-term stability of LCFCO-700 was confirmed by chronopotentiometry tests in O_2-saturated 0.1 M KOH solution at a fixed potential of -0.4 V vs. Ag/AgCl with a RDE rotation rate of 1600 rpm. As shown in Fig. 6.15a, LCFCO and LCFCO-700 show minimal difference in their stability over the testing duration, with the former retaining 94.5 % and the latter 94.8 %. The results imply that the same catalytic stability can be achieved when the perovskite is calcinated at lower temperatures. This confirms that the perovskite oxide activity is not adversely impacted by varying calcinating temperature and allows a good, stable catalyst to be synthesised at lower temperatures, saving costs on furnace and heating operation. Notably, the stability of LCFCO-700 remains slightly higher than that of Pt/C over the same testing duration and conditions (Fig. 6.15b). The results signify that LCFCO-700 is a highly active and stable electrocatalyst towards ORR.

The results demonstrate that the LCFCO-700 perovskite oxide is an excellent, cheap catalyst for ORR and is a promising candidate as an electrocatalyst for cathodes in real DAFC devices.

6.4. Conclusions

A series of LCO-based perovskite oxides including LCCO, LFCO and LCFCO were prepared by a simple sol-gel method and their ORR activity was studied in 0.1 M KOH solution at room temperature using a RDE technique. The extrinsic (surface area and particle size) and intrinsic (formation of oxygen vacancies, oxidation states, occupancy of e_g levels) properties of electrocatalysts were evaluated to explore the synergetic effects of doping both Cr and Fe at the B-site of LCO. Since LCFCO is a novel perovskite oxide, its synthesis method was explored by varying final calcinating temperatures. The key findings of the study are as follows:

(i) The highest and lowest ORR activities amongst the different electrocatalysts were exhibited by LCFCO and LCO respectively.

(ii) The presence of both Cr and Fe were found to play vital roles in enhancing activity, synergistically contributing towards ORR activity.

(iii) Doping of Cr was associated with induced changes in the surface oxygen vacancy formation and an increase in the number of transferred electrons to 4.

(iv) Introduction of Fe led to a clear enhancement in onset potential E_{onset}, with LCFCO, LFCO, LCCO and LCO exhibiting E_{onset} values of 0.97, 0.95, 0.83 and 0.80 V vs. RHE respectively.

(v) Effects of calcining temperatures were explored and LCFCO fired at 700 ^{o}C (LCFCO-700) was found to give superior activity, showing ability to obtain excellent performance at a lower synthesis temperature and cost.

(vi) Extremely similar E_{onset} potentials which were more positive than 0.95 V were obtained for both LCFCO-700 and Pt/C. $E_{1/2}$ values of 0.88 and 0.85 V were obtained for LCFCO-700 and Pt/C electrocatalysts respectively. Stability remained fairly similar over the testing period, with a retention of 94.8 and 92.7 % for LCFCO-700 and Pt/C respectively.

(vii) ORR activity of LCFCO-700 is not affected by the presence of a small amount of ammonia.

The results of this chapter conclude that LCFCO-700 is a promising electrocatalyst for ORR owed to its high activity and stability. A similar performance was obtained when using a PGM-based electrocatalyst, showing the potential to significantly reduce costs at the cathode side of DAFCs in practical applications.

CHAPTER 7 Optimisation of Cathode Electrode in a Direct Ammonia Fuel Cell

The works in this chapter form parts of the publications by the author in Applied Catalysis B: Environmental [68]. The content also forms part of a paper by the author which is currently under review in ACS Applied Materials & Interfaces [70].

7.1. Background

Electrochemical reactions occur at the three-phase interface of the CL; thus, CLs play a significant role in the performance of fuel cells. There are several critical requirements that must be satisfied to make a successful CL within a working fuel cell: (i) catalytic activity towards the given reaction (ii) electronic conductivity (iii) ionic conductivity and (iv) good chemical and mechanical stability. In the previous chapter, the first requirement was satisfied and showed that the LCFCO-700 perovskite oxide exhibited superb catalytic activity towards ORR. The other requirements, however, have not been studied and must be addressed for successful implementation of the catalyst into the CCL of a practical DAFC.

As mentioned earlier, the transport pathways of electrons, ions and reactants should be connected well to maximise interactions at the interface. It is widely known that CLs are a multi-composite structure composed of the catalyst, carbon supports, ionomer materials and void regions, whereby carbon and ionomers are used to provide the electron and ionic conduction networks respectively and void regions provide mass transport channels for the reactants and products. In turn, these components may satisfy the requirements mentioned earlier and be used to fabricate a successful CCL for DAFCs that can achieve high utilisation of the catalyst material and improve cell performance [226-228].

Despite the wider selection of electrocatalyst choice in DAFCs, their adoption requires further development to be competitive fuel cell devices. For example, optimisation of the entire CL for such systems has not been explored, despite the clear benefits of doing so in PEMFCs, as mentioned in Chapter 2. Moreover, many studies utilise commercial Pt/C where carbon is already embedded into the local structure of the catalyst [39, 58, 74, 76, 224, 226, 229, 231-235]. However, materials such as perovskite oxides, which offer excellent catalytic activity towards ORR and therefore serve as superb cathode catalysts, do not incorporate carbon into their conventional Pechini synthesis method. Although it has been recognised that physically mixing carbon with perovskites to form composites can act as a conductive support and increase electrical conductivity, the effect of mixing different catalyst to carbon ratios on CCL performance in DAFCs has not been explored [29]. This opens doors for further optimisation of CCLs in these devices.

This chapter builds upon aspects covered in Chapter 5 and Chapter 6 by employing the in-house DAFC device and the as-prepared perovskite oxide catalysts to assemble an efficient CCL and implement this into a working fuel cell device. Literature in the specific area of CCL optimisation in DAFCs is relatively unknown. This chapter therefore employs an optimised CCL, in terms of its carbon, PTFE and ionomer content to truly exploit the catalytic activity of the perovskite oxide and to satisfy the requirements of a successful CL. Furthermore, operating conditions such as cell temperature and KOH concentration were varied to explore the applicability of such a device under different settings. The perovskite-based CCL was then compared to a Pt/C-based CCL in a DAFC under the same conditions to compare cell performances.

7.2. Experimental

7.2.1. Materials

Carbon cloth (1071 HCB, Fuel Cell Store) was used as the diffusion substrate layer. Carbon black (Vulcan XC-72R) was used as a highly conductive material. PTFE was purchased as a suspension from Sigma Aldrich and used as the hydrophobic agent. PiperION BP-100 (PAP-BP-100) was used as the ionomer (Versogen) and a 20 µm PiperION-A20-HCO3 TP-85 (PAP-TP-85) membrane (Versogen) was employed. Other chemicals such as isopropanol and KOH were all analytical grade reagents purchased from Alfa Aesar. Furthermore, Pt/C was commercially purchased (commercial 20 wt. % platinum on carbon black, Alfa Aesar).

7.2.2. Electrode Preparation

The effects of carbon black, PTFE and ionomer content on fuel cell performance were sequentially tested and the general procedure for making the CCL is shown in Fig. 7.1.

First, carbon cloth was washed and sonicated in dilute hydrochloric acid, isopropanol and deionized water. Then, the LCFCO-700 perovskite oxide powder was physically mixed with high surface area carbon black (Vulcan XC-72R) at 10, 30, 50 or 80 wt. % relative to the perovskite weight. Utilising propanol as the solvent, the PiperION BP-100 ionomer was ultra-sonicated in an ice-water bath for 1 h with perovskite/carbon black (CB) using an arbitrary amount of PTFE and PiperION BP-100 at 10 wt. % and 20 wt. % relative to the perovskite weight respectively. The ink was then brushed onto the pre-treated carbon cloth to prepare a GDE and left to dry. The loading was found to be 1.28, 1.24, 1.23 and 1.32 mg_{oxide} cm^{-2} when carbon amounts of 10, 30, 50 or 80 wt. % were used respectively. When the optimum carbon wt. % was found, the PTFE content was adjusted to 0, 35 or 50 wt. % with respect to perovskite weight whilst the PiperION BP-100 content and remaining reagents were kept constant. The loading was found to be 1.20, 1.21 and 1.28 mg_{oxide} cm^{-2} when PTFE at 0, 35 and 50 wt. % was used respectively. Similarly, when both the optimum carbon and PTFE content was identified, the PiperION BP-100 content was adjusted to 0, 35 or 50 wt. % with respect to perovskite weight. The loading was found to be 1.29, 1.30 and 1.21 mg_{oxide} cm^{-2} respectively. All additives were adjusted according to perovskite weight, herein wt. % therefore simply refers to the weight percentage of the additive with respect to the LCFCO-700 perovskite oxide.

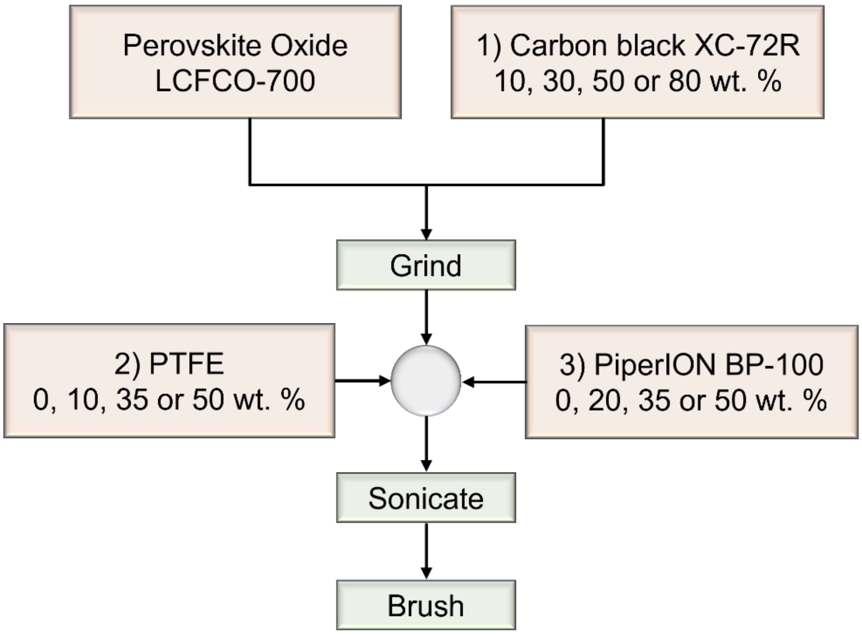

Fig. 7.1. General experimental procedure with weight percentages given with respect to perovskite weight [70].

For comparison, a similar method was employed to fabricate a Pt/C electrode (with a PTFE and PiperION BP-100 ionomer content of 10 and 20 wt. % with respect to Pt/C respectively) and a loading of 0.4 $mg_{PGM}cm^{-2}$ was achieved. PtIr(40 wt. %)/C(60 wt. %) powder was prepared using a method described elsewhere and was employed as the anode catalyst [410]. Utilising propanol and water as the solvent, the PiperION BP-100 ionomer (20 wt. %) was ultra-sonicated in an ice-water bath for 1 h with PtIr/C to form a uniform dispersion. The ink was then brushed onto a pre-treated carbon cloth and a loading of 2.2 $mg_{PGM}\cdot cm^{-2}$ was obtained.

7.2.3. Physicochemical Characterisation

XRD analysis was used to examine the phase and purity of the perovskite oxide powder and CLs. Measurements were carried out at room temperature on a PANalytical X'Pert Pro diffractometer (Cu Kα source, 1.5405 Å) and collected in the 2θ range of 20-80° with a step of 0.0167°. Phase analysis and identification was conducted via the HighScore software.

To evaluate the distribution of grain sizes and account for the non-coherent domains, SEM images were taken. SEM was used to examine the morphology of the CLs at the surface using a Zeiss SUPRA 55-VP, equipped with an EDS spectrometer for elemental and point analysis.

7.2.4. Single Cell Evaluation Test

The test conditions for the single cell with an active area of 1 cm^2 was anode fuel: 2 mL min^{-1} 7 M NH_4OH + 1 M KOH at 3 bar and cathode fuel: 180 mL min^{-1} CO_2-free air fed through a humidifier at a temperature of 95 °C at 2 bar. The operating temperature of the cell was 80 °C. The corresponding polarisation curves were obtained using a Solartron 1287A Electrochemical Station. EIS was conducted on a Solartron 1260A at a frequency range of 1 MHz to 0.01 Hz and the voltage was set to the OCV for each test conducted..

7.3. Results and Discussion

Due to its promising activity towards ORR and minimal change in the presence of small amounts of ammonia as discussed in Chapter 6, LCFCO-700 was considered as the cathode catalyst in the tested DAFCs. To assess the performance of the perovskite oxide, a catalyst ink was prepared and brushed onto the carbon cloth GDL to form a GDE. PtIr/C was used as an anode and PiperION-A20-HCO3 TP-85 was utilised as the membrane to form a MEA, shown in Fig. 7.2.

Fig. 7.2. Prepared MEA for DAFC.

To maximise fuel cell performance, transport pathways for electron and ionic conductivity as well as those for reactants within the CLs should be well-connected. These parameters can be controlled by addition of carbon, ionomer and a hydrophobic agent into the CCL design. The effects of each were investigated and several GDEs were fabricated to be tested in the DAFC.

As mentioned, a series of CCLs were fabricated based on varying carbon amount to find the optimum carbon content. Four GDEs were assembled where carbon in the CCL was varied to 10, 30, 50 or 80 wt. %, hereby referred to as CCL-C10, CCL-C30, CCL-C50 and CCL-C80 respectively. Meanwhile, arbitrary amounts of PTFE (10 wt. %) and ionomer (20 wt. %) were chosen. The carbon content delivering optimum performance was then used as a baseline as PTFE content was explored. Three further GDEs were assembled where PTFE in the CCL was varied to 0, 35 or 50 wt. %, hereby referred to as CCL-P0, CCL-P35 and CCL-P50 respectively. As a comparison, CCL-C50 (10 wt. % PTFE) was also compared in this series. Upon optimisation of both CB and PTFE, ionomer content was investigated. Three further GDEs were assembled where ionomer in the CCL was varied to 0, 35 or 50 wt. %, hereby referred to as CCL-I0, CCL-I35 and CCL-I50 respectively. Again, for comparative purposes, CCL-C50 (20 wt. % ionomer) was also compared in this series.

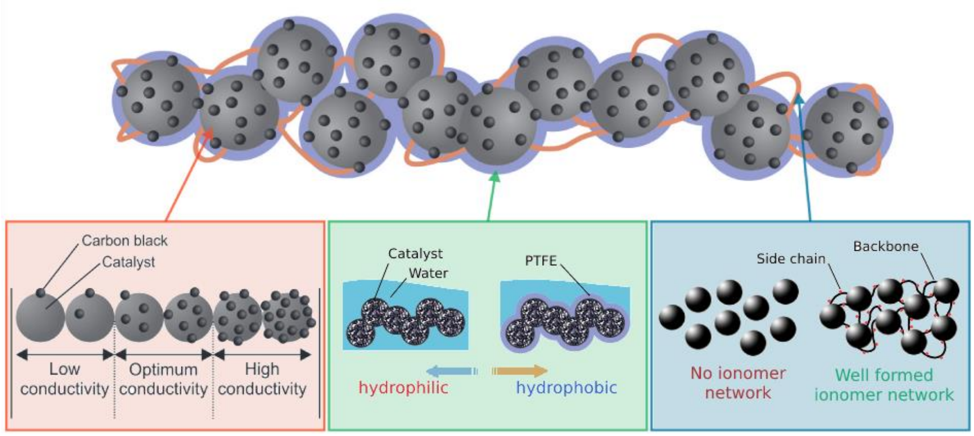

Fig. 7.3. Illustration demonstrating the contributing effects of different components within CCLs for DAFCs [70].

It should be noted that KOH was added to the anodic fuel in the tests since hydroxide ions are found to play a role in the reaction mechanisms that take place in DAFCs. To enhance the power density of fuel cells, OH^- ions are typically introduced at the anodic sites to increase the rate of the reaction stated in Eq. (1.3) and to reduce the mass transfer of OH^- ions across the AEM.

Furthermore, the use of CO_2-free air was paramount since CO_2 reacts with OH^- to form CO_3^{2-} ions [6]. Due to this, it is common practice to use pure O_2 or CO_2-free air as the oxidant at the cathode to avoid the formation of CO_3^{2-} ions and to accomplish practical longevity of AMFCs such as DAFCs [66, 88].

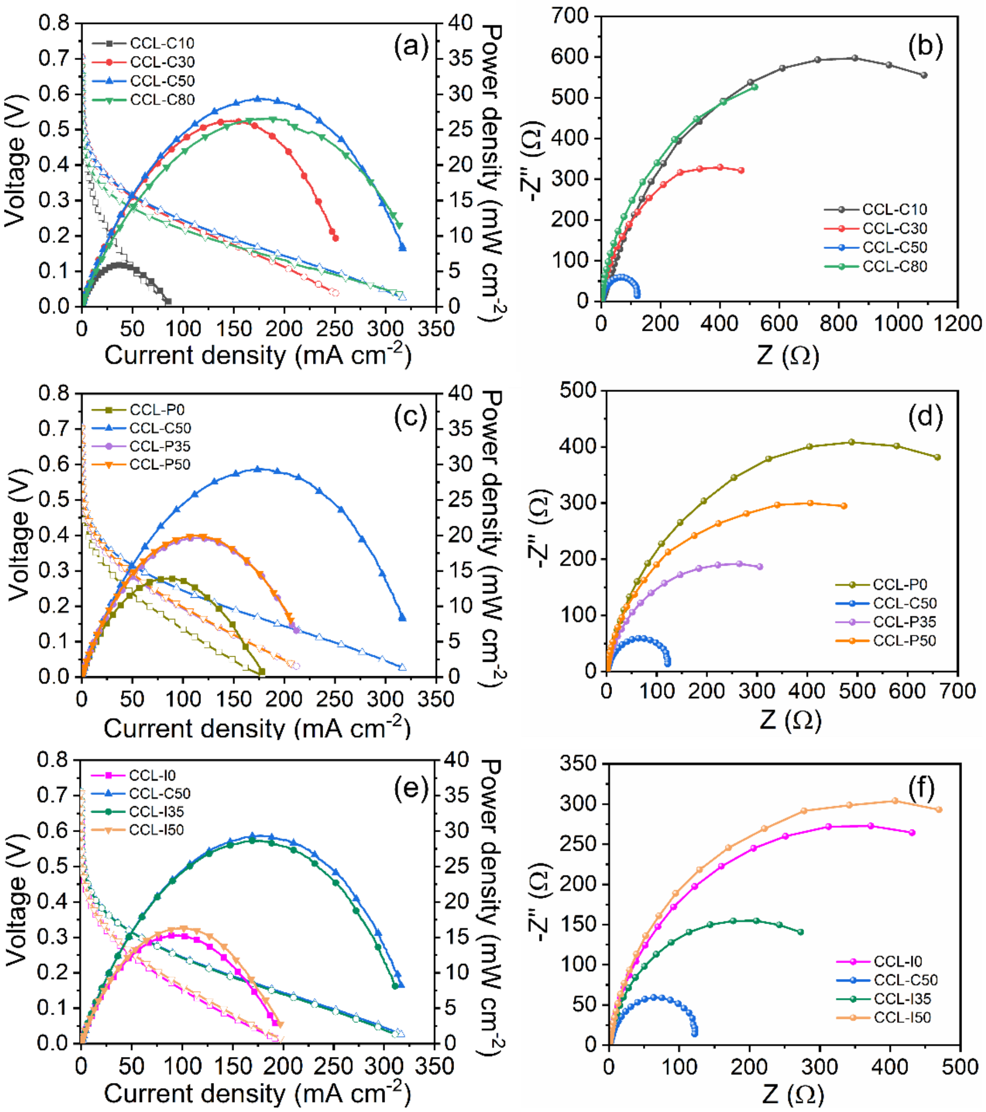

Fig. 7.4. (a) Polarisation and power density curve and (b) EIS data of CCLs with varying carbon content [70]. (c) Polarisation and power density curve and (d) EIS data of CCLs with varying PTFE content [70]. (e) Polarisation and power density curve [70]. (f) EIS data of CCLs with varying ionomer content [70]. Anode: 2.2 mg_{PGM} cm^{-2} PtIr(40 wt. %)/C(60 wt. %). Cathode: LCFCO. Test conditions: (1) Anode: 2 mL min^{-1} of 7 M NH_4OH with 1 M KOH; Anode back pressure: 3 bar_g (2) Cathode: 180 mL min^{-1} CO_2-free air through humidifier of T = 95 °C; Cathode back pressure: 2 bar_g. Cell temperature: 80 °C.

Figs. 7.4a, 7.4c and 7.4e show the cell performances of the ten corresponding DAFCs and the EIS data is shown in Figs. 7.4b, 7.4d and 7.4f. The results from the polarisation curves are further highlighted in Table 7.1.

Table. 7.1. DAFC performances based on varying carbon, PTFE and ionomer content in CCLs [70].

Optimisation		**Carbon wt. %**	**PTFE wt. %**	**Ionomer wt. %**	**OCV (V)**	**Maximum current density (mA cm^{-2})**	**PPD (mW cm^{-2})**
Carbon	CCL-C10	10	10	20	0.72	85.3	5.92
	CCL-C30	30	10	20	0.71	250	26.2
	CCL-C50	50	10	20	0.71	317	30.1
	CCL-C80	80	10	20	0.70	312	26.5
PTFE	CCL-P0	50	0	20	0.69	179	13.9
	CCL-P35	50	35	20	0.71	206	20.1
	CCL-P50	50	50	20	0.71	212	19.7
Ionomer	CCL-I0	50	10	0	0.65	192	15.2
	CCL-I35	50	10	35	0.71	311	28.6
	CCL-I50	50	10	50	0.71	197	16.3

All wt. % given with respect to perovskite weight.

The individual influence of varying carbon, PTFE and ionomer content were investigated in greater detail and are discussed in the following sections. To understand the effects of each component added, it is useful to consider the fuel cell performance in three regimes: (i) activation polarisation losses, (ii) ohmic polarisation losses and (iii) concentration polarisation losses which affect the low, middle and high current density regimes respectively [39, 411].

7.3.1. Effect of Carbon Content

Most traditional metal oxides have inherently low electrical conductivity at low temperature, therefore exploiting the true electrocatalytic activity of these catalysts is difficult. To overcome this limitation, addition of carbon to form perovskite/carbon composites is a useful strategy to improve ORR activity and the advantages of doing so are clearly evidenced by RDE experiments

[29, 124, 126, 143-145, 157, 158, 169, 174-185]. Addition of carbon black has therefore become a common method to measure and compare ORR activity of transition metal oxides [29]. Literature regarding variations in carbon black type as well as the mass ratio of perovskite:carbon has consequently been explored [29, 124, 126, 143-145, 157, 158, 169, 174-180]. These studies highlight the importance of properly tailoring perovskite:carbon ratios on ORR performance; yet these ratios may not directly translate to the best ratio in CCLs and such an effect has not widely been studied in the adoption towards practical applications such as in DAFCs.

Zou et al. was first to utilise perovskite oxides as non-PGM-based cathodes for use in a DAFC by physical mixing with carbon black in an arbitrary ratio of 5:1 to improve electrical conductivity [33, 34]. However, neither study explored the effects of properly tailoring and optimising the perovskite:carbon ratio on performance of the cell to truly appreciate the impact of a good electrical conductivity network throughout the CCL. The polarisation and EIS data of the DAFCs with varying carbon amount in the CCL is subsequently explored and the results are shown in Figs. 7.4a-b.

OCV, current density and PPD are often quoted in literature and are used as parameters to compare fuel cell performances. Amongst the four cells, OCV values remained fairly unchanged, with values of 0.72, 0.71, 0.71 and 0.70 V being obtained for CCL-C10, CCL-C30, CCL-C50 and CCL-C80 respectively. The results indicate that the effect of carbon content on OCV is minimal.

The current density shows a substantial improvement as the carbon content is varied from 10 to 30 wt. %, with values of 85.3 and 250 mA cm^{-2} respectively. As carbon content is increased to 50 wt. %, this further increases to 317 mA cm^{-2}. In CCL-C80, however, there is a slight decrease in current density to 312 mA cm^{-2} which may be due to potential blockage of the active sites on the perovskite catalyst by carbon. More notably perhaps, is that the PPD shows a great improvement, from 5.92 to 30.1 mW cm^{-2} as carbon content is increased from 10 to 50 wt. %. This demonstrates a performance increase of nearly five times by properly tailoring carbon content, highlighting the crucial significance and need to explore carbon ratios within the CCL.

When examining the polarisation curves in greater detail, further information regarding the effects of carbon content within the CCL can be extracted. The DAFC employing CCL-C10 shows a substantial drop in voltage at lower current density compared to the cells with higher carbon content. The overpotential associated with this regime arises from activation losses. It is known this activation overpotential (η_a) is linked to electron transfer at the electrode-electrolyte interface. Electron accumulation for example, due to inefficient electron transport at the electrode surface may produce an energy barrier for incoming electrons [11]. Since perovskite oxides have inherently low electrical conductivity, increasing the content of carbon in the catalyst layer can assist in reducing this overpotential by creating an electronic network. This is evidenced in the DAFCs employing CCL-C30, CCL-C50 and CCL-C80 which exhibit a smaller drop in voltage at lower current densities.

Furthermore, carbon black in CCLs can influence the extent of ohmic losses since these losses occur partially due to the resistance of electron flow through electrically conductive fuel cell components [412]. Thepkaew et al., for example, found that ohmic losses are heavily influenced by carbon [230]. Referring to the middle regime of the polarisation curves which is closely linked to ohmic overpotential (η_o), the drop in voltage becomes less prevalent as carbon content is increased from 10 to 50 wt. %. The results imply that the extent of ohmic losses are reduced upon increasing carbon amount throughout the CL. Since the remaining cell components such as electrolyte, GDL, FFPs, current collectors and interface contacts are unchanged throughout the tests, this can be owed to the superb electronic conductivity of carbon which provides a sufficient network for electrons to travel to and from active sites of the catalyst layer. As carbon content is further increased to 80 wt. % there is a slight decrease in performance. Nonetheless, the overall improvement in performance as carbon content is increased reinforces the notion that carbon black can facilitate electrical contact between the oxide particles and help eliminate issues relating to electronic conductivity [185].

Some studies have suggested that carbon plays a more complex role than just a simple conductive support. It has been suggested, for example, that formation of the perovskite-carbon interface could change the electronic/crystal structure of perovskite oxides by altering the oxidation state of the transition metal, subsequently affecting the reaction mechanism and performance towards oxygen electrocatalysis [29, 190, 191]. Though this has been stated, the perovskite/carbon composite in the described literature was prepared by first synthesising the perovskite oxide powder and then growing nitrogen-doped carbon deposits onto the perovskite surface using chemical vapour deposition [191]. It was found that the crystalline structure of the perovskite completely changed after carbon growth and the corresponding XRD pattern was complex.

To ensure that no changes in crystal structure arose from physically mixing perovskite to carbon black within CCL-C50, XRD analysis was conducted (Fig. 7.5). It was found that no changes occurred in the crystal structure of the perovskite oxide after addition of carbon in the CCL, and the reflective peaks belonging to the perovskite phase remain unchanged. Compared to the pure perovskite oxide powder, additional peaks at 2θ values of 18.0° and 31.5° arose due to the [100] and [110] planes of PTFE (PDF: 00-060-1504) in the CCL. XRD analysis also reveals presence of the carbon cloth diffusion layer which is included for reference.

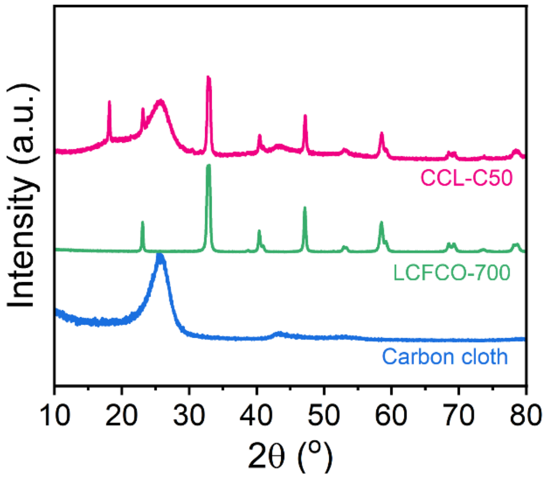

Fig. 7.5. XRD analysis of carbon cloth (blue), LCFCO perovskite powder (green) and CCL-C50 (pink) [70].

Moreover, some research groups have found that carbon black in perovskite/carbon composites actually participate in the ORR mechanistic pathway by first catalysing O_2 reduction to HO_2^- [29, 182, 183, 185, 192-196]. This, however, is more difficult to be precisely investigated. Regardless of its nature, the effect of carbon on increased DAFC performance is clear.

To study resistance of the cells, EIS of the cells was carried out. EIS data is commonly fitted to an equivalent circuit which combines resistances and specific electrochemical elements such as the double layer (modelled as capacitance) as well as inductance and Warburg diffusion elements [268, 413]. A constant phase element (CPE) tends to substitute the capacitance in electrochemical circuits due to the inhomogeneity of the testing conditions such as electrode roughness, coating and distribution of reaction rate [268, 414]. A simple equivalent circuit for electrochemical devices include the combined effects of solution resistance (R_s), anodic polarisation resistance (R_a) and cathodic polarisation resistance (R_c). The sum of such resistances (R_s, R_a and R_c) can be modelled as R_{in}. In systems where ohmic resistance is strong, such as in fuel cells, EIS can be employed to efficiently measure R_{in}, which takes into consideration resistances at the electrode-electrolyte interface [268, 413].

The plot in Fig. 7.4b shows EIS data of the different DAFCs employing CCLs with varying carbon content. The resistance includes the combined effects mentioned above and can be modelled as R_{in}. Since the remaining components within the fuel cell are constant throughout the different tests, the change in EIS data can be owed to the varying CCLs employed and therefore more closely resemble the cathode activation loses. As carbon content is increased from 10 to 50 wt. %, there is an obvious improvement in resistance which is evidenced by smaller semi-circles. The results imply that there may be better contact at the electrode-electrolyte interface. This can be owed to the large surface and contact area provided by Vulcan XC-72R. Since bulk perovskite oxides tend to be highly sintered due to the elevated temperatures required for phase formation, these materials tend to have a low specific surface area (of order of 2-10 m^2g^{-1}). This leads to poor mass activity towards oxygen electrocatalysis [38, 99]. Vulcan XC-72R, on the other hand, has a specific surface area of 216 m^2g^{-1} and is often used as a support to widen the surface utilisation of perovskites [29, 185]. Table 7.2 lists surface area values for LCFCO-700 and Vulcan XC-72R; Pt/C is also included for comparison. Moreover, when the carbon content was excessive and increased to 80 wt. %, there was an increased resistance present within the electrode.

Table 7.2. Surface area of materials used in catalyst layers [70].

Material	**Surface area ($m^2 \cdot g^{-1}$)**
Pt/C	103-112 [415]
LCFCO	5.2 [68]
Vulcan XC-72R	216 [185]

The need to optimise carbon content in CCLs is clear and is in accordance with literature where carbon is extensively used as a conductive support for a wide range of electrocatalysis applications due to its good electrical conductivity, low cost, good chemical stability and high surface area [29, 39]. The results demonstrate the importance of properly tailoring carbon content in the CCL and is reflected by the substantial differences in DAFC performance. In this study, an optimum carbon black weight of 50 wt. % with respect to the perovskite oxide was found to provide optimum DAFC performance and a sufficient electron network throughout the entire GDE.

7.3.2. Effect of PTFE Content

The effect of hydrophobicity in CCLs has extensively been explored in PEMFCs. These devices must effectively manage water generation at the cathode since the presence of water can fill voids in the gas diffusion layer and hinder gas transport leading to reactant starvation. Distinctive pathways for gas and liquid transport should therefore be provided to reduce reactant starvation. Hydrophobic nanoparticles such as PTFE are subsequently added to the CL structure to create two-phase flow for excess water removal and easy access for reactants to active catalyst sites [232].

Although the specific effects of varying hydrophobicity in CCLs of DAFCs has not been as widely investigated, it has been noted that the mere presence of a hydrophobic agent (PTFE) in the CCL can significantly improve DAFC performance and durability. Wang et al. showed that the rate of water exiting the cathode exhaust when the anode feed was aqueous ammonia was substantially higher than that measured when the anode feed was a hydrogen/water vapor mixture [77]. The results revealed a significant rate of liquid water crossover from anode to cathode in DAFCs, with most water crossing through the cathode CL before exiting the exhaust. Crossover from anode to cathode is often driven by high water concentration gradients between the two electrodes and is facilitated by the high water permeability of alkaline exchange membranes. This phenomena has been linked to oxygen transport limitations [77]. To reduce flooding tendency, a GDE-based cathode with PTFE was fabricated and an increase in the contact angle of water on the surface was found, thereby providing better resistance to water flooding and to the facilitation of oxygen transport in the CL. Compared to the CCM-based cathode with no PTFE, the GDE-based cathode with PTFE displayed higher performance, validating the need of PTFE. However, the effects of varying hydrophobicity in CCLs to find optimum content within the GDE on DAFC performance was not explored.

Since there is obvious evidence of flooding at the cathode due to liquid water cross over, water management is therefore still of interest in CCLs of DAFCs. Study into the effects of PTFE content and hydrophobicity of the CCL is consequently imperative. The polarisation and EIS data of the DAFCs with varying PTFE amount in the CCL is shown in Figs. 7.4c-d.

OCV of the four cells showed minimal deviation, with values of 0.69, 0.71, 0.71 and 0.71 V being obtained for CCL-P0, CCL-C50, CCL-P35, CCL-P50 respectively. The results imply that the presence of varying PTFE content had minimal impact on OCV.

In the absence of PTFE, the DAFC utilising CCL-P0 shows poorest performance, with a maximum current density and PPD of 179 mA cm^{-2} and 13.9 mW cm^{-2} respectively. As PTFE content is increased to 10 wt. %, performance almost doubles, with a maximum current density and PPD of 317 mA cm^{-2} and 30.1 mW cm^{-2} respectively. The results show that PTFE in the CCL is crucial for DAFC performance and may be explained by the construction of mesoporous hydrophobic channels through the CCL, which promote enhanced water management [232]. It is well recognised that binders such as PTFE often form a porous CL that efficiently facilitates hydrophobic channelling and transport of reactants and products [224, 226-229, 231-236]. This is due to the creation of void regions, which may otherwise be flooded by water, which can provide mass transport channels to and from the active site of the catalyst. On further increase of PTFE content however, performance declines, with PPDs of 20.1 and 19.7 mW cm^{-2} in the DAFCs employing CCL-P35 and CCL-P50 respectively.

When more carefully examining the polarisation curves, the performances of the cells vary greatly at the middle and high current density regime. In the

DAFC that employs CCL-P0 which has no PTFE, there is a large voltage drop within these regions. This may be due to water presence filling void regions within the CCL and blocking potential pathways for the supply of fresh fuel and oxidant as well as the route for product removal. This subsequently leads to losses from concentration overpotential (η_c) and may explain the low voltage at high current density. Furthermore, this implies a lack of catalyst utilisation within the CL [229]. This includes hinderance to the access of carbon particles which leads to electronic resistances and may explain the low voltage at medium current density.

To validate the phenomenon of large water coverage in the absence of PTFE, carbon cloths were prepared with the same PTFE loadings as in the CCLs and a water droplet was deposited to explore interactions at the GDL surface. Fig. 7.6 shows that in the absence of PTFE, water spreads over a greater area on the surface, resulting in a higher probability of water being able to fill void spaces on the diffusion layer. As PTFE content is increased, the contact angle of water on the surface increases, similar to that reported in literature, reducing the likelihood of water flooding [77].

As PTFE content is increased, the DAFC employing CCL-C50 which contains 10 wt. % showed a great improvement in performance and concentration overpotential. As PTFE content is further increased, however, the DAFCs employing CCL-P35 and CCL-P50 show a similar drop in voltage at medium and high current density, again owed to ohmic and concentration overpotentials respectively. This drop in voltage may be predominantly owed to blockage of the gas passageways by excessive PTFE content which may obstruct mass transport reactants and products to and from the active sites of the catalyst. This again hinders complete utilisation of the catalyst. Similar findings have been reported in literature, where PTFE content is often kept relatively low to avoid blocking gas passageways which may lead to mass transfer limitations [229]. A trade-off must subsequently be made, where enough PTFE is added to create void regions for hydrophobic channelling but not excessively such that there is blockage of gas passageways.

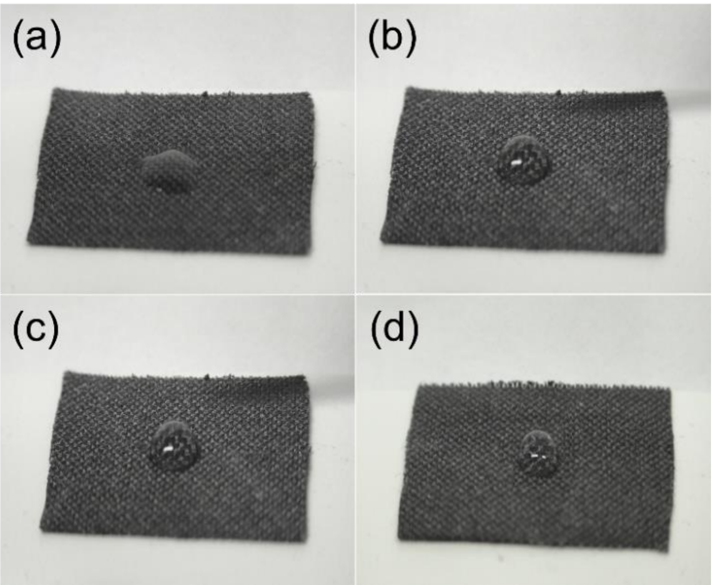

Fig. 7.6. Water droplet formation on gas diffusion layer surface with PTFE loadings reflective of (a) 0, (b) 10, (c) 35 and (d) 50 wt. % with respect to perovskite [70].

To further investigate reaction mass transport limitations, EIS was carried out and is shown in Fig. 7.4d. There are various interpretations of the low frequency arc including: (i) mass transport limitations of gas phase within the backing, (ii) mass transport limitation at the electrode, electrolyte and gas phase interface and (iii) back diffusion of water [232, 416-418].

To explore the combined resistance throughout the cells, EIS data was analysed and is shown in Fig. 7.4d. Once again, only the CCLs were changed throughout the different tests whilst the remaining components of the fuel cell were unchanged. It can therefore be reasonably deduced that variations in EIS data are owed to resistances at the cathode electrode-electrolyte interface. In the absence of PTFE, there is a large resistance most likely due to the high water amount in the CCL causing flooding at the cathode thus making it difficult for gas to diffuse through the layers and reach the active sites [232]. Increasing PTFE content was paralleled by a notable reduction in the size of the semi-circle for CCL-C50, implying improved mass transfer limitations. Similar results have been documented in literature due to lower saturation in the cathode gas diffusion layer by hydrophobic channelling amongst pores [229, 232]. It has been noted that an increase in porosity of the electrode is known to play a key role in diminishing mass transfer resistance [235]. This reduces flooding at electrode-electrolyte interface which otherwise may hinder oxygen diffusion and lead to high resistances [232]. As PTFE content is increased further, however, there is an increase in resistance, indicated by the larger arc sizes for CCL-P35 and CCL-P50. These results correlate well with the polarisation curves and may be owed to blockages of the active catalyst on the electrode surface causing limitations for the proceeding reaction.

Since the catalyst ink consists of multiple elements such as the LCFCO-700 powder, CB, PTFE and PiperION BP-100 ionomer in a solvent consisting of alcohol and water, there are various contributions to shape, size and surface properties making interactions fairly complex to analyse independently [231]. The effect of PTFE content was subsequently visualised via morphological characterisation through SEM (Fig. 7.7). The grey colour reflects the CCLs deposited onto the carbon cloth diffusion layers.

In CCL-C50, the CL remains fairly homogenous. Catalyst agglomeration, however, was clearly observed at higher PTFE concentrations, in both CCL-P35 and CCL-P50. The presence of agglomeration upon increased PTFE content is expected and has been reported previously in literature [419]. Such agglomeration can lead to reduced catalyst utilisation and blockage of pathways, leading to disruption of electronic and ionomer networks and a loss in the electrochemical surface-active area. Furthermore, the presence of agglomeration can lead to uneven CL surfaces and thicker electrodes which leads to higher diffusion resistances, reactant starvation and localised dehydrated or flooded regions in the catalyst layer [232]. These results may explain the decrease in DAFC performance with higher PTFE content in the CCL.

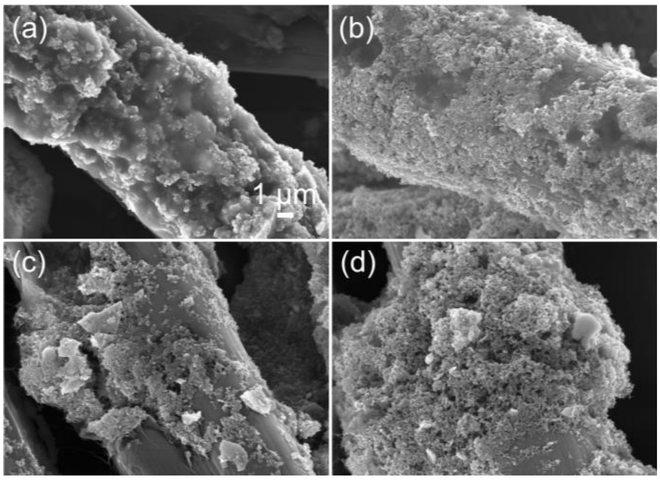

Fig. 7.7. SEM images of (a) CCL-P0, (b) CCL-C50, (c) CCL-P35 and (d) CCL-P50 [70].

The results demonstrate that an optimum PTFE content is essential in providing hydrophobic channelling for efficient water management whilst limiting the formation of agglomerates. A trade-off is therefore crucial and should be considered as a part of the CCL design. In this study, an optimum PTFE weight of 10 wt. % with respect to the perovskite oxide was found to provide optimum DAFC performance and provide sufficient porous network throughout the entire GDE.

7.3.3. Effect of Ionomer Content

The role of ionomer interactions in CL ink has been a major focus in the past decade [39, 226, 420, 421]. Since ionic transportation is essential for fuel cell mechanisms, lack of an ionomer leads to increased ionic resistance, rendering it difficult to utilise parts of the catalyst interface as active sites [234]. This study utilises PiperION BP-100 ionomer that has recently been documented to exhibit excellent hydroxide conductivity [80]. Moreover, this study exploits a PiperION-A20-HCO3 TP-85 membrane which has good compatibility and interface with the ionomer to create an effective network for hydroxide transportation across the MEA and to the active sites of the CLs for the given reactions to take place. Exploration into the ionomer content to manipulate such networks is therefore crucial for good DAFC performance. The polarisation and EIS data of the corresponding DAFCs with varying ionomer amount in the CCLs is shown in Figs. 7.4e-f.

The DAFC employing a CCL with no ionomer shows a lower OCV of 0.65 V compared to its counterparts. As ionomer content is increased in CCL-C50, CCL-I35 and CCL-I50, the OCV values increase, with 0.71 V being obtained for all three cells. Since the reactions that take place at the anode and cathode sites of a DAFC involve hydroxide ions (Eqs. (1.3-1.4)), this is most likely owed to the lack of an effective ionomer network to mediate the transfer of hydroxide ions to the catalytic active sites for the given reactions to occur.

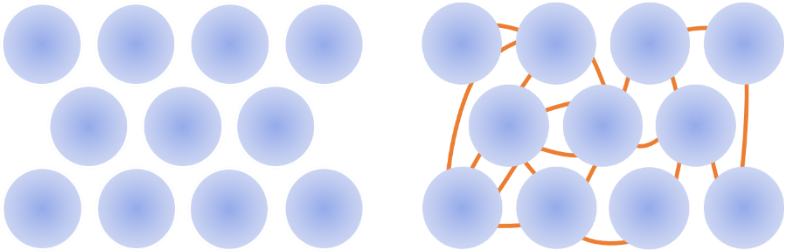

Fig. 7.8. Drawing demonstrating an efficient ionic network on introduction of ionomer (right) in the CCL.

The maximum current density and PPD shows great improvement on addition of ionomer, with values of 192 and 317 mA cm^{-2} and 15.2 and 30.1 mW cm^{-2} being achieved for DAFCs employing CCLs with 0 and 20 wt. % ionomer respectively. Notably, the PPD is nearly doubled when ionomer content increased to 20 wt. %, highlighting the importance of ionomer addition. As ionomer content is further increased, the performance gradually drops with PPDs of 28.6 and 16.3 mW cm^{-2} obtained when CCLs with 35 and 50 wt. % were implemented respectively.

The large ohmic loss present in the DAFC employing CCL-I0 indicates an insufficient ionic network causing a large ionic resistance and a decrease in performance due to poor ionic transfer between the electrolyte and catalyst. On addition of ionomer, the DAFC employing CCL-C50, which has 20 wt. % ionomer, shows better performance due to capability of forming a well-connected three-phase boundary (TPB) [233]. This is expected since good ionomer distribution in CLs is known to increase connectivity to the number of active sites. This increases the electrochemical surface area and forms a more continuous ionic transport network channel, enhancing ORR activity at the cathode site [227, 422]. As ionomer content is further increased in CCL-I35 and CCL-I50, the performance begins to decrease and there is notable reduction in voltage within the medium and high current density regimes. Although addition of ionomer is required for good ionic conduction, it is well known that excessive ionomer coverage blocks active sites on the catalyst [228, 423-425]. Oxygen diffusion paths to the active sites therefore becomes harder, which significantly increases mass transport resistance and slows down the rate of ORR [227, 228, 423-425]. Doing so may explain the increase in concentration overpotential as ionomer content is increased. This phenomenon is also observed in literature and indicates that a trade-off in the electrode must be made [227, 228, 233, 423-425]. Furthermore, it is possible for the ionomer network to block electron conductivity due to coverage of the carbon surface, leading to a decrease in complete utilisation of the CCL surface [235]. This may also contribute to the increase in ohmic resistance observed, specifically electron resistance, and may explain the ohmic overpotential experienced at relatively high ionomer content.

To further explore resistance, EIS data was analysed and is shown in Fig. 7.4f. Again, since only the CCL is changed throughout the different tests, it can be deduced that changes in EIS data are owed to resistances at the cathode electrode-electrolyte interface. Markedly, the cell with no ionomer addition shows the smallest semi-circle, implying the lowest mass transfer resistance. This is not uncommon as ionomers are known to partially cover the catalyst active sites and reduce reactant permeability [233, 426, 427]. Addition of ionomer content into the CCL will therefore unequivocally enhance mass transport resistance. This effect is amplified as ionomer content is increased, with CCL-C50 displaying the largest semi-circle at low frequency. Enough ionomer must therefore be added to not completely block access to catalyst active sites, which increases mass transfer resistance, but to sufficiently form a well-connected TPB.

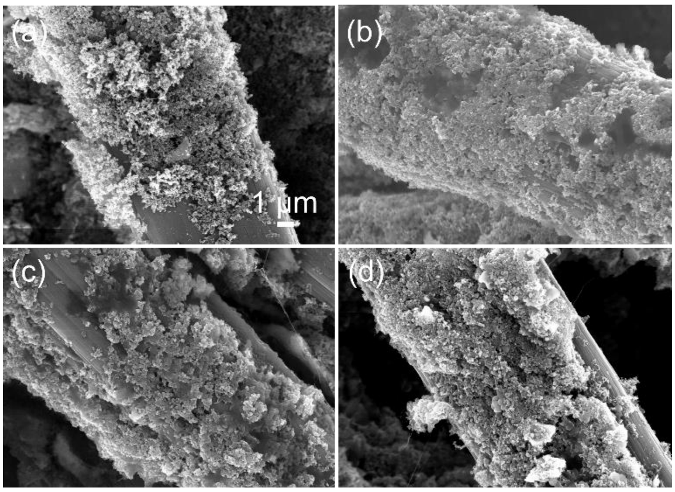

Fig. 7.9. SEM images of (a) CCL-I0, (b) CCL-C50, (c) CCL-I35 and (d) CCL-I50 [70].

To investigate surface morphology, SEM was conducted and is shown in Fig. 7.9. It should be noted that when ionomer content within the CCL was 20 wt. %, particles are more uniformly distributed. This may explain the enhanced mass transport and adequate formation of an ionic conducting network compared to higher ionomer content [428]. In CCL-I35 and CCL-I50, there is no longer homogenous coverage, which may indicate partial blockage of mesopores and additional resistance of oxygen transport through the CCL [236, 429, 430]. As ionomer content is increased to 50 wt. % in particular, agglomerates can clearly be observed within the CCL. Agglomeration has been widely studied when Nafion is used as an ionomer [39, 226, 231, 431]. Three effects have been of significant interest: (i) the effect of ionomer on self-agglomeration, (ii) its ability to form a coating layer on carbon black and (iii) the effect of ionomer on polymer interaction between carbon black aggregates [226]. Formation of ionomer agglomerates is therefore common, and a similar effect may subsequently be present with the PiperION BP-100 ionomer, explaining the increased mass transfer resistance and lowered DAFC performance at higher ionomer content [231, 431].

The above results imply that an optimum ionomer distribution is needed and a compromise must be considered in the design of CCLs [224, 226-229, 231-236, 423-425, 430]. In this study, an optimum ionomer weight of 20 wt. % with respect to the perovskite oxide was found to provide optimum DAFC performance and a sufficient ionomer network throughout the entire GDE. This 4:1 ratio of catalyst:ionomer is widely used in literature and therefore the data in this study agrees with these findings [80, 432].

7.3.4. Varying Operating Conditions

To truly appreciate the scope and applicability of CCLs, the DAFCs must be tested under varying conditions. The following section therefore explores the CCLs under different operational conditions such as temperature and hydroxide concentration.

The DAFCs were tested at an elevated operational temperature of 100 ^{o}C and the results are shown in Figs. 7.10a-c. The overall trends observed amongst the DAFCs with adjusted carbon, PTFE and ionomer content at this operational temperature followed the same trend as was seen in sections 7.3.1-7.3.3 where the operational temperature was 80 ^{o}C, with CCL-C50 showing optimum performance amongst the series of CCLs tested. As expected, the performance increases with an increase in temperature, with the DAFC employing CCL-C50 exhibiting a maximum current density of 379 mA cm^{-2} and PPD of 34.3 mWcm^{-2}. This positive increase in DAFC performance with an increase in operating temperature has commonly been observed in literature [75, 76]. More importantly, it demonstrates that the cell can be held at elevated temperatures without loss of functionality.

Since CCL-C50 was identified as the optimised composition, this catalyst layer was employed as the cathode for the following tests. To further explore the effects of varying temperature on DAFC performance, a single cell was set up and the operational temperature was varied from a larger range of 20-100 °C.

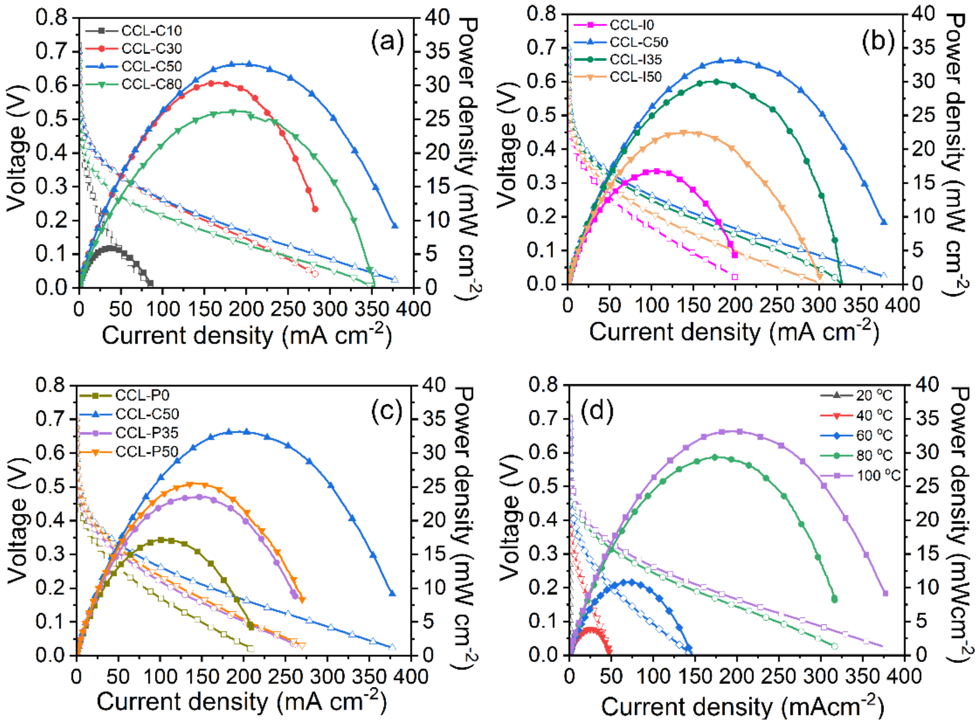

Fig. 7.10. Polarisation and power density curve of CCLs with varying (a) carbon, (b) PTFE and (c) ionomer content [70]. Anode: 2.2 mg_{PGM} cm^{-2} PtIr(40 wt. %)/C(60 wt. %). Cathode: LCFCO. Test conditions: (1) Anode: 2 mL min^{-1} of 7 M NH_4OH with 1 M KOH; Anode back pressure: 3 bar_g (2) Cathode: 180 mL min^{-1} CO_2-free air through humidifier of T = 95 °C; Cathode back pressure: 2 bar_g. Cell temperature: 100 °C. (d) Polarisation and power density curve of CCL-C50. Anode: 2.2 $mg_{PGM}cm^{-2}$ PtIr(50 wt. %)/C(50 wt. %). Cathode: 3.4 $mg_{oxide}cm^{-2}$ LCFCO-700(50 wt. %)/C(50 wt. %) [68]. Test conditions: (1) Anode: 2 $mLmin^{-1}$ of 7 M NH_4OH with 1 M KOH; Anode back pressure: 3 bar_g (2) Cathode: 180 $mLmin^{-1}$ CO_2-free air through humidifier of T = 95 °C; Cathode back pressure: 2 bar_g. Cell temperature: 20, 40, 60, 80 and 100 °C.

The data in Fig. 7.10d shows that as temperature increases, there is an obvious increase in overall performance of the DAFC. When temperature was increased from 20 to 40 °C in the DAFC, a significant increase in OCV was observed from 0.30 to 0.60 V. However, as temperature increased above 60

^{o}C, there was minimal change in OCV, with values of 0.69, 0.71 and 0.72 V being obtained at 60, 80 and 100 ^{o}C respectively. There is also a substantial increase in current density as operating temperature is increased, with a maximum current density of 379 mAcm^{-2} and peak power density of 34 mWcm^{-2} being obtained at 100 ^{o}C.

This positive increase in DAFC performance with an increase in operating temperature has commonly been observed in literature [75, 76]. Ishiyama et al. reported the effects of temperature on a DAFC employing PGM-based PtRu/C at both the anode and cathode site [75]. At an operating temperature of 50 ^{o}C, an OCV and maximum current density of around 0.45 V and 40 mAcm^{-2} was respectively obtained when using 5 M NH_4OH + 1 M KOH as the anodic fuel and air as the cathode stream. A corresponding PPD of 3 mWcm^{-2} was obtained. Under similar operating temperatures of 60 ^{o}C, the DAFC shown in Fig. 7.10d, which utilises similar anodic/cathodic streams (7 M NH_4OH + 1 M KOH/air), demonstrates a maximum current density and PPD of 145 mAcm^{-2} and 11 mWcm^{-2} respectively. Furthermore, when the operating temperature was increased to 80 ^{o}C in the aforementioned study, Ishiyama et al. observed that the OCV and maximum current density increased to around 0.55 V and 48 mAcm^{-2} respectively. A corresponding PPD of 4.5 mWcm^{-2} was obtained for the cell. At the same operating temperature, a maximum current density and PPD of 317 mAcm^{-2} and 30 mWcm^{-2} were respectively obtained in this study. These results illustrate the promising performance of CCL-C50 as an active and promising cathode under various operating conditions.

Furthermore, the effects of hydroxide concentration in the electrolyte were also studied and are shown in Fig. 7.11. These tests were conducted at an operating temperature of 80 ^{o}C. In the absence of hydroxide, the cell was still able to produce a maximum current density and PPD of 118 mA cm^{-2} and 8.8 mW cm^{-2} respectively. This is particularly useful if considering DAFCs for wastewater treatment technology since the high ammonia content in wastewater can be utilised to power such cells without the need for hydroxide addition, eliminating post purification processing and additional energy input. It should be noted however, a lower OCV of 0.38 V was obtained in the lack of KOH, most probably since the reaction mechanisms involve OH^- ions and absence of such affects the reactions at the respective electrodes (Eqs. (1.3-1.5)).

As hydroxide concentration in the electrolyte is increased to 3 M, there is an increase in performance, with an OCV, maximum current density and PPD of 0.71 V, 351 mA cm^{-2} and 35.6 mW cm^{-2} being achieved respectively. The increase in performance is likely due to greater availability of hydroxide ions to assist the electrode reactions. As hydroxide concentration is further increased to 5 M, however, the performance begins to decline. A similar trend in DAFC performance as hydroxide performance is excessively increased has also been observed in literature and is presumed to be due to transport limitations [58].

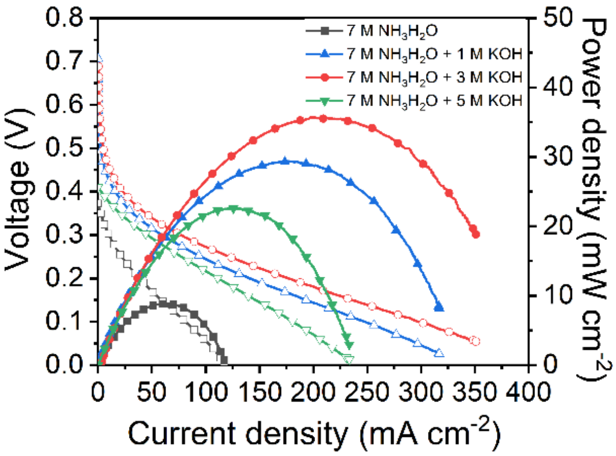

Fig. 7.11. Polarisation and power density curves of DAFC employing CCL-C50 fed with 7 M NH NH_4OH and different hydroxide concentrations at an operating temperature of 80 °C [70].

It should be recognised that key studies demonstrating relatively high DAFC performances employ pure O_2 as the oxidant [58, 76]. In this study, however, zero air (20 % O_2/80 % N_2) is used as the cathodic oxidant instead of pure O_2

which offers a much safer fuel, particularly for applications such as transport where consumer safety is of utmost importance. Nevertheless, a relatively high current density and high peak power density is still obtained when air is used despite the oxygen content being much lower than pure oxygen. Remarkably, the results in this study are the highest reported for DAFCs employing air as the cathode stream. The above findings reveal that CCL-C50 shows good activity in varying temperatures and electrolyte conditions, making it a promising CCL for DAFCs.

7.3.5. Comparison with PGM-based CCL

To judge the applicability of the optimised CCLs to replace PGM-based CCLs, a standard ink recipe was used to fabricate an electrode using Pt/C as the catalyst and the DAFCs were investigated under similar conditions.

The result of a DAFC employing the Pt/C-based CCL under operating temperatures of 80 and 100 ^oC is shown in Fig. 7.12a. For a clear comparison, Fig. 7.12b and Fig. 7.12c show the performances between the DAFCs employing the optimised LCFCO-700-based CCL and the Pt/C-based CCL operating at 80 and 100 ^oC respectively. It should be noted that different loadings were used between the PGM and non-PGM cathodes however, given the high expense of Pt/C as a cathode material, along with the cheap and easy synthesis nature of the LCFCO-700 perovskite, the latter is a promising candidate to replace Pt/C. This would significantly reduce cost of devices such as fuel cells and batteries which rely heavily on PGMs to assist ORR. Nevertheless, the two DAFCs demonstrate very similar performances and power densities and are investigated in further detail below.

The polarisation curves show that an OCV of 0.71 V was achieved when LCFCO was employed as the catalyst of the non-PGM-based CCL whereas a lower OCV of 0.60 V was obtained when Pt/C was used. The latter value is common for a DAFC employing Pt/C as a cathode catalyst material and is therefore expected [58]. As mentioned above, a maximum current density of 317 mAcm^{-2} and a PPD of 30.1 mWcm^{-2} was achieved at an operating temperature of 80 °C when LCFCO was employed as the catalyst. Remarkably, this performance was very similar to the DAFC employing Pt/C as the cathode catalyst, which obtained a maximum current density of 285 mAcm^{-2} and a peak power density of 32.2 mWcm^{-2} under similar operating conditions.

When the temperature was further increased to 100 °C, an observable enhancement in performance for both fuel cells was observed. Again, the performance was extremely similar, with the DAFC employing LCFCO as the cathode catalyst, obtaining a maximum current density of 379 mAcm^{-2} and a peak power density of 34 mWcm^{-2}, whilst the DAFC employing Pt/C obtained a maximum current density of 345 mAcm^{-2} and a peak power density of 40 mWcm^{-2}.

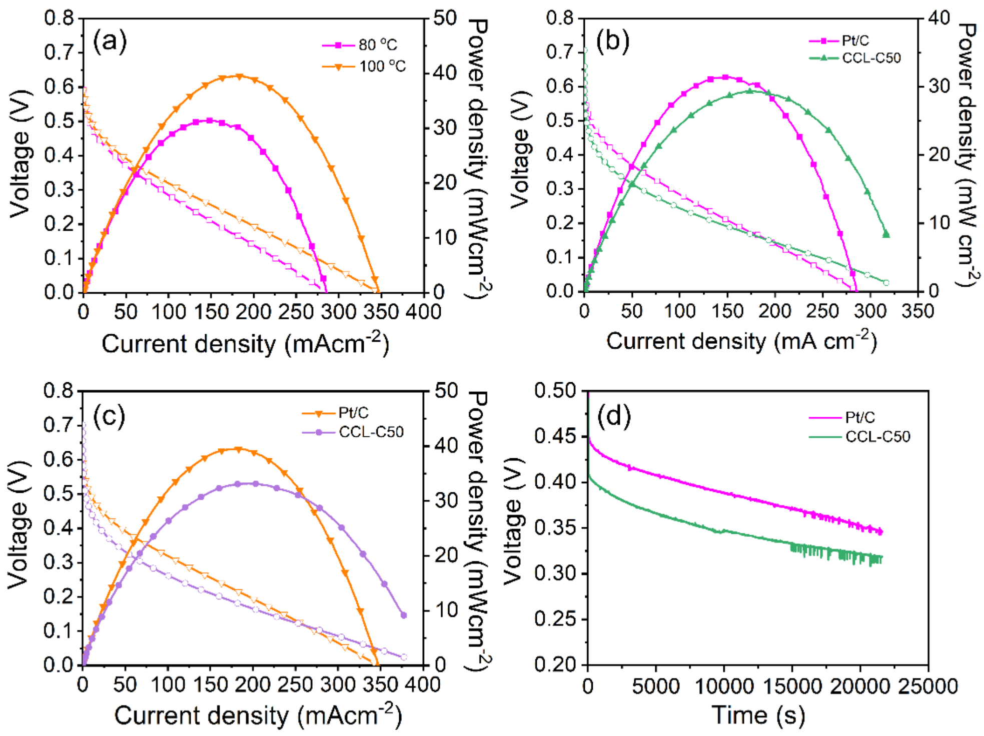

Fig. 7.12. Polarisation and power density curve of DAFC. (a) Anode: 2.2 mg$_{PGM}$cm^{-2} PtIr(50 wt. %)/C(50 wt. %). Cathode: 0.4 mg$_{PGM}$cm^{-2} Pt/C. Test conditions: (1) Anode: 2 mLmin^{-1} of 7 M NH_4OH with 1 M KOH; Anode back pressure: 3 bar$_g$ (2) Cathode: 180 mLmin^{-1} CO_2-free air through humidifier of T = 95 °C; Cathode back pressure: 2 bar$_g$. Cell temperature: 80

and 100 °C [68]. (b) Comparison between DAFC employing Pt/C (pink) and LCFCO-700 (orange) cathode at 80 °C [68]. (c) Comparison between DAFC employing Pt/C (pink) and LCFCO-700 (orange) cathode at 100 °C [68]. (d) Stability test of DAFC employing LCFCO-700 and Pt/C-based catalysts at operating temperature of 100 °C [68].

On closer evaluation of the comparative polarisation curves, there is a greater potential drop in the low current density regime of the LCFCO-700-based DAFC compared to that of the Pt/C. This region is dominated by the activation overpotential (η_a) observed at low current densities. As mentioned in Chapter 1, this is owed to: (i) surface conversions preceding the electron transfer such as adsorption on the electrode surface and chemical reactions which are inherit to the catalyst, (ii) electron transfer at the electrode surface of the electrode-electrolyte interface and/or (iii) surface conversions following the electron transfer such as desorption from the electrode surface and chemical reactions which are inherent to the catalyst. Based on these contributing factors, the larger activation overpotential may be due to the surface conversions that occur at Pt compared to LCFCO-700 which are inherent to the catalyst employed, with Pt facilitating more facile conversion mechanisms and thus lowering the activation overpotential associated with the reaction. Furthermore, the electron transfer step plays a key role in this type of overpotential. Since perovskite oxides have inherently lower electrical conductivity than platinum, this explanation is plausible and reinforces the need for good electrical contact between the oxide particles [29]. In this study, four different carbon ratios were explored, with the optimum found to be 50 wt.%. To further optimise carbon content, smaller increments between 30-80 wt.% may be implemented.

Moreover, the stability of the cells employing CCL-C50 and Pt/C-based CCLs were tested in a preliminary durability test at a continuous current density of 50 mA cm^{-2} (Fig. 7.12d). The results show that the two cells both demonstrate a steady decrease in voltage over the testing duration and follow the same overall trend, implying comparable nature between the two CCLs. The fluctuations recorded in the data is owed to ammonia crossover from the anode and cathode, which subsequently lowers voltage over time [89]. This was physically observed as small amounts of liquid were found to pass through the cathode outlet in the fuel cell set up and were collected in a separate beaker. The enhanced frequency of ammonia crossover towards the end of the testing duration may be due to (i) possible loosening of bolts on the fuel cell assembly, which may require a higher torque to be applied and reassessment of the cell assembly during long testing times under elevated temperatures or (ii) employment of such a thin membrane. The latter is often considered in the design of fuel cells since a trade-off must be implemented to ensure that the membrane is thin to reduce mass transport resistances but with reasonable mechanical strength. It has been noted that chemical degradation of the AEM is common during continuous operation, especially in harsh conditions such as alkaline environments and elevated temperatures (near 100 ^{o}C) [77]. Another likely reason for the steady drop in performance is that AOR catalysts may deactivate due to the formation of strongly chemisorbed ammonia oxidation intermediates during long time testing [77, 433].

After testing, the CCL-C50 CCL was characterised to observe any obvious differences before and after testing which may correlate to the performance observed. Fig. 7.13a shows CCL-C50 deposited onto the AEM after testing. The photograph shows clear imprint of the channel design and confirms good contact between the MEA assembly as predicted in Chapter 5.

Fig. 7.13b reveals XRD data of the CCL-C50 electrode before and after the stability test. Before testing, clear reflections belonging to carbon cloth, the LCFCO-700 perovskite oxide and PTFE can be seen. After testing, however, there are obvious losses in LCFCO-700 peaks, implying loss of active sites which may explain the gradual decrease in voltage over time. Moreover, the presence of reflections at 2θ values of 40.6 and 47.3^{o} belonging to the [222] and [400] planes of Co_3O_4 (PDF: 04-022-7367) respectively indicates that there may be structural changes after testing, further explaining the loss in performance over time.

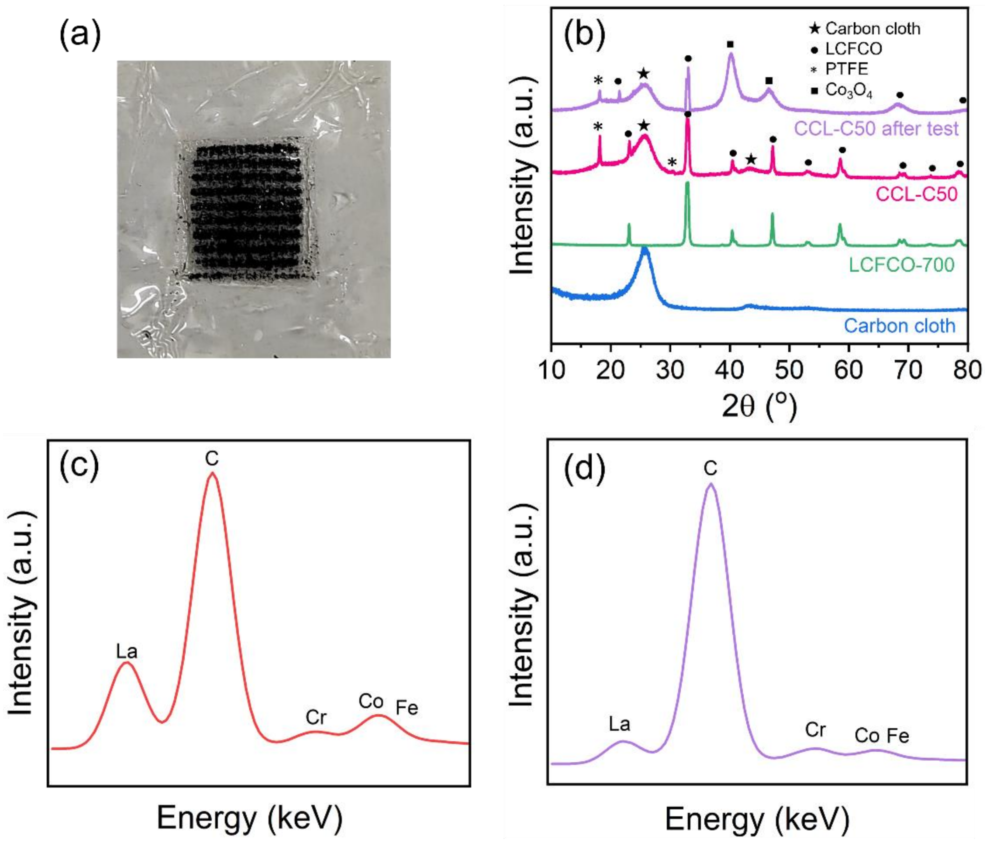

Fig. 7.13. (a) Photo of the CCL-C50 layer deposited onto the AEM after testing. (b) XRD of carbon cloth, LCFCO perovskite oxide, CCL-C50 before and after fuel cell durability test [70]. Anode: 2.2 mg$_{PGM}$ cm^{-2} PtIr(40 wt. %)/C(60 wt. %). Cathode: 1.23 mg$_{oxide}$ cm^{-2} LCFCO or 0.45 mg$_{PGM}$ cm^{-2} Pt/C. Test conditions: (1) Anode: 2 mL min^{-1} of 7 M with 1 M KOH; Anode back pressure: 3 bar$_g$ (2) Cathode: 180 mL min^{-1} CO_2-free air through humidifier of T = 95 ^oC; Cathode back pressure: 2 bar$_g$. Cell temperature: 80 ^oC [70]. Point analysis of CCL-C50 Elemental point analysis (c) before and (d) after durability test [70].

Fig. 7.13c and Fig. 7.13d shows that the relative intensity of the La and F elements which arise from the LCFCO-700 and PTFE components of the CCL respectively, decrease after testing. This further reinforces loss of CCL-C50 active sites and prompts room for improvement in the durability of CCL design.

To further characterise the CCL-C50 GDE after testing, SEM and EDS images were taken and are displayed in Fig. 7.14. Fig. 7.14a shows that the CCL particles remain evenly distributed on the carbon fibres of the diffusion layer with no signs of agglomeration. The EDS images presented in Figs. 7.14 b-f show that the La, Cr, Fe, Co and O elements also remain homogenously distributed.

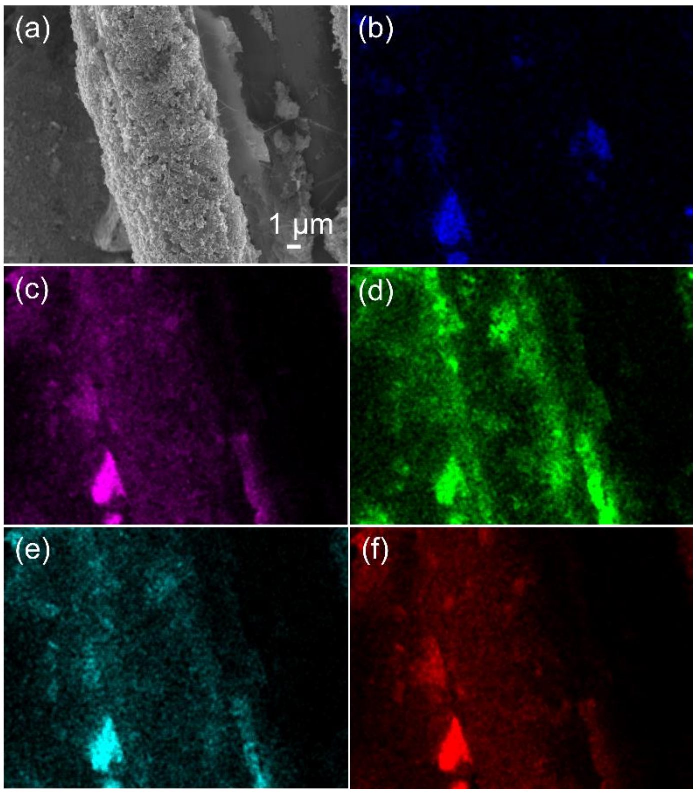

Fig. 7.14. (a) SEM of CCL-C50 after testing. Elemental mapping of (b) La, (c) Cr, (d) Fe, (e) Co and (f) O elements via EDS after testing [70].

Furthermore, it should be noted that the current collectors displayed signs of corrosion post testing (Fig. 7.15). This leads to an increased contact resistance, especially over long testing durations. This is often overcome by coating stainless steel with highly conductive metals such as gold. However, this was out of the budget of this research. It may subsequently be useful to explore anti-corrosive materials.

Fig. 7.15. Photo of corrosion displayed on current collector post testing.

7.4. Conclusion

To maximise performance at the electrode-electrolyte interface, transport pathways for electrons, ions and reactants should be connected well. This demands for a well-constructed microstructure in the CL. It is widely known such a CL is a multi-composite structure composed of a catalyst, carbon supports, ionomer materials and void regions, whereby carbon and ionomers are used to provide electron and ionic conduction networks respectively and void regions provide mass transport channels for reactants and products. An effective three-phase interface design is therefore necessary for improving cell performance and in reducing CL costs. Herein a CCL was designed and optimised for a DAFC using a perovskite oxide as the catalyst to reduce reliance on PGMs. The key findings of the study are as follows:

(i) By simply varying carbon, PTFE and ionomer content, the cell maximum current density and PPD increased from 85.3 mA cm^{-2} and 5.92 mWcm^{-2} to 317 mA cm^{-2} to and 30.1 mWcm^{-2}, highlighting the importance of CCL composition.

(ii) The optimum weight ratio of carbon black, PTFE and ionomer in this study was 50, 10 and 20 wt. % respectively relative to the weight of the perovskite oxide in the CCL (CCL-C50).

(iii) When varying operating conditions such as temperature, the DAFC employing CCL-C50 remained the optimised composition and displayed an increased maximum current density and PPD of 379 mA cm^{-2} and 34.3 $mWcm^{-2}$ respectively.

(iv) Even in absence of KOH, the cell was still able to produce a current density of 118 mA cm^{-2} and this was increased to 351 mA cm^{-2} when KOH concentration was increased to 3 M.

(v) The optimised CCL-C50 showed similar performance to a DAFC employing a Pt/C-based CCL, demonstrating potential to alleviate PGM dependence.

The results of this chapter highlight the significance of proper CCL design to optimise interactions at the electrode-electrolyte interface. The findings reveal that despite employment of an active catalyst for oxygen reduction at the cathode site, the true performance of the catalyst cannot be reflected unless it is supported by proper optimisation of the CCL. The study also reveals that by optimising the CCL, similar performances to those of Pt/C-based CCLs stated in literature can be attained. However, it should be noted that the results in this study have not been fully optimised. For example, only four ratios were tested for carbon content over a wide range from 0-80 wt. %. It is worth testing a narrower range between 30-80 wt. % since this is where the optimum performance lies. It may also be useful to utilise a design of experiment (DoE) method to find the optimum set of conditions across two or more factors.

Nevertheless, the cost reductions experienced in this study may be especially beneficial when considering scale up from laboratory to commercial, since one of the current major limitations of fuel cell progression is the cost of catalysts. Given that performances between DAFCs employing the PGM and non-PGM-based CCLs in this study are fairly similar, the design and optimisation of non-PGM-based CCLs is a crucial route for fuel cell progression and that perovskite oxides may be particularly promising candidates for such.

CHAPTER 8 Conclusions and Future Work

8.1. Conclusions

Energy plays an integral role in our economic and social development. A continuous growth in global population over the years has been paralleled by a continuous growth in energy consumption. Global recognition towards the need and development of clean energy is therefore evident. Sources such as wind and solar power, although appreciated as clean technologies, are often regarded as unreliable as they are intermittent in nature and rely heavily on external factors. This imposes regional limitations and restricts the extent to which renewable energy sources can contribute towards energy production. Subsequently, there is a driving incentive to find reliable clean energy sources which can be used in conjunction with existing technology, to create a stable and network of renewable energy production.

Fuel cells are electrochemical devices that convert chemical energy stored within a fuel into electrical energy. Although DAFCs are not as widely explored as PEMFCs, they do have explicit advantages such as the alleviation of harsh, acidic conditions, allowing for a wider range of materials to be used. The former also makes use of the fuel's high energy density, large-scale global production, extensive existing infrastructure, and low cost per unit energy. For this study, low temperature DAFCs are subsequently explored, namely AMFCs.

Perhaps one of the largest challenges for fuel cell technology, is the search of appropriate materials and manufacturing methods required for this technology type to become competitors of existing power generation systems. For example, most of the current literature focuses on use of platinum group metals, which are extremely expensive and thus greatly increase cost of these devices. This work therefore focuses on the optimisation routes and strategies that can be taken to improve DAFCs in terms of performance and cost.

Interactions at the electrode-electrolyte interface are at the heart of fuel cell performance and are dependent on several factors such as the ability of the catalyst to carry out the given reaction; the composition of the catalyst layers and the ability of fresh fuel/oxidant to reach the active sites. This may influence the low, middle and high current density regimes of polarisation curves respectively. These factors are therefore vital to consider for efficient fuel cell performance.

Despite not being implemented into a working cell, Chapter 4 investigated the use of perovskite oxide materials to assist AOR to explore the potential to alleviate use of PGMs at the anode of DAFCs. The half-cell reaction was studied using a standard three electrode test and it was found that LNCF-90 showed optimum activity towards ammonia oxidation due to the combined presence of Fe and oxygen vacancies. This chapter revealed that the perovskite worked well in an ammonia fed electrolyser and demonstrated an ammonia removal efficiency of 95.7 % over a testing duration of 100 hr in a simulated wastewater solution. Since the reactions that occur at the anode sites of ammonia fed electrolysers and DAFCs both depend on the ability of the catalyst to assist AOR, the perovskite has excellent potential to act as an anode in DAFCs in future work.

The individual components of a DAFC were carefully selected in Chapter 5 and their criteria was based on strength, availability, cost and compatibility with ammonia. Such components included the end plates, current collectors, flow field plates and gaskets. Based on the materials selected, simulations were carried out to optimise the flow field pattern to enhance fluid delivery to the active sites and in turn improve mass transport of fresh reactant/product to/from active sites respectively. The simulations revealed that two-dimensional tapering (PFFP-2D) of the manifolds improved the fluidic distribution of both liquid and gas, providing more uniform flow across the entire active area. This was further validated using 3D printed acrylic cells. The model was extended to the dimensions being used for laboratory scale experiments (1 cm^2) and a fuel cell was built based on the above findings of material and design choice.

Commercial expansion of fuel cells is largely limited by the sluggish nature of the ORR even on PGM-based surfaces, which are considered as the benchmark catalysts to date, despite their high expense. On this basis, exploration of effective electrocatalysts to assist ORR at the lowest possible cost is essential for future use of these devices. The alkaline environment of DAFCs in particular allow for faster ORR kinetics, the use of less corrosive conditions and use of cheaper non-PGM electrocatalysts such as perovskites. Based on this, a series of LCO based perovskite oxides including LCCO, LFCO and LCFCO were prepared in Chapter 6 and their ORR activity was studied in 0.1 M KOH solution at room temperature using a typical RDE technique. The extrinsic (surface area and particle size) and intrinsic (formation of oxygen vacancies, oxidation states, occupancy of e_g levels) properties of the electrocatalysts were evaluated to explore the synergetic effects of doping both Cr and Fe at the B-site of LCO. Since LCFCO is a novel perovskite oxide, its synthesis method was explored by varying final calcinating temperatures. The results revealed that LCFCO fired at a final calcinating temperature of 700 ^oC (LCFCO-700) demonstrated superior activity compared to its counterparts and displayed similar ORR activity to commercial Pt/C. Cr induced changes in the surface oxygen vacancy formation, increasing the number of transferred electrons in the ORR pathway to 4, whilst Fe led to clear enhancement of the onset potential. The findings highlight the promising possibility of replacing PGM-based electrocatalysts with properly tailored perovskite oxides for ORR catalysis in alkaline environments.

To maximise performance at the electrode-electrolyte interface in a working DAFC, the electrode must only be able to catalyse the given reaction, which the perovskite had shown to do, but also implies that transport pathways for electrons, ions and reactants should be connected well. This demands for a well-constructed microstructure in the CL. It is widely known such a CL is a multi-composite structure composed of a catalyst, carbon supports, ionomer materials and void regions, whereby carbon and ionomers are used to provide electron and ionic conduction networks respectively and void regions provide mass transport channels for reactants and products. When the same LCFCO-700 perovskite oxide electrocatalyst was used as the cathode in the constructed DAFC utilising zero air as the oxidant, the maximum current density and PPD increased from 85.3 and 317 mA cm^{-2} to 5.92 and 30.1 mWcm^{-2} respectively through proper carbon (50 wt. %), PTFE (10 wt. 5) and ionomer (20 wt. %) optimisation. This indicated that to truly reflect the capacity of the electrocatalytic material, proper design of the CL was essential. The composed DAFC utilising the optimised cathode catalyst layer (CCL-C50) was able to operate under various conditions such as elevated temperatures and alkalinity. The performance and stability of the DAFC with CCL-C50 was similar to a DAFC employing a Pt/C-based CL. Chapter 7 therefore showed by proper optimisation of the cathode, there is potential to alleviate PGM dependence and truly exploit the capacity of materials such as perovskite oxides.

8.2. Future Work

The content of this thesis primarily focuses on optimisation of the oxygen reduction electrocatalyst and cathode electrode. It should be noted, however, that AOR at the anodic site is also hindered by sluggish ammonia adsorption kinetics on the surface of the electrode and a suitable catalyst is of paramount importance to enhance DAFC performance. Currently, PGMs are often employed as anodic electrocatalysts which are easily poisoned by the strong adsorption of nitrogen bound species (N_{ads}) and have a high-cost association, making them unfavourable for practical application. Although testing and implementation of the anode in a working DAFC is out of the scope of this study, Chapter 4 revealed how perovskite oxides were exploited and tailored towards ammonia oxidation, which may serve as a foundation for further exploration. Future work may therefore focus on the implementation of such perovskite oxide catalysts into anode electrodes of DAFCs. For this, proper catalyst layer design is again important to truly optimise electrode-electrolyte interactions. Experiments may therefore focus on testing the LNCF-90 perovskite oxide with different carbon ratios and ionomer content to optimise electronic and ionic conductivity respectively. This implies that the LNCF-90 perovskite oxide must be tested with different carbon ratios and ionomer content to optimise electronic and ionic conductivity respectively, similar to the strategy presented in Chapter 7. A highly conductive carbon phase (Vulcan XC-72R) and the same ionomer (PiperION BP-100) should be exploited to carry out such tests to provide good compatibility. It should be noted, however, that PTFE content is not as necessary to add in the anode catalyst layer since this site is exposed to aqueous ammonia solution.

In Chapter 5, simulations were used to predict the behaviour of fluidic flow across the active area of flow field plates and the results were verified using 3D printed models. It was noted that the orientation may play a crucial role in such behaviour and that these tests were conducted with a horizontal orientation of the cell, whereas in practical applications, cells are placed vertically. Often, vertical orientation may enhance two-phase flow and decrease the number of gas slugs present, which in this study, has been assumed to be negligible since the anode is submerged in aqueous environment. However, if a highly active anode material is used, there may possibility of nitrogen gas formation which can lead to the presence of such two-phase flow. As such, vertical orientation may lead to an enhancement in removal of such gas. Nevertheless, a model should be computed to account for the presence of two-phase flow in both horizontal and vertical configuration to verify. Furthermore, the effects of other factors such as gravity should also included in such a model since vertical alignment is assumed to have a stronger gravitational contribution on flow distribution. Using such a model will more closely represent a more practical cell orientation.

Nevertheless, the findings of this project provide insight into the areas that can be optimised and manipulated to provide enhanced DAFC performance. There still, however, remains much room for exploration, in for example, the way the cell is constructed and tested. Humidity of the oxidant, backpressure and flow rates have a direct influence on the performance of fuel cells [434, 435]. It is subsequently useful to explore the humidity of the incoming oxidant, along with the backpressure and flow rates of both oxidant and fuel. The preparation and deposition of ink also remains a big area of improvement. In this study, carbon, ionomer and PTFE content were each only explored using four values. To obtain enhanced results, one should consider exploring smaller increments within a suitable range and find more accurate ratios. For example, of the four carbon ratios that were explored here (10, 30, 50 and 80 wt. %), it was discovered that from 30 to 50 wt. % carbon, there was an increase in cell performance. However, on further increase from 50 to 80 wt. %, there was a decrease in performance. The results indicate that between 30-80 wt. % lies an optimum carbon ratio. For this study, only 50 wt. % was studied, however, to achieve an enhanced composition, smaller increments e.g., 40, 50, 60, 70 wt. %, may be studied. A similar concept applies for the ionomer and PTFE content. Considering design of experiments (DoE) to find the optimum set of conditions across two or more factors may be useful. Moreover, deposition techniques, such as spraying and screen printing, influence the final surface of the electrode and should therefore also be investigated [436]. To date, many studies use spraying and screen printing to obtain thin, homogenous dispersion of the catalyst ink onto the surface of the diffusion layer. The viscosity and adhesion properties of the ink are subsequently crucial and had not been optimised in this study.

Also, current collectors displayed signs of corrosion post testing, which can lead to increases in contact resistance, especially over long testing durations. In literature, this is often overcome by coating stainless steel with highly conductive metals such as gold. However, due to the budget of this project, this was not feasible. Future work should consider this step as a crucial design parameter.

Overall, this project provides insight into the strategic routes one can take to enhance direct ammonia fuel cell performance and opens doors for future progress in the field.

Bibliography

[1] G. Jeerh, M. Zhang, S. Tao, Recent Progress in Ammonia Fuel Cells and Their Potential Applications, Journal of Materials Chemistry A, 9 (2021) 727-752.
[2] Total energy consumption - World Energy & Climate Statistics - Yearbook 2022, Enerdata, https://yearbook.enerdata.net/total-energy/world-consumption-statistics.html, 2022.
[3] W.P. Nel, C.J. Cooper, Implications of fossil fuel constraints on economic growth and global warming, Energ. Policy, 37 (2009) 166-180.
[4] H. Ritchie, M. Roser, P. Rosado, CO_2 and Greenhouse Gas Emissions, Our Wolrd in Data, https://ourworldindata.org/co2-and-other-greenhouse-gas-emissions, 2020.
[5] Share of renewables in electricity production - World Energy & Climate Statistics - Yearbook 2022, Enerdata, https://yearbook.enerdata.net/renewables/renewable-in-electricity-production-share.html, 2022.
[6] A. Afif, N. Radenahmad, Q. Cheok, S. Shams, J.H. Kim, A.K.J.R. Azad, S.E. Reviews, Ammonia-fed fuel cells: a comprehensive review, 60 (2016) 822-835.
[7] H. Lund, Renewable energy strategies for sustainable development, Energy, 32 (2007) 912-919.
[8] O. Siddiqui, I. Dincer, A review and comparative assessment of direct ammonia fuel cells, Thermal Science and Engineering Progress, 5 (2018) 568-578.
[9] J. Larminie, A. Dicks, Fuel Cell Systems Explained, John Wiley & Sons2003.
[10] B.C.H. Steele, A. Heinzel, Materials for fuel-cell technologies, Materials for Sustainable Energy, pp. 224-231.
[11] W. Wang, X. Wei, D. Choi, X. Lu, G. Yang, C. Sun, Electrochemical cells for medium- and large-scale energy storage: fundamentals, in: C. Menictas, M. Skyllas-Kazacos, T.M. Lim (Eds.) Advances in Batteries for Medium and Large-Scale Energy Storage, Woodhead Publishing, 2015, pp. 3-28.
[12] L. Khotseng, Oxygen Reduction Reaction, Oxygen Reduction Reaction: Electrocatalysts for Fuel Cells and Hydrogen Evolution - Theory to Design, A. Ray, I. Mukhopadhyay, R. K. Pati, IntechOpen, 2018, pp. 25-41.
[13] C. Spiegel, How to Predict Fuel Cell Performance - Fuel Cell Information, Fuel Cell Store, https://www.fuelcellstore.com/blog-section/how-to-predict-fuel-cell-performance#:~:text=The%20performance%20of%20a%20fuel%20cell%20stack%20can,will%20allow%20you%20to%20calculate%20the%20overall%20performance., 2019.
[14] R. O'Hayre, S.-W. Cha, W. Colella, F.B. Prinz, Fuel Cell Reaction Kinetics, Fuel Cell Fundamentals, John Wiley & Sons, 2016, pp. 77-116.
[15] M. Carmo, D. Stolten, Energy Storage Using Hydrogen Produced From Excess Renewable Electricity: Power to Hydrogen, in: P.E.V. Miranda (Ed.) Science and Engineering of Hydrogen-Based Energy Technologies - Hydrogen Production and Practical Applications in Energy Generation, Academic Press, 2019, pp. 165-199.
[16] H. Xu, M. Ni, High-temperature electrolysis and co-electrolysis, in: G. Spazzafumo (Ed.) Power to Fuel, Academic Press, 2021, pp. 51-73.
[17] W.R. Grove, On voltaic series and the combination of gases by platinum, Philosophical Magazine, 127 (1839).
[18] L.J.R. Zhou, S.E. Reviews, Progress and problems in hydrogen storage methods, 9 (2005) 395-408.

[19] I. Dincer, Technical, environmental and exergetic aspects of hydrogen energy systems, International Journal of Hydrogen Energy, 27 (2002) 265-285.
[20] I. Dincer, Environmental and sustainability aspects of hydrogen and fuel cell systems, International Journal of Energy Research, 31 (2007) 29-55.
[21] S. Mekhilef, R. Saidur, A.J.R. Safari, S.E. Reviews, Comparative study of different fuel cell technologies, 16 (2012) 981-989.
[22] O. Siddiqui, Development and investigation of alkaline electrolyte based direct ammonia fuel cells, University of Ontario Institute of Technology, Ontario, Canada, (2018) 111.
[23] G. Sdanghi, G. Maranzana, A. Celzard, V. Fierro, Review of the current technologies and performances of hydrogen compression for stationary and automotive applications, Renewable and Sustainable Energy Reviews, 102 (2019) 150-170.
[24] P.J. Bouwman, J. Konink, D. Semerel, L. Raymakers, M. Koeman, W. Kout, W. Dalhuijsen, E. Milacic, M.J.J. Mulder, Electrochemical Hydrogen Compression, ECS Transactions, 64 (2014) 1009-1018.
[25] R. Lan, J.T.S. Irvine, S. Tao, Ammonia and related chemicals as potential indirect hydrogen storage materials, International Journal of Hydrogen Energy, 37 (2012) 1482-1494.
[26] A comparison of hydrogen and propane fuels, U.S. Department of Energy, 2009.
[27] E. Rivard, M. Trudeau, K. Zaghib, Hydrogen Storage for Mobility: A Review, Materials, 12 (2019) 1973.
[28] X. Ge, A. Sumboja, D. Wuu, T. An, B. Li, F.W.T. Goh, T.S.A. Hor, Y. Zong, Z. Liu, Oxygen Reduction in Alkaline Media: From Mechanisms to Recent Advances of Catalysts, ACS Catalysis, 5 (2015) 4643-4667.
[29] Y. Zhu, W. Zhou, Z. Shao, Perovskite/Carbon Composites: Applications in Oxygen Electrocatalysis, Small, 13 (2017) 1603793.
[30] A. Brouzgou, S. Song, Z.-X. Liang, P. Tsiakaras, Non-Precious Electrocatalysts for Oxygen Reduction Reaction in Alkaline Media: Latest Achievements on Novel Carbon Materials, Catalysts, 6 (2016) 159.
[31] J. Suntivich, H.A. Gasteiger, N. Yabuuchi, H. Nakanishi, J.B. Goodenough, Y. Shao-Horn, Design principles for oxygen-reduction activity on perovskite oxide catalysts for fuel cells and metal–air batteries, Nature Chemistry, 3 (2011) 546-550.
[32] W.T. Hong, M. Risch, K.A. Stoerzinger, A. Grimaud, J. Suntivich, Y. Shao-Horn, Toward the rational design of non-precious transition metal oxides for oxygen electrocatalysis, Energy & Environmental Science, 8 (2015) 1404-1427.
[33] P. Zou, S. Chen, R. Lan, J. Humphreys, G. Jeerh, S. Tao, Investigation of Perovskite Oxide $SrFe_{0.8}Cu_{0.1}Nb_{0.1}O_{3-\delta}$ as Cathode for a Room Temperature Direct Ammonia Fuel Cell, International Journal of Hydrogen Energy, 44 (2019) 26554-26564.
[34] P. Zou, S. Chen, R. Lan, S. Tao, Investigation of Perovskite Oxide $SrCo_{0.8}Cu_{0.1}Nb_{0.1}O_{3-\delta}$ as a Cathode Material for Room Temperature Direct Ammonia Fuel Cells, ChemSusChem, 12 (2019) 2788-2794.
[35] M. Zhang, G. Jeerh, P. Zou, R. Lan, M. Wang, H. Wang, S.W. Tao, Recent development of perovskite oxide-based electrocatalysts and their applications in low to intermediate temperature electrochemical devices, Materials Today, 49 (2021) 351-377.
[36] J. Greeley, I.E.L. Stephens, A.S. Bondarenko, T.P. Johansson, H.A. Hansen, T.F. Jaramillo, J. Rossmeisl, I. Chorkendorff, J.K. Nørskov, Alloys of platinum and early transition metals as oxygen reduction electrocatalysts, Nature Chemistry, 1 (2009) 552-556.

[37] V.R. Stamenkovic, B. Fowler, B.S. Mun, G. Wang, P.N. Ross, C.A. Lucas, N.M. Marković, Improved Oxygen Reduction Activity on $Pt_3Ni(111)$ via Increased Surface Site Availability, Science, 315 (2007) 493-497.
[38] M. Retuerto, A.G. Pereira, F.J. Pérez-Alonso, M.A. Peña, J.L.G. Fierro, J.A. Alonso, M.T. Fernández-Díaz, L. Pascual, S. Rojas, Structural Effects of $LaNiO_3$ as Electrocatalyst for the Oxygen Reduction Reaction, Applied Catalysis B: Environmental, 203 (2017) 363-371.
[39] S. Holdcroft, Fuel Cell Catalyst Layers: A Polymer Science Perspective, Chemistry of Materials, 26 (2014) 381-393.
[40] F. Samimi, M.R. Rahimpour, Chapter 14 - Direct Methanol Fuel Cell, in: A. Basile, F. Dalena (Eds.) Methanol, Elsevier2018, pp. 381-397.
[41] E.W. Justi, W. Winsel, Brit. patent, 821, 6881955.
[42] J.V. Ashurst, T.M. Nappe, Methanol Toxicity, StatPearls, NCBI, https://www.ncbi.nlm.nih.gov/books/NBK482121/, 2021.
[43] B. Cox, K.J.J.o.P.S. Treyer, Environmental and economic assessment of a cracked ammonia fuelled alkaline fuel cell for off-grid power applications, 275 (2015) 322-335.
[44] F.R. García-García, J. Álvarez-Rodríguez, I. Rodríguez-Ramos, A. Guerrero-Ruiz, The use of carbon nanotubes with and without nitrogen doping as support for ruthenium catalysts in the ammonia decomposition reaction, Carbon, 48 (2010) 267-276.
[45] C. Zamfirescu, I. Dincer, Using ammonia as a sustainable fuel, Journal of Power Sources, 185 (2008) 459-465.
[46] K.T. Møller, T.R. Jensen, E. Akiba, H.-w. Li, Hydrogen - A sustainable energy carrier, Progress in Natural Science: Materials International, 27 (2017) 34-40.
[47] A. Klerke, C.H. Christensen, J.K. Nørskov, T. Vegge, Ammonia for hydrogen storage: challenges and opportunities, Journal of Materials Chemistry, 18 (2008) 2304-2310.
[48] S. Villalonga, F. Nony, C. Magnier, J.L. Yvernes, C. Thomas, B. Delmas, P. Mazabraud, Composite 700 bar-vessel for on-board compressed gaseous hydrogen storage, International Conference on Composite Materials ICCM, (2009) 10.
[49] Y. Bicer, I. Dincer, Evaluation of Renewable and Conventional Ammonia as a Potential Solution, in: T.S. Uyar (Ed.) Towards 100% Renewable Energy, Springer International Publishing, Cham, 2017, pp. 69-86.
[50] ChemicalSafetyFacts.org, Ammonia, https://www.chemicalsafetyfacts.org/ammonia/.
[51] T. Brown, Green ammonia plant proposed for Orkney, https://www.ammoniaenergy.org/articles/green-ammonia-plant-proposed-for-orkney/, 2020.
[52] W. Guo, K. Zhang, Z. Liang, R. Zou, Q. Xu, Electrochemical nitrogen fixation and utilization: theories, advanced catalyst materials and system design, Chemical Society Reviews, 48 (2019) 5658-5716.
[53] D.R. MacFarlane, P.V. Cherepanov, J. Choi, B.H.R. Suryanto, R.Y. Hodgetts, J.M. Bakker, F.M. Ferrero Vallana, A.N. Simonov, A Roadmap to the Ammonia Economy, Joule, 4 (2020) 1186-1205.
[54] T. Brown, Project GERI: BP's green ammonia feasibility study, https://www.ammoniaenergy.org/articles/project-geri-bp-green-ammonia-feasibility-study/?, 2020.
[55] T. Brown, Solar ammonia, available in Spain from 2021, https://www.ammoniaenergy.org/articles/solar-ammonia-available-in-spain-from-2021/, 2020.

[56] T. Brown, Saudi Arabia to export renewable energy using green ammonia, https://www.ammoniaenergy.org/articles/saudi-arabia-to-export-renewable-energy-using-green-ammonia/, 2020.
[57] Safety Data Sheet: Ammonia, Anhydrous, Safety Data Sheet, http://alsafetydatasheets.com/download/se/Ammonia_NOAL_0002_SE_EN.pdf.
[58] Y. Zhao, B.P. Setzler, J. Wang, J. Nash, T. Wang, B. Xu, Y. Yan, An Efficient Direct Ammonia Fuel Cell for Affordable Carbon-Neutral Transportation, Joule, 3 (2019) 2472-2484.
[59] R. Lan, S. Tao, Ammonia as a suitable fuel for fuel cells, Frontiers in energy research, 2 (2014) 35.
[60] C. Smith, A.K. Hill, L. Torrente-Murciano, Current and Future Role of Haber–Bosch Ammonia in a Carbon-Free Energy Landscape, Energy & Environmental Science, 13 (2020) 331-344.
[61] J. Hansson, S. Brynolf, E. Fridell, M. Lehtveer, The Potential Role of Ammonia as Marine Fuel—Based on Energy Systems Modeling and Multi-Criteria Decision Analysis, Sustainability, 12 (2020) 3265.
[62] Z. Cesaro, M. Ives, R. Nayak-Luke, M. Mason, R. Bañares-Alcántara, Ammonia to Power: Forecasting the Levelized Cost of Electricity From Green Ammonia in Large-Scale Power pPlants, Applied Energy, 282 (2021) 116009.
[63] D. Cheddie, Ammonia as a Hydrogen Source for Fuel Cells: A Review, in: D. Minic (Ed.) Hydrogen Energy: Challenges and Perspectives, IntechOpen, 2012.
[64] R. Lan, S. Tao, Direct Ammonia Alkaline Anion-Exchange Membrane Fuel Cells, Electrochemical and Solid-State Letters, 13 (2010) B83.
[65] M. Ni, M.K.H. Leung, D.Y.C. Leung, Ammonia-fed solid oxide fuel cells for power generation—A review, International Journal of Energy Research, 33 (2009) 943-959.
[66] G. Merle, M. Wessling, K. Nijmeijer, Anion exchange membranes for alkaline fuel cells: A review, Journal of Membrane Science, 377 (2011) 1-35.
[67] Y. Wang, Y. Pang, H. Xu, A. Martinez, K.S. Chen, PEM Fuel cell and electrolysis cell technologies and hydrogen infrastructure development – a review, Energy & Environmental Science, 15 (2022) 2288-2328.
[68] G. Jeerh, P. Zou, M. Zhang, S. Tao, Perovskite oxide $LaCr_{0.25}Fe_{0.25}Co_{0.5}O_{3-\delta}$ as an Efficient Non-Noble Cathode for Direct Ammonia Fuel Cells, Applied Catalysis B: Environmental, 319 (2022) 121919.
[69] G. Jeerh, P. Zou, M. Zhang, S. Chen, J. Humphreys, S. Tao, Electrooxidation of ammonia on A-site deficient perovskite oxide $La_{0.9}Ni_{0.6}Cu_{0.35}Fe_{0.05}O_{3-\delta}$ for wastewater treatment, Separation and Purification Technology, 297 (2022) 121451.
[70] G. Jeerh, P. Zou, M. Zhang, S. Tao, Optimisation of a perovskite oxide-based cathode catalyst layer on performance of direct ammonia fuel cells, Submitted to ACS Applied Materials & Interfaces, (2022).
[71] J.C.J.J.o.P.S. Ganley, An intermediate-temperature direct ammonia fuel cell with a molten alkaline hydroxide electrolyte, 178 (2008) 44-47.
[72] K. Kordesch, V. Hacker, J. Gsellmann, M. Cifrain, G. Faleschini, P. Enzinger, R. Fankhauser, M. Ortner, M. Muhr, R.R. Aronson, Alkaline fuel cells applications, Journal of Power Sources, 86 (2000) 162-165.
[73] S. Gottesfeld, The Direct Ammonia Fuel Cell and a Common Pattern of Electrocatalytic Processes, Journal of The Electrochemical Society, 165 (2018) J3405-J3412.
[74] H.M. Zhang, Y.F. Wang, Y.H. Kwok, Z.C. Wu, D.H. Xia, D.Y.C. Leung, A Direct Ammonia Microfluidic Fuel Cell using NiCu Nanoparticles Supported on Carbon Nanotubes as an Electrocatalyst, ChemSusChem, 11 (2018) 2889-2897.

[75] S. Ishiyama, N.C. Rosero-Navarro, A. Miura, K. Tadanaga, Mg-Al layered double hydroxide as an electrolyte membrane for aqueous ammonia fuel cell, Materials Research Bulletin, 119 (2019) 110561.
[76] B. Achrai, Y. Zhao, T. Wang, G. Tamir, R. Abbasi, B.P. Setzler, M. Page, Y. Yan, S. Gottesfeld, A Direct Ammonia Fuel Cell with a KOH-Free Anode Feed Generating 180 mW cm−2 at 120 °C, Journal of The Electrochemical Society, 167 (2020) 134518.
[77] T. Wang, Y. Zhao, B.P. Setzler, R. Abbasi, S. Gottesfeld, Y. Yan, A high-performance 75 W direct ammonia fuel cell stack, Cell Reports Physical Science, 3 (2022) 100829.
[78] M. Zhang, J. Zhang, G. Jeerh, P. Zou, B. Sun, M. Walker, K. Xie, S. Tao, A symmetric direct ammonia fuel cell using ternary NiCuFe alloy embedded in carbon network as electrodes, Journal of Materials Chemistry A, (2022, 10.1039/D2TA04129D).
[79] E.J. Park, Y.S. Kim, Quaternized aryl ether-free polyaromatics for alkaline membrane fuel cells: synthesis, properties, and performance – a topical review, Journal of Materials Chemistry A, 6 (2018) 15456-15477.
[80] J. Wang, Y. Zhao, B.P. Setzler, S. Rojas-Carbonell, C. Ben Yehuda, A. Amel, M. Page, L. Wang, K. Hu, L. Shi, S. Gottesfeld, B. Xu, Y. Yan, Poly(aryl piperidinium) Membranes and Ionomers for Hydroxide Exchange Membrane Fuel Cells, Nature Energy, 4 (2019) 392-398.
[81] C. Lu, C. Long, Y. Li, Z. Li, H. Zhu, Chemically stable poly(meta-terphenyl piperidinium) with highly conductive side chain for alkaline fuel cell membranes, Journal of Membrane Science, 598 (2020) 117797.
[82] A.L. Ong, S. Saad, R. Lan, R.J. Goodfellow, S. Tao, Anionic membrane and ionomer based on poly(2,6-dimethyl-1,4-phenylene oxide) for alkaline membrane fuel cells, Journal of Power Sources, 196 (2011) 8272-8279.
[83] A. Serov, I.V. Zenyuk, C.G. Arges, M. Chatenet, Hot topics in alkaline exchange membrane fuel cells, Journal of Power Sources, 375 (2018) 149-157.
[84] Q. Duan, S. Ge, C.-Y. Wang, Water uptake, ionic conductivity and swelling properties of anion-exchange membrane, Journal of Power Sources, 243 (2013) 773-778.
[85] R. Abbasi, B.P. Setzler, J. Wang, Y. Zhao, T. Wang, S. Gottesfeld, Y. Yan, Low-temperature direct ammonia fuel cells: Recent developments and remaining challenges, Current Opinion in Electrochemistry, 21 (2020) 335-344.
[86] W.-H. Lee, E.J. Park, J. Han, D.W. Shin, Y.S. Kim, C. Bae, Poly(terphenylene) Anion Exchange Membranes: The Effect of Backbone Structure on Morphology and Membrane Property, ACS Macro Letters, 6 (2017) 566-570.
[87] K.F.L. Hagesteijn, S. Jiang, B.P. Ladewig, A review of the synthesis and characterization of anion exchange membranes, Journal of Materials Science, 53 (2018) 11131-11150.
[88] S. Gottesfeld, D.R. Dekel, M. Page, C. Bae, Y. Yan, P. Zelenay, Y.S. Kim, Anion exchange membrane fuel cells: Current status and remaining challenges, Journal of Power Sources, 375 (2018) 170-184.
[89] S. Suzuki, H. Muroyama, T. Matsui, K. Eguchi, Fundamental studies on direct ammonia fuel cell employing anion exchange membrane, Journal of Power Sources, 208 (2012) 257-262.
[90] H. Zhang, M. Jin, Y. Xia, Enhancing the catalytic and electrocatalytic properties of Pt-based catalysts by forming bimetallic nanocrystals with Pd, Chemical Society Reviews, 41 (2012) 8035-8049.

[91] B.Y. Xia, Y. Yan, N. Li, H.B. Wu, X.W. Lou, X. Wang, A metal–organic framework-derived bifunctional oxygen electrocatalyst, Nature Energy, 1 (2016) 15006.

[92] F. Cheng, J. Chen, Metal–air batteries: from oxygen reduction electrochemistry to cathode catalysts, Chemical Society Reviews, 41 (2012) 2172-2192.

[93] D. Chen, C. Chen, Z.M. Baiyee, Z. Shao, F. Ciucci, Nonstoichiometric Oxides as Low-Cost and Highly-Efficient Oxygen Reduction/Evolution Catalysts for Low-Temperature Electrochemical Devices, Chemical Reviews, 115 (2015) 9869-9921.

[94] A. Jun, J. Kim, J. Shin, G. Kim, Perovskite as a Cathode Material: A Review of its Role in Solid-Oxide Fuel Cell Technology, ChemElectroChem, 3 (2016) 511-530.

[95] S.J. Skinner, Recent advances in Perovskite-type materials for solid oxide fuel cell cathodes, International Journal of Inorganic Materials, 3 (2001) 113-121.

[96] P. Kaur, K. Singh, Review of perovskite-structure related cathode materials for solid oxide fuel cells, Ceramics International, 46 (2020) 5521-5535.

[97] C. Sun, J.A. Alonso, J. Bian, Recent Advances in Perovskite-Type Oxides for Energy Conversion and Storage Applications, Advanced Energy Materials, 11 (2021) 2000459.

[98] H. Arai, M. Hayashi, SECONDARY BATTERIES – METAL-AIR SYSTEMS | Overview (Secondary and Primary), in: J. Garche (Ed.) Encyclopedia of Electrochemical Power Sources, Elsevier, Amsterdam, 2009, pp. 347-355.

[99] A. Safakas, G. Bampos, S. Bebelis, Oxygen reduction reaction on $La_{0.8}Sr_{0.2}Co_xFe_{1-x}O_{3-\delta}$ perovskite/carbon black electrocatalysts in alkaline medium, Applied Catalysis B: Environmental, 244 (2019) 225-232.

[100] J. Liu, L. Jiang, B. Zhang, J. Jin, D.S. Su, S. Wang, G. Sun, Controllable Synthesis of Cobalt Monoxide Nanoparticles and the Size-Dependent Activity for Oxygen Reduction Reaction, ACS Catalysis, 4 (2014) 2998-3001.

[101] Y. Zhu, W. Zhou, Y. Chen, J. Yu, X. Xu, C. Su, M.O. Tadé, Z. Shao, Boosting Oxygen Reduction Reaction Activity of Palladium by Stabilizing Its Unusual Oxidation States in Perovskite, Chemistry of Materials, 27 (2015) 3048-3054.

[102] Y. Anbo, X. Tian, S. Liping, L. Qiang, H. Lihua, Z. Hui, Effects of rare earth doping on electrochemical properties of $NdBaCo_2O_{6-\delta}$ cathode materials, Journal of Alloys and Compounds, 837 (2020) 155563.

[103] H. Zhu, P. Zhang, S. Dai, Recent Advances of Lanthanum-Based Perovskite Oxides for Catalysis, ACS Catalysis, 5 (2015) 6370-6385.

[104] J. Suntivich, K.J. May, H.A. Gasteiger, J.B. Goodenough, Y. Shao-Horn, A Perovskite Oxide Optimized for Oxygen Evolution Catalysis from Molecular Orbital Principles, Science, 334 (2011) 1383.

[105] Q. Sun, Z. Dai, Z. Zhang, Z. Chen, H. Lin, Y. Gao, D. Chen, Double perovskite $PrBaCo_2O_{5.5}$: An efficient and stable electrocatalyst for hydrogen evolution reaction, Journal of Power Sources, 427 (2019) 194-200.

[106] X. Xu, Y. Chen, W. Zhou, Z. Zhu, C. Su, M. Liu, Z. Shao, A Perovskite Electrocatalyst for Efficient Hydrogen Evolution Reaction, Advanced Materials, 28 (2016) 6442-6448.

[107] L. Shu, J. Sunarso, S.S. Hashim, J. Mao, W. Zhou, F. Liang, Advanced perovskite anodes for solid oxide fuel cells: A review, International Journal of Hydrogen Energy, 44 (2019) 31275-31304.

[108] N. Ramadass, ABO_3-type oxides—Their structure and properties—A bird's eye view, Materials Science and Engineering, 36 (1978) 231-239.

[109] J. Hwang, R.R. Rao, L. Giordano, Y. Katayama, Y. Yu, Y. Shao-Horn, Perovskites in catalysis and electrocatalysis, Science, 358 (2017) 751.

[110] M.A. Peña, J.L.G. Fierro, Chemical Structures and Performance of Perovskite Oxides, Chemical Reviews, 101 (2001) 1981-2018.

[111] J. Xu, C. Chen, Z. Han, Y. Yang, J. Li, Q. Deng, Recent Advances in Oxygen Electrocatalysts Based on Perovskite Oxides, Nanomaterials, 9 (2019).

[112] J.-I. Jung, M. Risch, S. Park, M.G. Kim, G. Nam, H.-Y. Jeong, Y. Shao-Horn, J. Cho, Optimizing nanoparticle perovskite for bifunctional oxygen electrocatalysis, Energy & Environmental Science, 9 (2016) 176-183.

[113] L. Yang, S. Wang, K. Blinn, M. Liu, Z. Liu, Z. Cheng, M. Liu, Enhanced Sulfur and Coking Tolerance of a Mixed Ion Conductor for SOFCs: $BaZr_{0.1}Ce_{0.7}Y_{0.2-x}Yb_xO_{3-d}$, Science, 326 (2009) 126.

[114] J.-h. Myung, D. Neagu, D.N. Miller, J.T.S. Irvine, Switching on electrocatalytic activity in solid oxide cells, Nature, 537 (2016) 528-531.

[115] W. Zhou, J. Sunarso, M. Zhao, F. Liang, T. Klande, A. Feldhoff, A Highly Active Perovskite Electrode for the Oxygen Reduction Reaction Below 600 °C, Angewandte Chemie International Edition, 52 (2013) 14036-14040.

[116] Y. Zhu, J. Sunarso, W. Zhou, S. Jiang, Z. Shao, High-performance $SrNb_{0.1}Co_{0.9-x}Fe_xO_{3-\delta}$ perovskite cathodes for low-temperature solid oxide fuel cells, Journal of Materials Chemistry A, 2 (2014) 15454-15462.

[117] Y.-F. Sun, Y.-Q. Zhang, J. Chen, J.-H. Li, Y.-T. Zhu, Y.-M. Zeng, B.S. Amirkhiz, J. Li, B. Hua, J.-L. Luo, New Opportunity for in Situ Exsolution of Metallic Nanoparticles on Perovskite Parent, Nano Letters, 16 (2016) 5303-5309.

[118] Y. Zhu, J. Sunarso, W. Zhou, Z. Shao, Probing CO_2 reaction mechanisms and effects on the $SrNb_{0.1}Co_{0.9-x}Fe_xO_{3-\delta}$ cathodes for solid oxide fuel cells, Applied Catalysis B: Environmental, 172-173 (2015) 52-57.

[119] J.T. Mefford, W.G. Hardin, S. Dai, K.P. Johnston, K.J. Stevenson, Anion charge storage through oxygen intercalation in $LaMnO_3$ perovskite pseudocapacitor electrodes, Nature Materials, 13 (2014) 726-732.

[120] Y.L. Liang Zhu, Dr. Chao Su, Prof. Wei Zhou, Prof. Meilin Liu, Prof. Zongping Shao, Perovskite $SrCo_{0.9}Nb_{0.1}O_{3-\delta}$ as an Anion-Intercalated Electrode Material for Supercapacitors with Ultrahigh Volumetric Energy Density, 55 (2016) 9576.

[121] S. Royer, D. Duprez, F. Can, X. Courtois, C. Batiot-Dupeyrat, S. Laassiri, H. Alamdari, Perovskites as Substitutes of Noble Metals for Heterogeneous Catalysis: Dream or Reality, Chemical Reviews, 114 (2014) 10292-10368.

[122] J. Zhu, H. Li, L. Zhong, P. Xiao, X. Xu, X. Yang, Z. Zhao, J. Li, Perovskite Oxides: Preparation, Characterizations, and Applications in Heterogeneous Catalysis, ACS Catalysis, 4 (2014) 2917-2940.

[123] M. Yasumiti, Y. Hirosi, T. Hideo, A new catalyst for cathodic reduction of oxygen: Lanthanum nickel oxide, Chemistry Letters, 4 (1975) 661-662.

[124] J. Sunarso, A.A.J. Torriero, W. Zhou, P.C. Howlett, M. Forsyth, Oxygen Reduction Reaction Activity of La-Based Perovskite Oxides in Alkaline Medium: A Thin-Film Rotating Ring-Disk Electrode Study, The Journal of Physical Chemistry C, 116 (2012) 5827-5834.

[125] J. Sun, L. Du, B. Sun, G. Han, Y. Ma, J. Wang, H. Huo, C. Du, G. Yin, Bifunctional $LaMn_{0.3}Co_{0.7}O_3$ Perovskite Oxide Catalyst for Oxygen Reduction and Evolution Reactions: The Optimized e_g Electronic Structures by Manganese Dopant, ACS Applied Materials & Interfaces, 12 (2020) 24717-24725.

[126] Z. Wang, Y. You, J. Yuan, Y.-X. Yin, Y.-T. Li, S. Xin, D. Zhang, Nickel-Doped $La_{0.8}Sr_{0.2}Mn_{1-x}Ni_xO_3$ Nanoparticles Containing Abundant Oxygen Vacancies as an Optimized Bifunctional Catalyst for Oxygen Cathode in Rechargeable Lithium–Air Batteries, ACS Applied Materials & Interfaces, 8 (2016) 6520-6528.

[127] M. Risch, Perovskite Electrocatalysts for the Oxygen Reduction Reaction in Alkaline Media, Catalysts, 7 (2017) 154.

[128] J. Irvine, J. Rupp, G. Liu, X. Xu, S.M. Haile, X. Qian, A. Snyder, R. Freer, D. Ekren, S. Skinner, O. Celikbilek, S. Chen, S.W. Tao, T.H. Shin, R. O'Hayre, J. Huang, C. Duan, M. Papac, S. Li, A. Russel, V. Celorrio, B. Hayden, H. Nolan, X. Huang, G. Wang, I. Metcalfe, D. Neagu, S.G. Martin, Roadmap on inorganic perovskites for energy applications, Journal of Physics: Energy, 3 (2021) 031502.

[129] D.B. Meadowcroft, Low-cost Oxygen Electrode Material, Nature, 226 (1970) 847-848.

[130] Y. Matsumoto, H. Yoneyama, H. Tamura, Catalytic activity for electrochemical reduction of oxygen of lanthanum nickel oxide and related oxides, Journal of Electroanalytical Chemistry and Interfacial Electrochemistry, 79 (1977) 319-326.

[131] Y. Matsumoto, H. Yoneyama, H. Tamura, Influence of the nature of the conduction band of transition metal oxides on catalytic activity for oxygen reduction, Journal of Electroanalytical Chemistry and Interfacial Electrochemistry, 83 (1977) 237-243.

[132] G. King, P.M. Woodward, Cation ordering in perovskites, Journal of Materials Chemistry, 20 (2010) 5785-5796.

[133] Y. Xue, H. Miao, S. Sun, Q. Wang, S. Li, Z. Liu, (La1−xSrx)0.98MnO3 perovskite with A-site deficiencies toward oxygen reduction reaction in aluminum-air batteries, Journal of Power Sources, 342 (2017) 192-201.

[134] J.B. Goodenough, Covalency Criterion for Localized vs Collective Electrons in Oxides with the Perovskite Structure, Journal of Applied Physics, 37 (1966) 1415-1422.

[135] M. Yasumichi, Y. Hiroshi, T. Hideo, The Mechanism of Oxygen Reduction at a LaNiO3 Electrode, Bulletin of the Chemical Society of Japan, 51 (1978) 1927-1930.

[136] X. Wang, X.J. Gao, L. Qin, C. Wang, L. Song, Y.-N. Zhou, G. Zhu, W. Cao, S. Lin, L. Zhou, K. Wang, H. Zhang, Z. Jin, P. Wang, X. Gao, H. Wei, e_g occupancy as an effective descriptor for the catalytic activity of perovskite oxide-based peroxidase mimics, Nature Communications, 10 (2019) 704.

[137] R.A. Van Santen, M. Neurock, Concepts in Theoretical Heterogeneous Catalytic Reactivity, Catalysis Reviews, 37 (1995) 557-698.

[138] W.T. Hong, K.A. Stoerzinger, Y.-L. Lee, L. Giordano, A. Grimaud, A.M. Johnson, J. Hwang, E.J. Crumlin, W. Yang, Y. Shao-Horn, Charge-transfer-energy-dependent oxygen evolution reaction mechanisms for perovskite oxides, Energy & Environmental Science, 10 (2017) 2190-2200.

[139] B. Hammer, Special Sites at Noble and Late Transition Metal Catalysts, Topics in Catalysis, 37 (2006) 3-16.

[140] X. Liu, H. Gong, T. Wang, H. Guo, L. Song, W. Xia, B. Gao, Z. Jiang, L. Feng, J. He, Cobalt-Doped Perovskite-Type Oxide $LaMnO_3$ as Bifunctional Oxygen Catalysts for Hybrid Lithium–Oxygen Batteries, Chemistry – An Asian Journal, 13 (2018) 528-535.

[141] M. Wang, B. Han, J. Deng, Y. Jiang, M. Zhou, M. Lucero, Y. Wang, Y. Chen, Z. Yang, A.T. N'Diaye, Q. Wang, Z.J. Xu, Z. Feng, Influence of Fe Substitution into $LaCoO_3$ Electrocatalysts on Oxygen-Reduction Activity, ACS Applied Materials & Interfaces, 11 (2019) 5682-5686.

[142] X. Gao, Z. Sun, J. Ran, J. Li, J. Zhang, D. Gao, High efficiency electrocatalyst of $LaCr_{0.5}Fe_{0.5}O_3$ nanoparticles on oxygen-evolution reaction, Scientific Reports, 10 (2020) 13395.

[143] R.S. Kalubarme, G.-E. Park, K.-N. Jung, K.-H. Shin, W.-H. Ryu, C.-J. Park, $LaNi_xCo_{1-x}O_{3-\delta}$ Perovskites as Catalyst Material for Non-Aqueous Lithium-Oxygen Batteries, Journal of The Electrochemical Society, 161 (2014) A880-A889.
[144] Z. Du, P. Yang, L. Wang, Y. Lu, J.B. Goodenough, J. Zhang, D. Zhang, Electrocatalytic performances of $LaNi_{1-x}Mg_xO_3$ perovskite oxides as bi-functional catalysts for lithium air batteries, Journal of Power Sources, 265 (2014) 91-96.
[145] D. Zhang, Y. Song, Z. Du, L. Wang, Y. Li, J.B. Goodenough, Active $LaNi_{1-x}Fe_xO_3$ bifunctional catalysts for air cathodes in alkaline media, Journal of Materials Chemistry A, 3 (2015) 9421-9426.
[146] S.M. Rafi, Transition Metal Oxide-Based Perovskite Structures as a Bifunctional Oxygen Electrocatalysts: Fe Doped $LaCoO_3$ Nanoparticles, International Journal of Engineering and Advanced Technology, 9 (2019).
[147] J.O.M. Bockris, T. Otagawa, The Electrocatalysis of Oxygen Evolution on Perovskites, Journal of The Electrochemical Society, 131 (1984) 290-302.
[148] X. Xu, Y. Pan, W. Zhou, Y. Chen, Z. Zhang, Z. Shao, Toward Enhanced Oxygen Evolution on Perovskite Oxides Synthesized from Different Approaches: A Case Study of $Ba_{0.5}Sr_{0.5}Co_{0.8}Fe_{0.2}O_{3-\delta}$, Electrochimica Acta, 219 (2016) 553-559.
[149] W.T. Hong, R.E. Welsch, Y. Shao-Horn, Descriptors of Oxygen-Evolution Activity for Oxides: A Statistical Evaluation, The Journal of Physical Chemistry C, 120 (2016) 78-86.
[150] M. Zhang, P. Zou, G. Jeerh, B. Sun, M. Walker, S. Tao, Oxygen Vacancy-Rich $La_{0.5}Sr_{1.5}Ni_{0.9}Cu_{0.1}O_{4-\delta}$ as a High-Performance Bifunctional Catalyst for Symmetric Ammonia Electrolyzer, Advanced Functional Materials, (2022) 2204881.
[151] M. Zhang, H. Li, X. Duan, P. Zou, G. Jeerh, B. Sun, S. Chen, J. Humphreys, M. Walker, K. Xie, S. Tao, An Efficient Symmetric Electrolyzer Based On Bifunctional Perovskite Catalyst for Ammonia Electrolysis, Advanced Science, DOI: 10.1002/advs.202101299 (2021) 2101299.
[152] J.-I. Jung, H.Y. Jeong, M.G. Kim, G. Nam, J. Park, J. Cho, Fabrication of $Ba_{0.5}Sr_{0.5}Co_{0.8}Fe_{0.2}O_{3-\delta}$ Catalysts with Enhanced Electrochemical Performance by Removing an Inherent Heterogeneous Surface Film Layer, Advanced Materials, 27 (2015) 266-271.
[153] F. Cheng, T. Zhang, Y. Zhang, J. Du, X. Han, J. Chen, Enhancing Electrocatalytic Oxygen Reduction on MnO_2 with Vacancies, Angewandte Chemie International Edition, 52 (2013) 2474-2477.
[154] Y.A. Mastrikov, R. Merkle, E. Heifets, E.A. Kotomin, J. Maier, Pathways for Oxygen Incorporation in Mixed Conducting Perovskites: A DFT-Based Mechanistic Analysis for (La, Sr)$MnO_{3-\delta}$, The Journal of Physical Chemistry C, 114 (2010) 3017-3027.
[155] J.W. Han, B. Yildiz, Enhanced one dimensional mobility of oxygen on strained $LaCoO_3$(001) surface, Journal of Materials Chemistry, 21 (2011) 18983-18990.
[156] C. Yang, A. Grimaud, Factors Controlling the Redox Activity of Oxygen in Perovskites: From Theory to Application for Catalytic Reactions, Catalysts, 7 (2017) 149.
[157] J. Du, T. Zhang, F. Cheng, W. Chu, Z. Wu, J. Chen, Nonstoichiometric Perovskite $CaMnO_{3-\delta}$ for Oxygen Electrocatalysis with High Activity, Inorganic Chemistry, 53 (2014) 9106-9114.
[158] C.-F. Chen, G. King, R.M. Dickerson, P.A. Papin, S. Gupta, W.R. Kellogg, G. Wu, Oxygen-deficient $BaTiO_{3-x}$ perovskite as an efficient bifunctional oxygen electrocatalyst, Nano Energy, 13 (2015) 423-432.
[159] Y. Zhu, W. Zhou, J. Yu, Y. Chen, M. Liu, Z. Shao, Enhancing Electrocatalytic Activity of Perovskite Oxides by Tuning Cation Deficiency for

Oxygen Reduction and Evolution Reactions, Chemistry of Materials, 28 (2016) 1691-1697.

[160] L. Yan, Y. Lin, X. Yu, W. Xu, T. Salas, H. Smallidge, M. Zhou, H. Luo, $La_{0.8}Sr_{0.2}MnO_3$-Based Perovskite Nanoparticles with the A-Site Deficiency as High Performance Bifunctional Oxygen Catalyst in Alkaline Solution, ACS Applied Materials & Interfaces, 9 (2017) 23820-23827.

[161] R.-h. Yuan, Y. He, W. He, M. Ni, M.K.H. Leung, Bifunctional electrocatalytic activity of $La_{0.8}Sr_{0.2}MnO_3$-based perovskite with the A-site deficiency for oxygen reduction and evolution reactions in alkaline media, Applied Energy, 251 (2019) 113406.

[162] Q. Ji, L. Bi, J. Zhang, H. Cao, X.S. Zhao, The role of oxygen vacancies of ABO_3 perovskite oxides in the oxygen reduction reaction, Energy & Environmental Science, 13 (2020) 1408-1428.

[163] Y. Zhu, Y. Lin, X. Shen, J. Sunarso, W. Zhou, S. Jiang, D. Su, F. Chen, Z. Shao, Influence of crystal structure on the electrochemical performance of A-site-deficient $Sr_{1-s}Nb_{0.1}Co_{0.9}O_{3-\delta}$ perovskite cathodes, RSC Advances, 4 (2014) 40865-40872.

[164] Y. Zhu, W. Zhou, Y. Chen, Z. Shao, An Aurivillius Oxide Based Cathode with Excellent CO2 Tolerance for Intermediate-Temperature Solid Oxide Fuel Cells, Angewandte Chemie International Edition, 55 (2016) 8988-8993.

[165] G. Wu, J. Wang, W. Ding, Y. Nie, L. Li, X. Qi, S. Chen, Z. Wei, A Strategy to Promote the Electrocatalytic Activity of Spinels for Oxygen Reduction by Structure Reversal, Angewandte Chemie International Edition, 55 (2016) 1340-1344.

[166] P.W. Menezes, A. Indra, N.R. Sahraie, A. Bergmann, P. Strasser, M. Driess, Cobalt–Manganese-Based Spinels as Multifunctional Materials that Unify Catalytic Water Oxidation and Oxygen Reduction Reactions, ChemSusChem, 8 (2015) 164-171.

[167] G. Wang, T. Xu, S. Wen, M. Pan, Structure-dependent electrocatalytic activity of $La_{1-x}Sr_xMnO_3$ for oxygen reduction reaction, Science China Chemistry, 58 (2015) 871-878.

[168] S. Malkhandi, B. Yang, A.K. Manohar, A. Manivannan, G.K.S. Prakash, S.R. Narayanan, Electrocatalytic Properties of Nanocrystalline Calcium-Doped Lanthanum Cobalt Oxide for Bifunctional Oxygen Electrodes, The Journal of Physical Chemistry Letters, 3 (2012) 967-972.

[169] D. Chen, J. Wang, Z. Zhang, Z. Shao, F. Ciucci, Boosting oxygen reduction/evolution reaction activities with layered perovskite catalysts, Chemical Communications, 52 (2016) 10739-10742.

[170] C. Zhao, X. Zhang, M. Yu, A. Wang, L. Wang, L. Xue, J. Liu, Z. Yang, W. Wang, Cooperative Catalysis toward Oxygen Reduction Reaction under Dual Coordination Environments on Intrinsic $AMnO_3$-Type Perovskites via Regulating Stacking Configurations of Coordination Units, Advanced Materials, 32 (2020) 2006145.

[171] J.-I. Jung, S. Park, M.-G. Kim, J. Cho, Tunable Internal and Surface Structures of the Bifunctional Oxygen Perovskite Catalysts, Advanced Energy Materials, 5 (2015) 1501560.

[172] J.-I. Jung, H.Y. Jeong, J.-S. Lee, M.G. Kim, J. Cho, A Bifunctional Perovskite Catalyst for Oxygen Reduction and Evolution, Angewandte Chemie, 126 (2014) 4670-4674.

[173] J. Suntivich, H.A. Gasteiger, N. Yabuuchi, Y. Shao-Horn, Electrocatalytic Measurement Methodology of Oxide Catalysts Using a Thin-Film Rotating Disk Electrode, Journal of The Electrochemical Society, 157 (2010) B1263.

[174] W. Zhou, J. Sunarso, Enhancing Bi-functional Electrocatalytic Activity of Perovskite by Temperature Shock: A Case Study of $LaNiO_{3-\delta}$, The Journal of Physical Chemistry Letters, 4 (2013) 2982-2988.
[175] M. Cheriti, A. Kahoul, Double perovskite oxides Sr2MMoO6 (M=Fe and Co) as cathode materials for oxygen reduction in alkaline medium, Materials Research Bulletin, 47 (2012) 135-141.
[176] A. Mathur, H.S. Kushwaha, R. Vaish, A. Halder, Enhanced electrocatalytic performance of perovskite supported iron oxide nanoparticles for oxygen reduction reaction, RSC Advances, 6 (2016) 94826-94832.
[177] C. Jin, X. Cao, F. Lu, Z. Yang, R. Yang, Electrochemical study of $Ba_{0.5}Sr_{0.5}Co_{0.8}Fe_{0.2}O_3$ perovskite as bifunctional catalyst in alkaline media, International Journal of Hydrogen Energy, 38 (2013) 10389-10393.
[178] C. Jin, Z. Yang, X. Cao, F. Lu, R. Yang, A novel bifunctional catalyst of $Ba_{0.9}Co_{0.5}Fe_{0.4}Nb_{0.1}O_{3-\delta}$ perovskite for lithium–air battery, International Journal of Hydrogen Energy, 39 (2014) 2526-2530.
[179] K.R. Yoon, D.S. Kim, W.-H. Ryu, S.H. Song, D.-Y. Youn, J.-W. Jung, S. Jeon, Y.J. Park, I.-D. Kim, Tailored Combination of Low Dimensional Catalysts for Efficient Oxygen Reduction and Evolution in Li–O_2 Batteries, ChemSusChem, 9 (2016) 2080-2088.
[180] Z. Ma, X. Yuan, L. Li, Z.-F. Ma, The double perovskite oxide $Sr_2CrMoO_{6-\delta}$ as an efficient electrocatalyst for rechargeable lithium air batteries, Chemical Communications, 50 (2014) 14855-14858.
[181] R. Mohamed, E. Fabbri, P. Levecque, R. Kotz, T.J. Schmidt, O. Conrad, Understanding the Influence of Carbon on the Oxygen Reduction and Evolution Activities of BSCF/Carbon Composite Electrodes in Alkaline Electrolyte, ECS Transactions, 58 (2014) 9-18.
[182] K. Nishio, S. Molla, T. Okugaki, S. Nakanishi, I. Nitta, Y. Kotani, Effects of carbon on oxygen reduction and evolution reactions of gas-diffusion air electrodes based on perovskite-type oxides, Journal of Power Sources, 298 (2015) 236-240.
[183] K. Nishio, S. Molla, T. Okugaki, S. Nakanishi, I. Nitta, Y. Kotani, Oxygen reduction and evolution reactions of air electrodes using a perovskite oxide as an electrocatalyst, Journal of Power Sources, 278 (2015) 645-651.
[184] W.G. Hardin, D.A. Slanac, X. Wang, S. Dai, K.P. Johnston, K.J. Stevenson, Highly Active, Nonprecious Metal Perovskite Electrocatalysts for Bifunctional Metal–Air Battery Electrodes, The Journal of Physical Chemistry Letters, 4 (2013) 1254-1259.
[185] T. Poux, F.S. Napolskiy, T. Dintzer, G. Kéranguéven, S.Y. Istomin, G.A. Tsirlina, E.V. Antipov, E.R. Savinova, Dual Role of Carbon in the Catalytic Layers of Perovskite/Carbon Composites for the Electrocatalytic Oxygen Reduction Reaction, Catalysis Today, 189 (2012) 83-92.
[186] R. Burch, Importance of electronic ligand effects in metal alloy catalysts, Accounts of Chemical Research, 15 (1982) 24-31.
[187] T. Bligaard, J.K. Nørskov, Ligand effects in heterogeneous catalysis and electrochemistry, Electrochimica Acta, 52 (2007) 5512-5516.
[188] X. Ma, H. Meng, M. Cai, P.K. Shen, Bimetallic Carbide Nanocomposite Enhanced Pt Catalyst with High Activity and Stability for the Oxygen Reduction Reaction, Journal of the American Chemical Society, 134 (2012) 1954-1957.
[189] D.A. Slanac, A. Lie, J.A. Paulson, K.J. Stevenson, K.P. Johnston, Bifunctional Catalysts for Alkaline Oxygen Reduction Reaction via Promotion of Ligand and Ensemble Effects at Ag/MnOx Nanodomains, The Journal of Physical Chemistry C, 116 (2012) 11032-11039.
[190] E. Fabbri, M. Nachtegaal, X. Cheng, T.J. Schmidt, Superior Bifunctional Electrocatalytic Activity of Ba0.5Sr0.5Co0.8Fe0.2O3-δ/Carbon Composite

Electrodes: Insight into the Local Electronic Structure, Advanced Energy Materials, 5 (2015) 1402033.

[191] K. Elumeeva, J. Masa, J. Sierau, F. Tietz, M. Muhler, W. Schuhmann, Perovskite-based bifunctional electrocatalysts for oxygen evolution and oxygen reduction in alkaline electrolytes, Electrochimica Acta, 208 (2016) 25-32.

[192] T. Poux, A. Bonnefont, A. Ryabova, G. Kéranguéven, G.A. Tsirlina, E.R. Savinova, Electrocatalysis of hydrogen peroxide reactions on perovskite oxides: experiment versus kinetic modeling, Physical Chemistry Chemical Physics, 16 (2014) 13595-13600.

[193] T. Poux, A. Bonnefont, G. Kéranguéven, G.A. Tsirlina, E.R. Savinova, Electrocatalytic Oxygen Reduction Reaction on Perovskite Oxides: Series versus Direct Pathway, ChemPhysChem, 15 (2014) 2108-2120.

[194] S. Malkhandi, P. Trinh, A.K. Manohar, K.C. Jayachandrababu, A. Kindler, G.K. Surya Prakash, S.R. Narayanan, Electrocatalytic Activity of Transition Metal Oxide-Carbon Composites for Oxygen Reduction in Alkaline Batteries and Fuel Cells, Journal of The Electrochemical Society, 160 (2013) F943-F952.

[195] X. Li, W. Qu, J. Zhang, H. Wang, Electrocatalytic Activities of $La_{0.6}Ca_{0.4}CoO_3$ and $La_{0.6}Ca_{0.4}CoO_3$-Carbon Composites Toward the Oxygen Reduction Reaction in Concentrated Alkaline Electrolytes, Journal of The Electrochemical Society, 158 (2011) A597.

[196] V. Hermann, D. Dutriat, S. Müller, C. Comninellis, Mechanistic studies of oxygen reduction at $La_{0.6}Ca_{0.4}CoO_3$-activated carbon electrodes in a channel flow cell, Electrochimica Acta, 46 (2000) 365-372.

[197] E.P. Bonnin, E.J. Biddinger, G.G. Botte, Effect of catalyst on electrolysis of ammonia effluents, Journal of Power Sources, 182 (2008) 284-290.

[198] C. Zhong, W.B. Hu, Y.F. Cheng, Recent advances in electrocatalysts for electro-oxidation of ammonia, Journal of Materials Chemistry A, 1 (2013) 3216-3238.

[199] A. Ponrouch, S. Garbarino, E. Bertin, C. Andrei, G.A. Botton, D. Guay, Highly Porous and Preferentially Oriented {100} Platinum Nanowires and Thin Films, Advanced Functional Materials, 22 (2012) 4172-4181.

[200] S. Le Vot, L. Roué, D. Bélanger, Synthesis of Pt–Ir catalysts by coelectrodeposition: Application to ammonia electrooxidation in alkaline media, Journal of Power Sources, 223 (2013) 221-231.

[201] Z. Ni, J. Liu, Y. Wu, B. Liu, C. Zhao, Y. Deng, W. Hu, C. Zhong, Fabrication of platinum submonolayer electrodes and their high electrocatalytic activities for ammonia oxidation, Electrochimica Acta, 177 (2015) 30-35.

[202] L. Cunci, C.A. Velez, I. Perez, A. Suleiman, E. Larios, M. José-Yacamán, J.J. Watkins, C.R. Cabrera, Platinum Electrodeposition at Unsupported Electrochemically Reduced Nanographene Oxide for Enhanced Ammonia Oxidation, ACS Applied Materials & Interfaces, 6 (2014) 2137-2145.

[203] J.A. Herron, P. Ferrin, M. Mavrikakis, Electrocatalytic oxidation of ammonia on transition-metal surfaces: a first-principles study, The Journal of Physical Chemistry C, 119 (2015) 14692-14701.

[204] W. Xu, R. Lan, D. Du, J. Humphreys, M. Walker, Z. Wu, H. Wang, S.W. Tao, Directly growing hierarchical nickel-copper hydroxide nanowires on carbon fibre cloth for efficient electrooxidation of ammonia, Applied Catalysis B: Environmental, 218 (2017) 470-479.

[205] W. Xu, D. Du, R. Lan, J. Humphreys, D.N. Miller, M. Walker, Z. Wu, J.T. Irvine, S. Tao, Electrodeposited NiCu bimetal on carbon paper as stable non-noble anode for efficient electrooxidation of ammonia, Applied Catalysis B: Environmental, 237 (2018) 1101-1109.

[206] N.M. Adli, H. Zhang, S. Mukherjee, G. Wu, Review—Ammonia Oxidation Electrocatalysis for Hydrogen Generation and Fuel Cells, Journal of The Electrochemical Society, 165 (2018) J3130-J3147.
[207] M. Zhu, Y. Yang, S. Xi, C. Diao, Z. Yu, W.S.V. Lee, J. Xue, Deciphering NH_3 Adsorption Kinetics in Ternary Ni–Cu–Fe Oxyhydroxide toward Efficient Ammonia Oxidation Reaction, Small, 17 (2021) 2005616.
[208] L. Candido, J.A.C.P. Gomes, Evaluation of anode materials for the electro-oxidation of ammonia and ammonium ions, Materials Chemistry and Physics, 129 (2011) 1146-1151.
[209] A. Estejab, D.A. Daramola, G.G. Botte, Mathematical model of a parallel plate ammonia electrolyzer for combined wastewater remediation and hydrogen production, Water Research, 77 (2015) 133-145.
[210] A. Kapałka, A. Cally, S. Neodo, C. Comninellis, M. Wächter, K.M. Udert, Electrochemical behavior of ammonia at $Ni/Ni(OH)_2$ electrode, Electrochemistry Communications, 12 (2010) 18-21.
[211] X. Xu, C. Su, Z. Shao, Fundamental Understanding and Application of $Ba_{0.5}Sr_{0.5}Co_{0.8}Fe_{0.2}O_{3-\delta}$ Perovskite in Energy Storage and Conversion: Past, Present, and Future, Energy & Fuels, 35 (2021) 13585-13609.
[212] X. Xu, Y. Pan, Y. Zhong, C. Shi, D. Guan, L. Ge, Z. Hu, Y.-Y. Chin, H.-J. Lin, C.-T. Chen, H. Wang, S.P. Jiang, Z. Shao, New Undisputed Evidence and Strategy for Enhanced Lattice-Oxygen Participation of Perovskite Electrocatalyst through Cation Deficiency Manipulation, Advanced Science, 9 (2022) 2200530.
[213] X. Xu, W. Wang, W. Zhou, Z. Shao, Recent Advances in Novel Nanostructuring Methods of Perovskite Electrocatalysts for Energy-Related Applications, Small Methods, 2 (2018) 1800071.
[214] P. Goel, S. Sundriyal, V. Shrivastav, S. Mishra, D.P. Dubal, K.-H. Kim, A. Deep, Perovskite materials as superior and powerful platforms for energy conversion and storage applications, Nano Energy, 80 (2021) 105552.
[215] Y. Miao, Y. Ke, N. Wang, W. Zou, M. Xu, Y. Cao, Y. Sun, R. Yang, Y. Wang, Y. Tong, W. Xu, L. Zhang, R. Li, J. Li, H. He, Y. Jin, F. Gao, W. Huang, J. Wang, Stable and bright formamidinium-based perovskite light-emitting diodes with high energy conversion efficiency, Nature Communications, 10 (2019) 3624.
[216] A. Kostopoulou, K. Brintakis, N.K. Nasikas, E. Stratakis, Perovskite nanocrystals for energy conversion and storage, Nanophotonics, 8 (2019) 1607-1640.
[217] G.S. Hegde, A. Ghosh, R. Badam, N. Matsumi, R. Sundara, Role of Defects in Low-Cost Perovskite Catalysts toward ORR and OER in Lithium–Oxygen Batteries, ACS Applied Energy Materials, 3 (2020) 1338-1348.
[218] X. Liu, L. Zhang, Y. Zheng, Z. Guo, Y. Zhu, H. Chen, F. Li, P. Liu, B. Yu, X. Wang, J. Liu, Y. Chen, M. Liu, Uncovering the Effect of Lattice Strain and Oxygen Deficiency on Electrocatalytic Activity of Perovskite Cobaltite Thin Films, Advanced Science, 6 (2019) 1801898.
[219] H. Wang, X. Chen, D. Huang, M. Zhou, D. Ding, H. Luo, Cation Deficiency Tuning of $LaCoO_3$ Perovskite as Bifunctional Oxygen Electrocatalyst, ChemCatChem, 12 (2020) 2768-2775.
[220] Z. Wei, H. Chen, K. Yan, S. Yang, Inkjet Printing and Instant Chemical Transformation of a CH3NH3PbI3/Nanocarbon Electrode and Interface for Planar Perovskite Solar Cells, Angewandte Chemie International Edition, 53 (2014) 13239-13243.
[221] Z. Li, S.A. Kulkarni, P.P. Boix, E. Shi, A. Cao, K. Fu, S.K. Batabyal, J. Zhang, Q. Xiong, L.H. Wong, N. Mathews, S.G. Mhaisalkar, Laminated Carbon Nanotube Networks for Metal Electrode-Free Efficient Perovskite Solar Cells, ACS Nano, 8 (2014) 6797-6804.

[222] Y. Chen, W. Zhou, D. Ding, M. Liu, F. Ciucci, M. Tade, Z. Shao, Advances in Cathode Materials for Solid Oxide Fuel Cells: Complex Oxides without Alkaline Earth Metal Elements, Advanced Energy Materials, 5 (2015) 1500537.
[223] D. Ding, X. Li, S.Y. Lai, K. Gerdes, M. Liu, Enhancing SOFC cathode performance by surface modification through infiltration, Energy & Environmental Science, 7 (2014) 552-575.
[224] S. Du, W. Li, H. Wu, P.-Y. Abel Chuang, M. Pan, P.-C. Sui, Effects of Ionomer and Dispersion Methods on Rheological Behavior of Proton Exchange Membrane Fuel Cell Catalyst Layer Ink, International Journal of Hydrogen Energy, 45 (2020) 29430-29441.
[225] S. Shahgaldi, J. Zhao, I. Alaefour, X. Li, Investigation of Catalytic vs Reactant Transport Effect of Catalyst Layers on Proton Exchange Membrane Fuel Cell Performance, Fuel, 208 (2017) 321-328.
[226] M. So, T. Ohnishi, K. Park, M. Ono, Y. Tsuge, G. Inoue, The Effect of Solvent and Ionomer on Agglomeration in Fuel Cell Catalyst Inks: Simulation by the Discrete Element Method, International Journal of Hydrogen Energy, 44 (2019) 28984-28995.
[227] H. Ren, Y. Teng, X. Meng, D. Fang, H. Huang, J. Geng, Z. Shao, Ionomer Network of Catalyst Layers for Proton Exchange Membrane Fuel Cell, Journal of Power Sources, 506 (2021) 230186.
[228] S. Woo, S. Lee, A.Z. Taning, T.-H. Yang, S.-H. Park, S.-D. Yim, Current Understanding of Catalyst/Ionomer Interfacial Structure and Phenomena Affecting the Oxygen Reduction Reaction in Cathode Catalyst Layers of Proton Exchange Membrane Fuel Cells, Current Opinion in Electrochemistry, 21 (2020) 289-296.
[229] A. Therdthianwong, P. Saenwiset, S. Therdthianwong, Cathode Catalyst Layer Design for Proton Exchange Membrane Fuel Cells, Fuel, 91 (2012) 192-199.
[230] J. Thepkaew, A. Therdthianwong, S. Therdthianwong, Key Parameters of Active Layers Affecting Proton Exchange Membrane (PEM) Fuel Cell Performance, Energy, 33 (2008) 1794-1800.
[231] S. Takahashi, J. Shimanuki, T. Mashio, A. Ohma, H. Tohma, A. Ishihara, Y. Ito, Y. Nishino, A. Miyazawa, Observation of Ionomer in Catalyst Ink of Polymer Electrolyte Fuel Cell Using Cryogenic Transmission Electron Microscopy, Electrochimica Acta, 224 (2017) 178-185.
[232] G.S. Avcioglu, B. Ficicilar, I. Eroglu, Effect of PTFE Nanoparticles in Catalyst Layer with High Pt Loading on PEM Fuel Cell Performance, International Journal of Hydrogen Energy, 41 (2016) 10010-10020.
[233] C.-Y. Ahn, J.-Y. Cheon, S.-H. Joo, J. Kim, Effects of Ionomer Content on Pt Catalyst/Ordered Mesoporous Carbon Support in Polymer Electrolyte Membrane Fuel Cells, Journal of Power Sources, 222 (2013) 477-482.
[234] S. Jeon, J. Lee, G.M. Rios, H.-J. Kim, S.-Y. Lee, E. Cho, T.-H. Lim, J. Hyun Jang, Effect of Ionomer Content and Relative Humidity on Polymer Electrolyte Membrane Fuel Cell (PEMFC) Performance of Membrane-Electrode Assemblies (MEAs) Prepared by Decal Transfer Method, International Journal of Hydrogen Energy, 35 (2010) 9678-9686.
[235] S.J. Shin, J.K. Lee, H.Y. Ha, S.A. Hong, H.S. Chun, I.H. Oh, Effect of the Catalytic Ink Preparation Method on the Performance of Polymer Electrolyte Membrane Fuel Cells, Journal of Power Sources, 106 (2002) 146-152.
[236] S. Ott, A. Orfanidi, H. Schmies, B. Anke, H.N. Nong, J. Hübner, U. Gernert, M. Gliech, M. Lerch, P. Strasser, Ionomer Distribution Control in Porous Carbon-Supported Catalyst Layers for High-Power and Low Pt-Loaded Proton Exchange Membrane Fuel Cells, Nature Materials, 19 (2020) 77-85.

[237] R. Friedmann, T.V. Nguyen, Optimization of the Cathode Catalyst Layer Composition using a Novel 2-step Preparation Method, ECS Transactions, 16 (2008) 2021-2029.
[238] S. Litster, G. McLean, PEM fuel cell electrodes, Journal of Power Sources, 130 (2004) 61-76.
[239] M. Marino, J. Melchior, A. Wohlfarth, K.J.J.o.M.S. Kreuer, Hydroxide, halide and water transport in a model anion exchange membrane, 464 (2014) 61-71.
[240] F. Foglia, Q. Berrod, A.J. Clancy, K. Smith, G. Gebel, V.G. Sakai, M. Appel, J.-M. Zanotti, M. Tyagi, N. Mahmoudi, T.S. Miller, J.R. Varcoe, A.P. Periasamy, D.J.L. Brett, P.R. Shearing, S. Lyonnard, P.F. McMillan, Disentangling Water, Ion and Polymer Dynamics in an Anion Exchange Membrane, Nature Materials, 21 (2022) 555-563.
[241] V. Dubey, A. Maiti, S. Daschakraborty, Predicting the Solvation Structure and Vehicular Diffusion of Hydroxide Ion in an Anion Exchange Membrane Using Nonreactive Molecular Dynamics Simulation, Chemical Physics Letters, 755 (2020) 137802.
[242] M.E. Tuckerman, D. Marx, M. Parrinello, The Nature and Transport Mechanism of Hydrated Hydroxide Ions in Aqueous Solution, Nature, 417 (2002) 925-929.
[243] C. Chen, Y.-L.S. Tse, G.E. Lindberg, C. Knight, G.A. Voth, Hydroxide Solvation and Transport in Anion Exchange Membranes, Journal of the American Chemical Society, 138 (2016) 991-1000.
[244] D. Dong, W. Zhang, A.C.T. van Duin, D. Bedrov, Grotthuss versus Vehicular Transport of Hydroxide in Anion-Exchange Membranes: Insight from Combined Reactive and Nonreactive Molecular Simulations, The Journal of Physical Chemistry Letters, 9 (2018) 825-829.
[245] W. Zhang, D. Dong, D. Bedrov, A.C.T. van Duin, Hydroxide Transport and Chemical Degradation in Anion Exchange Membranes: A Combined Reactive and Non-Reactive Molecular Simulation Study, Journal of Materials Chemistry A, 7 (2019) 5442-5452.
[246] T. Zelovich, L. Vogt-Maranto, M.A. Hickner, S.J. Paddison, C. Bae, D.R. Dekel, M.E. Tuckerman, Hydroxide Ion Diffusion in Anion-Exchange Membranes at Low Hydration: Insights from Ab Initio Molecular Dynamics, Chemistry of Materials, 31 (2019) 5778-5787.
[247] S. Park, J.-W. Lee, B.N. Popov, Effect of PTFE content in microporous layer on water management in PEM fuel cells, Journal of Power Sources, 177 (2008) 457-463.
[248] Z. Qi, A. Kaufman, Improvement of water management by a microporous sublayer for PEM fuel cells, Journal of Power Sources, 109 (2002) 38-46.
[249] L. Dimesso, Pechini Processes: An Alternate Approach of the Sol–Gel Method, Preparation, Properties, and Applications, in: L. Klein, M. Aparicio, A. Jitianu (Eds.) Handbook of Sol-Gel Science and Technology, Springer International Publishing, Cham, 2016, pp. 1-22.
[250] W.L. Bragg, Crystal Structure: The Crystalline State Science, 80 (1934) 290-291.
[251] T. Runčevski, C.M. Brown, The Rietveld Refinement Method: Half of a Century Anniversary, Crystal Growth & Design, 21 (2021) 4821-4822.
[252] A.C. Larson, R.B.V. Dreele, General structure analysis system (GSAS), The Reagents of the University of California, Los Alamos National Laboratory Report, 2004.
[253] B.H. Toby, EXPGUI, a graphical user interface for GSAS, Journal of Applied Crystallography, 34 (2001) 210-213.

[254] Scanning Electron Microsope, Radiological and Environmental Management, Purdue University, 2019. Accessed: 05/01/2022.
[255] A. Nanakoudis, EDX Analysis with SEM: How Does it Work?, ThermoFisher SCIENTIFIC, https://www.thermofisher.com/blog/microscopy/edx-analysis-with-sem-how-does-it-work/, 11/28/2019. Accessed: 05/01/2022.
[256] What is Raman spectroscopy?, Edinburgh Instruments, https://www.edinst.com/blog/what-is-raman-spectroscopy/, 2022.
[257] C.V. Raman, K.S. Krishnan, A New Type of Secondary Radiation, Nature, 121 (1928) 501-502.
[258] E. Smith, G. Dent, Modern Raman Spectroscopy: A Practical Approach, Second Edition, Wiley, 2019.
[259] D.C. Harris, M.D. Bertolucci, Symmetry and Spectroscopy: An Introduction to Vibrational and Electronic Spectroscopy, Dover Publications, 1989.
[260] J.F. Moulder, W.F. Stickle, P.E. Sobol, K.D. Bomben, Handbook of X-ray Photoelectron Spectroscopy, Perkin-Elmer Corporation, 1993.
[261] P.M.V. Raja, A.R. Barron, BET Surface Area Analysis of Nanoparticles, OpenStax CNX. Rice University https://chem.libretexts.org/@go/page/55840.
[262] C. Du, Q. Tan, G. Yin, J. Zhang, Rotating Disk Electrode Method, in: W. Xing, G. Yin, J. Zhang (Eds.) Rotating Electrode Methods and Oxygen Reduction Electrocatalysts, Elsevier, Amsterdam, 2014, pp. 171-198.
[263] Rotating Disk Electrode - Hydrodynamic Working Electrode, Electrochemistry resource, https://electrochemistryresources.com/rotating-disk-electrode/, 2016.
[264] A. Peroff, Rotating Disk Electrode (RDE) Theory, PINE research, https://pineresearch.com/shop/kb/theory/hydrodynamic-electrochemistry/rotating-disk-electrode-theory/, 2020.
[265] E. Barsoukov, J.R. Macdonald, Impedance Spectroscopy: Theory, Experiment, and Applications, Second Edition, John Wiley & Sons, 2005.
[266] Basics of Electrochemical Impedance Spectroscopy, GAMRY Instruments, https://www.gamry.com/application-notes/EIS/basics-of-electrochemical-impedance-spectroscopy/, 2022.
[267] Electrochemical Impedance Spectroscopy, Engineering LibreTexts, https://eng.libretexts.org/Bookshelves/Materials_Science/Supplemental_Modules_(Materials_Science)/Insulators/Electrochemical_Impedance_Spectroscopy, 2021.
[268] Z. He, F. Mansfeld, Exploring the use of electrochemical impedance spectroscopy (EIS) in microbial fuel cell studies, Energy & Environmental Science, 2 (2009) 215-219.
[269] M.F. Sunding, K. Hadidi, S. Diplas, O.M. Løvvik, T.E. Norby, A.E. Gunnæs, XPS characterisation of in situ treated lanthanum oxide and hydroxide using tailored charge referencing and peak fitting procedures, Journal of Electron Spectroscopy and Related Phenomena, 184 (2011) 399-409.
[270] K. Chu, F. Liu, J. Zhu, H. Fu, H. Zhu, Y. Zhu, Y. Zhang, F. Lai, T. Liu, A General Strategy to Boost Electrocatalytic Nitrogen Reduction on Perovskite Oxides via the Oxygen Vacancies Derived from A-Site Deficiency, Advanced Energy Materials, 11 (2021) 2003799.
[271] Q. Shen, S. Li, G. Yang, B. Sunden, J. Yuan, Effect of A-/B-site Doping on Oxygen Non-Stoichiometry, Structure characteristics, and O2 Releasing Behavior of $La_{1-x}Ca_xCo_{1-y}Fe_yO_{3-\delta}$ Perovskites, Energies, 12 (2019) 410.
[272] J. Wu, J.-P. Dacquin, N. Djelal, C. Cordier, C. Dujardin, P. Granger, Calcium and copper substitution in stoichiometric and La-deficient LaFeO3 compositions: A starting point in next generation of Three-Way-Catalysts for gasoline engines, Applied Catalysis B: Environmental, 282 (2021) 119621.

[273] T. Caronna, F. Fontana, I.N. Sora, R. Pelosato, Chemical synthesis and structural characterization of the substitution compound $LaFe_{1-x}Cu_xO_3$ (x=0–0.40), Materials Chemistry and Physics, 116 (2009) 645-648.
[274] P.I. Cowin, C.T.G. Petit, R. Lan, J.T.S. Irvine, S.W. Tao, Recent Progress in the Development of Anode Materials for Solid Oxide Fuel Cells, Advanced Energy Materials, 1 (2011) 314-332.
[275] D. Wang, Y. Peng, Q. Yang, S. Xiong, J. Li, J. Crittenden, Performance of Modified $La_xSr_{1-x}MnO_3$ Perovskite Catalysts for NH_3 Oxidation: TPD, DFT, and Kinetic Studies, Environmental Science & Technology, 52 (2018) 7443-7449.
[276] H. Oswin, M. Salomon, The anodic oxidation of ammonia at platinum black electrodes in aqueous KOH electrolyte, Canadian journal of Chemistry, 41 (1963) 1686-1694.
[277] R. Wang, H. Liu, K. Zhang, G. Zhang, H. Lan, J. Qu, Ni(II)/Ni(III) redox couple endows Ni foam-supported Ni2P with excellent capability for direct ammonia oxidation, Chemical Engineering Journal, 404 (2021) 126795.
[278] X. Cui, W. Guo, M. Zhou, Y. Yang, Y. Li, P. Xiao, Y. Zhang, X. Zhang, Promoting Effect of Co in NimCon (m + n = 4) Bimetallic Electrocatalysts for Methanol Oxidation Reaction, ACS Applied Materials & Interfaces, 7 (2015) 493-503.
[279] S.-L. Yau, F.-R.F. Fan, T.P. Moffat, A.J. Bard, In situ Scanning Tunneling Microscopy of Ni(100) in 1 M NaOH, The Journal of Physical Chemistry, 98 (1994) 5493-5499.
[280] A. Allagui, S. Sarfraz, E.A. Baranova, Ni_xPd_{1-x} (x=0.98, 0.93, and 0.58) nanostructured catalysts for ammonia electrooxidation in alkaline media, Electrochimica Acta, 110 (2013) 253-259.
[281] H. Zhang, Y. Wang, Z. Wu, D.Y.C. Leung, An ammonia electrolytic cell with NiCu/C as anode catalyst for hydrogen production, Energy Procedia, 142 (2017) 1539-1544.
[282] J. Liu, B. Chen, Y. Kou, Z. Liu, X. Chen, Y. Li, Y. Deng, X. Han, W. Hu, C. Zhong, Pt-Decorated highly porous flower-like Ni particles with high mass activity for ammonia electro-oxidation, Journal of Materials Chemistry A, 4 (2016) 11060-11068.
[283] F. Almomani, M. Ali H Salah Saad, Electrochemical oxidation of ammonia (NH4+/NH_3) on synthesized nickel-cobalt oxide catalyst, International Journal of Hydrogen Energy, 46 (2021) 4678-4690.
[284] F. Almomani, R. Bhosale, M. Khraisheh, A. Kumar, M. Tawalbeh, Electrochemical oxidation of ammonia on nickel oxide nanoparticles, International Journal of Hydrogen Energy, 45 (2020) 10398-10408.
[285] Y. Kang, W. Wang, J. Li, Q. Li, S. Liu, Z. Lei, A Highly Efficient Pt-NiO/C Electrocatalyst for Ammonia Electro-Oxidation, Journal of The Electrochemical Society, 164 (2017) F958-F965.
[286] Y. Li, X. Li, H.S. Pillai, J. Lattimer, N. Mohd Adli, S. Karakalos, M. Chen, L. Guo, H. Xu, J. Yang, D. Su, H. Xin, G. Wu, Ternary PtIrNi Catalysts for Efficient Electrochemical Ammonia Oxidation, ACS Catalysis, 10 (2020) 3945-3957.
[287] J.R. Barbosa, M.N. Leon, C.M. Fernandes, R.M. Antoniassi, O.C. Alves, E.A. Ponzio, J.C.M. Silva, $PtSnO_2$/C and Pt/C with preferential (100) orientation: High active electrocatalysts for ammonia electro-oxidation reaction, Applied Catalysis B: Environmental, 264 (2020) 118458.
[288] H. Kim, W. Yang, W.H. Lee, M.H. Han, J. Moon, C. Jeon, D. Kim, S.G. Ji, K.H. Chae, K.-S. Lee, J. Seo, H.-S. Oh, H. Kim, C.H. Choi, Operando Stability of Platinum Electrocatalysts in Ammonia Oxidation Reactions, ACS Catalysis, 10 (2020) 11674-11684.

[289] N. Hanada, Y. Kohase, K. Hori, H. Sugime, S. Noda, Electrolysis of ammonia in aqueous solution by platinum nanoparticles supported on carbon nanotube film electrode, Electrochimica Acta, 341 (2020) 136027.
[290] K. Siddharth, Y. Hong, X. Qin, H.J. Lee, Y.T. Chan, S. Zhu, G. Chen, S.-I. Choi, M. Shao, Surface engineering in improving activity of Pt nanocubes for ammonia electrooxidation reaction, Applied Catalysis B: Environmental, 269 (2020) 118821.
[291] F. Vitse, M. Cooper, G.G. Botte, On the use of ammonia electrolysis for hydrogen production, Journal of Power Sources, 142 (2005) 18-26.
[292] M. Qin, C. White, S. Zou, Z. He, Passive separation of recovered ammonia from catholyte for reduced energy consumption in microbial electrolysis cells, Chemical Engineering Journal, 334 (2018) 2303-2307.
[293] L. Du, L. Xing, G. Zhang, X. Liu, D. Rawach, S. Sun, Engineering of electrocatalyst/electrolyte interface for ambient ammonia synthesis, SusMat, 1 (2021) 150-173.
[294] Y. Yang, J. Kim, H. Jo, A. Seong, M. Lee, H.-K. Min, M.-g. Seo, Y. Choi, G. Kim, A rigorous electrochemical ammonia electrolysis protocol with in operando quantitative analysis, Journal of Materials Chemistry A, 9 (2021) 11571-11579.
[295] X. Liu, Y. Liu, X. Guo, S. Lu, Y. Wang, J. Zhang, W. Guo, B. Xi, High degree of contaminant removal and evolution of microbial community in different electrolysis-integrated constructed wetland systems, Chemical Engineering Journal, 388 (2020) 124391.
[296] Q. Xue, Y. Zhao, J. Zhu, Y. Ding, T. Wang, H. Sun, F. Li, P. Chen, P. Jin, S. Yin, Y. Chen, PtRu nanocubes as bifunctional electrocatalysts for ammonia electrolysis, Journal of Materials Chemistry A, 9 (2021) 8444-8451.
[297] M.K. Chan, N. Abdullah, E.H.A. Rageh, P. Kumaran, Y.S. Tee, Oxidation of ammonia using immobilised FeCu for water treatment, Separation and Purification Technology, 254 (2021) 117612.
[298] B.K. Boggs, G.G. Botte, On-board hydrogen storage and production: An application of ammonia electrolysis, Journal of Power Sources, 192 (2009) 573-581.
[299] M. Yáñez, F. Relvas, A. Ortiz, D. Gorri, A. Mendes, I. Ortiz, PSA purification of waste hydrogen from ammonia plants to fuel cell grade, Separation and Purification Technology, 240 (2020) 116334.
[300] K. Fang, W. He, F. Peng, K. Wang, Ammonia recovery from concentrated solution by designing novel stacked FCDI cell, Separation and Purification Technology, 250 (2020) 117066.
[301] B. Lin, M. Hu, J. Ma, Y. Jiang, S. Tao, G. Meng, Stable, easily sintered $BaCe_{0.5}Zr_{0.3}Y_{0.16}Zn_{0.04}O_{3-\delta}$ electrolyte-based protonic ceramic membrane fuel cells with $Ba_{0.5}Sr_{0.5}Zn_{0.2}Fe_{0.8}O_{3-\delta}$ perovskite cathode, Journal of Power Sources, 183 (2008) 479-484.
[302] G.W. Crabtree, M.S. Dresselhaus, The Hydrogen Fuel Alternative, MRS Bulletin, 33 (2008) 421-428.
[303] W. Xu, Z.C. Wu, S.W. Tao, Recent Progress in Electrocatalysts with Mesoporous Structures for Application in Polymer Electrolyte Membrane Fuel Cells, Journal of Materials Chemistry A, 4 (2016) 16272-16287.
[304] D.-K. Lim, A.B. Plymill, H. Paik, X. Qian, S. Zecevic, C.R.I. Chisholm, S.M. Haile, Solid Acid Electrochemical Cell for the Production of Hydrogen from Ammonia, Joule, 4 (2020) 2338-2347.
[305] M. Zhang, P. Zou, G. Jeerh, S. Chen, J. Shields, H. Wang, S. Tao, Electricity Generation from Ammonia in Landfill Leachate by an Alkaline Membrane Fuel Cell Based on Precious-Metal-Free Electrodes, ACS Sustainable Chemistry & Engineering, 8 (2020) 12817-12824.

[306] J.A. Camargo, Á. Alonso, Ecological and toxicological effects of inorganic nitrogen pollution in aquatic ecosystems: A global assessment, Environment International, 32 (2006) 831-849.
[307] X. Zhang, F. Zhu, L. Chen, Q. Zhao, G. Tao, Removal of ammonia nitrogen from wastewater using an aerobic cathode microbial fuel cell, Bioresource Technology, 146 (2013) 161-168.
[308] G. Del Moro, L. Prieto-Rodríguez, M. De Sanctis, C. Di Iaconi, S. Malato, G. Mascolo, Landfill leachate treatment: Comparison of standalone electrochemical degradation and combined with a novel biofilter, Chemical Engineering Journal, 288 (2016) 87-98.
[309] P. Mandal, B.K. Dubey, A.K. Gupta, Review on landfill leachate treatment by electrochemical oxidation: Drawbacks, challenges and future scope, Waste Management, 69 (2017) 250-273.
[310] Y. Zeng, A. De Guardia, C. Ziebal, F.J. De Macedo, P. Dabert, Nitrification and microbiological evolution during aerobic treatment of municipal solid wastes, Bioresource Technology, 110 (2012) 144-152.
[311] J.J. Medvedev, Y. Tobolovskaya, X.V. Medvedeva, S.W. Tatarchuk, F. Li, A. Klinkova, Pathways of ammonia electrooxidation on nickel hydroxide anodes and an alternative route towards recycled fertilizers, Green Chemistry, 24 (2022) 1578-1589.
[312] X. Jiang, D. Ying, X. Liu, M. Liu, S. Zhou, C. Guo, G. Zhao, Y. Wang, J. Jia, Identification of the role of Cu site in Ni-Cu hydroxide for robust and high selective electrochemical ammonia oxidation to nitrite, Electrochimica Acta, 345 (2020) 136157.
[313] Y.-J. Shih, Y.-H. Huang, C.P. Huang, In-situ electrochemical formation of nickel oxyhydroxide (NiOOH) on metallic nickel foam electrode for the direct oxidation of ammonia in aqueous solution, Electrochimica Acta, 281 (2018) 410-419.
[314] K. Endo, Y. Katayama, T. Miura, A rotating disk electrode study on the ammonia oxidation, Electrochimica Acta, 50 (2005) 2181-2185.
[315] D. Song, X. Shao, M. Yuan, L. Wang, W. Zhan, Y. Guo, Y. Guo, G. Lu, Selective catalytic oxidation of ammonia over MnO_x–TiO_2 mixed oxides, RSC Advances, 6 (2016) 88117-88125.
[316] L. Zhang, C. Zhang, H. He, The role of silver species on Ag/Al2O3 catalysts for the selective catalytic oxidation of ammonia to nitrogen, Journal of Catalysis, 261 (2009) 101-109.
[317] X. Cui, J. Zhou, Z. Ye, H. Chen, L. Li, M. Ruan, J. Shi, Selective catalytic oxidation of ammonia to nitrogen over mesoporous CuO/RuO2 synthesized by co-nanocasting-replication method, Journal of Catalysis, 270 (2010) 310-317.
[318] G. Olofsson, L. Reine Wallenberg, A. Andersson, Selective catalytic oxidation of ammonia to nitrogen at low temperature on Pt/CuO/Al2O3, Journal of Catalysis, 230 (2005) 1-13.
[319] S.A.C. Carabineiro, B.E. Nieuwenhuys, Selective oxidation of ammonia over Ir(110), Surface Science, 505 (2002) 163-170.
[320] G. Monsch, P. Klüfers, $[Fe(H_2O)_5(NO)]^{2+}$, the “Brown-Ring” Chromophore, Angewandte Chemie International Edition, 58 (2019) 8566-8571.
[321] H. Jeong, J. Park, H. Kim, Determination of NH4+ in Environmental Water with Interfering Substances Using the Modified Nessler Method, Journal of Chemistry, 2013 (2013) 359217.
[322] E. Turro, A. Giannis, R. Cossu, E. Gidarakos, D. Mantzavinos, A. Katsaounis, Electrochemical oxidation of stabilized landfill leachate on DSA electrodes, Journal of Hazardous Materials, 190 (2011) 460-465.

[323] N. Yang, H. Liu, G.-q. Zhan, D.-p. Li, Sustainable ammonia-contaminated wastewater treatment in heterotrophic nitrifying/denitrifying microbial fuel cell, Journal of Cleaner Production, 245 (2020) 118923.
[324] J. Ding, L. Wei, H. Huang, Q. Zhao, W. Hou, F.T. Kabutey, Y. Yuan, D.D. Dionysiou, Tertiary treatment of landfill leachate by an integrated Electro-Oxidation/Electro-Coagulation/Electro-Reduction process: Performance and mechanism, Journal of Hazardous Materials, 351 (2018) 90-97.
[325] A. Fernandes, M.J. Pacheco, L. Ciríaco, A. Lopes, Review on the electrochemical processes for the treatment of sanitary landfill leachates: Present and future, Applied Catalysis B: Environmental, 176-177 (2015) 183-200.
[326] C. Zhang, D. He, J. Ma, T.D. Waite, Active chlorine mediated ammonia oxidation revisited: Reaction mechanism, kinetic modelling and implications, Water Research, 145 (2018) 220-230.
[327] H. Zöllig, C. Fritzsche, E. Morgenroth, K.M. Udert, Direct electrochemical oxidation of ammonia on graphite as a treatment option for stored source-separated urine, Water Research, 69 (2015) 284-294.
[328] G. Zhang, J. Ruan, T. Du, Recent Advances on Photocatalytic and Electrochemical Oxidation for Ammonia Treatment from Water/Wastewater, ACS ES&T Engineering, 1 (2021) 310-325.
[329] P. Mandal, M.K. Yadav, A.K. Gupta, B.K. Dubey, Chlorine mediated indirect electro-oxidation of ammonia using non-active PbO_2 anode: Influencing parameters and mechanism identification, Separation and Purification Technology, 247 (2020) 116910.
[330] B. Zhou, Z. Yu, Q. Wei, H. Long, Y. Xie, Y. Wang, Electrochemical oxidation of biological pretreated and membrane separated landfill leachate concentrates on boron doped diamond anode, Applied Surface Science, 377 (2016) 406-415.
[331] A. Ghanbarian, M.J. Kermani, J. Scholta, M. Abdollahzadeh, Polymer electrolyte membrane fuel cell flow field design criteria – Application to parallel serpentine flow patterns, Energy Conversion and Management, 166 (2018) 281-296.
[332] M.G. Santarelli, M.F. Torchio, Experimental analysis of the effects of the operating variables on the performance of a single PEMFC, Energy Conversion and Management, 48 (2007) 40-51.
[333] M. Ghasabehi, M. Ashrafi, M. Shams, Performance analysis of an innovative parallel flow field design of proton exchange membrane fuel cells using multiphysics simulation, Fuel, 285 (2021) 119194.
[334] M.Z. Chowdhury, B. Timurkutluk, Transport phenomena of convergent and divergent serpentine flow fields for PEMFC, Energy, 161 (2018) 104-117.
[335] W.-M. Yan, H.-C. Liu, C.-Y. Soong, F. Chen, C.H. Cheng, Numerical study on cell performance and local transport phenomena of PEM fuel cells with novel flow field designs, Journal of Power Sources, 161 (2006) 907-919.
[336] M.Z. Chowdhury, Y.E. Akansu, Novel convergent-divergent serpentine flow fields effect on PEM fuel cell performance, International Journal of Hydrogen Energy, 42 (2017) 25686-25694.
[337] B. Timurkutluk, M.Z. Chowdhury, Numerical Investigation of Convergent and Divergent Parallel Flow Fields for PEMFCs, Fuel Cells, 18 (2018) 441-448.
[338] M. Ashrafi, H. Kanani, M. Shams, Numerical and experimental study of two-phase flow uniformity in channels of parallel PEM fuel cells with modified Z-type flow-fields, Energy, 147 (2018) 317-328.
[339] M. Ashrafi, M. Shams, The effects of flow-field orientation on water management in PEM fuel cells with serpentine channels, Applied Energy, 208 (2017) 1083-1096.

[340] L. Fan, Z. Niu, G. Zhang, K. Jiao, Optimization design of the cathode flow channel for proton exchange membrane fuel cells, Energy Conversion and Management, 171 (2018) 1813-1821.
[341] Y. Yin, X. Wang, X. Shangguan, J. Zhang, Y. Qin, Numerical investigation on the characteristics of mass transport and performance of PEMFC with baffle plates installed in the flow channel, International Journal of Hydrogen Energy, 43 (2018) 8048-8062.
[342] S. Barati, B. Khoshandam, M.M. Ghazi, An investigation of channel blockage effects on hydrogen mass transfer in a proton exchange membrane fuel cell with various geometries and optimization by response surface methodology, International Journal of Hydrogen Energy, 43 (2018) 21928-21939.
[343] H.-H. Lin, C.-H. Cheng, C.-Y. Soong, F. Chen, W.-M. Yan, Optimization of key parameters in the proton exchange membrane fuel cell, Journal of Power Sources, 162 (2006) 246-254.
[344] L.F. Arenas, C. Ponce de León, F.C. Walsh, Redox flow batteries for energy storage: their promise, achievements and challenges, Current Opinion in Electrochemistry, 16 (2019) 117-126.
[345] S. Asghari, M.H. Shahsamandi, M.R. Ashraf Khorasani, Design and manufacturing of end plates of a 5kW PEM fuel cell, International Journal of Hydrogen Energy, 35 (2010) 9291-9297.
[346] E. Alizadeh, M.M. Barzegari, M. Momenifar, M. Ghadimi, S.H.M. Saadat, Investigation of contact pressure distribution over the active area of PEM fuel cell stack, International Journal of Hydrogen Energy, 41 (2016) 3062-3071.
[347] T.A.M. Suter, K. Smith, J. Hack, L. Rasha, Z. Rana, G.M.A. Angel, P.R. Shearing, T.S. Miller, D.J.L. Brett, Engineering Catalyst Layers for Next-Generation Polymer Electrolyte Fuel Cells: A Review of Design, Materials, and Methods, Advanced Energy Materials, 11 (2021) 2101025.
[348] E. Alizadeh, M. Ghadimi, M.M. Barzegari, M. Momenifar, S.H.M. Saadat, Development of contact pressure distribution of PEM fuel cell's MEA using novel clamping mechanism, Energy, 131 (2017) 92-97.
[349] X. Lai, D.a. Liu, L. Peng, J. Ni, A mechanical–electrical finite element method model for predicting contact resistance between bipolar plate and gas diffusion layer in PEM fuel cells, Journal of Power Sources, 182 (2008) 153-159.
[350] P. Zhou, C.W. Wu, G.J. Ma, Contact resistance prediction and structure optimization of bipolar plates, Journal of Power Sources, 159 (2006) 1115-1122.
[351] Z. Wu, Y. Zhou, G. Lin, S. Wang, S.J. Hu, An improved model for predicting electrical contact resistance between bipolar plate and gas diffusion layer in proton exchange membrane fuel cells, Journal of Power Sources, 182 (2008) 265-269.
[352] P. Zhou, P. Lin, C.W. Wu, Z. Li, Effect of nonuniformity of the contact pressure distribution on the electrical contact resistance in proton exchange membrane fuel cells, International Journal of Hydrogen Energy, 36 (2011) 6039-6044.
[353] L. Zhang, Y. Liu, H. Song, S. Wang, Y. Zhou, S.J. Hu, Estimation of contact resistance in proton exchange membrane fuel cells, Journal of Power Sources, 162 (2006) 1165-1171.
[354] G.E. Thompson, Porous anodic alumina: fabrication, characterization and applications, Thin Solid Films, 297 (1997) 192-201.
[355] O. Siddiqui, I. Dincer, Experimental investigation and assessment of direct ammonia fuel cells utilizing alkaline molten and solid electrolytes, Energy, 169 (2019) 914-923.

[356] R.K. Mallick, S.B. Thombre, N.K. Shrivastava, A critical review of the current collector for passive direct methanol fuel cells, Journal of Power Sources, 285 (2015) 510-529.
[357] S.S. Munjewar, S.B. Thombre, R.K. Mallick, A comprehensive review on recent material development of passive direct methanol fuel cell, Ionics, 23 (2017) 1-18.
[358] S. Yousefi, M. Zohoor, Conceptual design and statistical overview on the design of a passive DMFC single cell, International Journal of Hydrogen Energy, 39 (2014) 5972-5980.
[359] B.A. Braz, V.B. Oliveira, A.M.F.R. Pinto, Optimization of a passive direct methanol fuel cell with different current collector materials, Energy, 208 (2020) 118394.
[360] W.M. Yang, S.K. Chou, C. Shu, Effect of current-collector structure on performance of passive micro direct methanol fuel cell, Journal of Power Sources, 164 (2007) 549-554.
[361] H. Wu, H. Zhang, P. Chen, J. Guo, T. Yuan, J. Zheng, H. Yang, Integrated anode structure for passive direct methanol fuel cells with neat methanol operation, Journal of Power Sources, 248 (2014) 1264-1269.
[362] P.J. Hamilton, B.G. Pollet, Polymer Electrolyte Membrane Fuel Cell (PEMFC) Flow Field Plate: Design, Materials and Characterisation, Fuel Cells, 10 (2010) 489-509.
[363] C. Spiegel, Fuel Cell Gaskets, Spacers, and End Plates, Fuel Cell Store, https://www.fuelcellstore.com/blog-section/fuel-cell-gaskets-spacers-and-end-plates, 2017.
[364] C.-W. Lin, C.-H. Chien, J. Tan, Y.J. Chao, J.W. Van Zee, Chemical degradation of five elastomeric seal materials in a simulated and an accelerated PEM fuel cell environment, Journal of Power Sources, 196 (2011) 1955-1966.
[365] J. Tan, Y.J. Chao, H. Wang, J. Gong, J.W. Van Zee, Chemical and mechanical stability of EPDM in a PEM fuel cell environment, Polymer Degradation and Stability, 94 (2009) 2072-2078.
[366] C.-W. Lin, C.-H. Chien, J. Tan, Y.-J. Chao, J.W. Van Zee, Dynamic mechanical characteristics of five elastomeric gasket materials aged in a simulated and an accelerated PEM fuel cell environment, International Journal of Hydrogen Energy, 36 (2011) 6756-6767.
[367] G. Li, J. Tan, J. Gong, Degradation of the elastomeric gasket material in a simulated and four accelerated proton exchange membrane fuel cell environments, Journal of Power Sources, 205 (2012) 244-251.
[368] J. Tan, Y.J. Chao, M. Yang, W.-K. Lee, J.W. Van Zee, Chemical and mechanical stability of a Silicone gasket material exposed to PEM fuel cell environment, International Journal of Hydrogen Energy, 36 (2011) 1846-1852.
[369] A. Ostadfar, Fluid Mechanics and Biofluids Principles, in: A. Ostadfar (Ed.) Biofluid Mechanics, Academic Press2016, pp. 1-60.
[370] B.H. Lim, E.H. Majlan, W.R.W. Daud, T. Husaini, M.I. Rosli, Effects of flow field design on water management and reactant distribution in PEMFC: a review, Ionics, 22 (2016) 301-316.
[371] A. Hakenjos, H. Muenter, U. Wittstadt, C. Hebling, A PEM fuel cell for combined measurement of current and temperature distribution, and flow field flooding, Journal of Power Sources, 131 (2004) 213-216.
[372] M. Ghasabehi, A. Jabbary, M. Shams, Cathode side transport phenomena investigation and Multi-Objective optimization of a tapered parallel flow field PEMFC, Energy Conversion and Management, 265 (2022) 115761.
[373] H. Yang, T.S. Zhao, Q. Ye, In situ visualization study of CO2 gas bubble behavior in DMFC anode flow fields, Journal of Power Sources, 139 (2005) 79-90.

[374] M.P. Pechini, USA Patent, 3.330.697 (1967).
[375] M. Jahan, Q. Bao, K.P. Loh, Electrocatalytically Active Graphene–Porphyrin MOF Composite for Oxygen Reduction Reaction, Journal of the American Chemical Society, 134 (2012) 6707-6713.
[376] S. Ajmal, I. Bibi, F. Majid, S. Ata, K. Kamran, K. Jilani, S. Nouren, S. Kamal, A. Ali, M. Iqbal, Effect of Fe and Bi doping on LaCoO3 structural, magnetic, electric and catalytic properties, Journal of Materials Research and Technology, 8 (2019) 4831-4842.
[377] A. Ishikawa, J. Nohara, S. Sugai, Raman Study of the Orbital-Phonon Coupling in $LaCoO_3$, Physical Review Letters, 93 (2004) 136401.
[378] S. Ivanova, A. Senyshyn, E. Zhecheva, K. Tenchev, R. Stoyanova, H. Fuess, Crystal structure, microstructure and reducibility of LaNixCo1−xO3 and LaFexCo1−xO3 Perovskites (0<x≤0.5), Journal of Solid State Chemistry, 183 (2010) 940-950.
[379] A. Gholizadeh, The effects of A/B-site substitution on structural, redox and catalytic properties of lanthanum ferrite nanoparticles, Journal of Materials Research and Technology, 8 (2019) 457-466.
[380] N.A. Merino, B.P. Barbero, P. Ruiz, L.E. Cadús, Synthesis, characterisation, catalytic activity and structural stability of $LaCo_{1-y}Fe_yO_{3\pm\lambda}$ perovskite catalysts for combustion of ethanol and propane, Journal of Catalysis, 240 (2006) 245-257.
[381] R. Shannon, Revised effective ionic radii and systematic studies of interatomic distances in halides and chalcogenides, Acta Crystallographica Section A, 32 (1976) 751-767.
[382] M. Popa, L.V. Hong, M. Kakihana, Nanopowders of $LaMeO_3$ perovskites obtained by a solution-based ceramic processing technique, Physica B: Condensed Matter, 327 (2003) 233-236.
[383] W.T. Hong, M. Gadre, Y.-L. Lee, M.D. Biegalski, H.M. Christen, D. Morgan, Y. Shao-Horn, Tuning the Spin State in $LaCoO_3$ Thin Films for Enhanced High-Temperature Oxygen Electrocatalysis, The Journal of Physical Chemistry Letters, 4 (2013) 2493-2499.
[384] M.C. Biesinger, B.P. Payne, A.P. Grosvenor, L.W.M. Lau, A.R. Gerson, R.S.C. Smart, Resolving surface chemical states in XPS analysis of first row transition metals, oxides and hydroxides: Cr, Mn, Fe, Co and Ni, Applied Surface Science, 257 (2011) 2717-2730.
[385] X. Wang, X. Peng, H. Ran, B. Lin, J. Ni, J. Lin, L. Jiang, Influence of Ru Substitution on the Properties of $LaCoO_3$ Catalysts for Ammonia Synthesis: XAFS and XPS Studies, Industrial & Engineering Chemistry Research, 57 (2018) 17375-17383.
[386] Y. Liu, H. Dai, J. Deng, S. Xie, H. Yang, W. Tan, W. Han, Y. Jiang, G. Guo, Mesoporous Co_3O_4-supported gold nanocatalysts: Highly active for the oxidation of carbon monoxide, benzene, toluene, and o-xylene, Journal of Catalysis, 309 (2014) 408-418.
[387] L.F. Liotta, G. Di Carlo, G. Pantaleo, A.M. Venezia, G. Deganello, Co_3O_4/CeO_2 composite oxides for methane emissions abatement: Relationship between Co_3O_4–CeO_2 interaction and catalytic activity, Applied Catalysis B: Environmental, 66 (2006) 217-227.
[388] Y. Lu, A. Ma, Y. Yu, R. Tan, C. Liu, P. Zhang, D. Liu, J. Gui, Engineering Oxygen Vacancies into $LaCoO_3$ Perovskite for Efficient Electrocatalytic Oxygen Evolution, ACS Sustainable Chemistry & Engineering, 7 (2019) 2906-2910.
[389] Y. Zhu, R. Tan, T. Yi, S. Gao, C. Yan, L. Cao, Preparation of nanosized La2CuO4 perovskite oxide using an amorphous heteronuclear complex as a precursor at low-temperature, Journal of Alloys and Compounds, 311 (2000) 16-21.

[390] P.V. Gosavi, R.B. Biniwale, Pure phase LaFeO3 perovskite with improved surface area synthesized using different routes and its characterization, Materials Chemistry and Physics, 119 (2010) 324-329.
[391] T.-N. Tran, M.Y. Song, K.P. Singh, D.-S. Yang, J.-S. Yu, Iron–polypyrrole electrocatalyst with remarkable activity and stability for ORR in both alkaline and acidic conditions: a comprehensive assessment of catalyst preparation sequence, Journal of Material Chemistry A, 4 (2016) 8645-8657.
[392] T.-W. Chen, P. Kalimuthu, G. Anushya, S.-M. Chen, R. Ramachandran, V. Mariyappan, D.C. Muthumala, High-Efficiency of Bi-Functional-Based Perovskite Nanocomposite for Oxygen Evolution and Oxygen Reduction Reaction: An Overview, Materials (Basel), 14 (2021) 2976.
[393] D.E. Beltrán, S. Litster, Half-Wave Potential or Mass Activity? Characterizing Platinum Group Metal-Free Fuel Cell Catalysts by Rotating Disk Electrodes, ACS Energy Letters, 4 (2019) 1158-1161.
[394] F. Jaouen, J. Herranz, M. Lefèvre, J.-P. Dodelet, U.I. Kramm, I. Herrmann, P. Bogdanoff, J. Maruyama, T. Nagaoka, A. Garsuch, J.R. Dahn, T. Olson, S. Pylypenko, P. Atanassov, E.A. Ustinov, Cross-Laboratory Experimental Study of Non-Noble-Metal Electrocatalysts for the Oxygen Reduction Reaction, ACS Applied Materials & Interfaces, 1 (2009) 1623-1639.
[395] A. Serov, M.H. Robson, K. Artyushkova, P. Atanassov, Templated non-PGM cathode catalysts derived from iron and poly(ethyleneimine) precursors, Applied Catalysis B: Environmental, 127 (2012) 300-306.
[396] A. Serov, K. Artyushkova, P. Atanassov, Fe-N-C Oxygen Reduction Fuel Cell Catalyst Derived from Carbendazim: Synthesis, Structure, and Reactivity, Advanced Energy Materials, 4 (2014) 1301735.
[397] X. Li, G. Liu, B.N. Popov, Activity and stability of non-precious metal catalysts for oxygen reduction in acid and alkaline electrolytes, Journal of Power Sources, 195 (2010) 6373-6378.
[398] W. Xia, J. Zhu, W. Guo, L. An, D. Xia, R. Zou, Well-defined carbon polyhedrons prepared from nano metal–organic frameworks for oxygen reduction, Journal of Materials Chemistry A, 2 (2014) 11606-11613.
[399] Y.-Q. Lyu, F. Ciucci, Activating the Bifunctionality of a Perovskite Oxide toward Oxygen Reduction and Oxygen Evolution Reactions, ACS Applied Materials & Interfaces, 9 (2017) 35829-35836.
[400] Y. Sun, Z. Liu, W. Zhang, X. Chu, Y. Cong, K. Huang, S. Feng, Unfolding B-O-B Bonds for an Enhanced ORR Performance in ABO_3-Type Perovskites, Small, 15 (2019) 1803513.
[401] R. Mondal, H. Ratnawat, S. Mukherjee, A. Gupta, P. Singh, Investigation of the Role of Sr and Development of Superior Sr-Doped Hexagonal $BaCoO_{3-\delta}$ Perovskite Bifunctional OER/ORR Catalysts in Alkaline Media, Energy & Fuels, 36 (2022) 3219-3228.
[402] F. Lu, J. Sui, J. Su, C. Jin, M. Shen, R. Yang, Hollow spherical $La_{0.8}Sr_{0.2}MnO_3$ perovskite oxide with enhanced catalytic activities for the oxygen reduction reaction, Journal of Power Sources, 271 (2014) 55-59.
[403] E. García-López, G. Marcì, F. Puleo, V. La Parola, L.F. Liotta, $La_{1-x}Sr_xCo_{1-y}Fe_yO_{3-\delta}$ perovskites: Preparation, characterization and solar photocatalytic activity, Applied Catalysis B: Environmental, 178 (2015) 218-225.
[404] R. Schmidt, J. Wu, C. Leighton, I. Terry, Dielectric response to the low-temperature magnetic defect structure and spin state transition in polycrystalline $LaCoO_3$, Physical Review B, 79 (2009) 125105.
[405] M.A. Korotin, S.Y. Ezhov, I.V. Solovyev, V.I. Anisimov, D.I. Khomskii, G.A. Sawatzky, Intermediate-spin state and properties of $LaCoO_3$, Physical Review B, 54 (1996) 5309-5316.

[406] A. Tsuruta, S. Kawasaki, M. Mikami, Y. Kinemuchi, Y. Masuda, A. Fujita, I. Terasaki, Co-Substitution Effect in Room-Temperature Ferromagnetic Oxide $Sr_{3.1}Y_{0.9}Co_4O_{10.5}$, Materials, 13 (2020).
[407] A.M. Durand, D.P. Belanger, C.H. Booth, F. Ye, S. Chi, J.A. Fernandez-Baca, M. Bhat, Magnetism and phase transitions in $LaCoO_3$, Journal of Physics: Condensed Matter, 25 (2013) 382203.
[408] C.S. Naiman, R. Gilmore, B. DiBartolo, A. Linz, R. Santoro, Interpretation of the Magnetic Properties of $LaCoO_3$, Journal of Applied Physics, 36 (1965) 1044-1045.
[409] K.R. Lee, D. Song, S.B. Park, J.-i. Han, A direct ammonium carbonate fuel cell with an anion exchange membrane, RSC Advances, 4 (2014) 5638-5641.
[410] M.H.M.T. Assumpção, S.G. da Silva, R.F.B. de Souza, G.S. Buzzo, E.V. Spinacé, A.O. Neto, J.C.M. Silva, Direct Ammonia Fuel Cell Performance Using PtIr/C as Anode Electrocatalysts, International Journal of Hydrogen Energy, 39 (2014) 5148-5152.
[411] J. Zhang, H. Zhang, J. Wu, J. Zhang, Chapter 10 - High-Temperature PEM Fuel Cells, in: J. Zhang, H. Zhang, J. Wu, J. Zhang (Eds.) Pem Fuel Cell Testing and Diagnosis, Elsevier, Amsterdam, 2013, pp. 243-282.
[412] F. Barbir, CHAPTER 3 - Fuel Cell Electrochemistry, in: F. Barbir (Ed.) PEM Fuel Cells, Academic Press, Burlington, 2005, pp. 33-72.
[413] X.-Z. Yuan, C. Song, H. Wang, J. Zhang, Electrochemical Impedance Spectroscopy in PEM Fuel Cells, Fundamentals and Applications, Springer2010.
[414] C.H. Hsu, F. Mansfeld, Technical Note: Concerning the Conversion of the Constant Phase Element Parameter Y0 into a Capacitance, Corrosion, 57 (2001).
[415] S.V. Bhide, A.V. Virkar, Stability of BaCeO3-Based Proton Conductors in Water-Containing Atmospheres, Journal of The Electrochemical Society, 146 (1999) 2038-2044.
[416] T.E. Springer, T.A. Zawodzinski, M.S. Wilson, S. Gottesfeld, Characterization of Polymer Electrolyte Fuel Cells Using AC Impedance Spectroscopy, Journal of The Electrochemical Society, 143 (1996) 587-599.
[417] P. Kurzweil, H.J. Fischle, A new monitoring method for electrochemical aggregates by impedance spectroscopy, Journal of Power Sources, 127 (2004) 331-340.
[418] V.A. Paganin, C.L.F. Oliveira, E.A. Ticianelli, T.E. Springer, E.R. Gonzalez, Modelisticinterpretation of the impedance response of a polymer electrolyte fuel cell1Presented in part at the 192nd Meeting of The Electrochemical Society, Paris, France, 1997.1, Electrochimica Acta, 43 (1998) 3761-3766.
[419] G.S. Avcioglu, B. Ficicilar, A. Bayrakceken, I. Eroglu, High Performance PEM Fuel Cell Catalyst Layers with Hydrophobic Channels, International Journal of Hydrogen Energy, 40 (2015) 7720-7731.
[420] S. Srinivasan, D.J. Manko, H. Koch, M.A. Enayetullah, A.J. Appleby, Recent Advances in Solid Polymer Electrolyte Fuel Cell Technology with Low Platinum Loading Electrodes, Journal of Power Sources, 29 (1990) 367-387.
[421] K.-H. Kim, K.-Y. Lee, H.-J. Kim, E. Cho, S.-Y. Lee, T.-H. Lim, S.P. Yoon, I.C. Hwang, J.H. Jang, The Effects of Nafion® Ionomer Content in PEMFC MEAs Prepared by a Catalyst-Coated Membrane (CCM) Spraying Method, International Journal of Hydrogen Energy, 35 (2010) 2119-2126.
[422] J. Cho, J. Ko, S. Park, Comprehensive Analysis of Critical Factors Determining Limiting Current of PEMFC: O2 and H+ Transport Resistance without Cathode Humidification, Journal of The Electrochemical Society, 167 (2020) 084511.

[423] A. Ohma, K. Fushinobu, K. Okazaki, Influence of Nafion® Film on Oxygen Reduction Reaction and Hydrogen Peroxide Formation on Pt Electrode for Proton Exchange Membrane Fuel Cell, Electrochimica Acta, 55 (2010) 8829-8838.
[424] R. Subbaraman, D. Strmcnik, A.P. Paulikas, V.R. Stamenkovic, N.M. Markovic, Oxygen Reduction Reaction at Three-Phase Interfaces, ChemPhysChem, 11 (2010) 2825-2833.
[425] M. Lee, M. Uchida, H. Yano, D.A. Tryk, H. Uchida, M. Watanabe, New Evaluation Method for the Effectiveness of Platinum/Carbon Electrocatalysts Under Operating Conditions, Electrochimica Acta, 55 (2010) 8504-8512.
[426] G. Sasikumar, J.W. Ihm, H. Ryu, Dependence of Optimum Nafion content in Catalyst Layer on Platinum Loading, Journal of Power Sources, 132 (2004) 11-17.
[427] E. Passalacqua, F. Lufrano, G. Squadrito, A. Patti, L. Giorgi, Nafion Content in the Catalyst Layer of Polymer Electrolyte Fuel Cells: Effects on Structure and Performance, Electrochimica Acta, 46 (2001) 799-805.
[428] Y.-C. Park, K. Kakinuma, H. Uchida, M. Watanabe, M. Uchida, Effects of Short-Side-Chain Perfluorosulfonic Acid Ionomers as Binders on the Performance of Low Pt Loading Fuel Cell Cathodes, Journal of Power Sources, 275 (2015) 384-391.
[429] A. Kongkanand, M.F. Mathias, The Priority and Challenge of High-Power Performance of Low-Platinum Proton-Exchange Membrane Fuel Cells, The Journal of Physical Chemistry Letters, 7 (2016) 1127-1137.
[430] A. Orfanidi, P.J. Rheinländer, N. Schulte, H.A. Gasteiger, Ink Solvent Dependence of the Ionomer Distribution in the Catalyst Layer of a PEMFC, Journal of The Electrochemical Society, 165 (2018) F1254-F1263.
[431] M. Yamaguchi, T. Matsunaga, K. Amemiya, A. Ohira, N. Hasegawa, K. Shinohara, M. Ando, T. Yoshida, Dispersion of Rod-Like Particles of Nafion in Salt-Free Water/1-Propanol and Water/Ethanol Solutions, Journal of Physical Chemistry B, 118 (2014) 14922-14928.
[432] S. Gu, R. Cai, T. Luo, Z. Chen, M. Sun, Y. Liu, G. He, Y. Yan, A Soluble and Highly Conductive Ionomer for High-Performance Hydroxide Exchange Membrane Fuel Cells, Angewandte Chemie, 121 (2009) 6621-6624.
[433] N.J. Bunce, D. Bejan, Mechanism of electrochemical oxidation of ammonia, Electrochimica Acta, 56 (2011) 8085-8093.
[434] M. Amirinejad, S. Rowshanzamir, M.H. Eikani, Effects of operating parameters on performance of a proton exchange membrane fuel cell, Journal of Power Sources, 161 (2006) 872-875.
[435] T. Wang, Y. Zhao, B.P. Setzler, Y. Yan, Improving Performance and Durability of Low Temperature Direct Ammonia Fuel Cells: Effect of Backpressure and Oxygen Reduction Catalysts, Journal of the Electrochemical Society, 168 (2021) 014507.
[436] M.R. Somalu, A. Muchtar, W.R.W. Daud, N.P. Brandon, Screen-printing inks for the fabrication of solid oxide fuel cell films: A review, Renewable and Sustainable Energy Reviews, 75 (2017) 426-439.